Imperial College London

An automated fluorescence lifetime imaging multiwell plate reader: application to high content imaging of protein interactions and label free readouts of cellular metabolism

Douglas James Kelly

Photonics Group

Department of Physics

Imperial College London

Thesis submitted in partial fulfilment of the requirements
for the degree of Doctor of Philosophy (Ph. D.)

Imperial College of Science, Technology and Medicine

To my family and to my friends

Abstract

This thesis reports on work performed in the development and application of an automated plate reading microscope implementing wide field time gated fluorescence lifetime imaging technology.

High content analysis (HCA) imaging assays enabled by automated microscopy platforms allow hundreds of conditions to be tested in a single experiment. Though fluorescence lifetime imaging (FLIM) is established in life sciences applications as a method whereby quantitative information may be extracted from time-resolved fluorescence signals, FLIM has not been widely adopted in an HCA context. The FLIM plate reader developed throughout this PhD has been designed to allow HCA-FLIM experiments to be performed and has been demonstrated to be capable of recording multispectral, FLIM and bright field data from 600 fields of view in less than four hours.

FLIM is commonly used as a means of reading out Förster resonance energy transfer (FRET) between fluorescent fusion proteins in cells. Using the FLIM plate reader to investigate large populations of cells per experimental condition without significant user input has allowed statistically significant results to be obtained in FRET experiments that present relatively small changes in mean fluorescent lifetime. This capability has been applied to investigations of FOXM1 SUMOylation in response to anthracycline treatment, and to studies of the spatiotemporal activation profiles of small GTPases. Furthermore, the FLIM plate reader allows FLIM-FRET to be applied to protein-protein interaction screening. The application of the instrument to screening RASSF proteins for interaction with MST1 is discussed.

The FLIM plate reader was also configured to utilise ultraviolet excitation radiation and optimised for the measurement of autofluorescence lifetime for label-free assays of biological samples. Experiments investigating the autofluorescence lifetime of live cells under the influence of metabolic modulators are presented alongside the design considerations necessary when using UV excitation for HCA-FLIM.

Author declaration

All the work presented in this thesis was performed by the author with the following exceptions:

- Sample preparation for RASSF-MST1 interaction screen experiments was performed by Dr Anca Margineanu and Jia Chan.
- Sample preparation for RhoA GTPase experiments was performed by Natalie Welsh.
- Sample preparation and manual image segmentation for Rac1 GTPase experiments was performed by Jessica McCormack.
- Sample preparation for cartilage autofluorescence lifetime experiments was performed by Dr Mohammad Nickdel.

Copyright declaration

Acknowledgements

First and foremost, I would like to thank my supervisors Paul, Chris and Eric, for originally giving me the opportunity to pursue a Ph. D., and for their continued advice, guidance and patience throughout my Masters and Ph. D. projects.

The successes I enjoyed in the course of the project would certainly not have been possible without the knowledgeable input of many postdocs in Photonics and beyond. In particular Anca Margineanu and Sunil Kumar in Photonics, and Ka Kei Ho in the Department of Surgery and Cancer, contributed significantly to my progress.

I've been fortunate enough to work alongside a great group of people over the course of my time at Imperial, whose combination of intellectual conversation and "barrack room banter" has often ensured that long hours in the lab have not felt like a burden. Particular thanks are owed to Sean, Dom, Gift and Romain for their assistance in the areas of programming, high content analysis assays, molecular biology and horticulture, respectively.

I would like to extend thanks, too, to those involved at various levels in the Institute of Chemical Biology, whilst the importance of the assistance provided by Martin and Simon in the workshop and Judith, Sarah and Marcia in the Photonics admin office cannot be overstated. I would also like to acknowledge the studentship funding provided by the Engineering and Physical Sciences Research Council via the Institute of Chemical Biology.

Finally, I would like to thank my friends and family for their support and advice throughout what has at times felt like a never-ending process. I couldn't have reached this point without you.

Table of contents

Abstract 5

Author declaration 6

Copyright declaration 6

Acknowledgements 7

List of figures 13

List of tables 19

List of abbreviations 21

Chapter 1: Thesis overview 23

Chapter 2: Introduction 25

2.1 Introduction to fluorescence 26

2.1.1 Molecular basis of fluorescence 26

2.1.2 Properties of fluorescence 28

2.2 Biological applications of fluorescence 30

2.2.1 Biological applications of fluorescent dyes 31

2.2.2 Genetically expressed fluorescent constructs: fluorescent proteins 32

2.2.3 Other genetically expressed fluorescent constructs 34

2.2.4 Techniques for transfecting genetically encoded fluorescent constructs 35

2.2.5 Strategies for obtaining stable cell lines expressing genetically encoded constructs 36

2.2.6 Endogenous fluorophores 36

2.3 Förster Resonance Energy Transfer 37

2.3.1 FRET principles 37

2.3.2 FRET biosensors 40

2.3.3 Means of measuring FRET 42

2.3.4 FRET issues 45

2.4 Fluorescence microscopy instrumentation 47

2.4.1 Epifluorescence microscopy 47

2.4.2 Sectioning methods in fluorescence microscopy 47

2.4.3 Fluorescence lifetime imaging microscopy 48

2.5 Automated fluorescence microscopy and high content analysis 54
2.5.1 Assay quality parameter Z' 55
2.5.2 Homogeneous fluorescence assays for HTS: flow cytometry 57
2.5.3 Homogeneous fluorescence assays for HTS: assays of protein-protein interactions 57
2.5.4 Fluorescence intensity-based imaging methods for HCA 58
2.5.5 FLIM plate readers for HCA 60
2.6 Summary 61
Chapter 3: Development of an automated FLIM plate reader for high content FLIM imaging 62
3.1 FLIM plate reader hardware 63
3.1.1 Pulsed illumination for time resolved fluorescence measurements 65
3.1.2 Time resolved fluorescence detection 68
3.1.3 Bright field imaging 69
3.1.4 Liquid handling for time lapse assays 70
3.2 FLIM plate reader software 72
3.2.1 Extension of automated acquisition sequence capabilities 72
3.2.2 "Prefind" tools 74
3.2.3 Development of user interface 80
3.3 Preliminary HRI characterisation 81
3.3.1 Photon-digital number conversion factor 82
3.3.2 Gate profiles and generation of library IRFs 86
3.3.3 Concluding remarks: current standards for HRI choice 88
3.4 FLIM fitting software 89
3.4.1 Segmentation 90
3.4.2 "FRET model" fitting 90
3.5 FRET construct test samples 91
3.5.1 Methods: generating FRET constructs plates 93
3.5.2 Methods: Imaging parameters 93
3.5.3 Methods: Analysis of FRET constructs plates 94
3.5.4 Comparison of cell lines 94
3.5.5 Comparison of live cell and fixed cell imaging 97

3.5.6 Comparison of growth substrate 98
3.5.7 Pseudo dose response: comparison of data models 98
3.5.8 FRET construct plates for characterisation of instrument speed 103
3.6 Summary 107
3.7 Future development 107
Chapter 4: Intermolecular FRET 109
4.1 SUMOylation of FOXM1 110
4.1.1 Biological context 110
4.1.2 Preliminary experiment: timecourse of doxorubicin treatment, TCSPC FLIM 117
4.1.3 Preliminary experiment: doxorubicin background fluorescence 119
4.1.4 Preliminary experiment: optimisation of transfection conditions 122
4.1.5 FOXM1-SUMOylation in response to anthracycline treatment time course 127
4.1.6 Summary 138
4.1.7 Future work 138
4.2 RASSF family-MST1 interaction screen 140
4.2.1 MST1 and the RASSF-family proteins: biological context 140
4.2.2 Sample preparation 141
4.2.3 Image acquisition and analysis 144
4.2.4 Results 146
4.2.5 Discussion 153
4.2.6 Summary 155
4.2.7 Future work 155
Chapter 5: Automated FLIM–FRET of Raichu biosensors 158
5.1 Spatio-temporal profiles of RhoA small GTPase activation in response to calcium stimulation for the formation of adherens junction 160
5.1.1 Biological context 160
5.1.2 Sample preparation 163
5.1.3 Image acquisition and analysis 164
5.1.4 Results 167
5.1.5 Discussion 169

5.2 Localisation of Rac1 small GTPase activation modulated by CdGAP 171
5.2.1 Biological context 171
5.2.2 Sample preparation 172
5.2.3 Image acquisition and analysis 173
5.2.4 Results 175
5.2.5 Discussion 177
5.3 Summary 178
5.4 Future work 178
Chapter 6: Autofluorescence 180
6.1 Biological background to cell autofluorescence imaging 181
6.1.1 Reduced nicotinamide adenine dinucleotide 181
6.1.2 Flavins 184
6.1.3 Nicotinamide adenine dinucleotide phosphate 184
6.1.4 Cellular metabolism, redox state and disease 185
6.1.5 Means of modulating metabolic state *in vitro* 185
6.2 Fluorescence as a means of studying metabolism 187
6.3 Application of FLIM to NADH imaging 189
6.4 UV-specific instrument development 190
6.5 Characterisation and solution-based experiments 191
6.5.1 Fitting UV-excited FLIM data 191
6.5.2 Background fluorescence characterisation 194
6.5.3 NADH binding in solution 196
6.6 Cell-based assays 197
6.6.1 MCF7 cells: control plate 198
6.6.2 MCF7 cells: Viability study 201
6.6.3 MCF7 cells: Metabolic modulation experiments 204
6.6.4 Breast cancer cell line screening 215
6.6.5 Doxorubicin response 217
6.6.6 Cisplatin response 220
6.7 Tissue autofluorescence 222

6.7.1 Biological background and motivation 223
6.7.2 Development of methods 223
6.7.3 Results 224
6.7.4 Conclusions 225
6.8 Summary 226
6.9 Future work 227
Chapter 7: Conclusions and outlook 229
7.1 Summary of thesis 229
7.2 Ongoing projects and future work 231
Publications and conferences 234
References 236
Appendix 1: Derivation of expression for appropriate thresholding of HRI photon counting images 263
Appendix 2: FRET constructs: further details 264

List of figures

Figure 2-1 Jabłoński diagram outlining molecular processes involved in luminescence. 26
Figure 2-2 Exemplar absorption and emission spectra. 27
Figure 2-3 Example structures of fluorescent dyes. 31
Figure 2-4 Contrasting approaches in immunofluorescence imaging. 32
Figure 2-5 Structure of Green Fluorescent Protein. 33
Figure 2-6 Illustration of processes of transfection. 35
Figure 2-7 Definition of angles between donor and acceptor dipole moments, and orientation factors resulting from different relative orientations of donor- and acceptor dipole moments. 38
Figure 2-8 Illustration of the dependence of FRET efficiency on fluorophore separation. 39
Figure 2-9 Illustration of spectral overlap between FRET donor emission and FRET acceptor excitation spectra for an EGFP-mCherry FRET pair. 40
Figure 2-10 Illustration of different means of implementing FRET biosensors. 41
Figure 2-11 Illustration of the effects of FRET as measured by sensitised emission. 43
Figure 2-12 Illustration of the effects of FRET as measured by fluorescence lifetime. 44
Figure 2-13 Illustration of κ^2 and FRET efficiency distributions in the static averaging regime. 46
Figure 2-14 A schematic diagram showing features of a microscope configured for measurement of epifluorescence. 47
Figure 2-15 Illustration of relevant measurements in frequency domain FLIM. 49
Figure 2-16 Illustration of the principles of time correlated single photon counting for fluorescence lifetime measurement. 50
Figure 2-17 Illustration of the principles of wide field time gated FLIM. 52
Figure 2-18 A schematic showing the critical elements of a high rate imager system and the amplification steps in its operation as a gated optical intensifier. 53
Figure 2-19 Multiwell plates for use in HTS/HCA experiments. 55
Figure 2-20 Illustration of dose response curves for assays of different quality. 56
Figure 3-1 Photographs of the FLIM plate reader system. 64
Figure 3-2 Schematic showing electronic connectivity between the components that make up the FLIM plate reader. 65
Figure 3-3 Schematic showing the layout of the "spectral selection unit" for coupling pulsed laser light into a single mode fibre. 66
Figure 3-4 Comparison of temporal drift for multimode and single mode fibres 67
Figure 3-5 Plots showing differences between nominal and measured delays set by HDG delay boxes before applying software calibration table corrections. 69
Figure 3-6 Characterisation of a simple automated liquid handling system for integration into the FLIM plate reader. 71

Figure 3-7 Screenshots illustrating the linearised least squares method of determining lifetime previews. 73
Figure 3-8 Flow chart describing the generalised process followed by the prefind tools implemented in the plate reader acquisition software. 75
Figure 3-9 Screenshot of the control window for setting up the cell prefind tool in the FLIM plate reader acquisition control software, illustrating the range of prefind options available. 75
Figure 3-10 An illustration of the deployment of low magnification phase contrast cell prefind on the FLIM plate reader using MCF7 cells. 77
Figure 3-11 Spectral sensitivity curves for two HRIs used to collect data in this thesis. 82
Figure 3-12 A schematic showing the experimental set up used to determine the relationship between photons detected by an HRI and the mean recorded signal in digital numbers. 83
Figure 3-13 Exemplar regions from photon counting experiments to establish photon flux on the photocathode of an HRI. 84
Figure 3-14 Results of experiments to determine conversion factor k between recorded signal in digital numbers, and detected photons. 85
Figure 3-15 A schematic showing the experimental set up used to generate gate profiles for HRIs. 86
Figure 3-16 Exemplar gate profiles from the single edge and blue-sensitive model HRIs. 87
Figure 3-17 Flow chart summarizing the methods used for generation and analysis of FRET construct test samples. 92
Figure 3-18 Exemplar phase contrast and mCerulean fluorescence intensity images for each of the three cell lines under investigation. 95
Figure 3-19 Results of experiment investigating FRET construct lifetime across three different cell lines. 96
Figure 3-20 Results of experiment investigating FRET construct lifetime measured in live MCF7 cells at 37oC in comparison to fixed MCF7 cells measured at room temperature. 97
Figure 3-21 Results of experiment investigating FRET construct lifetime measured in live MCF7 cells plated on plastic in comparison to live MCF7 cells plated on glass measured at 37^{o}C. 98
Figure 3-22 Illustration of plating strategy for a "pseudo-dose response" FRET constructs plate. 99
Figure 3-23 Results of a monoexponential fit to data acquired from a "pseudo-dose response" FRET constructs plate. 100
Figure 3-24 Results of a global biexponential fit to data acquired from a "pseudo-dose response" FRET constructs plate. 101
Figure 3-25 Results of fitting an “ECFP-FRET” model to data acquired from a "pseudo-dose response" FRET constructs plate. 102
Figure 3-26 Charts showing breakdown of acquisition timing for acquisition of FRET construct plates. 104
Figure 3-27 Plots of assay quality parameter Z' and standard error calculated cellwise against number of fields of view acquired. 106

Figure 3-28 False colour lifetime plate map for a monoexponential fit to Coumarin 6 dye. 107
Figure 4-1 Chemical structures of (a) doxorubicin and (b) epirubicin. (c) X-ray diffraction structure of DNA-doxorubicin complex illustrating intercalation. 111
Figure 4-2 Schematic showing mechanism of ROS generation by anthracyclines. 111
Figure 4-3 A schematic of the SUMOylation pathway 114
Figure 4-4 Summary of phosphorylation and SUMOylation post-translational modifications of FOXM1. 115
Figure 4-5 FOXM1-SUMOylation experiment fluorescent constructs 116
Figure 4-6 Results from preliminary experiment into FOXM1 SUMOylation measured by FLIM on a TCSPC system. 118
Figure 4-7 Absorption and emission spectra of doxorubicin, overlaid with transmission spectra of filters in the FLIM plate reader. 119
Figure 4-8 Results of experiment showing background effect of treating with doxorubicin in untransfected cells. 121
Figure 4-9 Illustration of plate layout and combinations of plasmids transfected to investigate effects of acceptor construct and free FP overexpression on FOXM1-eGFP lifetime. 123
Figure 4-10 Results of experiment showing effects of increasing SUMO1-TRT expression in the absence of doxorubicin treatment. 125
Figure 4-11 Flow chart summarizing the methods used for generation and analysis of FOXM1-SUMOylation assay samples. 127
Figure 4-12 Plating strategy (plate 1) for experiment investigating FOXM1-SUMOylation in response to doxorubicin treatment. 128
Figure 4-13 Plating strategy (plate 2) for experiment investigating FOXM1-SUMOylation in response to doxorubicin treatment. 129
Figure 4-14 Results of monoexponential fit to data from the first plate experiment designed to investigate FOXM1-SUMOylation in response to doxorubicin treatment. 132
Figure 4-15 Results of a global fit of a biexponential model to data from the first plate experiment designed to investigate FOXM1-SUMOylation in response to doxorubicin treatment. 133
Figure 4-16 Results of monoexponential fit to data from the second plate experiment designed to investigate FOXM1-SUMOylation in response to doxorubicin treatment. 135
Figure 4-17 An overview of RASSF family protein structures. 141
Figure 4-18 Schematic representation of the fluorescent constructs used in the RASSF-MST1 interaction screen. 142
Figure 4-19 Plate layouts for RASSF-family MST1 interaction screen experiments 142
Figure 4-20 Flow chart summarizing the methods used for generation and analysis of RASSF family interaction screen assay samples. 143

Figure 4-21 Results of monoexponential fits for first RASSF plate containing donor only, donor + acceptor, and donor + acceptor + KRas constructs. 146
Figure 4-22 Plots illustrating correlation between ratio of measured acceptor:donor intensities, and fitted donor lifetime for cells from wells in which RASSF-family protein-eGFP fusions are cotransfected with MST1-mCherry. 147
Figure 4-23 Results of monoexponential fits for second RASSF plate containing donor only, donor + truncated acceptor, and donor + negative control mutated acceptor constructs 148
Figure 4-24 Plots illustrating correlation between ratio of measured acceptor:donor intensities, and fitted donor lifetime for cells from wells in which RASSF-family protein-eGFP fusions are cotransfected with truncated acceptor construct SARAH-mCherry. 150
Figure 4-25 Results from biexponential fit to data acquired from cells cotransfected with classical RASSF-eGFP proteins and full length MST1-mCherry constructs. 152
Figure 4-26 Results from biexponential fit to data acquired from cells cotransfected with classical RASSF-eGFP proteins and truncated SARAH-mCherry constructs. 153
Figure 4-27 Exemplar donor channel integrated intensity images for RASSF-family proteins to illustrate anomalous fluorescence distribution for cells expressing RASSF8 alone. 154
Figure 5-1 Schematic overview of polarised epithelial cells and adherens junction structures 161
Figure 5-2 Schematic of Raichu-RhoA FRET biosensor for RhoA activation mediated by RhoA-GEFs and RhoA-GAPs. 162
Figure 5-3 Flow chart summarizing the methods used for generation and analysis of RhoA small GTPase activation samples. 163
Figure 5-4 The effects of bright fibroblasts on automated segmentation of keratinocyte samples 165
Figure 5-5 Illustration of implementation of manual cell segmentation tools. 166
Figure 5-6 Overview of segmentation of cells and subcellular regions used for analysis of RhoA calcium switch data 166
Figure 5-7 Results of experiment investigating RhoA activation in response to a calcium switch, lateral membrane segmentation applied. 168
Figure 5-8 Results of experiment investigating RhoA activation in response to a calcium switch, cytosol segmentation applied. 169
Figure 5-9 Results of biochemical experiments carried out in parallel with FLIM experiments by Natalie Welsh in the National Heart and Lung Institute, Imperial College London 171
Figure 5-10 Schematic of Raichu-Rac1 FRET biosensor for Rac1 activation mediated by Rac1-GEFs and Rac1-GAPs. 172
Figure 5-11 Flow chart summarizing the methods used for generation and analysis of Rac1 small GTPase activation samples. 172
Figure 5-12 Plate map showing transfection conditions across 36 wells for Rac1 experiment 173

Figure 5-13 Results of experiment investigating Rac1 activation mediated by cdGAP overexpression with manual cell segmentation. 176
Figure 5-14 Results of experiment investigating Rac1 activation mediated by cdGAP overexpression with automated cell segmentation. 177
Figure 6-1 Schematic of major metabolic pathways involving NADH. 182
Figure 6-2 Measured NADH absorption and emission spectra 188
Figure 6-3 Schematic showing the optical path for wide filed time gated FLIM acquisitions using UV-wavelength excitation on the FLIM plate reader. 191
Figure 6-4 Stilbene fluorescence lifetime data acquired under 370 nm excitation across a range of emission wavelengths using the spectrofluorimeter. 193
Figure 6-5 Simulated data illustrating lifetime fitting performance using a long lifetime reference dye. 194
Figure 6-6 Background fluorescence contributions under UV excitation. 195
Figure 6-7 Results of experiment investigating repeatability of lifetime measurements across wells. 197
Figure 6-8 Plate maps showing spatial distribution of fitted lifetime for untreated MCF7 plate. 199
Figure 6-9 Untreated MCF7 plate mean lifetimes. 200
Figure 6-10 Results of vital dye exclusion assay following UV-excited FLIM imaging sequence. 203
Figure 6-11 Exemplar bright field images interleaved with a long-term course of FLIM measurements of BT474 cells for investigation of morphology. 204
Figure 6-12 Global fit results from automated rotenone time course experiment in which stimulation with control media or 1 μM rotenone occurs immediately before the fourth time point. 205
Figure 6-13 Imagewise fit results from an automated rotenone time course experiment. 206
Figure 6-14 Global fit results from a manual FCCP time course experiment. 208
Figure 6-15 Imagewise fit results from a manual FCCP time course experiment in which stimulation with control media or 1 μM FCCP occurs immediately before the fourth time point. 209
Figure 6-16 Imagewise fit results from a manual 2-deoxyglucose time course experiment in which stimulation with 10 mM 2DG is made immediately after the third time point. 211
Figure 6-17 Global fit results for a hydrogen peroxide dose response experiment. 213
Figure 6-18 Imagewise fit results for a hydrogen peroxide dose response experiment. 214
Figure 6-19 Mean lifetimes across cell types and seeding densities. 216
Figure 6-20 Doxorubicin treatment dose response, fitted mean lifetimes. 218
Figure 6-21 Fit parameters for drug resistant and sensitive cells plotted against drug concentration. 219
Figure 6-22 Plate maps for cisplatin experiment. 220
Figure 6-23 Exemplar fields of view across cisplatin dose and treatment time, showing phase contrast and false-coloured mean lifetime images. 221
Figure 6-24 Fitted parameters from cisplatin treated cells. 222
Figure 6-25 Results of wide field time gated FLIM imaging of enzyme-treated porcine cartilage explants. 225

Figure 7-1 Preliminary data acquired with FLIM plate reader during a project to investigate protein-protein interactions during mitosis in genome-edited cell lines expressing fluorescent protein fusions at endogenous levels. 232
Figure 7-2 Preliminary data showing relative dissociation constants as calculated from FLIM plate reader data as outlined in Chapter 4: section 4.2.7. 233

List of tables

Table 2-1 Summary of properties of selected fluorescent proteins. 34
Table 2-2 A simple categorisation for interpretation of Z'-factor values applied to HTS/HCA assays[116]. 56
Table 3-1 Summary of UV transmission properties of diffuser wheels, measured at 365 nm. 68
Table 3-2 A summary of manufacturer specifications for two HRIs used to collect data in this thesis. 81
Table 3-3 Calculated k-factors (and 95% confidence intervals on fitted parameters), showing the relationship between detected photons and recorded signal in digital numbers for incident radiation at 623 nm. 85
Table 3-4 Formulation of imaging media. 93
Table 3-5 NTH segmentation parameters used for FRET construct plate analysis. 94
Table 3-6 Global fit parameters and average χ^2 resulting from a global fit of a biexponential model to data acquired from a "pseudo-dose response" FRET constructs plate. 101
Table 3-7 Global fit parameters and average χ^2 resulting from a global fit of an "ECFP-FRET" model to data acquired from a "pseudo-dose response" FRET constructs plate. 102
Table 3-8 Summary of means by which acquisition time may be decreased for FLIM plate reader experiments. 105
Table 4-1 NTH segmentation parameters for automated segmentation of MCF7 expressing FOXM1-eGFP or FOXM1mut-eGFP. 124
Table 4-2 NTH segmentation parameters for automated segmentation of MCF7 expressing FOXM1-eGFP or FOXM1mut-eGFP. 130
Table 4-3 Globally fit lifetime parameters from bioexponential model fit to data from the first plate experiment designed to investigate FOXM1-SUMOylation in response to doxorubicin treatment. 133
Table 4-4 Table showing constituents of buffer for electroporation of Cos7 cells. 143
Table 4-5 Segmentation parameters for two-scale NTH segmentation algorithm used in RASSF-famliy protein screen. 144
Table 4-6 Summary of biexponential fit results for different classical RASSF family proteins in cells cotransfected with MST1-mCherry 152
Table 4-7 Summary of biexponential fit results for different classical RASSF family proteins in cells cotransfected with SARAH-mCherry. 153
Table 5-1 NTH segmentation parameters for automated segmentation of keratinocytes expressing Racihu-Rac1 174
Table 6-1 Chemical equations showing substrates and products at key stages in cellular respiration. 182
Table 6-2 Simulation and resulting fit parameters for long lifetime reference dye. 193
Table 6-3 Sample holder parameters 195
Table 6-4 Globally fitted lifetime results from rotenone time course experiment. 205

Table 6-5 Globally fitted lifetime results from FCCP time course experiment. 208
Table 6-6 Globally fitted lifetime results from hydrogen peroxide response experiment. 213
Table 6-7 Summary of cell lines investigated.[331–336] 215

List of abbreviations

2DG	2-deoxyglucose
AA	Amino acid
Ab	Antibody
ADC	Analogue-to-digital converter
ADP	Adenosine diphosphate
ATP	Adenosine triphosphate
BiFC	Bimolecular fluorescence complementation assay
CCD	Charge coupled device
CFD	Constant fraction discriminator
CLSM	Confocal laser scanning microscopy
CMOS	Complementary metal oxide semiconductor
CRISPR	Clusters of regularly interspaced short palindromic repeats
DAPI	4', 6-diamidino-2-phenylindole
DAQ	Data acquisition
DASPI	2-(p-dimethylaminostyryl)-pyridylmethyl iodide
DMEM	Dulbecco's modified Eagle's medium
DN	Digital numbers
DSB	Double strand break
dsDNA	Double-stranded deoxyribonucleic acid
ETC	Electron transport chain
FAD	Flavin adenine dinucleotide
FAP	Fluorogen-activating protein
FCCP	Carbonyl cyanide 4-(trifluoromethoxy)phenylhydrazone
FCS	Foetal calf serum
FLIM	Fluorescence lifetime imaging microscopy
FOXM1	Forkhead box protein M1
FP	Fluorescent protein
FPGA	Field programmable gate array
FRET	Förster resonance energy transfer
GAP	GTPase-activating protein
GEF	Guanine nucleotide exchange factor
GFP	Green fluorescent protein
GOI	Gated optical intensifier

GTP	Guanosine triphosphate
GUI	Graphical user interface
HBSS	Hank's buffered salt solution
HCA	High content analysis
HCA	High content analysis
HRI	High rate imager
HTS	High throughput screening
IR	Infra-red
IRF	Instrument response function
LDH	Lactate dehydrogenase
mMDH	Mitochondrial malate dehydrogenase
MST1	Mammalian sterile 20-like kinase 1
NADH	Reduced nicotinamide adenine dinucleotide
ND	Neutral density
NTH	Non-linear top hat segmentation
OA	Osteoarthritis
PBS	Phosphate buffered saline
PKN	Protein kinase N1
PMT	Photomultiplier tube
RASSF	Ras association domain family proteins
ROS	Reactive oxygen species
SARAH	Salvador-RASSF-Hippo domain
SIM	SUMO-interacting motif
SUMO	Small ubiquitin-like modifier
TAC	Time-to-amplitude converter
TALEN	Transcription activator-like effector nuclease
TCP	Transmission control protocol
TCSPC	Time correlated single photon counting
TDC	Time-to-digital converter
TRT	TagRFP-T
UV	Ultra violet
VI	LabVIEW virtual instrument
ZFN	Zinc finger nuclease

Chapter 1: Thesis overview

This thesis describes the development and application of an automated fluorescence lifetime imaging (FLIM) multiwell plate reader utilising wide field time gating FLIM technology. The work has aimed to explore the broad potential of fluorescence lifetime imaging as a readout for high content analysis assays. Its applications have included investigations of cell signalling pathways and protein-protein interactions using Förster resonance energy transfer (FRET) and the measurement of lifetimes associated with endogenous fluorophores linked to cell metabolism and structural proteins. For these applications the capability of the FLIM plate reader to provide automated acquisition of large data sets has proved invaluable to enable statistically robust quantitative analysis of the underlying biology.

Chapter 2: introduces basic principles of fluorescence and its measurable properties, including fluorescence lifetime. In particular, FRET measurements are discussed as a means to investigate protein-protein interactions by FLIM. An overview of approaches to implementing FLIM experiments is presented with particular focus on the wide field time gating method employed for high content FLIM assays on the automated plate reader. The concept of high content assays is introduced and literature pertaining to previous implementations plate reader implementations of FLIM experiments is summarised.

In Chapter 3:, the FLIM plate reader that I have developed over the course of the PhD project is presented. The hardware components that make up the FLIM plate reader are outlined with justification for the decisions that I made in the design process. Elements of the software that was continuously developed throughout the project are described. A series of experiments characterising the enabling high rate imager technology are presented and a study using standard FRET constructs to illustrate the performance of the FLIM plate reader is discussed.

Two separate projects that make use of intermolecular FRET are presented in Chapter 4:. The first of these projects is concerned with the addition of small ubiquitin-like modifier (SUMO) to the transcription factor and oncoprotein FOXM1 in response to DNA damage caused when cells are treated with anthracycline anti-cancer drugs. The challenges and optimisation of the experimental protocol, including the investigation of the effect of treatment time on FOXM1-SUMOylation, are described with the resulting FLIM data. The intermolecular FRET project presented in the second part of the chapter is a screening assay to identify binding partners for mammalian sterile 20-like kinase 1 protein from the RASSF family of proteins: this series of experiments illustrates the potential for the FLIM plate reader to be used in the context of protein-protein interaction screening.

Chapter 5 concerns FLIM assays of intramolecular FRET using genetically expressed biosensors to read out the activation of small GTPase proteins associated with the formation of cell-cell junctions between

keratinocytes. Two separate intramolecular FRET biosensors are utilised in separate studies to investigate the spatio-temporal profile of RhoA activation in response to calcium stimulation and the effects on the localisation of Rac1 activation induced by overexpression of the GTPase activating protein CdGAP. The experimental challenges are discussed and a new software tool that I developed for tablet-based image segmentation is presented.

Chapter 6: is concerned with the application of the automated FLIM plate reader to label-free lifetime-based readouts of endogenous fluorophores. The modifications to the plate reader necessary to facilitate autofluorescence readouts with ultraviolet excitation are outlined, alongside the experimental protocols developed to take account of the particular challenges such measurements present. The first report of automated FLIM assays utilising readouts of metabolite autofluorescence lifetime is presented with their application to assay cellular responses to drug treatments. In addition, the application of the ultraviolet-excited FLIM plate reader to label-free readouts of tissue matrix properties is presented. Here FLIM was applied to ex vivo cartilage tissue to study the potential of autofluorescence lifetime to read out stages of biochemical degradation, which served as a model of osteoarthritis. This work supports the development of a FLIM-based instrumentation that could be used to stage progression of the disease.

Chapter 7: provides a summary of the developments and findings presented in this thesis, as well as outlining a number of potential avenues for future research utilising automated FLIM multiwell plate readers.

Chapter 2: Introduction

Over the past half century, fluorescence techniques have become ever more ubiquitous in the life sciences, providing a class of non-destructive methods capable of resolving spatio-temporal dynamics in live biological systems that are typically obscured when performing biochemical assays. This chapter introduces the phenomenon of fluorescence and seeks to provide an overview of associated methods and their application to biological experiments. This chapter serves as an introduction to the concepts of Förster Resonance Energy Transfer (FRET) and Fluorescence Lifetime Imaging (FLIM), and provides context for the application of these methods to high content analysis (HCA) experiments investigating protein interactions in cells. Topics covered in this chapter include:

- The molecular basis for and measurable properties of fluorescence.
- Biological applications of fluorescence and the different means of fluorescently labelling intracellular molecules of interest.
- The phenomenon of FRET, different approaches to designing FRET probes and methods for measuring FRET.
- Fluorescence microscopy instrumentation; including an overview of methods and hardware for the acquisition of FLIM data.
- An overview of recent advances in automated microscopy and high content analysis hardware and applications in the life sciences.

2.1 Introduction to fluorescence

2.1.1 Molecular basis of fluorescence

Fluorescence is a type of luminescence and is the emission of a photon by a molecule following excitation by a photon of higher energy (shorter wavelength). The molecular processes involved in fluorescence can be represented using a Jabłoński diagram: Figure 2-1 presents such a simplified picture of the energy levels associated with a fluorescent molecule (fluorophore). The diagram outlines the possible transitions between ground- and first excited singlet states (S_0 and S_1), as well as those involving the triplet state T_1. Within each of these states, there are numerous vibrational and rotational sublevels. For clarity, only three vibrational levels are shown for each state.

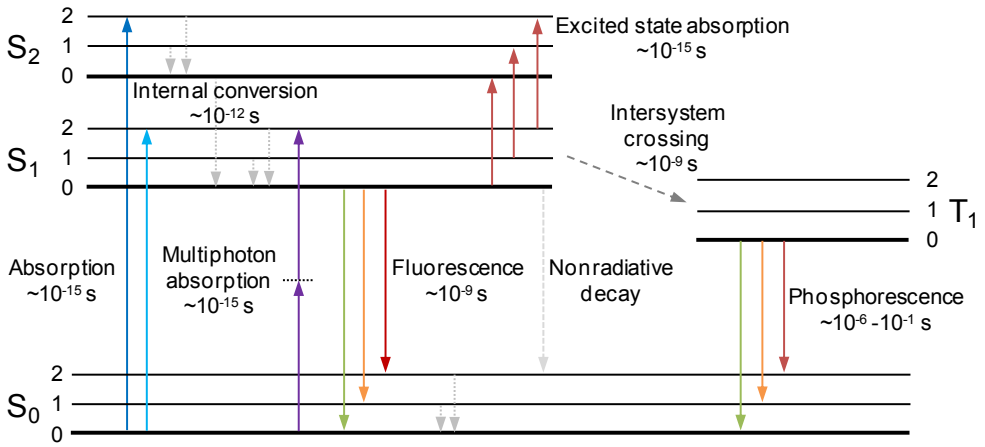

Figure 2-1 Jabłoński diagram outlining molecular processes involved in luminescence.
S_n, T_n denote n^{th} singlet and triplet states, respectively. The first three vibrational levels for each state are labelled 0, 1, 2. Rotational levels at each vibrational level are not shown. The approximate timescales of transitions are given in seconds. Coloured lines show transitions linked to the absorption or emission of photons of different energies/wavelengths, dotted lines show transitions linked to thermal (vibrational) relaxation, and dashed lines show other processes.

Several key phenomena relating to fluorescence are illustrated in the Jabłoński diagram. The relative transition rates shown indicate the favourability of transitions[1]. Critically, absorption and internal conversion to the lowest vibrational level of the S_1 state are fast, as predicted respectively by application of Einstein's coefficients combined with the spectral energy density of the excitation field[2], and the Franck-Condon principle which predicts that transitions occur more readily between states with overlapping wave functions (i.e. small energy gaps). This latter factor is the origin of Kasha's rule: stated simply, since all fluorescence emission originates from the lowest S_1 level, the emission wavelength will be independent of the wavelength of excitation light[3].

The Jabłoński diagram illustrates the necessity for excitation photons to have energies greater than the energy gap between the ground and first excited states, $\Delta E_{S_{0,0} \rightarrow S_{1,0}}$. In terms of the maximum wavelength of light λ required to transition to the first excited state, this can be restated

$$\frac{hc}{\lambda} \geq \Delta E_{S_{0,0} \rightarrow S_{1,0}} \qquad \textbf{2.1}$$

where c is the speed of light, and h is Planck's constant. Excess energy imparted by absorption of the photon is transferred into the rotational and vibrational energy states of S_1; thus a range of wavelengths may be absorbed leading to broad fluorescence excitation spectra. By similar arguments, the existence of a multiplicity of vibrational and rotational levels in the ground state leads to broad fluorescence emission spectra, which appear continuous because of collisions with solvent molecules further broadening rotational levels[4]. Since vibrational levels are similar in ground and excited states, it is typical to see emission spectra resembling a mirror image of excitation spectra: the so-called "mirror image rule"[5].

Stokes' shift is another important property of fluorescence that can be understood with reference to the Jabłoński diagram. The relatively fast relaxation to the lowest excited state (S_1) means that excitation photons generally have more energy than emitted photons. Thus, as stated above, fluorescent emission is typically of longer wavelength than the light used to excite the sample. Stoke's shift is of key importance in the practical application of fluorescence, since the difference between excitation and emission wavelengths allows separation of emitted fluorescence from scattered excitation light using spectral filters[4]. Stoke's shift, along with Kasha's rule and the mirror image rule are illustrated in the example spectra shown in Figure 2-2.

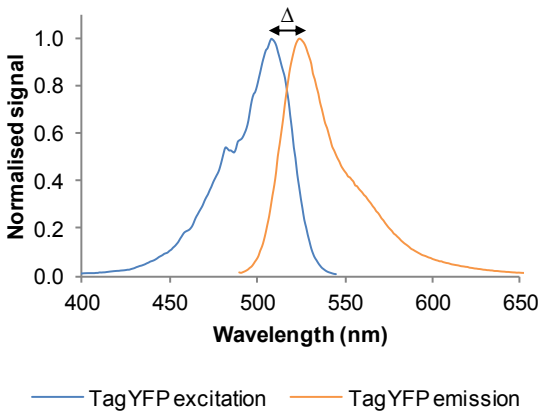

Figure 2-2 Exemplar absorption and emission spectra.
TagYFP excitation and emission spectra provided by Evrogen[6]. Δ indicates Stoke's shift between excitation and emission spectra. Excitation and emission spectra illustrate the mirror image rule.

Finally, the Jabłoński diagram presented in Figure 2-1 indicates the possibility of molecules undergoing *intersystem crossing*, a classically forbidden transition to the triplet state. When molecules are in the T_1 state, decay to the ground state is also classically forbidden and so occurs at a much slower rate than from S_1; thus photons are emitted at a much slower rate, giving rise to *phosphorescence*. The relatively long-lived nature of the excited T_1 state can lead to deleterious effects: reactions that transform the fluorophore into a non-fluorescent species, an effect known as *irreversible photobleaching,* are more probable from the triplet state[4]. In addition, triplet excited states of fluorescent species can interact with molecular oxygen to form

singlet oxygen, which is highly reactive with other singlet species and highly toxic to cells[7]. Generation of these reactive oxygen species and the resultant damage to cells is an example of *phototoxicity*.

2.1.2 Properties of fluorescence

Several different properties of fluorescent molecules may be exploited in an experimental setting. A number of these properties are outlined below.

Absorption

Knowledge of the absorption properties of molecular species at specific wavelengths allows measurements of absorption to be linked to concentration by the Beer-Lambert law,

$$\frac{I}{I_0} = 10^{-\varepsilon(\lambda)LC} \qquad \textbf{2.2}$$

where L is path length through the sample in cm, C is the concentration of species in M and $\varepsilon(\lambda)$ is the molar extinction coefficient for the species: therefore, a monochromatic light source and a photodetector may be sufficient to determine the concentration of a species if $\varepsilon(\lambda_{\text{source}})$ is known.

(Emission) intensity

Measured changes in fluorescence intensity of a fluorophore population can reflect the changes in concentration or quantum yield η, defined as the ratio of emitted photons (N_e) to absorbed photons (N_a). The quantum yield may also be expressed in terms of radiative (Γ) and non-radiative decay (k_{nr}) rates:

$$\eta = \frac{N_e}{N_a} = \frac{\Gamma}{\Gamma + k_{nr}}. \qquad \textbf{2.3}$$

Radiative and non-radiative decay rates can depend on many factors, including solvent refractive index[4], rotational mobility and collisional quenching of fluorophores. As such, measurements of fluorescence intensity may be used to infer changes in binding state or conformation of fluorescent species, or viscosity, pH or ion concentration of its environment. Quantitative measurements based on fluorescence intensity are hampered by the effects of scattering of excitation and emission light, and the presence of background signal.

Fluorescence emission spectra

Different molecules have different energy level structures (see section 2.1.1 above), and thus have different emission (and absorption) spectra. Measurements in which emitted fluorescence is resolved by wavelength, either across a continuous spectrum or in specific spectral windows, can also yield useful information on the fluorophore or its environment. The contributions to fluorescent signal of molecular species with distinct spectral profiles can be determined by unmixing algorithms, allowing conclusions to be drawn regarding relative concentrations of fluorescent species[8]. In imaging applications, the ability to separate fluorescence emission from different dye label species permits colocalisation imaging. Here, the

presence of fluorescence signal in the same pixel across multiple channels simultaneously is taken to indicate colocalisation of the specifically labelled molecules. Further, because fluorescence emission spectra depend on energy level structures, they can be modified through changes in the fluorophore environment; thus measurements of emission spectra can be used to report on parameters such as solvent polarity[9].

Fluorescence lifetime

The fluorescence lifetime of a fluorophore is the average time it spends in the excited state, and is related to the radiative and non-radiative decay rates by

$$\tau = \frac{1}{\Gamma + k_{nr}} = \frac{\eta}{\Gamma}. \qquad \textbf{2.4}$$

The lifetime of the excited state, and hence the fluorescence lifetime, is typically on the order of nanoseconds. The number of molecules in the excited state, $n(t)$, depends on the decay rates according to the differential equation

$$\frac{\partial n(t)}{\partial t} = -(\Gamma + k_{nr})n(t). \qquad \textbf{2.5}$$

The observed fluorescence intensity of a homogeneous population of fluorophores following excitation with a δ-function pulse therefore exhibits a decay, following

$$I(t) = I_0 \exp\left(-t/\tau\right) \text{ for } t \geq 0, \qquad \textbf{2.6}$$

where I_0 is the initial intensity of the sample, such that the fluorescence intensity decays to $1/e$ of that value in time τ. Such a monoexponential decay profile is only observed for the simplest fluorescent samples; typically more complex decays are observed that can be described by linear sums of exponentials with characteristic decay times τ_i and pre-exponential factors β_i:

$$I(t) = I_0 \sum_i \beta_i \exp\left(-t/\tau_i\right), \qquad \textbf{2.7}$$

In such cases, it can be useful to define a single "mean lifetime" parameter, which we define:

$$\bar{\tau} = \sum_i \beta_i \tau_i \qquad \textbf{2.8}$$

Consideration of measured fluorescence lifetimes can inform on many of the same parameters (pH, conformation, quencher concentration) as quantum yield. Pre-exponential factors from complex exponential models can yield information on the concentration ratios of mixtures of fluorescent species. Measurements of fluorescence lifetime are inherently ratiometric, meaning that they are less susceptible to

fluctuations in excitation laser power and fluorophore concentrations that make inferences of molecular parameters from intensity (quantum yield) measurements prone to artefact.

Fluorescence polarisation

Fluorophores typically possess an excitation dipole moment defined by a direction within the molecule along which electrons can move more easily. When plane polarised light is incident on an isotropic disordered population of fluorophores, those fluorophores possessing excitation dipole moments with components aligned with the electric field of the excitation light are preferentially excited. This process is known as *photoselection*[5]. If the excited state lifetime of the fluorophore is short compared to the rotational correlation time of the molecule – a measure of how fast the molecule rotates – any fluorescence is therefore emitted with a polarisation parallel to the emission dipole of the molecule. If, however, molecules reorientate between excitation and emission, then typically the emitted fluorescence from an ensemble will be more depolarised – that is, will exhibit lower *fluorescence anisotropy,* r*,* calculated as

$$r = \frac{I_{\parallel} - I_{\perp}}{I_{\parallel} + 2I_{\perp}} \qquad \textbf{2.9}$$

where $I_{\parallel}$ represents fluorescence emission polarised parallel to the excitation light, and $I_{\perp}$ represents emission polarised perpendicular to the excitation light. The degree of depolarisation of fluorescence can be used to report on factors affecting rotational diffusion time, including viscosity and protein folding[5]. Furthermore, depolarisation of fluorescence can result from non-radiative energy transfer between like fluorophores (homo-FRET), and thus be used to report on molecular association and clustering[10,11]. Time-resolved fluorescence anisotropy measurements, though requiring more complex instrumentation, permits more robust quantification of parameters and simultaneous measurement of fluorescence lifetime and rotational diffusion times[12].

2.2 Biological applications of fluorescence

Fluorescence is widely exploited in the biological sciences, both for imaging and single point measurement applications. In imaging applications, fluorescence labelling can be used to elucidate structural information at a cellular level, as well as functional information, for example pertaining to metabolism, cell cycle, and (co)localisation for proteins involved in a wide range of signalling pathways. In general, colocalisation studies are limited in spatial precision by the resolution of the imaging instrumentation. However, spectroscopic readouts of fluorescence can be sensitive to changes in the local fluorophore environment, including the proximity of the fluorophore to other molecules on scales below the imaging resolution. Forster resonance energy transfer (FRET) is an example of such a spectroscopic approach and is discussed in greater depth in section 2.3. In this section, a summary of the use of molecular labelling techniques that might be used for FRET or other fluorescence-based experiments in the life sciences is presented. In addition, the concept of exploiting endogenous fluorophores for fluorescence measurements of biological samples is introduced.

2.2.1 Biological applications of fluorescent dyes

A significant number of synthetic organic compounds exhibit fluorescence and are commonly described as fluorescent dyes. Typically, such molecules exhibit aromatic or conjugated chain structures, as illustrated in Figure 2-3, that have weakly bound or delocalised electrons giving rise to energy level structures that yield visible wavelength transitions between the ground and first excited states[4]. Synthetic fluorophores cover a range of wavelengths from UV to IR, and can be tuned to some degree to specific wavelengths[13]. Fluorescent dyes also typically have large extinction coefficients, high quantum yields and low molecular weights meaning that labelling density can be high: these factors result in high brightness for fluorescence imaging.

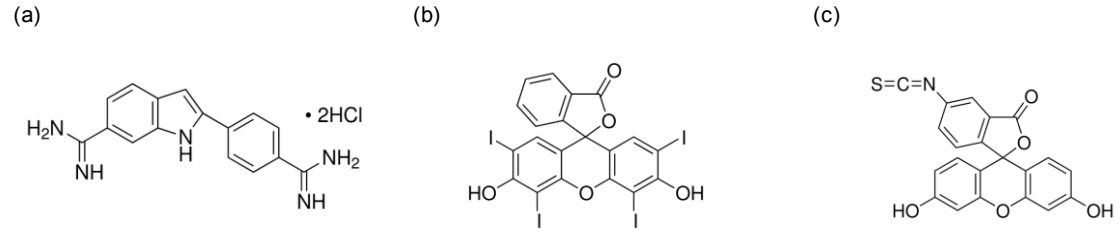

Figure 2-3 Example structures of fluorescent dyes.
(a) 4',6-Diamidino-2-phenylinodole dihydrochloride (DAPI), a DNA-binding dye. (b) Erythrosin B, used in viability assays. (c) Fluorescein isothiocyanate isomer I (FITC), commonly used as a fluorescence label in immunofluorescence assays. Images adapted from sigmaaldrich.com

Fluorescent dyes are used in various contexts in the life sciences, either in staining methods or in molecular labelling techniques. Membrane-permeant DNA-binding dyes such as DAPI or Hoechst are used ubiquitously to identify cell nuclei in fluorescence imaging applications, and can also inform on progression of the cell cycle. These dyes benefit from reduced background since the quantum yield increases by approximately 20-fold upon formation of dsDNA:dye complexes in which the DAPI is shielded from solvent[14,15]. Fluorescent dyes such as acridine orange, ethidium bromide and erythrosine can be used as stains to differentiate between necrotic, apoptotic and healthy cells by highlighting changes in membrane integrity, chromatin condensation and nuclear fragmentation[16–18].

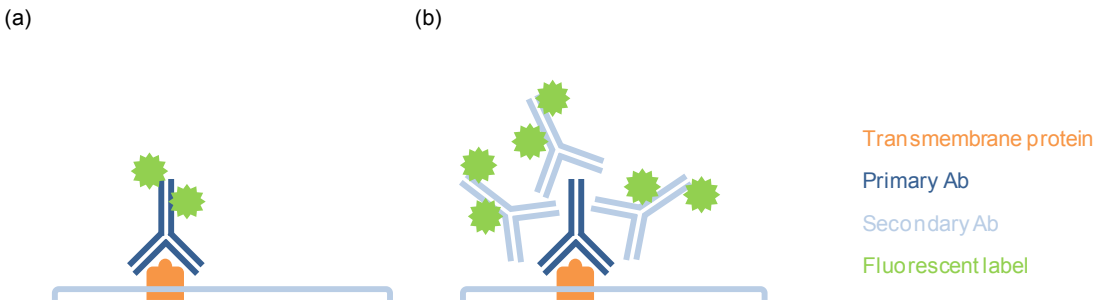

Figure 2-4 Contrasting approaches in immunofluorescence imaging.
(a) Direct approach to immunofluorescence staining. (b) Indirect approach to immunofluorescence staining, illustrating signal amplification observed when using this technique.

Dye-conjugated antibodies allow fluorescent staining to be targeted to specific proteins of interest. Immunofluorescent staining allows intracellular localisation of proteins of interest to be investigated by fluorescence imaging. Typically, one of two approaches is adopted: a dye-conjugated antibody against an antigen of interest may be introduced to the sample, leading to fluorescent staining of the protein of interest. Alternatively, the primary antibody may be introduced to bind to the antigen of interest, followed by introduction of a secondary dye-conjugated antibody that binds to the primary. The latter method is more complicated to implement but exhibits less non-specific binding, and has the advantage of amplifying the fluorescent signal at each antigen as illustrated in Figure 2-4. Though immunofluorescence imaging generally requires fixation and permeablisation of cell samples, membrane-associated proteins with domains on the cell surface may be investigated in live cells[19,20] and *in vivo*[21]. Research is ongoing into methods of introducing antibodies to the cytoplasm of living cells to further the applicability of antibody staining methods to protein dynamics. Such techniques are discussed in a 2014 review by Kaiser et al.[22], in which methods are classified according to focus: either on the uptake of antibodies by live cells, or on expression of genetically-encoded fluorescent-fusion antibody fragments (intrabodies). Recent studies have investigated the potential for labelling endogenous oncoproteins using GFP-fusion intrabodies[23]. This work highlights the possibility for labelling endogenous proteins and potential application of dual-labelling techniques to avoid potential issues with background signal, and represents a combination of immunofluorescence labelling methods with techniques revolving around expression of genetically encoded proteins, discussed below.

2.2.2 Genetically expressed fluorescent constructs: fluorescent proteins

Direct fluorescent labelling of proteins in live cells allows visualisation of the dynamics of protein trafficking and localisation, as well as providing insights into interactions between two or more proteins in approximately physiological conditions. Over the past two decades, since the isolation of Green Fluorescent Protein (GFP) from *Aequorea victoria*[24], labelling of cellular proteins with genetically expressed fluorescent proteins has become ubiquitous in life sciences labs using fluorescence assays. By inserting the DNA sequence encoding the fluorescent protein into the gene encoding the protein under investigation and introducing the resulting plasmid into cells by standard transfection techniques, it is possible to

conduct fluorescence-based assays on the protein of interest with high labelling specificity, and without further labelling steps.

GFP might be considered the "original" genetically encoded fluorescent protein, and has been extensively studied and refined since its first use as a genetically encoded fluorescent label[25]. Mutations of the wild-type GFP to improve folding efficiency, decrease multimerisation and offer superior photophysical properties have increased the practicality of using GFP-derived fluorescent protein labelling in a wide range of biological experiments[26]. Further mutations of GFP allow fluorescent proteins with different excitation and emission profiles to be generated. In parallel, many longer wavelength fluorescent proteins have been derived from various other marine species. The "original" FP in this class was DsRed; again, numerous point mutations have led to increased spectral coverage and improved applicability.

Despite these differences, FPs across the board exhibit broadly similar structures. All have a molecular weight of ~27-30kDa; all consist of a tripeptide chromophore enclosed within a beta-barrel structure made up of eleven β-sheets, as shown in Figure 2-5. Once folded into an almost-native conformation, the residues comprising the fluorophore undergo chemical alterations, typically involving molecular oxygen, before becoming fluorescent[26,27]. This multistep process is known as maturation, and since slow or incomplete maturation of genetically expressed fluorescent constructs is deleterious to many fluorescence measurements, maturation time is a parameter considered in the rational design of fluorescent proteins and FP-based biosensors. An overview of the mutations and resulting differences in photophysical and structural properties of a range of fluorescent proteins is given in Shaner et al.[28]

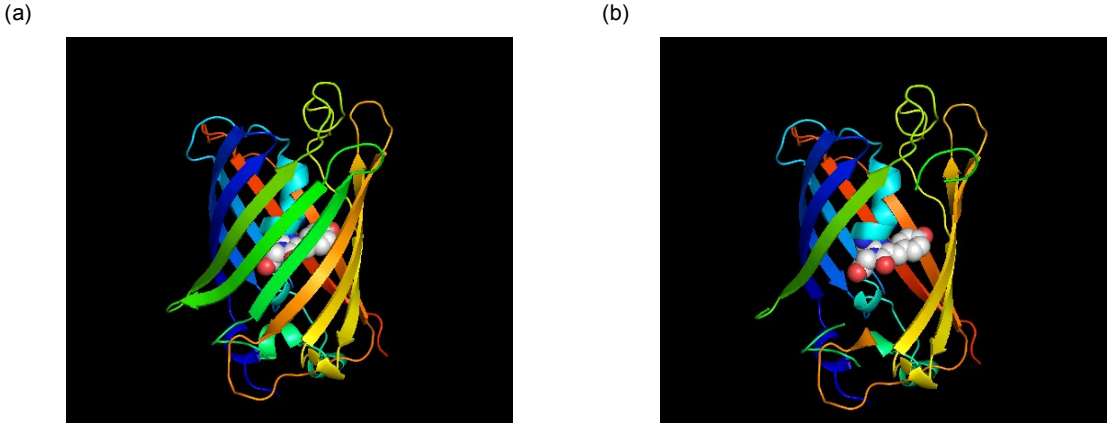

Figure 2-5 Structure of Green Fluorescent Protein.
(a) Structure of GFP, accessed from PDB 1GFL[29] and rendered in PyMOL. (b) Structure of GFP with two β-sheets removed to expose the chromophore, rendered as a space filling model.

The properties of a huge range of fluorescent proteins have been discussed in depth elsewhere[30–32]; for brevity, only properties of those FPs employed in the work presented in this thesis are summarised in Table 2-1. The development of FPs is an active field of research, as further improvements in photophysical properties[33], more diverse wavelengths[34], and methods of functional imaging using FPs alone are sought[35].

FP	λ_{ex}^{max}, nm	λ_{em}^{max}, nm	η	$\varepsilon(\lambda_{ex}^{max})$, $M^{-1}cm^{-1}$	Chromphore[28]	*Parent FP* + selected relevant mutations	References
EGFP	488	507	0.64	51 000	TYG	*wtGFP* + F64L (improved folding at 37°C); S65T (faster maturation, higher extinction coefficient)	Heim et al.[36], Tsien[26]
mCherry	587	610	0.22	72 000	MYG	*DsRed* + GFP-ised temini; M163Q (suppresses short wavelength absorption); V7I, M182K (improved folding)	Shaner et al.[37]
TagRFP-T	555	584	0.41	81 000	CYG	*eqFP578* + multiple (monomeric form); S158T (improved photostability)	Merzlyak et al.[38], Shaner et al.[39]
mRFP	584	607	0.25	44 000	QYG	*DsRed* + multiple (monomeric form); N42Q, V44A (faster maturation)	Shaner et al.[37], Campbell et al.[40]
mCerulean	433	475	0.62	43 000	TWG	*ECFP* + S72A (improved folding at 37°C); Y145A (improved photostability); H148D (monoexponential decay); A206K (monomeric form)	Rizzo et al.[41], Rizzo et al.[42]
mVenus	515	528	0.57	92 200	GYG	*YFP* + multiple (decreased Cl^- sensitivity); F64L (improved folding at 37°C); A206K (monomeric form)	Nagai et al.[43], Rizzo et al.[42]

Table 2-1 Summary of properties of selected fluorescent proteins.
Standard single letter codes for amino acids used to describe chromophores and point mutations. ECFP and YFP derived from wtGFP isolated from the jellyfish *Aequorea victoria*, DsRed isolated from the mushroom coral *Discosoma sp.*, eqFP578 isolated from the sea anemone *Entacmaea quadricolor*.

In comparison to immunofluorescence techniques presented above, labelling of proteins of interest with fluorescent proteins has the advantage of high specificity, as well as being easy to adapt from membrane-based to cytosol- or nucleus-based protein assays. However, the size of fluorescent proteins relative to the protein of interest that they are used to label presents a potential problem in investigations of protein localisation and protein-protein interactions due to potential steric hindrances. Furthermore, traditional methods of transfection result in levels of expression of the protein of interest that deviate significantly from physiologically relevant conditions. Possible alternative labelling techniques that bypass the need to attach a large label to the protein of interest are presented in section 2.2.3; some methods of labelling endogenous proteins for investigations of proteins at physiologically relevant concentrations are presented in section 2.2.5. Despite these issues, fluorescent protein labelling remains a popular technique due to the existence of well-established protocols for development of fluorescent protein constructs, the flexibility afforded by a large palette of excitation and emission wavelengths available, and the continued development of ever-brighter, more photostable, monomeric versions of fluorescent proteins with monoexponential lifetime decay profiles.

2.2.3 Other genetically expressed fluorescent constructs

In addition to fluorescent protein fusions, other genetically encoded modifications can be used to facilitate fluorescent labelling of proteins of interest. It is possible to engineer bio-orthogonal unnatural amino acids into proteins of interest, either to allow subsequent specific labelling using a fluorescent dye or to yield an intrinsically fluorescent protein product by use of fluorescent artificial amino acids[44–46]. Biarsenical labelling techniques (FlAsH or ReAsH) exploit the high affinity of binding between arsenic and thiol groups. FlAsH compounds are rendered non-fluorescent in complexes with 1,2-ethanedithiol

(EDT); upon encountering a six-amino acid domain containing four cysteine residues that might be engineered into a protein of interest, EDT is displaced and the FlAsH compound becomes fluorescent, effectively labelling the protein[47,48]. Biarsenical labelling, like labelling with artificial amino acids, has the benefit over fluorescent protein labelling that the fluorescent label is relatively small, decreasing the chances of erroneous results caused by steric hindrances imposed by large labels. Finally, incorporation of fluorogen activating proteins (FAPs) into fusion proteins can allow protein-specific labelling upon addition of fluorogens: molecules that only become fluorescent upon binding to FAPs[49].

2.2.4 Techniques for transfecting genetically encoded fluorescent constructs

In order that cell samples might express the genetically encoded fluorescent fusion proteins, DNA plasmids must be introduced into the cells in a process known as *transfection*; multiple different methods exist to achieve this goal. Lipid-based transfection methods are based on the concept of negatively charged vector DNA becoming associated with cationic lipid structures – often liposomes – which subsequently fuse with cell membranes and release the plasmid into the cell. Many transfection reagents are available for the practical application of this method, including Lipofectamine™ (Invitrogen) and XtremeGene HP™ (Roche). Such an approach often requires multiple incubation and washing steps, but is easily scalable. Electroporation – the permeablisation of cell membranes by application of an electric field – is another method of introducing exogenous DNA into cells. Care must be taken that buffers used for electroporation have an appropriate salt balance since the cells' ability to regulate ion fluxes is compromised. Furthermore, dependent on the instrumentation available, the necessity to transfect a specific minimum number of cells per condition means that electroporation is not always practically applicable in well plate assays, for example in screening applications where many different transfection conditions are required. Reverse transfection techniques have been demonstrated to be useful in the context of high content imaging[50,51], but have not been pursued in the work presented in this thesis. Microinjection of plasmid DNA directly into cell nuclei is of crucial importance in organism- and tissue-based studies of genetically expressed fluorescent fusion proteins[52], but this technique is less applicable to studies where large populations of cells must be transfected.

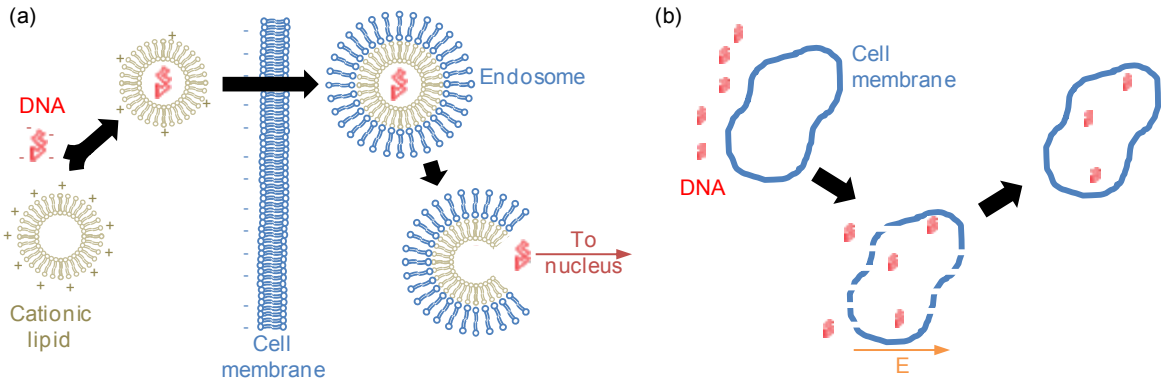

Figure 2-6 Illustration of processes of transfection.
(a) Lipid transfection: DNA forms complexes with cationic lipids which be taken up by endocytosis; DNA is subsequently released and trafficked to the nucleus. Adapted from Parker et al.[53] (b) Electroporation: application

of a pulsed electric field permeablises the cell membrane allowing DNA in the surrounding buffer to enter the cell. Membranes subsequently heal, and DNA is trafficked to the nucleus.

2.2.5 Strategies for obtaining stable cell lines expressing genetically encoded constructs

In *transient* transfection techniques, the cells express the exogenous DNA fragment but do not incorporate it into the genome; thus expression is lost over several days by cell division. Rather than perform transient transfections before every experiment, which may lead to repeat experiments being less consistent due to the potential for different levels of protein expression between experiments, it is possible to establish stably-transfected cell lines. Following introduction of the plasmid to the cell by any of the methods outlined above, there is a certain probability that the exogenous DNA will be integrated into the genome via non-homologous recombination[54]. If DNA coding for the protein of interest is cotransfected alongside a gene conferring antibiotic resistance, selection pressure can be applied on the population of transfected cells; thus after a period of days to weeks, only those cells that have incorporated the fluorescent fusion protein-resistance vector into the genome will survive, and all progeny will express the fusion. This results in the generation of a *stably-transfected* cell line.

Application of the transfection techniques presented in section 2.2.4 above result in the fluorescent fusion protein of interest being expressed in parallel with the endogenous copies of the protein of interest. Generally speaking, such an approach leads to overexpression of the protein, though this is less marked in stable cell lines than in transient transfections. In applications investigating cell signalling, this deviation from physiological conditions may have a significant impact on the biological relevance of results gained from such experiments. *Genome editing* transfection methods overcome this issue. Using zinc-finger nuclease (ZFN)[55,56], transcription activator-like effector nuclease (TALEN), or clustered regularly interspaced short palindromic repeat (CRSIPR)[57] methodologies, it is possible to target specific regions of genomic DNA for insertion of exogenous DNA coding for fluorescent proteins, leading to the generation of labelled endogenous proteins and thus restricting copy number of the protein of interest to physiological levels. In cases where multiple copies of the gene encoding the protein of interest exist, it may be important to ensure that cells are homozygous for the labelled protein – the importance of this factor is likely to vary between applications, and is an active area of research.

2.2.6 Endogenous fluorophores

As an alternative to introducing exogenous fluorophores into samples, the endogenous autofluorescence of certain biomolecules may be exploited in cell or tissue samples. Tryptophan residues present in many proteins present a fluorescent signal at 300-350 nm when excited around 280 nm; spectral properties of this fluorescent signal have been used to investigate protein folding and environment. Metabolites such as reduced nicotinamide adenine dinucleotide (NADH) and flavin adenine dinucleotide (FAD) cause cellular autofluorescence which may be exploited in the study of metabolic state in both cell and tissue samples. Alternatively, structural proteins such as collagen exhibit a fluorescent signal that can be used to study

tissue organisation at a molecular level. The applications of measurements of endogenous fluorescence are discussed in greater detail in Chapter 6:.

2.3 Förster Resonance Energy Transfer

Förster resonance energy transfer (FRET) is the phenomenon whereby energy may be non-radiatively transferred from an excited donor fluorophore to an acceptor fluorophore by dipole-dipole coupling. Originally proposed by Theodor Förster in 1948[58,59], the rate of resonant energy transfer between a FRET donor and a FRET acceptor depends strongly on their separation over length scales of 1-10 nm. This property of FRET in particular has led to its adoption as a fluorescence imaging technique in the life sciences, where spatio-temporal dynamics of events occurring on such length scales (protein-protein interactions, changes in protein conformation, DNA hybridisation) are inaccessible to traditional fluorescence imaging methods that are subject to the limits of diffraction. The following sections provide an overview of the principles of FRET that describe the phenomenon outlined in Förster's work, followed by a discussion of the practical consequences of these principles for the measurement of FRET efficiency.

2.3.1 FRET principles

When FRET occurs, an additional non-radiative means of losing energy is accessible to excited donors. Associated with this additional decay path is a transition rate, given by

$$k_{FRET} = (k_r + k_{nr})\left(\frac{R_0}{r}\right)^6, \qquad \textbf{2.10}$$

where r gives the separation of donor and acceptor fluorophores, and k_r and k_{nr} are the radiative and non-radiative decay rates in the absence of FRET. R_0 is known as the "Förster radius", and is given by

$$(R_0)^6 = \eta_D \kappa^2 \frac{9000\ln(10)}{128\pi^5 N_A n^4} J \qquad \textbf{2.11}$$

Here η_D is the quantum yield of the donor fluorophore, n is the refractive index of the medium and N_A is Avogadro's number. J is a measure of the degree of spectral overlap between the donor emission and acceptor excitation spectra:

$$J = \int q_D(\lambda)\varepsilon_A(\lambda)\lambda^4 d\lambda, \qquad \textbf{2.12}$$

where $q_D(\lambda)$ is the normalised donor emission intensity as a function of wavelength, λ, and $\varepsilon_A(\lambda)$ is the extinction coefficient of the acceptor as a function of wavelength.

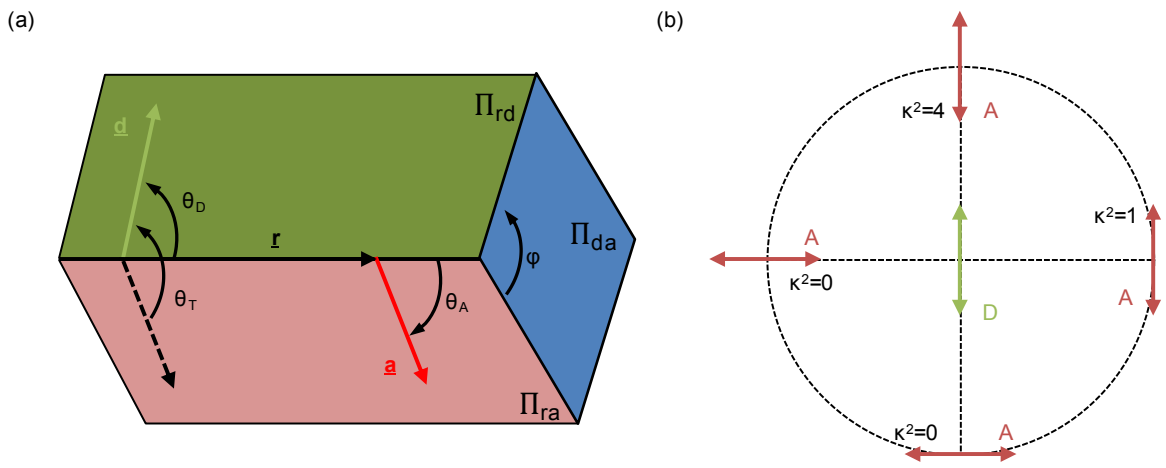

Figure 2-7 Definition of angles between donor and acceptor dipole moments, and orientation factors resulting from different relative orientations of donor- and acceptor dipole moments.
(a) Definition of angles which are used in the definition of orientation factor κ^2: θ_D is the angle between the donor dipole moment d and the vector defining the separation of donor and acceptor, r; θ_A is the angle between the acceptor dipole moment a and the vector defining the separation of donor and acceptor, r; θ_T is the angle between the donor dipole moment d and the acceptor dipole moment a. Π denotes the planes containing pairs of vectors; ϕ is the angle between the planes Π_{rd} and Π_{ra}. (b) The effect of different donor and acceptor dipole orientations on κ^2. Adapted from Valeur[1].

κ^2 is known as the "orientation factor", calculated from the angles between the dipoles, thus:

$$\begin{aligned}\kappa^2 &= (\cos\theta_T - 3\cos\theta_D \cos\theta_A)^2 \\ &= (\sin\theta_D \sin\theta_A \cos\phi - 2\cos\theta_D \cos\theta_A)^2\end{aligned} \qquad \textbf{2.13}$$

where θ_D is the angle between the emission dipole moment of the donor and the vector joining the donor and acceptor dipole moments **r**, θ_A is the angle between the absorption dipole moment of the acceptor and **r**, θ_T is the angle between the donor and acceptor moments, and ϕ is the angle between the planes defined by **r** and the donor moment and **r** and the acceptor moment. These parameters are defined as shown in Figure 2-7 (a).

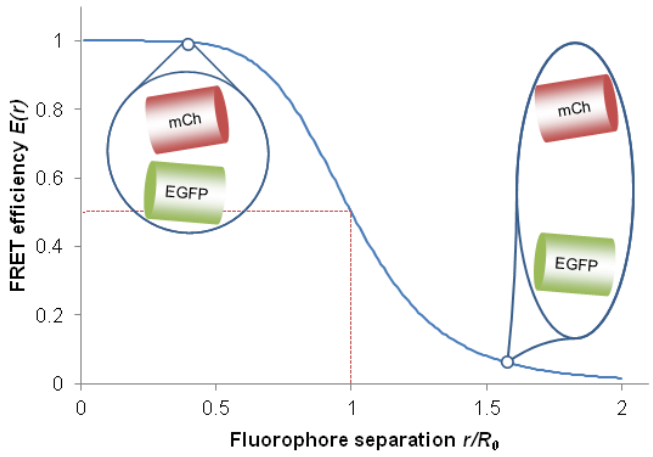

Figure 2-8 Illustration of the dependence of FRET efficiency on fluorophore separation.
Separation displayed in units of Förster radius. Cartoons overlaid to illustrate high-FRET efficiency and low-FRET efficiency cases.

It is convenient to use the concept of FRET efficiency, E, defined as the ratio between the rate of energy transfer by FRET and the total decay rate in the presence of acceptor, which gives the expression

$$E = \frac{k_{FRET}}{k_{FRET} + k_r + k_{nr}} = \frac{k_{FRET}}{(\tau_D)^{-1} + k_{FRET}}, \qquad 2.14$$

where $\tau_D = (k_r + k_{nr})^{-1}$, the lifetime of the donor in the absence of the acceptor. Combining equations 2.10 and 2.14, FRET efficiency may be expressed in terms of the Forster radius and the separation between donor and acceptor fluorophores:

$$E = \frac{{R_0}^6}{{R_0}^6 + r^6}. \qquad 2.15$$

From the preceding formulae (equations 2.10 – 2.15), it is clear that FRET efficiency depends on three main factors, summarised in Figure 2-7 – Figure 2-9. Firstly, there is a strong (6th power) dependence on the separation between donor and acceptor fluorophores, r: for FRET to occur, the separation must be on the order of $2R_0$ or less (Figure 2-8). In practical FRET systems, R_0 is such that this condition implies that FRET occurs on scales smaller than ~ 10 nm. This is a useful length scale in molecular biology, and is crucially much less than the practical optical resolution limit (~ 250 nm). This leads to the application of FRET both as a "spectral ruler" to attempt to determine separations between two fluorophores, for example at each terminus of a protein, and also as a reporter on protein-protein interactions. Such practical applications are discussed further in section 2.3.2

Secondly, the angle formed between donor and acceptor dipoles captured by the orientation factor κ^2 plays an important role in determining the FRET efficiency at a given fluorophore separation. In particular, if the dipoles are aligned perpendicular to each other, no FRET occurs as there can be no

coupling between the dipoles in this configuration (Figure 2-7 (b)). In estimations of R_0, κ^2 is often taken to be $^2/_3$: this approximation is true in the *dynamic averaging* regime in which the dipole orientation is quickly randomised. The validity of this approximation is discussed further in section 2.3.4 below.

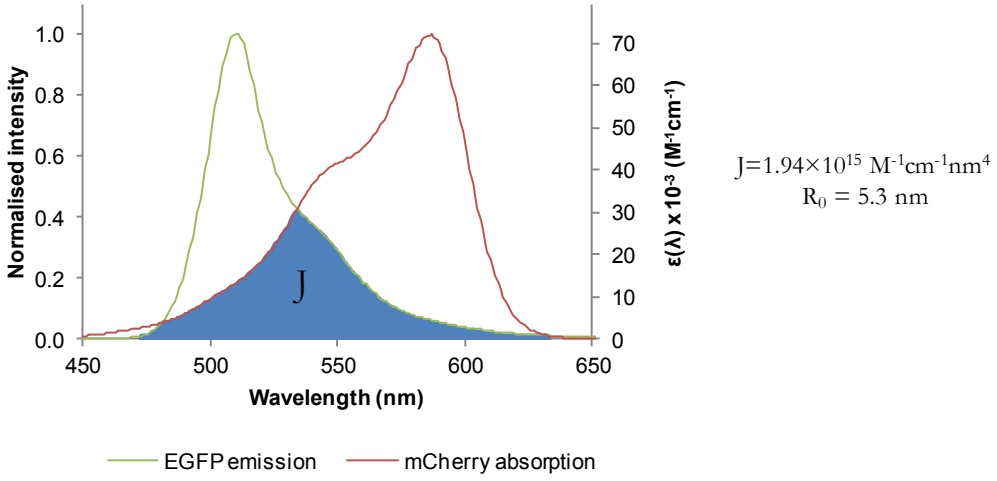

Figure 2-9 Illustration of spectral overlap between FRET donor emission and FRET acceptor excitation spectra for an EGFP-mCherry FRET pair.

Shaded area labelled J represents the spectral overlap integral. The value presented for R_0 is calculated using $\kappa^2 = {}^2/_3$, and agrees with literature values[60]. Reference spectra are generated by the Tsien lab, accessed online[61].

Finally, the degree to which the donor emission spectrum overlaps with the acceptor excitation spectrum plays a crucial role in determining R_0, and thus the suitability of two fluorophores to act as FRET pairs (Figure 2-9). Such considerations are clearly crucial in choosing fluorescent proteins in the design of probes for use in FRET experiments.

If the Stokes' shift associated with a fluorophore is small, there is significant overlap between the emission and excitation spectra, and FRET between two identical fluorophores (homoFRET) is possible. This effect, first evident in measurements of highly concentrated fluorescent dyes[58,62], is generally measured by means of polarisation anisotropy, though homoFRET can also be manifest in changing fluorescence lifetimes if excited state structure is sufficiently complex. Potential benefits of exploiting homoFRET in biological applications include the relative ease of transfecting a single construct for protein clustering assays[63], the lack of mismatched donor and acceptor fluorescent protein maturation rates, and the increased potential for spectral multiplexing.

2.3.2 FRET biosensors

A wide variety of fluorescent probes have been used to investigate biological processes by means of FRET. These may be broken down into two main categories: *intra*molecular and *inter*molecular FRET constructs, each of which have a range of applications, advantages and disadvantages.

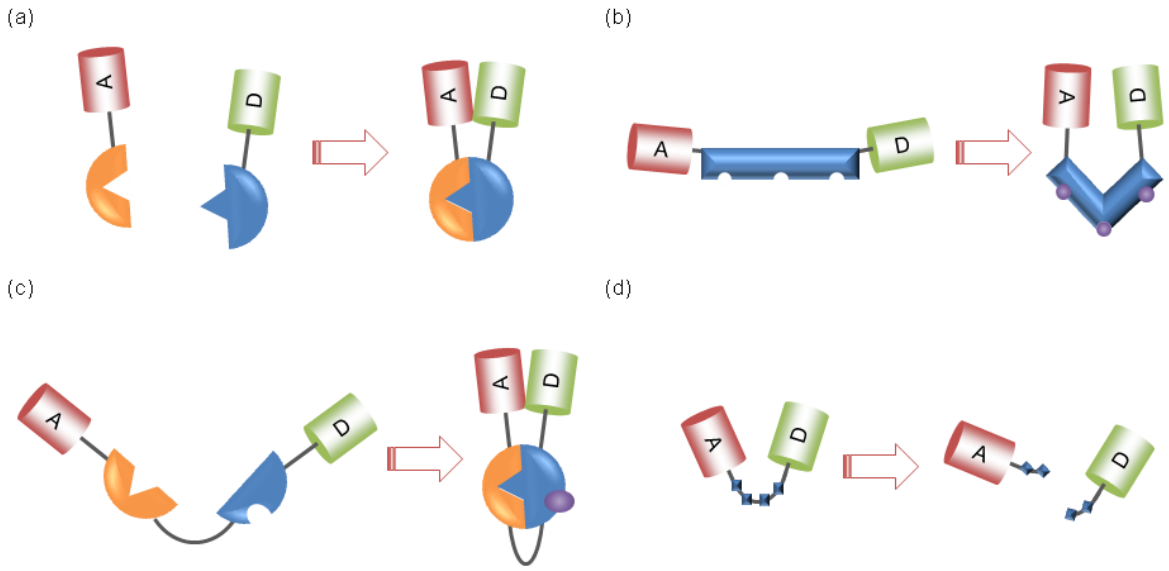

Figure 2-10 Illustration of different means of implementing FRET biosensors.
(a) Intermolecular FRET biosensor, FRET increases on binding event. (b) Intramolecular FRET biosensor, FRET increases due to conformational change on ligand binding. (c) Intramolecular FRET biosensor, FRET increases due to binding event on protein activation. (d) Intramolecular FRET biosensor, FRET decreases upon cleavage by proteinase.

Intermolecular FRET

Intermolecular (bimolecular) FRET biosensors comprise two distinct proteins, each of which is labelled with a fluorophore to act as donor and acceptor in a FRET pair as illustrated in Figure 2-10 (a). This approach is conceptually simple, and is amenable to studies of protein-protein interactions or protein aggregation by FRET. Intermolecular FRET systems benefit from having a high dynamic range due to basal FRET being low, and are relatively easy to design as long as fluorophores are positioned in such a way as to avoid interfering with the protein binding. An additional benefit comes from the relative ease of cloning if different fluorescent proteins are to be substituted to allow imaging to be performed in a different spectral window: donor and acceptor construct cloning can be performed in parallel. Intermolecular FRET experiments have in the past included investigations of Gag protein clustering in HIV virion formation[63], small GTPase activity[64], and growth factor receptor phosphorylation[65].

Intramolecular FRET

Intramolecular FRET biosensors consist of a single molecule, typically labelled at opposing termini with donor and acceptor fluorescent proteins. Intramolecular FRET sensors may be applied in multiple configurations depending on the biology under investigation. The region between the two fluorophores may be a single protein or domain which undergoes a change in conformation upon binding of a ligand, changing the distance between the fluorophores and allowing changes in FRET efficiency to be used to sense levels of ligands such as Ca^{2+} or ATP[64,66,67] (Figure 2-10 (b)). Alternatively, domains from two different proteins that interact when one is activated by an upstream signalling event may be used to report on that event; binding of the proteins results in the donor and acceptor being brought within

FRETting distance, for example GTPase activity sensing in cell signalling pathways[68,69] (Figure 2-10 (c)). Finally, intramolecular FRET sensors may be used to report on the activity of a proteinase which acts to cleave the sensing domain, ostensibly removing any means of donor and acceptor fluorophores being found within FRETting distance of one another – this modality has been used in studies of caspase activity[70] (Figure 2-10 (d)).

With the exception of cleavage-based single chain FRET probes, it is generally expected that the dynamic range of intramolecular FRET biosensors tends to be lower than for intermolecular models since the distance between the donor and acceptor fluorophores is constrained even in the inactive state. This situation may be improved by optimising linker design[69] and, in general, intramolecular FRET biosensors require considerably more care in design than intermolecular systems: in particular, the choice of fluorophores affects R_0, which can be important in determining the dynamic range. Furthermore, the dissociation constant that determines the sensitivity of the FRET sensor is likely to be artificially increased by the co-localisation of interacting components imposed by the sensor. An advantage of unimolecular FRET is reduced sensitivity to inter-cell variability in expression, since the stoichiometry between donor and acceptor fluorophores is always unity for a well-expressed construct with favourable fluorophore maturation properties. Thus, intramolecular sensors allow more quantitative information to be gleaned when measurement methods incapable of unwrapping population binding fraction from FRET efficiency are used.

2.3.3 Means of measuring FRET

There are multiple means of measuring the occurrence of FRET in biological systems, relating to the different ways in which energy transfer affects the fluorescence properties of the fluorophores involved. Different measurement methods require instrumentation with different levels of complexity, often reflecting the robustness of the measurement and the ability to extract quantitative data from the FRET measurement: all, however, can be useful for generating contrast in FRET experiments.

Intensity-based FRET measurement

In the most conceptually simple case, the energy lost from the donor by FRET can be considered to be represented by the loss of intensity in the donor channel when FRET occurs, giving

$$E = 1 - \frac{F_{DA}}{F_D}, \qquad \textbf{2.16}$$

where F_{DA} is the donor intensity in the presence of acceptor, and F_D is the donor intensity in the absence of acceptor. In practice, F_D is measured following photobleaching of the acceptor fluorophores. The phototoxicity associated with the bleaching process mean that this technique may be harmful to samples. Furthermore, irreversible photobleaching means that this technique can be applied to only one measurement per sample, making it unsuitable for time course experiments.

Spectral FRET measurement

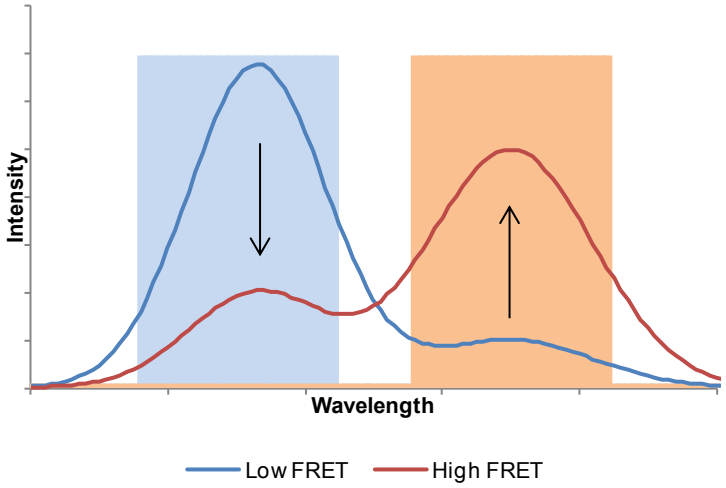

Figure 2-11 Illustration of the effects of FRET as measured by sensitised emission.
Curves serve as exemplar sample spectra in the presence and absence of FRET; blue shaded area represents donor emission channel, orange shaded area represents acceptor emission channel.

As well as a decrease in donor emission when FRET occurs, there is a corresponding increase in acceptor emission as energy is transferred. This phenomenon underpins the measurement of FRET by sensitised emission, whereby FRET efficiency is calculated based on measurements of donor- and acceptor-channel fluorescence under donor excitation. Though this technique is ratiometric and therefore robust against fluctuations in excitation power, spectral cross-talk nevertheless renders it difficult to gain quantitative FRET data from sensitised emission data. Various methods of correcting for spectral bleed-through between detection channels and direct acceptor excitation have been proposed[71], though these invariably require control measurements of additional fluorescent constructs, and typically degrade the signal-to-noise ratio of the resulting FRET images. Even when corrections for spectral cross-talk have been applied, sensitised emission measurements are still restricted as they report only "effective FRET efficiency": that is, the product of the fraction of FRETting donors and the FRET efficiency. The stoichiometry of interactions between donor and acceptor fusions is therefore inaccessible unless positive control constructs can be cloned which reflect the exact FRET efficiency (fluorophore separation and orientation) expected from the donor-acceptor interaction associated with protein binding: alternatively, spectral FRET may be used in parallel with lifetime-based reference measurements to extract information on binding stoichiometry[72].

Lifetime-based FRET measurement

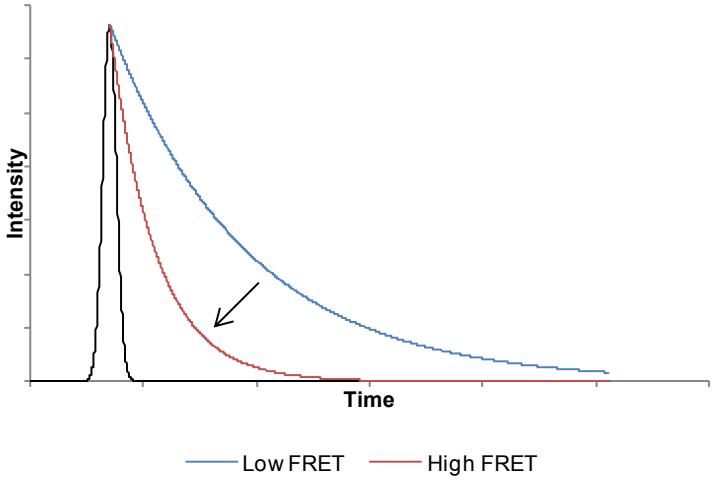

Figure 2-12 Illustration of the effects of FRET as measured by fluorescence lifetime.
Curves illustrate fluorescence decay as a function of time in the presence and absence of FRET.

When a donor fluorophore undergoes FRET, it may be considered that an extra means of non-radiative decay has been introduced to the system. Rearranging equation 2.14 gives an expression for the donor lifetime in the presence of acceptor,

$$\tau_{DA} = (1 - E)\tau_D, \qquad \textbf{2.17}$$

which tends to τ_D in the case of low FRET efficiency. Thus by measuring the lifetime in the presence of acceptor, with knowledge of the donor-only (i.e. non-FRETting) lifetime, FRET efficiencies can be extracted from lifetime measurements. In contrast to intensity- and spectral-based measurements, the measured parameter is independent of the concentration of fluorophores in the sample and the spectral characteristics of both sample and instrument. Lifetime measurements are inherently ratiometric, and therefore insensitive to fluctuations in excitation source power. Moreover, FLIM-FRET measurements are more quantitative than other means of measuring FRET[73], and the use of dark acceptors[74] or homo-FRET[63,75] in lifetime measurements allows greater scope for spectrally multiplexing more than one FRET probe.

In cases where not all donors in an interrogation volume (pixel) are associated with acceptors, monoexponential fitting typically returns an "effective FRET efficiency" similar to that described above for spectral ratiometric measurements. If a complex decay model (c.f. equation 2.7) can be fit to data, lifetime measurements can be used to decouple FRET efficiency from stoichiometry:

$$I(t) = I_0\left(\beta_D \exp\left({}^{-t}/_{\tau_D}\right) + \beta_{DA} \exp\left({}^{-t}/_{\tau_{DA}}\right)\right). \qquad \textbf{2.18}$$

Here, the fraction of FRETting donor β_{DA} is a parameter directly fitted to the data, whilst FRET efficiency E might be calculated from τ_{DA} and τ_D according to equation 2.17 above.

Polarisation-based FRET measurement

Fluorescence polarisation anisotropy measurements can be used to inform on both homo- and hetero-FRET systems. In the case of fluorescent protein labelling, the rotational correlation time is typically large compared to the fluorescence lifetime; therefore in the absence of FRET, anisotropy is high. When homoFRET occurs, energy is transferred to molecules with dipole orientations that would not otherwise have been excited due to photoselection rules, decreasing the anisotropy measurably[10,11]. When combined with spectral resolution, polarisation measurements of sensitised emission can increase the dynamic range of heteroFRET readouts: when FRET occurs, the donor emission shows higher anisotropy due to a reduced fluorescence lifetime, whilst sensitised emission shows a decrease in anisotropy as the orientation of acceptor-emitted light is not wholly constrained by the excitation polarisation and photoselection[42,76]. Alternatively, fluorescence anisotropy can be combined with time-resolved techniques: here, an additional short component in anisotropy decays is indicative of FRET occurring[77].

Polarisation anisotropy-based FRET measurements share the benefits of lifetime in terms of insensitivity to fluctuations in laser power, fluorophore concentration and scattering[10], though spectral cross-talk can be an issue for sensitised emission polarisation measurements. The ability to read out homoFRET between like fluorophores regardless of energy level composition is unique amongst FRET measurement techniques, and the dynamic range of homoFRET measurements can be increased by the application of time-resolved fluorescence anisotropy imaging[11]. Separately, sensitised emission anisotropy has been claimed to offer as much as 15 times greater contrast than that of fluorescence lifetime in certain circumstances[42]. Disadvantages of polarisation-based FRET imaging relate to the trade-off between instrumental complexity and the degree to which the contrast observed can be used to quantify FRET parameters (efficiency and FRETting donor fractions). Complex time-resolved models must be fit in order to determine all relevant parameters, which require large numbers of photons for robust determination – although this issue may be addressed by careful choice of model in global fitting[77,78]. It has been observed that the specific polarisation properties of microscope optics should be considered when implementing fluorescence anisotropy as, in even the simplest cases, these can make such methods challenging[42].

2.3.4 FRET issues

Though FRET provides a means of measuring biological events on a cellular level inaccessible though traditional means of imaging, there are nevertheless issues which must be considered both when designing FRET experiments, and when analysing FRET data. Some such issues relating to particular means of measuring FRET have been described above; others are inherent to FRET as applied in the life sciences. The design of FRET biosensors as discussed in section 2.3.2 above requires considerations not only of the sensitivity of the biological system being exploited to generate the probe, but also of photophysical aspects. As mentioned previously, the placement of fluorophores can affect the dynamic range of FRET biosensors. In addition, differences in maturation rates of the donor and acceptor fluorescent proteins on a biosensor, or indeed the failure of one of the fluorophores in the FRET pair to

mature fully, can lead to anomalous FRET results. In the case of mCherry and EGFP this effect has been suggested to be a potentially significant source of erroneous results[79,80].

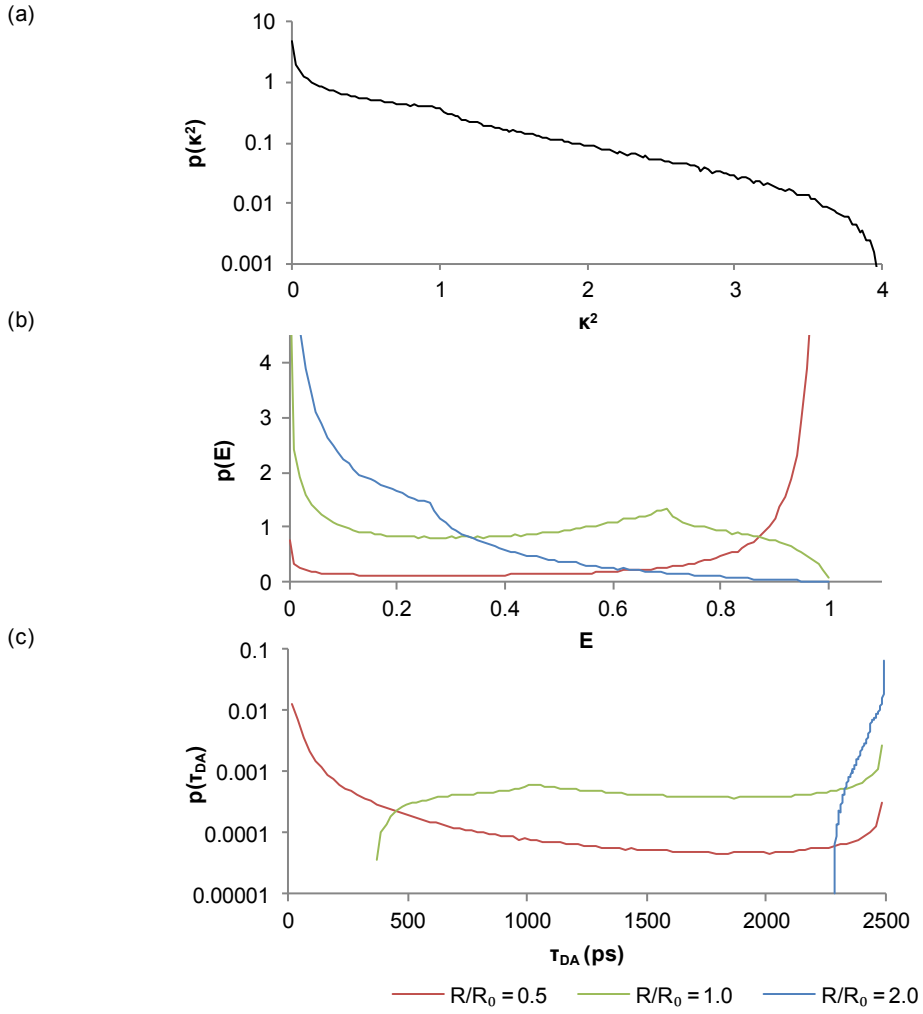

Figure 2-13 Illustration of κ^2 and FRET efficiency distributions in the static averaging regime.
(a) Distribution of κ^2 in the static averaging regime, calculated by Monte Carlo methods following Vogel et al.[81] (b) Resulting distribution of FRET efficiencies in the static averaging regime at 3 different fluorophore separations, calculated based on κ^2 in (a). (c) Resulting distribution of FRETting lifetimes at 3 different fluorophore separations, calculated based on E in (b).

Another potential source of erroneous FRET results was highlighted by Vogel et al. in a 2012 paper[82], having previously been raised by Dale in a 1978 publication[83]. The authors discussed the validity of the generally adopted assumption of complete rotational freedom such that donor and acceptor rotate randomly, rapidly and independently during the fluorescence decay that leads to the use of $\kappa^2 = {}^2/_3$. This paper stresses that FRET measurements conducted with fluorescent proteins are more likely to fall into the *static averaging regime* where the rotation time of the fluorophore's dipole is long compared to the excited state lifetime, and in which the assumption of $\kappa^2 = {}^2/_3$ is not applicable, resulting in a distribution of FRET efficiencies and lifetimes such as that shown in Figure 2-13. Clearly the presence of this distribution of FRETting lifetimes (τ_{DA}) will have consequences for the accurate quantification of

FRET efficiencies and FRETting donor fractions measured by fluorescence lifetime. Subsequently, Vogel et al. have published a lookup table based on Monte Carlo simulations to relate measured (apparent) FRET efficiencies to fluorophore separations in FP-based FRET systems[81].

2.4 Fluorescence microscopy instrumentation

2.4.1 Epifluorescence microscopy

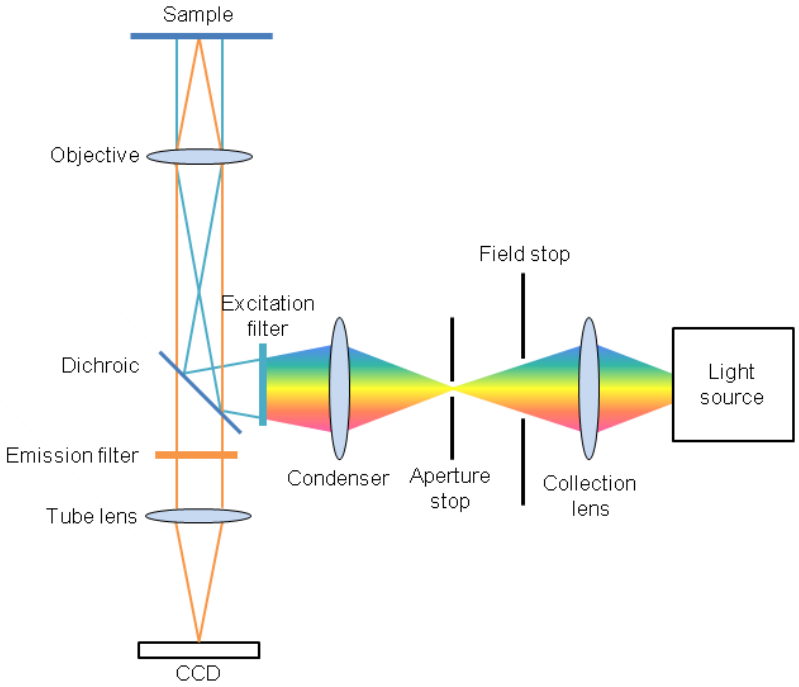

Figure 2-14 A schematic diagram showing features of a microscope configured for measurement of epifluorescence.

In epifluorescence microscopy, the same objective lens is used to excite fluorescence from a sample and to collect the emitted light. Excitation light is provided using a broadband source, typically a mercury or halogen lamp, and an excitation interference filter. A dichroic mirror is used to separate excitation light from emitted fluorescence, which is typically orders of magnitude less intense: correct choice of filters allows very weak fluorescence to be measured with appropriate detectors, down to single photon detection from single molecule emitters[84]. Observation, through an emission interference filter, is conducted by eye through eyepieces or on a camera, typically a charge coupled device (CCD).

2.4.2 Sectioning methods in fluorescence microscopy

In epifluorescence microscopy, the fluorescence that may be collected from a single point in the sample forms a solid cone extending above and below focus[85]. Thus, fluorescence originating from points outside the focal plane can degrade contrast in the image captured at that plane. Additionally, regions of the sample outside the focal plane are illuminated by excitation light, potentially leading to out-of-plane photobleaching that acts to confound z-stack imaging. The former problem may be addressed by use of a confocal pinhole in a scanning confocal microscope configuration such that only fluorescence originating from a plane optically conjugate (confocal) to that of the pinhole is detected, as proposed by Minksy in

1957[86]. A similar method using an array of pinholes scanned across the sample by means of a rotating disk[87] – known as a Nipkow disk – offers an increase in imaging speed over single-point scanning methods by effectively parallelising the scanning process. This increase in imaging speed, along with the reduced photobleaching afforded by lower local excitation intensity[88], make Nipkow disk optical sectioning particularly useful for imaging biological samples. The relatively low transmission of light through a standard Nipkow disk can be improved by the addition of a matching array of microlenses, as implemented in a CSU-X1 system (Yokogawa). Unlike most modern confocal laser scanning microscopy (CLSM) systems, however, pinhole size and spacing in Nipkow disk systems are typically fixed, so that optimal sectioning performance and axial resolution is only realised for a specific objective numerical aperture. This constraint is addressed to some extent in the CrEST™ X-Light™ Confocal Module, which in the ArrayScan XTU High Content Analysis reader (Thermo Scientific)[89] allows a choice between two pinhole sizes in the Nipkow disk. Alternatively, parallelisation can be achieved using swept field confocal (SFC) scanning, exemplified in the Opterra system (Bruker). Here, a 1-D linear array of pinhole images is swept across the sample using galvanometer and piezoelectric scanners: in this setup, four different pinhole configurations are available, increasing flexibility in choice of objective NA[90,91].

An alternative means of achieving optical sectioning microscopy is multiphoton excitation, first realised by Denk et al. in 1990[92]. In the case of 2-photon excitation, fluorophores are only excited if two photons are simultaneously absorbed, the probability of which depends on the square of the average power of incident light and inversely on the pulsewidth of the incident light[93]. Since excitation probability falls off according to $1/z^2$ with distance z from the focal plane, two-photon microscopy mitigates for out-of-focal plane photobleaching[93] as well as affording optical sectioning. For a given fluorophore, the wavelength of illumination required for two-photon excitation is typically twice that used for standard one-photon fluorescence measurements. This requirement has the benefit of allowing near-infrared light to be used for measurements of thick biological samples to reduce the deleterious effects of scattering and absorption on fluorescence imaging; however, the same requirement for longer wavelength excitation light causes multiphoton microscopy to have lower inherent spatial resolution than confocal imaging[94]. As with CLSM, the necessity to scan an excitation point across the sample limits acquisition speed; acquisition time can be decreased by employing multiple scanning beams to parallelise acquisition[95].

2.4.3 Fluorescence lifetime imaging microscopy

Fluorescence lifetime imaging microscopy is the technique whereby fluorescence lifetime measurements are made across all pixels in an image, adding spatial information to the molecular-level information conferred by fluorescence lifetime measurements. Multiple methods exist to generate FLIM images; these can broadly be categorised according to their implementation in the time- or frequency-domains, and whether the method of generating images depends on spot scanning or wide field detection.

Wide field frequency domain FLIM

In frequency domain FLIM measurements, the sample illumination is modulated at a defined frequency, ω. The emitted fluorescent signal will be modulated at the same frequency, but will exhibit a phase lag and magnitude offset due to the delay between excitation of and emission by the fluorophore. The ratio of the AC and DC components of the signal as illustrated in Figure 2-15 may be used to calculate fluorescence lifetimes using

$$\tau_m = \sqrt{\frac{1-\left(\frac{B\cdot a}{A\cdot b}\right)^2}{\omega^2\left(\frac{B\cdot a}{A\cdot b}\right)^2}}. \qquad 2.19$$

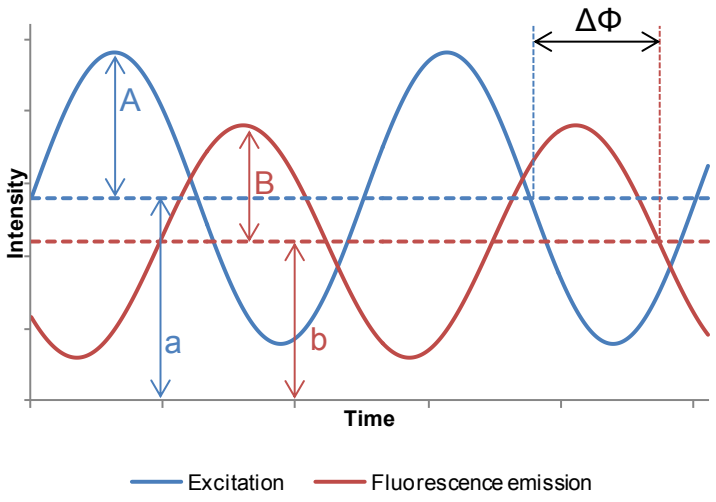

Figure 2-15 Illustration of relevant measurements in frequency domain FLIM.
A and B represent the amplitudes of excitation and emission signal respectively; a and b represent the DC offsets of excitation and emission signal respectively. $\Delta\phi$ represents the phase shift between excitation light and emitted fluorescence.

Alternatively, the phase lag between excitation and emission signal may be used to calculate the lifetime:

$$\tau_\phi = \frac{\tan(\Delta\phi)}{\omega} \qquad 2.20$$

For a monoexponential decay, these two lifetimes are identical. In practice, data is often acquired either using an image intensifier modulated at the same frequency as the source (homodyne detection) read out by a CCD, or using a directly modulated CCD/CMOS camera[96]. Multiple images are read out at different phase shifts, from which the parameters outlined in Figure 2-15, and subsequently the lifetime parameters in equations 2.19 and 2.20, may be calculated[97]. Frequency domain FLIM benefits from wide-field detection such that all pixels in a field of view are interrogated for lifetime simultaneously. Global, fit-free

data analysis can be performed using the polar or phasor technique for frequency domain FLIM data[98]; alternatively, quantitative data analysis by "lifetime unmixing", based on prior knowledge of fluorophore lifetime, has been proposed[99].

Point scanning frequency domain FLIM

Though frequency domain FLIM is most commonly implemented using a wide field approach, it is also possible to modify point-scanning microscopes to measure lifetime data in the frequency domain. One example of this approach is digital frequency domain (DFD) FLIM, whereby a heterodyne detection method deployed on a field programmable gate array (FPGA) chip generates frequency domain lifetime data with photon efficiency comparable to time domain single photon counting methods[100]. One example of the application of DFD-FLIM has been a study of the activity of Ca^{2+}/calmodulin-dependent protein kinase II by FLIM-FRET[101]. However, point scanning FLIM is most commonly implemented in the time domain, usually using time correlated single photon counting.

Point scanning time domain FLIM

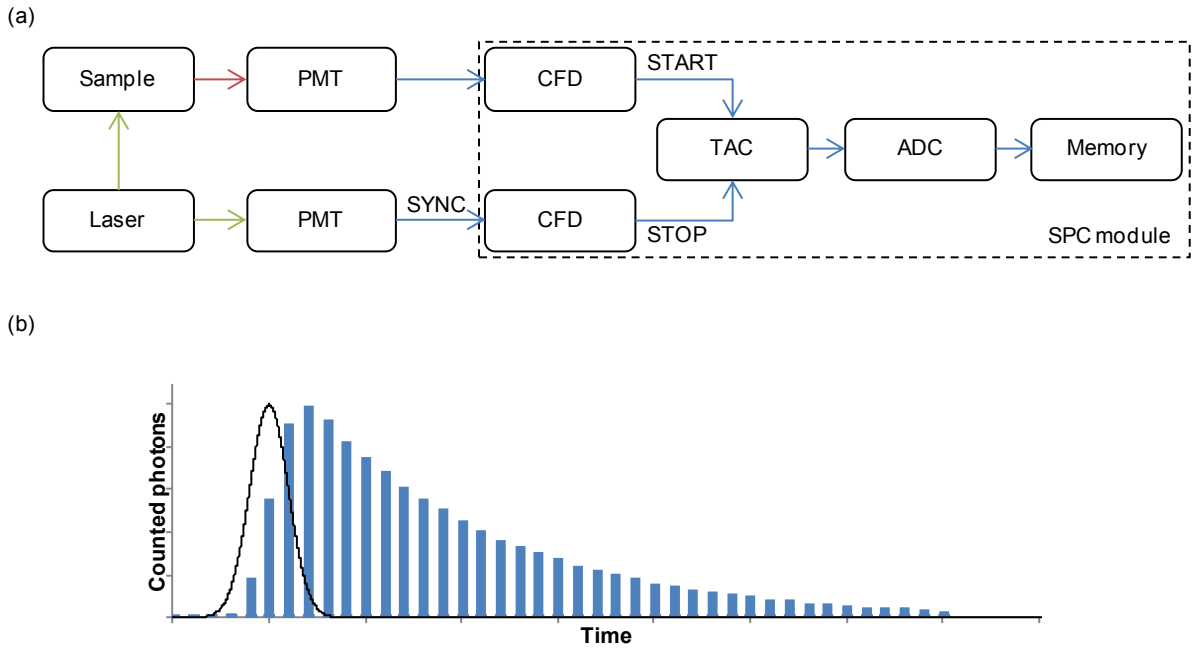

Figure 2-16 Illustration of the principles of time correlated single photon counting for fluorescence lifetime measurement.

(a) Schematic showing components in a photon counting system running in reversed start-stop mode as implemented by Becker and Hickl. Green arrows represent excitation light, red arrows fluorescence photons, and blue arrows electronic signals. PMT: photo-multiplier tube, CFD: constant fraction discriminator, TAC: time-to-amplitude converter, ADC: analogue-to-digital converter. Figure adapted from The bh TCSPC handbook[102]. (b) An exemplar histogram resulting from a TCSPC acquisition, from which lifetime parameters may be extracted.

In time correlated single photon counting (TCSPSC), a point in the fluorescent sample is excited with a pulsed laser. As implemented in systems marketed by Becker & Hickl GmbH, individual fluorescence photons are detected and converted into electronic signals by a photo-multiplier tube (PMT) and a constant fraction discriminator (CFD), and time correlated with a reference signal from the excitation

pulse. This time correlation is achieved using a time-to-amplitude converter (TAC), which operates as a capacitor that starts charging upon a 'start' trigger; a voltage is built up across the TAC until a 'stop' pulse is received, at which point the voltage is read out using an analogue-to-digital converter (ADC). The arrival times of individual photons are plotted on a histogram, from which fluorescence decay parameters (equation 2.7) may be extracted. This process is summarised in Figure 2-16. Other implementations of TCSPC exist, including TimeHarp devices (Picoquant GmbH) that make use of fast time to digital converters (TDC) and field programmable gate array (FPGA)-based circuitry to minimise electronic dead time and increase readout speed[103].

In fluorescence lifetime imaging, TCSPC is typically implemented in a laser scanning confocal or multiphoton microscope. When correctly configured, TCSPC is extremely photon-efficient, offering optimal signal-to-noise per emitted photon[104]. However, the necessity to scan a beam across the field of view imposes a lower limit on acquisition time. This is exacerbated by the necessity to collect less than one photon per 100 excitation pulses to avoid potentially biasing lifetime measurements to shorter decay times due to pulse pile-up effectss[102]. Furthermore, the high peak power in a scanned laser spot precludes increasing excitation power when imaging biological samples due to associated photobleaching and phototoxicity, making rapid imaging of cell line samples particularly challenging.

An alternative method for acquiring FLIM images using laser scanning confocal or multiphoton microscopes is based on time gating electronics that assign photons to "bins" depending on arrival time at the detector[105]. This approach has been applied to imaging of lipid order in response to stimulation with epidermal growth factor[106].

It should be noted that regardless of the implementation of time domain FLIM employed, it is generally necessary that the response of the instrument to an impulse of light should be considered when analysing decay profiles: finite pulse width and the optical response of detection electronics result in the measured signal being the result of a convolution of the instrument response and the fluorescence decay of the sample. Instrument response can be determined using a sample that scatters part of the excitation signal into the detection optics; otherwise a fluorescent sample with a known lifetime can be used in the fitting algorithm[78,107]. In some approaches, the effect of the instrument response is effectively ignored by sampling the fluorescence decay profile from >500 ps after the peak[105], though such an approach risks obscuring short-lifetime components in the data.

Wide field time domain FLIM

Wide field time domain FLIM allows time resolved fluorescence images to be built up without the need for scanning an excitation point across the sample. In one implementation, a photomultiplier with a quadrant detector is used to associate recorded photon events with their position of origin within the sample[108]. By combining such a detector with TCSPC electronics, FLIM images can be generated. In this approach, acquisition speed is no longer limited by concerns relating to high peak power of a scanned

spot, though TCSPSC detection rates act to place a lower limit on imaging time. When applied to imaging of tagRFP-EGFP FRET constructs, this method allowed robust lifetime data to be acquired across time course experiments with two FLIM images (at different emission wavelengths) acquired every 60 seconds[109].

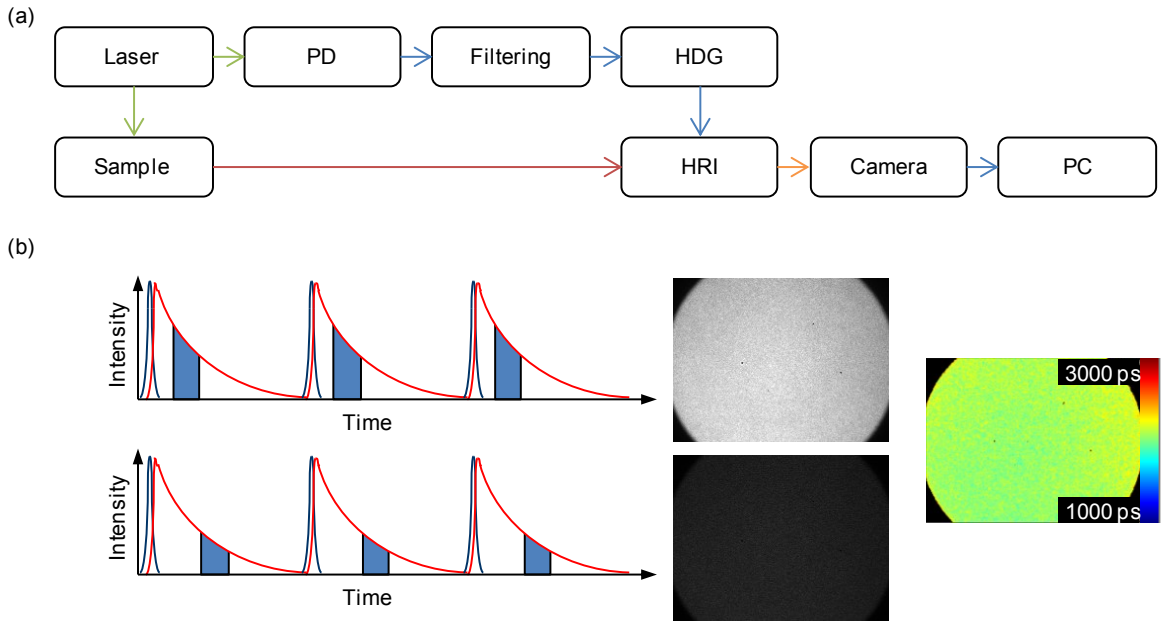

Figure 2-17 Illustration of the principles of wide field time gated FLIM.
(a) Schematic showing the necessary components in a wide field time gated FLIM system. Green arrows represent excitation light, red arrows fluorescence photons, blue arrows electronic signals and orange arrows HRI phorsphorescence. PD: photodiode, HDG: delay generator. (b) Illustration of the means of acquiring time-resolved fluorescence using wide field time gated FLIM: recorded signal at each "gate" is integrated by the camera over many laser pulses; the gate is moved relative to the excitation pulse using a delay line. Fluorescence lifetime images may be generated from the resulting intensity decay images in software.

The method used throughout this thesis for the acquisition of wide field FLIM data is wide field, time gated FLIM. Conceptually, time gated FLIM may be considered equivalent to equipping a camera with an ultrafast shutter and a delay line, such that fluorescence decays may be sampled over "gates" at multiple delays with respect to the excitation pulse. In practice, this is achieved using a gated optical intensifier (HRI, Kentech). The critical elements of the HRI – the photocathode, the multichannel plate and the phosphor screen – are shown in Figure 2-18. Photons incident on the front face of the HRI cause photoelectrons to be ejected from the photocathode with a probability governed by the quantum efficiency of the particular photocathode. Under time gated operation, an onboard impulse generator produces pulses at MHz frequencies, switching the voltage on the photocathode. The front face of the MCP is grounded; the voltage between the photocathode and the microchannel plate is switched from a small positive potential ("off") to a larger negative "gating" voltage ("on"). Thus in the "on" state, photoelectrons are accelerated to the MCP; in the "off" state, dark current is reduced. The MCP acts to amplify the signal by the generation of secondary electrons in multiple steps[110], where the gain factor which gives the final number of secondary electrons is dependent on the user-defined gain voltage (typically 650-850 V). The final process of time gated image acquisition is the generation of photons by

phosphorescence following the acceleration of secondary electrons onto a phosphor screen. The resulting gated, intensified image can then be read out using a camera.

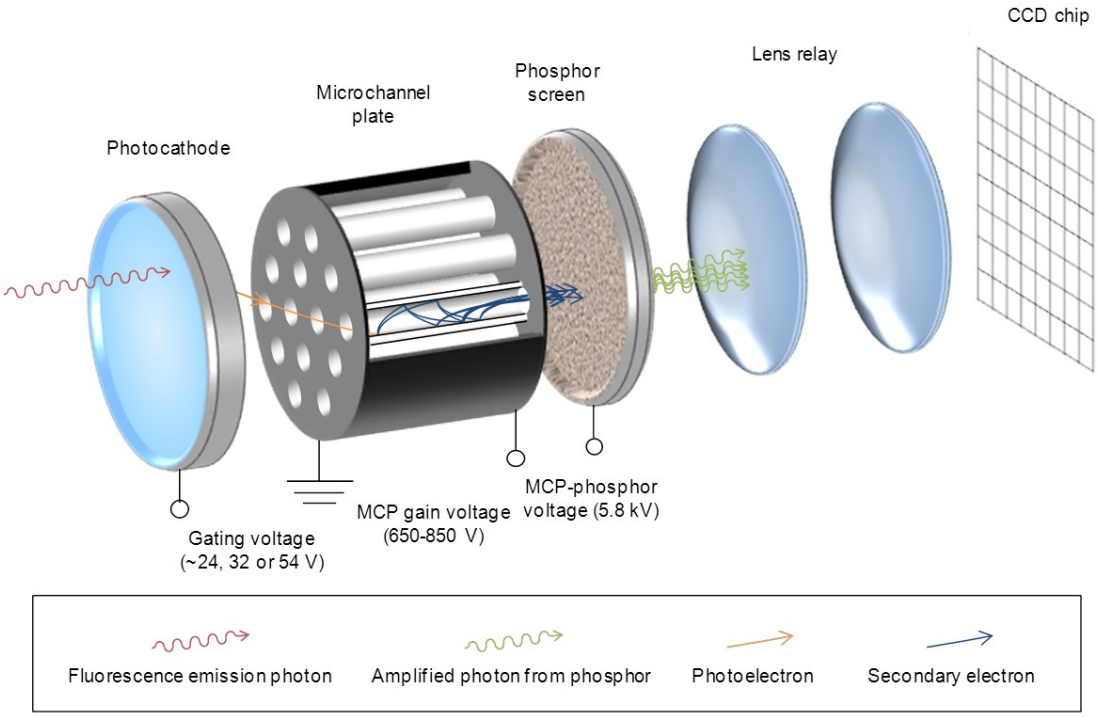

Figure 2-18 A schematic showing the critical elements of a high rate imager system and the amplification steps in its operation as a gated optical intensifier.
Voltages shown at each stage are typical nominal values.

Time gated detection is less photon efficient than TCSPC, as only those photons arriving within the current gate "on" time are collected. Additionally, the sequential nature of acquisition may cause lifetime artefacts if the sample moves between the first and final gates of the acquisition, or if the sample bleaches in the course of the acquisition, or if background changes in the course of the acquisition. Such artefacts are also expected to cause anomalous results in wide field frequency domain FLIM, which requires sequential acquisition of phase-resolved images. However, wide field time gated FLIM allows all pixels in a field of view to be interrogated in parallel without beam scanning, increasing the speed of acquisitions compared to time domain point scanning measurements and increasing signal-to-noise ratio per unit acquisition time. In addition, there is no limit to the maximum photon flux as is the case in TCSPC. This makes wide field time gated detection particularly suited to applications of time domain FLIM that require high-speed acquisition, including tissue imaging in endoscopy[111] and high content analysis. Time gated imaging provides a higher accuracy per photon detected than frequency domain FLIM with sinusoidal excitation[112], and does not suffer from the problems associated with aliasing that are encountered with high speed frequency domain FLIM using pulsed excitation[113].

2.5 Automated fluorescence microscopy and high content analysis

Over a number of decades, the advancement of enabling technologies – particularly robotic sample handling and increased computing power – has led to increased usage of high throughput methods in the life sciences. Automated, high throughput methods allow the rapid testing of hundreds of thousands of experimental conditions; the ability to rapidly explore parameter space means that such methods are suitable for application throughout the process of drug discovery, including target identification, target validation and toxicology stages. Additionally, the statistical robustness conferred by the ability to examine multiple repeats per condition lead to high throughput methods being attractive across a range of applications in academia and the pharmaceuticals industry.

The distinction between high throughput screening (HTS) and high content analysis (HCA) is discussed in greater depth in sections 2.5.2 and 2.5.4 below. In both cases, assays are designed to test a wide range of experimental conditions in a single experimental run. Types of readout in cell based assays vary from the relatively simple – for example, homogeneous colorimetric or fluorescence intensity readouts in HTS – to more complex, image-based phenotypic measurements based on cell morphology, translocation of labelled proteins or co-location of multiple labelled proteins in HCA. The aims of cell based assays include to the determination of "hits" in a screen for drug candidates, to measure the on-target dose response of compounds, or to investigate the dose-dependence of undesirable effects in toxicology assays. They can also be applied to screen for protein interactions or other molecular processes in order to analyse cell signalling responses.

A subset of HTS and HCA assays are conducted in multiwell plate formats. Multiwell plates provide a growth substrate for imaging adherent cell lines that is not available in flow-based implementations, and permits different treatments to be applied to subpopulations of cells based on well position that would be impossible when using spotted coverslips. The multiwell plate chosen for a particular application will depend on several experiment parameters. For homogeneous measurements, round-bottomed wells can be used. For imaging experiments, the profile of the plate bottom should mimic that of a microscope slide cover slip. Light transmission properties, well volume, number of wells per plate and cell substrate coatings must also be considered when choosing multiwell plates for a given experiment. A small selection of plate types is presented in Figure 2-19. Plate choice is discussed in the context of UV-excitation wavelength FLIM assays in Chapter 6:.

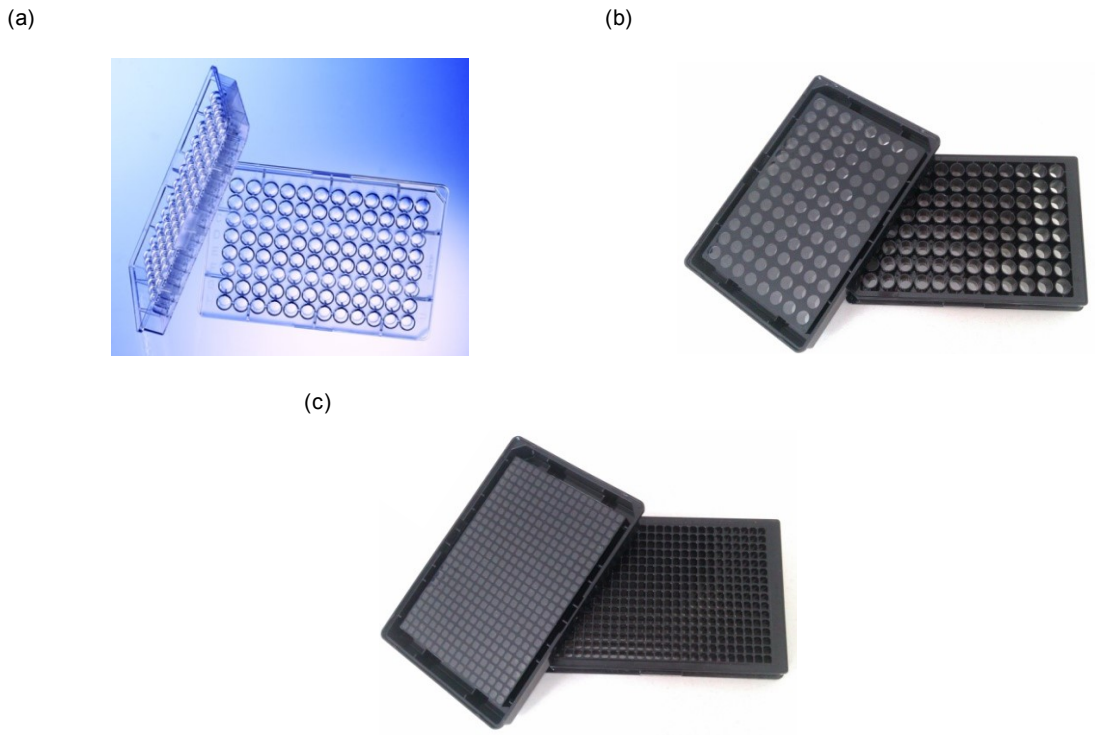

Figure 2-19 Multiwell plates for use in HTS/HCA experiments.
(a) Round, polystyrene bottom 96-well plates for solution-based colorimetric measurements (image from sigmaaldrich.com). (b) Plastic (Greiner μClear®), flat bottom 96-well plates for fluorescence imaging. (c) Glass, flat bottom 384-well plates for fluorescence imaging, suitable for use with short wavelength excitation.

The remainder of this section is intended to introduce high throughput screening (HTS) and high content analysis (HCA) and provide a brief overview of different fluorescence-based methods applied in HTS and HCA, highlighting instrumentation used and assay quality parameters (where available).

2.5.1 Assay quality parameter Z'

The NIH Centre for Clinical Excellence Guidance for Assay Development and HTS document provides a comprehensive overview of considerations for design, development and optimisation of HTS assays that may also be applied to HCA fluorescence imaging assays[114]. Amongst these considerations, the importance of establishing an assay quality metric is highlighted. Multiple such metrics exist, including the "signal window", the assay quality factor Z'[115], and "strictly standardised mean difference" (SSMD)[116]. Though the latter method is developed to give a metric that has a solid basis in probability and is robust against outliers, use of the Z' factor is more widespread and was therefore adopted in our laboratory as a means of assessing assay quality in HTS and HCA for ease of comparison. Z' is defined as

$$Z' = 1 - \frac{3(\sigma_+ + \sigma_-)}{|\bar{x}_+ - \bar{x}_-|}, \qquad 2.21$$

where σ_+ and σ_- are the standard deviations associated with the positive and negative controls respectively, and $\bar{x}_+$ and $\bar{x}_-$ are the mean results associated with the positive and negative controls

respectively. Crude interpretations of Z' value are shown in Table 2-2 below; examples of dose response curves for different qualities of assay are illustrated in Figure 2-20.

Z' value	Interpretation
1	An ideal assay
$1 > Z' > 0.5$	An excellent assay
$0.5 > Z' \geq 0$	A binary assay
<0	Screening is essentially impossible

Table 2-2 A simple categorisation for interpretation of Z'-factor values applied to HTS/HCA assays[115].

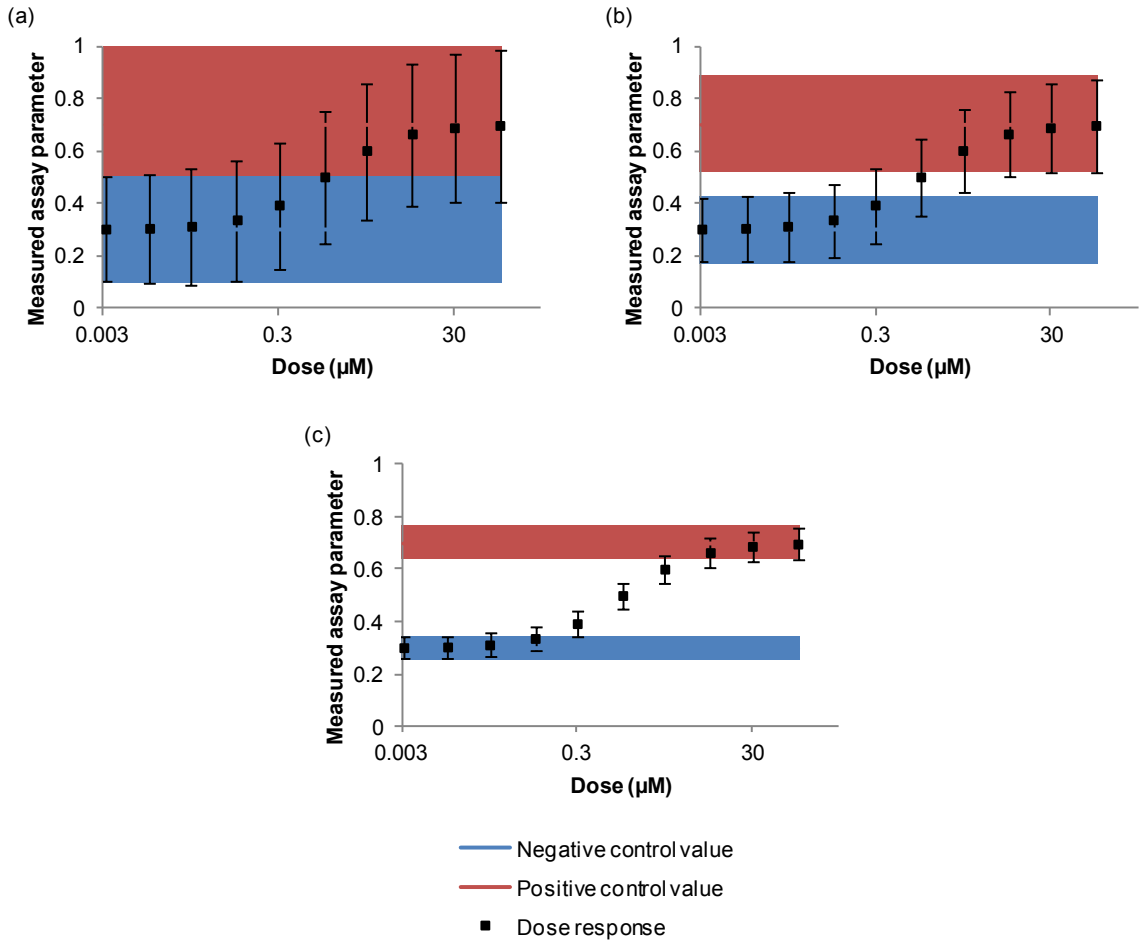

Figure 2-20 Illustration of dose response curves for assays of different quality.
(a) Dose response curve for assay with $Z' = -0.25$. (b) Dose response curve for assay with $Z' = 0.25$. (c) Dose response curve for assay with $Z' = 0.75$. In each case, blue and red lines show values obtained by measurement of negative and positive control samples respectively. Shaded areas show the degree of overlap between controls, where the height of the shaded region above/below the control value is given by $3\sigma_-$ (blue region) and $3\sigma_+$ (red region).

Many factors can act to degrade Z' in HCA experiments. These might be linked to the instrumentation used in the experiment, for example irregular pipetting of reagents or unstable fluorescence excitation might cause increased variation in measured results. Biological factors may also play a role in decreasing

the Z' score: variations in expression of protein constructs, or the presence of non-responsive cell populations in a drug efficacy assay, might both contribute to poor assay performance.

2.5.2 Homogeneous fluorescence assays for HTS: flow cytometry

High throughput screening may be either cell-free or cell-based, but in either case describes the automated acquisition of data across a large number of conditions (>10^5, as defined by the Guidance for Assay Development & HTS docment[114]) without user intervention. HTS is commonly implemented in multiwell plate or flow cytometry formats. Flow cytometry is a means of splitting a population of cells into subpopulations based on fluorescence characteristics. Suspensions of cells are passed through a flow cell engineered such that a single cell passes through an interrogation beam at a time; the fluorescence properties (typically spectrally-resolved intensity) and scattering properties of each cell in the population may then be recorded. When combined with appropriate labelling and liquid handling methods, flow cytometry can be used in HTS assays. For example, a flow cytometry method was used by Surviladze et al. to identify small GTPase inhibitors from a library of 200 000 compounds based on the intensity of fluorescence from GTPase-conjugated fluorescent beads[117]; the authors reported the quality parameter of this assay to be $Z' = 0.87$. A detailed review of flow cytometry in HTS has been presented by Black et al.[118]

2.5.3 Homogeneous fluorescence assays for HTS: assays of protein-protein interactions

Homogenous time-resolved FRET measurements exploiting the long fluorescence lifetimes of certain lanthanide-based fluorophores can be used to separate signal from relatively short-lived autofluorescence by temporal gating. Low repetition nitrogen lasers are typically used to excite samples with the required short wavelength radiation, and the large (~300 nm) Stokes' shift associated with lanthanide fluorophores means that fluorescence is detected in the red region of the spectrum. HTRF measurements have been conducted in a range of biological systems, including an investigation of phosphorylation of the elF4E kinase in tumour spheroids[119]; this assay, described in an Application Note from BioTek Instruments Inc., yielded an assay quality parameter of $Z' > 0.7$.

Bimolecular complementation (BiFC) assays have also been used to this end. In BiFC experiments, two non-fluorescent complimentary fragments of a fluorescent protein are linked to two separate proteins of interest: should these proteins interact, then there is a chance that the fragments will associate and mature to form a fluorescent protein. If a library of proteins fused to GFP fragment F[1] is generated, then these can be screened against a protein of interest fused to GFP fragment F[2]. This approach was adopted in a 2004 study by Remy and Michnik that led to the identification of Ft1 as a regulator of the protein kinase Akt[120]. A crucial drawback of this method is the possibility of false negatives being caused by transient interactions that occur on a timescale too fast to allow the association and maturation of a fully fluorescent FP, or false positives by the affinity of the two GFP fragments to each other.

2.5.4 Fluorescence intensity-based imaging methods for HCA

High content analysis (HCA) assays might be considered a specialised subset of high throughput methods, using imaging in parallel with instrument automation to detect more complex phenotypes than is typically possible in HTS in models that more closely match physiological conditions whilst maintaining subcellular spatio-temporal information. When combined with advanced image analysis and bioinformatics, the information yielded by HCA methods is therefore potentially significantly greater than HTS assays. Typically fewer conditions per experiment are probed due to the slower and more complex nature of the acquisition and analysis process, though an study of candidate compounds for disrupting protein interactions involving p53 ("the guardian of the genome") conducted in 2010 investigated a library of $>10^5$ inhibitor species[121].

HCA methods have been applied using a range of different automated microscopy platforms making use of multiple fluorescence intensity-based readout parameters to assay diverse biological systems. For example, work published by Nadler-Holly et al. in 2012 sought to use HCA methods to investigate the effect of mutations in the eukaryotic chaperonin containing t-complex polypeptide 1 (CCT/TRiC) on the expression levels of a library of ~5100 GFP-tagged endogenous yeast proteins[122]. HCA was performed in 384-well plate format using an *Olympus ScanR* modular imaging system equipped with a 60x air objective and a robotic arm (Hamilton) to minimise user intervention. The authors performed image analysis in native ScanR software to assess changes in expression level and localisation of the endogenous yeast proteins in response to CCT mutations based on GFP fluorescence intensity images; HCA results highlighted the role of the CCT3 subunit in the proper folding of glutamine-/asparagine-rich proteins.

A plate reading imager equipped for both Nipkow disk and wide field fluorescence imaging *(BD Pathway 855 Bioimager)* was used to acquire images in three spectral channels for an HCA investigation of inhibition of Akt pathways in work published by Link et al. in 2009[123]. Analysis of the degree of nuclear localisation shown by FOXO3a-GFP was used as an assay endpoint to reflect the activity of upstream elements of the Akt pathway. A *Beckman Biomek 1000* automated workstation was employed to administer inhibitor candidates[124] – a total of 33,992 small molecules – to samples in 96 well plate format. Based on the results of the HCA localisation screen, the authors reported the development of a potent and selective inhibitor of phosphoinositide 3-kinases. The assay quality factor is reported (separately) to be $Z' = 0.54$[125].

In the 2010 study of p53 protein interaction inhibitors, a *Thermo-Scientific ArrayScan VTI* instrument was used to acquire images from up to 50 384-well plates of cells a day, employing multiple automated liquid-handling and sample preparation devices (*Titertek Zoom, Velocity11 VPrep, BioTek ELx405, Titertek MapC*) to decrease user intervention across the 697 plate experiment campaign. By imaging fluorescence intensity in three spectral windows and employing simple image processing algorithms, Dudgeon et al. were able to use reduced colocalisation of p53-GFP and its binding partner hDM2-RFP as a metric to determine the

efficacy of inhibitor compounds. The assay quality factor for the assay developed in this work was reported to be $Z' = 0.64$.

As noted in section 2.3.1 above, colocalisation of fluorescent protein constructs is not a sufficient condition to determine that two proteins of interest are interacting. Mammalian-2-hybrid (M2H) screening is one means by which interaction partners may be determined. Similarly to yeast-2-hybrid assays, two proteins of interest may be ectopically expressed as fusions with the transcriptional activating domain (AD) and DNA-binding domain (DBD) respectively of GAL4: should the proteins interact, the resulting association between AD and DBD results in the transcription of a fluorescent reporter gene with a GAL4-upstream activation sequence. This methodology was adopted by Fiebitz et al. in a screen to assess hormone-dependent interactions with p53 using a Gal4-pZsGreen reporter[126]. In this application, the authors generated arrays of cells expressing 160 different combinations of prey and bait proteins by reverse transfection on a single microscope slide, spotted using a sciFlexArrayer piezodispensing instrument (Scienion AG). A *PE Applied Biosystems BIOCCD Image Reader* was used to acquire fluorescence images at low magnification, using Zeiss AxioVision LE software. Cell seeding and treatments were performed manually. Though not given explicitly, the assay quality parameter for this work may be estimated from supplementary information to be $Z' = 0.04$.

Despite the success reported by Fiebitz et al. in application of M2H screening to studying the modulation of protein-protein interactions, the low Z' score combined with reported problems of false positives highlight the limits of such an approach. As an alternative, FRET represents a good candidate as a technique to allow robust, high content analysis assays of protein-protein interactions to be conducted.

HCA FRET assays have also been employed in applications in which the central aim is not to elucidate protein-protein interactions. In a 2008 paper, Takanaga et al. conducted a high content FRET assay using an eCFP-YFP FRET biosensor which displayed a change in FRET state upon binding glucose[127]: this sensor was used as an assay end point for a siRNA knockdown screen of glucose uniporters (GLUT). A *Molecular Devices ImageXpress 5000A* platform controlled by *MetaXpress* software was used to acquire images in two spectral channels for measurement of FRET by sensitised emission, and a third (Cy3) channel in order to assess the transfection efficiency of siRNA. From FRET data the authors were able to conclude that GLUT1 and GLUT9 are critical in controlling glucose flux.

Separately, a 2007 study by Tian et al. sought to use HCA FRET to study anticancer activity of compounds from herbal medicine[128]. A *Perkin-Elmer Victor³* imaging plate reader was used to generate sensitised emission FRET images which were used to infer caspase 3 activity by cleavage of a FRET probe containing a DEVD caspase target sequence, similar to that depicted in Figure 2-10 (d). The authors report the success of the technique in measuring apoptotic response to a range of standard drug therapies with a high quality factor ($Z' = 0.87$); they also identified two novel compounds derived from plants used in traditional Chinese medicine.

2.5.5 FLIM plate readers for HCA

As discussed in section 2.3.3 above, FLIM offers a robust and quantitative readout of FRET. Despite this, and possibly because of the relative complexity of FLIM instrumentation, there is a limited number of applications of FLIM-FRET in an HCA context. The first implementation of fluorescence lifetime imaging on an automated plate reader for high content analysis was presented in 2007 by Esposito et al[129]. This instrument was developed in-house and based upon a fully automated *Zeiss Axiovert 200M* microscope, further equipped with an acousto-optically modulated laser source and a sinusoidally-modulated HRI (LaVision) to permit wide field frequency domain FLIM images to be acquired[130].

A similar wide field frequency domain plate reader was used by Grecco et al. to investigate FRET between Cy5-conjugated anti-phosphotyrosine antibodies and an array of YFP-labelled proteins in order to identify tyrosine kinase substrates. This study was performed in fixed cell arrays seeded on slides and reverse transfected using a gelatine-based transfection mixture spotted using a *Genetix Qarray2* spotter system[65] using a custom built FD-FLIM microscope platform equipped with a laser distance sensor to permit hardware autofocussing. The system was reported to be capable of measuring 384 different transfection conditions ("spots") every hour with an average of 50 transfected cells being present on each spot; the large number of individual cells assayed permitted the authors to draw inferences about variation within cell populations.

Time correlated single photon counting is generally considered too slow to be of practical value in HCA-FRET applications[63]; however, an instrument presented by Matthews et al. in 2012 illustrated the role that can be played by TCSPC-FLIM when deployed in parallel with other methods of measuring FRET[76], applied to interaction inhibitor screening. In this implementation, fluorescence anisotropy measurements of FRET were used as a means of pre-screening 96 well plates for potential interactions before FLIM measurements were taken to generate more quantitative data. Matthews et al. suggest that a 96 well plate might be read in five hours (108 images in total), though tyrosine kinase inhibitor screen data took >13 hours to acquire (~3 minutes per image). The instrument used in this study is modular in nature, and instructions on constructing such an instrument have been made available by the authors under an open licence along with the acquisition software[131].

In the Photonics group at Imperial College London, considerable work has been undertaken in developing a FLIM plate reader capable of reading out live cell fluorescence for FRET and other purposes in practical experiment times. The wide field time gated FLIM technology suitable for application to a plate reader for HCA was first published by Grant et al. in 2007: a home-built FLIM microscope based around an Olympus IX-81 frame with sectioned imaging capabilities afforded by a Nipkow spinning disk unit (CSU-X10, Yokogawa) and time-resolved detection provided by a high rate imager (HRI, Kentech) was used to demonstrate the capabilities of such a system[132]. Talbot et al. demonstrated the first application of wide field time gated FLIM in HCA on the same system adapted to read multiwell plates; plates of cells expressing a bimolecular FRET system were imaged to investigate

interactions between K-Ras and the Ras-binding domain (RBD) of Raf in response to EGF[133]. Typical FLIM acquisition times were 10 seconds per field of view, such that 96 images might in principle have been imaged in ~15 minutes.

A second FLIM plate reader was developed at Imperial College London based around a *GE Healthcare INCell Analyser 1000* plate reading system adapted by addition of a Nipkow spinning disk unit (CSU-X1, Yokogawa) and high rate imager (HRI, Kentech). This system benefitted over its predecessor by the improved performance of a newer generation of sectioning unit, a piezo-driven z-drive for fast refocusing, and updated control software. This system was applied by Kumar et al. to the measurement of EGFP-mCherry FRET constructs to illustrate its capabilities in increasing the precision of FLIM-FRET measurements over manual techniques, as well as to preliminary work studying the formation of HIV virions by FRET[134].

The study of virion formation in HIV was pursued on the home built plate FLIM plate reader described in Chapter 3: below, with a Nipkow spinning disk unit (CSU-X1, Yokogawa) used to afford optical sectioning. In 2013, Alibhai et al. reported the application of a CFP-YFP FRET-based aggregation assay to a study of the effects of N-myristoyltransferase inhibitors on Gag protein clustering in the HIV life cycle, resulting in successful elucidation of dose response curves and IC50 values[63]. The published work also illustrated the potential for homo-FRET – FRET occurring between identical fluorescent proteins – to be utilised in HCA studies, by successfully demonstrating that the change in CFP lifetime allows FRET aggregation studies to be carried out with a single fluorescent protein construct. Finally, this work showed the benefits of conducting such studies using HCA imaging rather than point measurements: segmentation of the cell membrane, where the interaction is expected to occur, increased the dynamic range of the assay and improved the assay quality parameters to $Z' = 0.67$ for the homo-FRET assay and $Z' = 0.82$ for the hetero-FRET readout.

2.6 Summary

This chapter has sought to provide an introduction to basic concepts in fluorescence and the parameters relating to fluorescence which may practically be measured. A discussion of the application of fluorescence measurements to problems in the life sciences has been presented, with specific reference to the means of achieving labelling of specific intracellular proteins by genetic methods. The phenomenon of Förster Resonance Energy transfer and a range of historical applications in the life sciences have been discussed. Further, means of measuring FRET, including by fluorescence lifetime, have been outlined. Instrumentation for fluorescence microscopy, and for fluorescence lifetime imaging (FLIM) in particular, has been introduced, and an overview of the state-of-the-art in high throughput screening and high content analysis has been included in order to provide the context for subsequent chapters in which work performed to develop FLIM as a practical HCA method is discussed.

Chapter 3: Development of an automated FLIM plate reader for high content FLIM imaging

Driven by the goal of applying wide field time gated fluorescence lifetime imaging microscopy to high content imaging assays, I have worked on the development of a FLIM plate reader throughout my PhD project. This work built upon and extended that previously undertaken in the Photonics group at Imperial College London[133,134]. Prior to the start of this project, development of FLIM plate reader technology had centred on extending a commercial INCell Analyzer 1000 (GE Life Sciences) for use as a plate reading FLIM microscope, following initial proofs of concept carried out on a home-built system. For my project it was decided that focus should be shifted to development of a FLIM plate reader around a motorised Olympus IX81 microscope frame in order to take advantage of the greater degree of flexibility afforded by this system. In particular, such an approach allows a choice between wide field and sectioned imaging, and permits the use of short wavelength laser excitation that is incompatible with the spinning disk unit used in previous plate reading FLIM systems in the group. In this chapter,

- An overview of hardware components in a home-built plate reading FLIM microscope with a combination of capabilities including time resolved and multispectral fluorescence and phase contrast imaging is presented.
- Key aspects of acquisition software development are described.
- Characterisation experiments for two different HRIs and implications for HRI specification are discussed.
- Assays of live and fixed cell samples transfected with fluorescent constructs, used to increase understanding of the scope of applicability of the system to FLIM-FRET biological assays, are considered.

3.1 FLIM plate reader hardware

The FLIM plate reader is built around an Olympus IX81 microscope frame and takes advantage of several motorised Olympus modules including a ZDC autofocus unit, a motorised nosepiece for objective selection and an automated filter cube cassette. The frame is supplemented with a motorised stage (Corvus, Marzhauser) that allows the sample position to be controlled by software. The microscope chassis is enclosed in a blacked-out incubator chamber with optional temperature and CO_2 control (Solent Scientific), facilitating the medium-to-long term imaging of live cell samples. An overview of the FLIM plate reader is presented in the schematic and photographs in Figure 3-1, electronic connections between different components are presented in Figure 3-2 and a more detailed schematic of the laser illumination and spectral selection unit is presented in Figure 3-3. Different aspects of the system are discussed in the following sections.

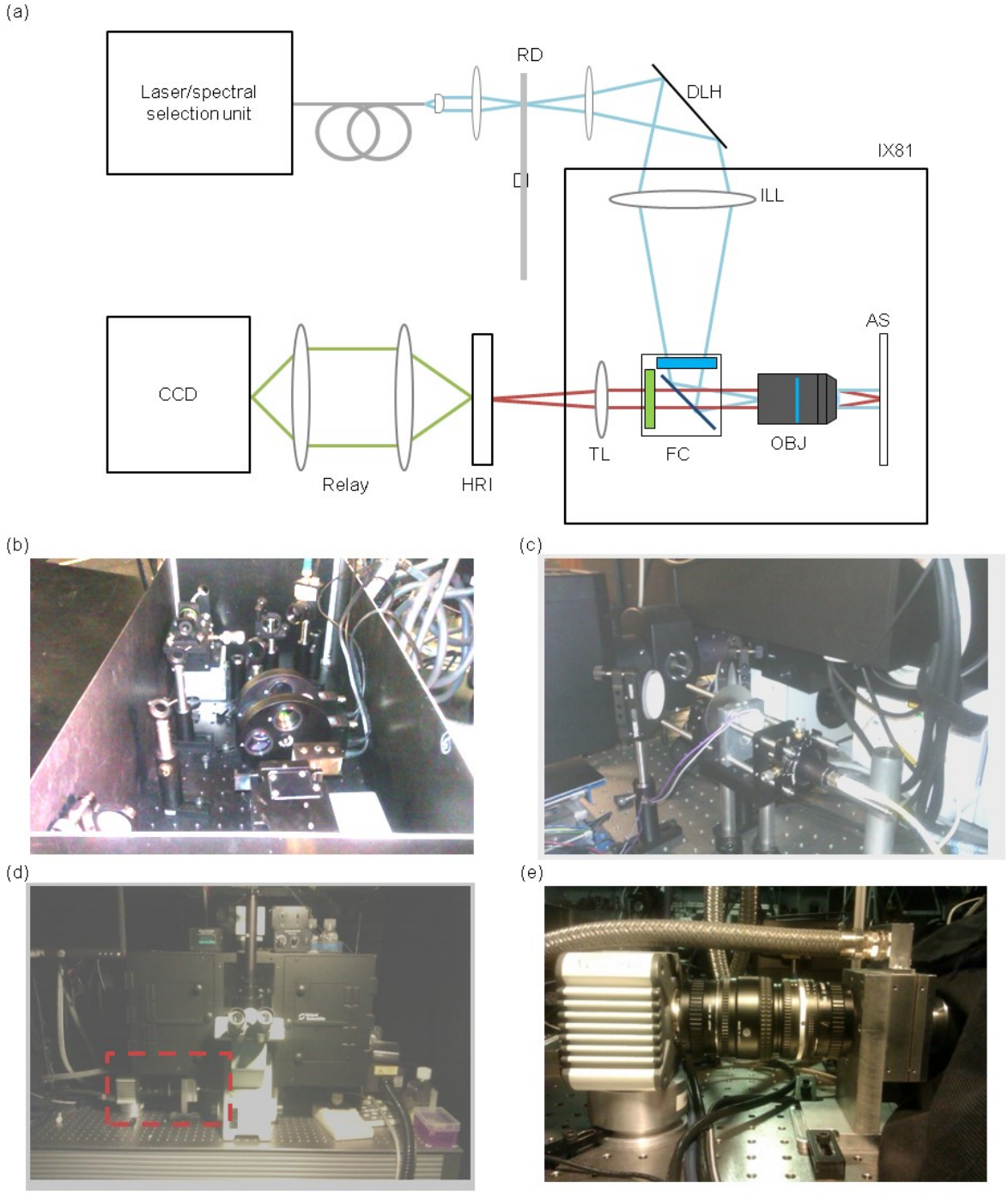

Figure 3-1 Photographs of the FLIM plate reader system.

(a) Schematic showing the optical path for wide field time gated FLIM acquisitions on the FLIM plate reader. RD: rotating diffuser, DLH: dual lamp house unit mirror, IX81: Olympus IX81 microscope frame, ILL: microscope fluorescence illuminator, FC: filter cube, OBJ: objective, AS: automated stage, TL: microscope tube lens, HRI: high rate imager. (b) Photograph showing detail of the spectral selection unit. (c) Photograph of the diffuser wheel assembly for coupling pulsed laser light into the microscope frame for wide field illumination. (d) Photograph showing a front view of plate reader system. Time gated FLIM acquisition arm is at bottom left, highlighted by the red dashed square; non-FLIM imaging arm is in the centre, connected to the trinocular. (e) Photograph showing the time gated FLIM acquisition arm (Camera, relay and HRI, from left to right).

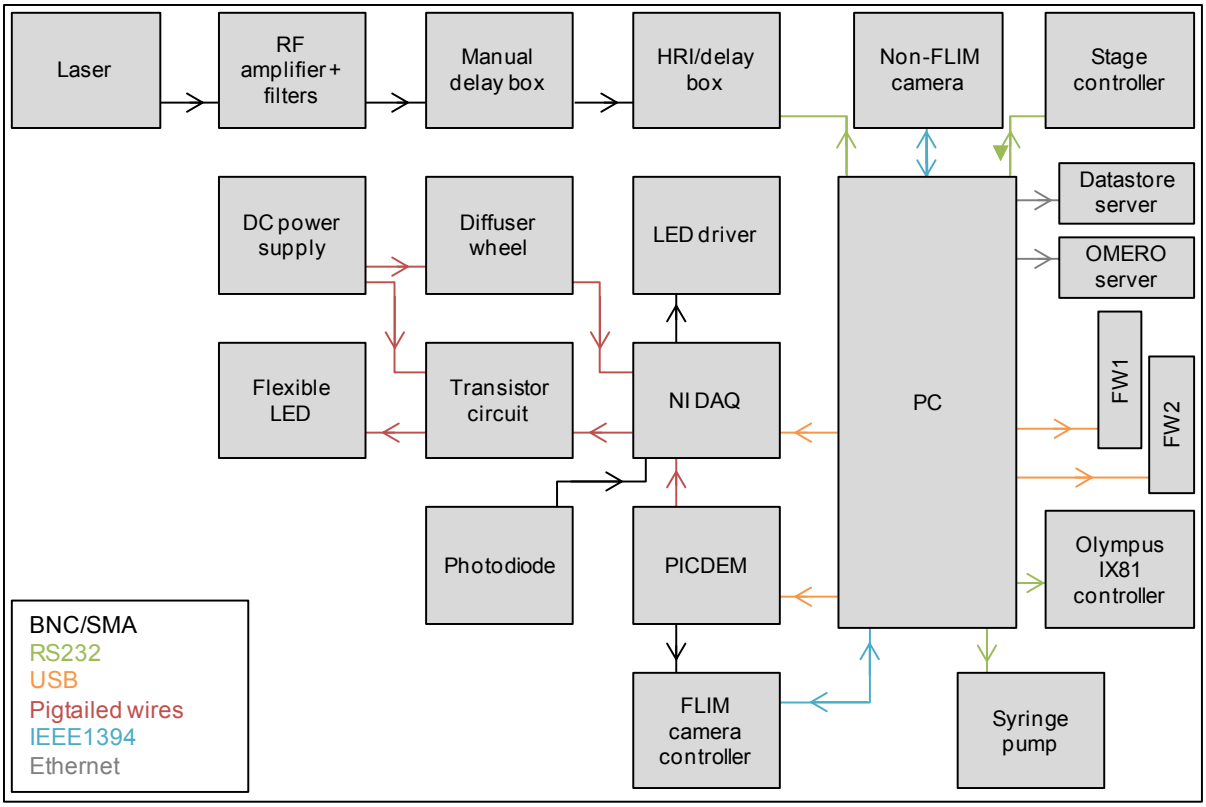

Figure 3-2 Schematic showing electronic connectivity between the components that make up the FLIM plate reader.
Connections are colour coded according to cable type.

3.1.1 Pulsed illumination for time resolved fluorescence measurements

For FLIM measurements, ultrafast laser sources are used to illuminate samples. To maximise flexibility within a set space on an optical bench, excitation lasers were coupled into optical fibres to permit convenient coupling of any laser on the optical table to any nearby instrument. Such an arrangement has the added benefit of minimising disruption when switching between wide field and optically sectioned imaging modalities. Visible wavelength studies were performed using a supercontinuum fibre laser as an illumination source. For all of the work presented in this thesis, a Fianium SC400-6 was used, providing 6 ps pulses at 60 MHz repetition rate with 1.5-5 mW/nm output over visible wavelengths (400-700 nm). Excitation wavelength selection and power adjustment was afforded by motorised six-position filter wheels (FW102B, Thorlabs). Laser power is monitored using a photodiode (DET10A, Thorlabs) from a 4% reflection from a glass flat in the beam path; the voltage output from the photodiode is read to the controlling PC using a DAQ card (USB6008, National Instruments). Broadband dielectric mirrors (BB1-E02, Thorlabs) were chosen to steer the beam into a fibre launch system consisting of a 3 axis microblock stage (MBT612/M, Thorlabs) and an achromatic Olympus objective (UPlanFL 20x/0.5, Olympus). The objective was chosen such that its focal length was appropriate for the numerical aperture of the fibres employed[135], and for its suitability for the anticipated range of (visible) excitation wavelengths. The whole "spectral selector" unit is mounted on a breadboard to allow easy repositioning should elements on the

optical bench need to be rearranged, and pinholes are positioned to facilitate quick and easy alignment. A schematic showing the layout of elements of the unit is presented in Figure 3-3.

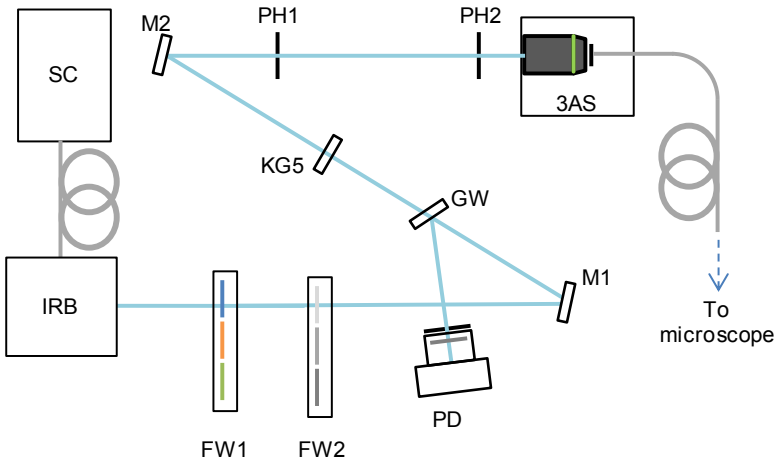

Figure 3-3 Schematic showing the layout of the "spectral selection unit" for coupling pulsed laser light into a single mode fibre.
SC: supercontinuum laser, IRB: infra-red mirror block, FW1: spectral filter wheel, FW2: neutral density filter wheel, PD: photodiode, M1: steering mirror 1, GW: glass window, KG5: Schott KG5 IR filter, M2: steering mirror 2, PH: pinhole, 3AS: 3-axis microblock stage.

In the duration of my PhD project, multiple different fibres have been used to couple light from the spectral selection unit to the microscope frame. These have included single mode fibres designed for use with visible light and connectorised for compatibility with Yokogawa CSU spinning disk units (QPMJ-3AFSP,3S-405/640-3/125-5AS-3-1-SP, OZ Optics), fibres designed to be single mode at ultra-violet wavelengths (QSMJ-3U,3U-320-2/125-3A-2, OZ Optics), and multimode fibres (M67L02, Thorlabs). The latter fibres have the benefit that it is simple to achieve high coupling efficiency. However, the ability of these fibres to carry many transmission modes leads to pulse broadening by mode dispersion ($\Delta T \sim 6$ ps[136]), and it was found that the multimode fibre was more susceptible to drift as illustrated in Figure 3-4 below. Here, time course measurements of fluorescein dye acquired at five minute intervals over four hours with finely (50 ps) spaced gates around the rising edge of the decay profile were used taken, and analysed in MATLAB to show shifts in the position of the measured decay with respect to the electronic synchronisation signal from the laser. Figure 3-4 (a) and (c) show overlaid traces of the leading edge across time course acquisitions for multimode and single mode fibres respectively; Figure 3-4 (b) and (d) show the shift in the position of the steepest part of the rising edge with respect to the zero time point position across the time course for each fibre. This data highlights the importance of using single mode fibres for acquiring data in which it is necessary to resolve changes in lifetime on the order of tens of picoseconds.

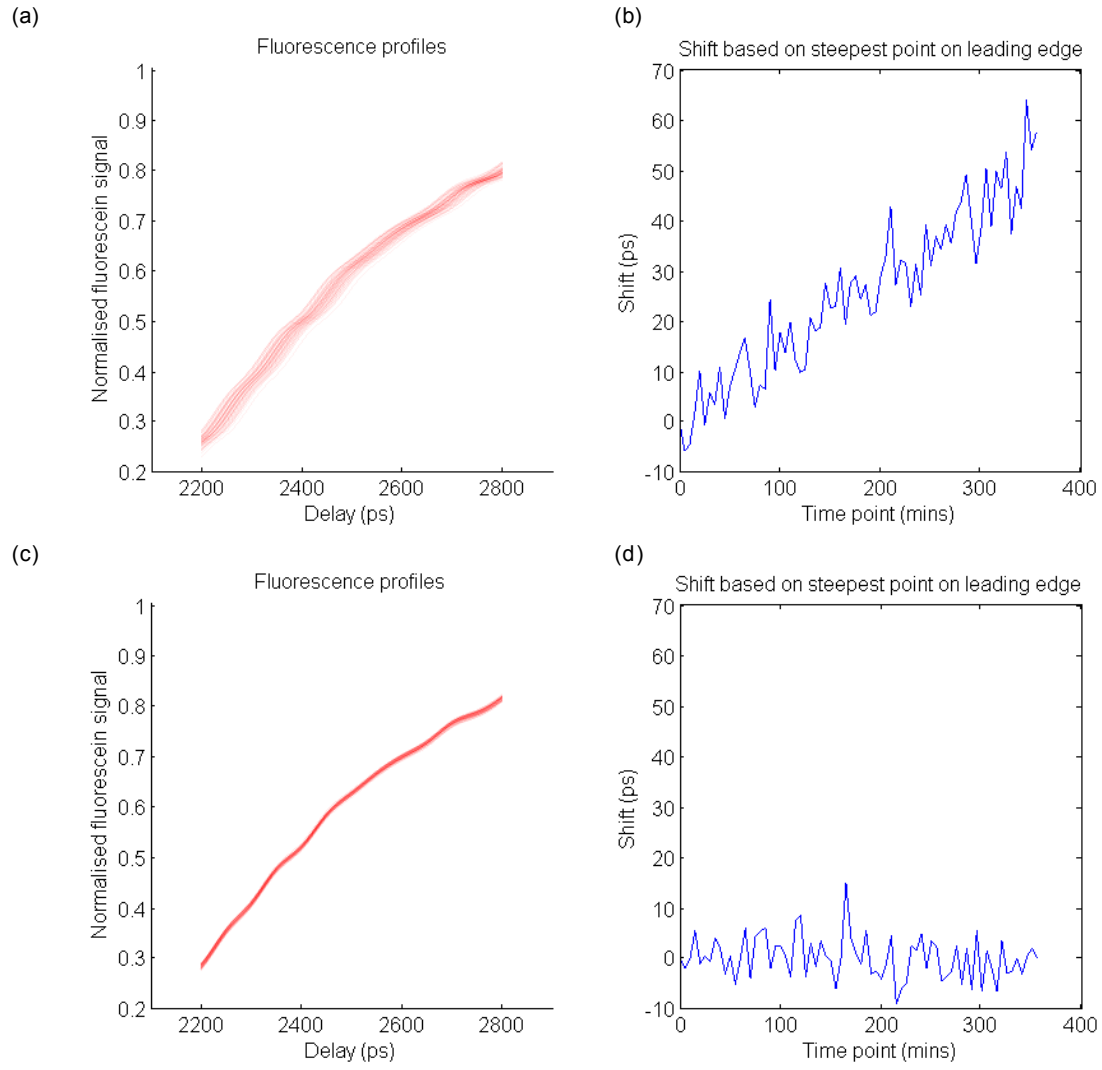

Figure 3-4 Comparison of temporal drift for multimode and single mode fibres
(a) Overlaid decay profiles showing the leading edge of measured fluorescence from a fluorescein sample acquired using a multimode fibre. (b) Temporal shift of the leading edge, defined by changes in the position of the maximum of the gradient of the decay profile, across a time course when using a multimode fibre. (c) Overlaid decay profiles showing the leading edge of measured fluorescence from a fluorescein sample acquired using a single mode fibre. (d) Temporal shift of the leading edge across a time course when using a multimode fibre.

For wide field imaging, pulsed illumination light is delivered to the sample plane via the fluorescence illuminator in the back port of the IX81 microscope frame. To reduce the spatial coherence of the excitation light that might otherwise lead to interference fringes at the sample plane, a spinning diffuser is included in the light path between the end of the fibre and the fluorescence illuminator (IX2-RFA, Olympus) in the back port of the microscope frame (Figure 3-1 (a) and (c)). For compatibility with UV illumination for autofluorescence measurements, a sheet of light shaping diffuser material on UV-transmitting acrylic (Luminit) was chosen rather than the ground glass diffuser wheels previously available in the lab (Table 3-1). The motor that drives rotation of the diffuser is connected to a power supply and to the DAQ box in order that the acquisition software can ensure that the diffuser wheel is running. To enable safe inspection of sample fluorescence by eye, a dual lamp house adapter (U-DULHA, Olympus)

is included in the illumination path to allow the illumination source to be switched between a mercury lamp and the pulsed laser source.

Diffuser	Transmission %	Notes
Plastic diffuser wheel	52	Previously used in lab, sample from Physical Optics Corporation.
1" ground glass diffuser	70	
Luminit UVT LSD, first order	77	Performed under specification, returned to manufacturer
Luminit UVT LSD, second order	90	

Table 3-1 Summary of UV transmission properties of diffuser wheels, measured at 365 nm.

For experiments in which optical sectioning is important for biological outcomes, light may be introduced to the sample via a Nipkow spinning disk unit (CSU-X1, Yokogawa) that is inserted prior to the detection arm (HRI and camera) on the left hand port of the IX81, as described elsewhere[63].

3.1.2 Time resolved fluorescence detection

Adjustment of the gated optical intensifier opening time with respect to a synchronisation pulse originating from the laser allows time resolved measurements to be completed. This is generally achieved using a delay generator that takes a filtered sinusoid as input, and outputs a trigger signal with approximately 50% duty cycle with a fast negative edge that can be used to trigger switching of a gated optical intensifier. For this project, the photodiode trigger output from the laser source is high pass filtered to remove any DC offset (BHP-25+, Mini-Circuits), and low pass filtered to remove high frequency components and noise from the signal (BLP-90+, Mini-Circuits) before amplification with a 40 dB RF amplifier (HSA-X-2-40, FEMTO). The signal is input to a slow switching delay generator (Precision Programmable Delay Generator, Kentech) and thence to fast switching delay generator (HDG, Kentech) that is interfaced with the controlling PC to allow sampling of the decay fluorescence at different delays relative to the excitation pulse.

The HDG "delay box" units used to sample fluorescence decays are typically programmed with calibration tables in firmware that allow delays to be accurately set when the electronic input originates from lasers with repetition rates of 40 MHz or 80 MHz. When a 60 MHz repetition rate laser is used, it is necessary to use a software-based calibration table incorporated in acquisition software to ensure that the actual delay used reflects the nominal delay set. Using a MATLAB script originally written by Sean Warren and an oscilloscope equipped with Ethernet connectivity (TDS 3014, Tektronix), calibration tables may be automatically generated for different delay boxes by measuring the phase shift between a synchronisation signal from a photodiode exposed to the pulsed laser source and the output signal from the HDG unit. Exemplar plots illustrating the need for calibration tables to be used are shown in Figure 3-5 below.

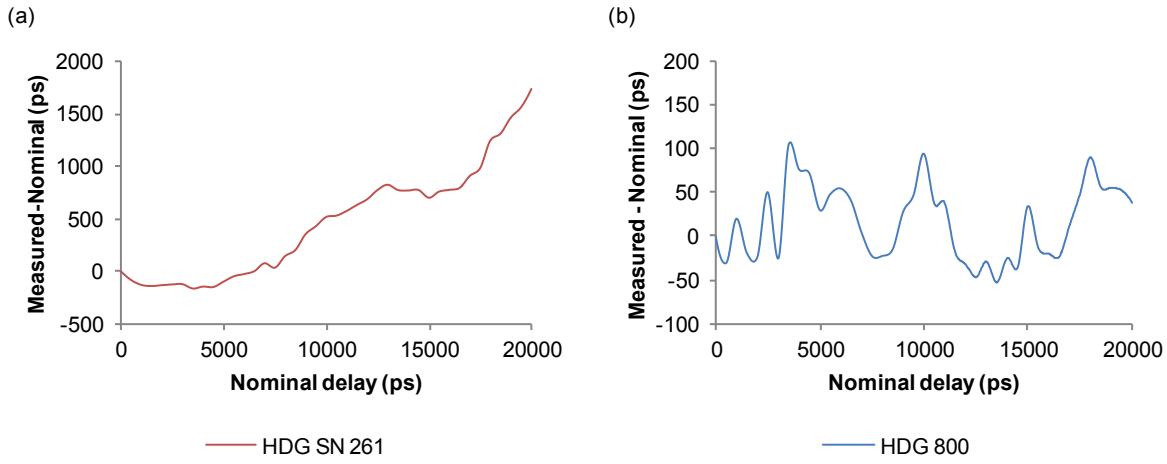

Figure 3-5 Plots showing differences between nominal and measured delays set by HDG delay boxes before applying software calibration table corrections.
(a) Differences between measured and nominal delays across the full range of nominal delays for an HDG delay box with a 60 MHz input signal. (b) Differences between measured and nominal delays across the full range of nominal delays for a next generation HDG800 delay box with a 60 MHz input signal. Note differences in vertical scale.

Two different gated optical intensifiers (HRI, Kentech) are used to acquire the data presented in this thesis. These are described as the "blue-sensitive" model, and the "single edge" model. They are distinguished from each other by spectral sensitivity, spatial resolution, and gate width range. Further details on HRI performance and operation may be found in section 3.3. The phosphor of the GOI is read out using a cooled CCD camera (ORCA-II-ER, Hamamatsu), coupled via a pair of camera lenses, providing 0.7x demagnification between the HRI and the CCD. This demagnification allows a larger field of view to be imaged. Combined with typical 2x2 binning of the CCD camera pixels, oversampling of the back face of the HRI is reduced. The camera integration time is controlled by an external clock signal generated using a microcontroller. For the majority of this project, a PICDEM board (PICDEM FS USB Demo board, Microchip) was used as the microcontroller. The PICDEM was later replaced with an Arduino Uno board to improve compatibility with recent versions of Windows and ease of programming. Crucially, controlling camera triggering and integration time from an external clock means that it is possible to synchronise laser power monitoring measurements with individual camera frame acquisitions, in principle enabling correction for any fluctuations in laser intensity between gates in a decay profile.

3.1.3 Bright field imaging

To enable information to be gleaned from datasets regarding cell health, morphology and confluence, phase contrast image capability was incorporated into the design of the plate reader. The option of a Ph2 contrast ring was included when purchasing a long working distance UV compatible 40x objective (LUCPLFLN 40x, Olympus) in order that high magnification phase contrast images might be acquired in line with FLIM images without requiring movement of the nosepiece. To increase the speed of acquisitions in which phase contrast imaging was to be interleaved with fluorescence imaging, it was necessary to replace the halogen transmitted light source present on the microscope frame for a white

LED source (MCWHL2-C1, Thorlabs); this source could be switched on or off significantly more quickly than the previous set up. Automated control of the LED is achieved by connecting the LED driver (LEDD1B, Thorlabs) to a DAQ box using a pigtailed BNC cable.

Typically, to avoid any risk of damaging the HRI photocathode, phase contrast images are acquired using the non-FLIM channel of the microscope. This may be automatically selected by switching between imaging path from the left hand port to the trinocular, upon which is mounted a small, lightweight firewire camera (FLEA2, Point Grey Research). A pair of 1" achromatic doublets are used in the lens tube that couples the camera to the trinocular to afford a 0.4x demagnification in order that the non-FLIM field of view size matches the FLIM field of view (along the long dimension of the chip).

3.1.4 Liquid handling for time lapse assays

In certain experiments it is desirable to interrogate the response of a FLIM signal to chemical stimulus. If it is necessary that a fast transient response should be measured in live cells, or if the baseline signal level varies significantly from cell to cell, it may be impractical or impossible to treat different wells for specific, well-defined time periods before imaging to extract the dynamic response profile. The only way to perform such experiments in the context of the automated plate reader is to integrate a liquid handling system capable of delivering stimulant or treatments to individual wells according to when the relevant command is encountered in the software.

In the absence of a commercial liquid handling solution to fulfil this role, a system was put together consisting of a syringe pump (Syringe Pump 200, KD Scientific) and a dispenser head constructed from a gel loading pipette tip and a rigid plastic tube for structural support. Polypropylene tubing was used to connect a disposable syringe in the pump to the dispenser head, which was suspended above the stage using posts attached to the microscope chassis. To permit communication with software, a standard telephone cable was modified so that the ground, transmit and receive pins on the RJ14 plug were matched with the appropriate pins on a 9-pin RS232 connector. Modular software was then written in LabVIEW to allow appropriate commands to be sent to the syringe pump to start or stop dispensing. These tools were then incorporated into the sequenced acquisition software and changes made to the user interface to allow a time course to be set up to include a "stimulation step" in user-defined wells. Due to the specific model of the syringe pump available, no more complicated commands than "start" and "stop" can be sent; it is therefore necessary for the user to set up the pump manually with the correct dispensing volume and syringe settings before starting the time course.

To test the reliability of this method of delivering liquid to the sample, and to allow the most suitable size of syringe to be chosen, different syringes were filled with water that was then dispensed onto a high precision weighing balance (A1204, Oxford Balances). The accuracy of successive dispensing steps could then be calculated based on the mass of water accumulating on the balance. The results of this experiment are presented as percentage errors in measured dispensed volume compared to nominal

volume, in Figure 3-6 (a). For clarity, only three situations are shown: dispensing using a manual pipette, dispensing from the automated system using a 5 ml syringe and a standard pipette tip-based dispensing head, and dispensing from the automated system using a 5 ml syringe and a gel-loading pipette tip-based dispensing head. The deviations from nominal dispensing volume that is evident when a standard pipette tip is used with the automated system can be linked empirically to retention of liquid on the pipette tip resulting in less than the nominal volume of liquid being delivered; on the next step, the excess retained on the tip contributes to a greater volume being dispensed. Since this retention depends on the tip, rather than on the volume dispensed, the percentage error in dispensed volume decreases with increasing nominal volume.

An initial test of the integrated liquid handling system and its related control software was carried out. A plate was set up with 100 µl 20 µM Rhodamine 6G (monoexponential fitted lifetime 4050 ps) in five wells, and the syringe was filled with 41 µM Rhodamine B (monoexponential fitted lifetime 1569 ps). 100 µl of Rhodamine B was dispensed immediately prior to the fourth time point in an 80 second time course for each well. The resulting fitted data is presented in Figure 3-6 (b). The results match well with the predicted values; the exception at the time point immediately following stimulation might be associated with finite mixing time.

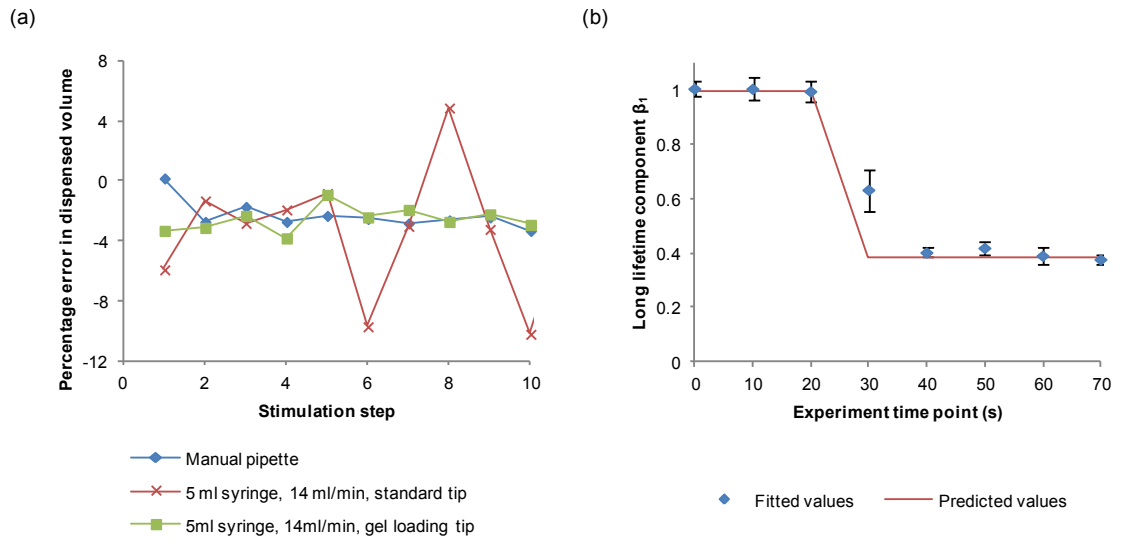

Figure 3-6 Characterisation of a simple automated liquid handling system for integration into the FLIM plate reader.
(a) Plot showing deviations of measured dispensed volume from nominal dispensed volumes across 10 dispensing steps. (b) Plot showing the measured and theoretically predicted lifetime values following automated dispensing of a short lifetime dye into a well containing an equal volume of long lifetime dye.

3.2 FLIM plate reader software

In order to maintain continuity with previous software and to ensure compatibility with tools written for other instruments in the lab, the software used to run the FLIM plate reader was developed in LabVIEW. This built on prior work by Dr Sunil Kumar, Dr James McGinty and Dr Clifford Talbot. LabVIEW provides a modular, graphical programming approach that, in principle, allows non-experts to combine modules (LabVIEW *virtual instruments*, or VIs) to automate particular experiments not supported by the default acquisition software.

The basic function of the acquisition software is to collect FLIM data from multiple positions across a sample, typically a 96 well plate. Prior to the beginning of this project, functionality extended to simple automatic assessment of the suitability of fields of view prior to FLIM imaging ("prefind"), autofocussing on the sample, automatic scaling of camera integration time to maximise dynamic range, and limited control over in-line imaging across different spectral channels, z-planes and time points in time-lapse experiments. In order to take full advantage of the functionality afforded by the hardware, and to meet the needs presented by samples throughout the project, I have continuously developed and updated the plate reader acquisition software. These developments are broken down here into those relating to changes in the automated acquisition process, changes in the prefind process for identification of samples of interest, and changes to the user interface made with the goal of increasing ease-of-use for the software.

3.2.1 Extension of automated acquisition sequence capabilities

The functionality associated with the automated acquisition of FLIM images was extended in line with demands posed by biological applications throughout my PhD project. The acquisition of images across multiple spectral windows was modified in order to present a more flexible approach to such acquisitions: HRI, delay and camera settings may now all be linked to a particular named filter configuration. This modification allows intensity information to be generated in different spectral windows without the necessity to acquire a FLIM sequence, and enables camera and HRI settings be optimised in cases where the relative intensity changes significantly across channels.

A greater degree of flexibility was also afforded in setting up time lapse imaging sequences, allowing the user to set custom time points, and to control whether the software adheres strictly to the time course laid out or completes all requested measurements before proceeding to the next time point. Changes were made to the sequenced acquisition tools to permit imaging of samples at low magnifications for fast surveying whilst retaining autofocus functionality: since the Olympus ZDC autofocus system does not function with low magnification objectives, this required a separation in the acquisition set up variables between the imaging and autofocus objectives.

Effort was devoted to the possibility of deploying a preview tool to afford near-instant feedback on measured lifetime values in the course of a sequenced acquisition. Whilst lifetimes presented by such a

tool would need to be treated with caution, this output might provide reassurance on the success of an assay or flag up potential issues prior to more in-depth analysis. Preview lifetime data may be generated using the linearised least squares determination method[78,137]. Briefly, after each field of view has been acquired, user defined intensity thresholds are applied to images summed across delays. Thresholded data is then analysed pixelwise, applying the expression

$$\langle \tau \rangle = -\frac{N\sum_i t_i^2 - (\sum_i t_i)^2}{N\sum_i t_i \ln I_i - (\sum_i t_i)(\sum_i \ln I_i)} \qquad 3.1$$

to generate a "mean photon arrival time" image from N gated images, where t_i and I_i represent the delay and (pixelwise) intensity at the i^{th} gate. Resulting mean lifetime images are presented during the acquisition (Figure 3-7 (a)). The average lifetime value of thresholded mean lifetime images is saved according to well position within the plate, in order that the user might be presented with an overview of lifetime trends across the plate immediately upon completion of the acquisition sequence (Figure 3-7 (b)).

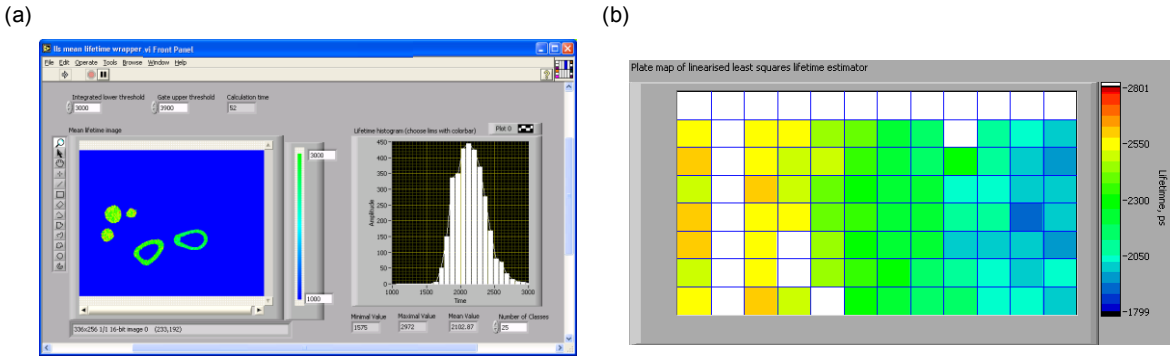

Figure 3-7 Screenshots illustrating the linearised least squares method of determining lifetime previews. (a) A screenshot of the LabVIEW VI that calculates linearised least squares determination method lifetimes pixelwise for each field of view in line with acquisition. (b) A screenshot of the resulting plate map of linearised least squares determination method lifetimes combined wellwise as presented in LabVIEW following acquisition. Exemplar data acquired from a FRET construct sample (see section 3.4).

The means by which data acquired in automated sequences might be stored and shared was also considered. The Open Microscopy Environment (OME) is a joint venture between academic and industrial research groups in conjunction with software engineers to develop open source software and data standards for storage and manipulation of microscopy data[138]. OMERO represents a data management tool for the storage, visualisation, analysis and sharing of microscopy data within and between research groups[139]. I worked towards establishing a standardised pipeline for importing time gated FLIM data into OMERO; in the course of developing the FLIM plate reader software, preliminary work has been undertaken to this end. Integration of modified MATLAB code, originally written by Dr Yuriy Alexsandrov, into LabVIEW now allows FLIM data, along with additional fluorescence intensity or brightfield images and metadata, to be uploaded to OMERO servers in line with acquisition. For the time being, this represents a duplication of data, and the format of uploaded data is such that each gated image in a FLIM sequence is represented by a different TIFF file. In future it is likely that the FLIM data

standards adopted will instead save wide field time gated fields of view in a single, multipage TIFF. A DLL was written and integrated into the LabVIEW acquisition program to facilitate saving FLIM data in a multipage TIFF format with acquisition metadata bundled in the file header, using an arbitrary standard. Saving in this format yields an improvement in disk writing time compared to using LabVIEW IMAQ VIs to save multiple TIFFs (factor of 4).

3.2.2 "Prefind" tools

The default behaviour for an automated acquisition in which multiple fields of view per well are to be imaged is simply to image the first field of view at the well centre, then spiral outwards acquiring non-overlapping fields until the required number of images have been recorded. For plates in which cells are sparsely seeded, or in which there are relatively few transfected cells per well, simply acquiring FLIM images of fields of view spiralling outwards from the centre of the well is inefficient since many of these fields of view are likely not to contain fluorescent cells. In these cases, it is useful to perform a "prefind" step before taking FLIM images, whereby a single image is acquired across an array of search positions and is assessed for suitability for inclusion in the FLIM measurement sequence. The generalised process behind all the prefind methods discussed here is shown in Figure 3-8. A simple version of such a tool existed previously in software developed for running the FLIM-adapted INCell Analyser 1000. With this method, the test images are acquired using the same objective as is eventually used for FLIM imaging and the criteria for suitability of a field of view is based on intensity (to separate fluorescent cells or objects of interest from background) and percentage coverage of the field of view. This approach has the benefit of simplicity: the controls for thresholding, percentage coverage, the number of FOVs to find, and the number of attempts per FOV could be integrated into the front panel of the main acquisition program without overcrowding the user interface. However, this method can still be time consuming dependent on the sample sparseness and how stringent the brightness and coverage thresholds have been chosen to be. Especially in the absence of piezo-controlled fine focus adjustment, it was not uncommon that the prefind step should take even longer to complete than the FLIM acquisition itself using this procedure.

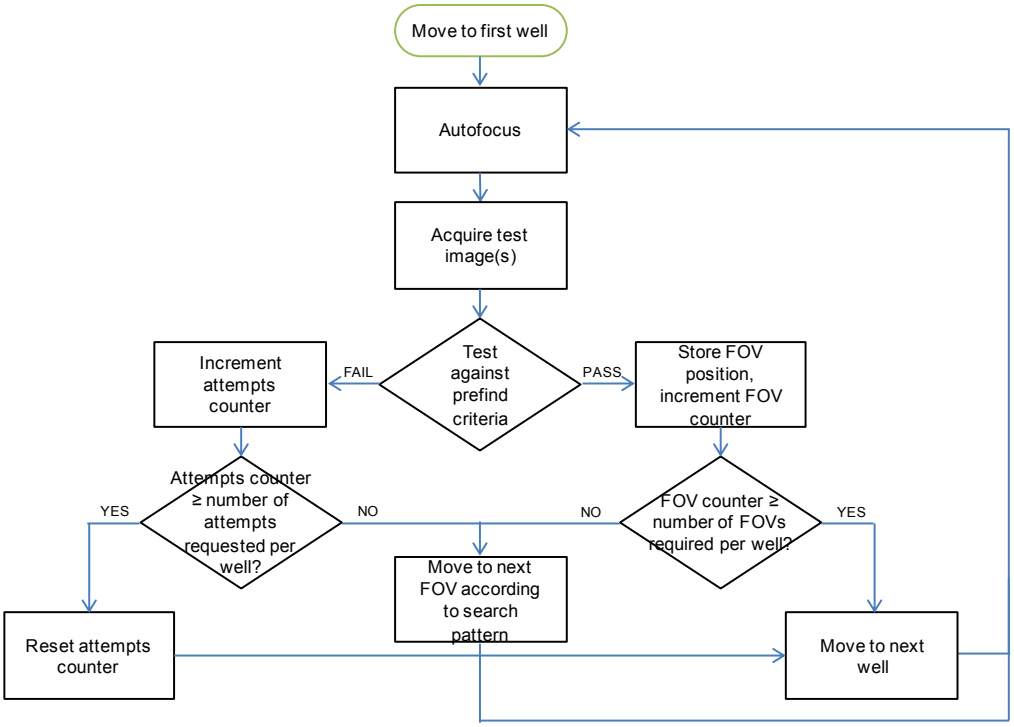

Figure 3-8 Flow chart describing the generalised process followed by the prefind tools implemented in the plate reader acquisition software.

To improve the speed and increase the breadth of functionality of the cell prefind tool, a series of sub-VIs were designed from scratch. The controls for setting prefind parameters were moved from the front panel to a separate set up window (Figure 3-9) to avoid cluttering the main UI window. The changes in functionality are laid out in brief in the following subsections.

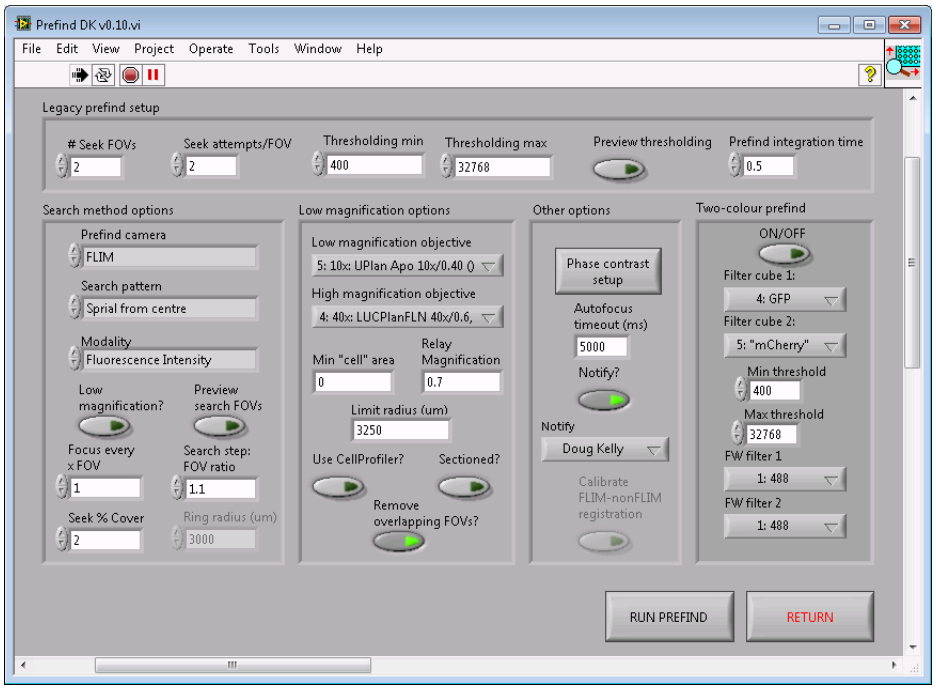

Figure 3-9 Screenshot of the control window for setting up the cell prefind tool in the FLIM plate reader acquisition control software, illustrating the range of prefind options available.

Prefind search pattern

This control allows the user to specify the arrangement of search FOVs within a well. "One shot" leads to a single position being assessed per well; "Spiral from centre" is the default search pattern whereby the search starts at the centre of the well and searches through an array of positions resulting in tiled FOVs following a spiral pattern. The "Ring" search option was introduced in response to samples in which the density of fluorescent cells in the centre of the well is lower than at larger radii due to seeding technique or cells being washed away from the centre of the well by pipetting. This option is implemented such that the user may choose the search radius.

Prefind imaging modality

It is typical for FLIM experiments that only a subpopulation of the cells in any given well may express the fluorescent construct under consideration at sufficient levels to be of use: therefore, a fluorescence intensity thresholded search is usually the preferred method for identifying cells of interest. However, for autofluorescence lifetime experiments, or in the case where cells have been stably transfected, all cells present may be assumed to be bright enough to perform FLIM experiments and so intensity-based criteria are not useful. Furthermore, it is generally not desirable to subject the sample to more fluorescence excitation light than is necessary in order to prevent possible photobleaching. For these reasons, if the cells are sufficiently sparsely seeded that a prefind is necessary, then it is desirable to use phase contrast imaging to allow the software to identify cells and hence suitable fields of view.

After a review of relevant literature and some exploration of image processing tools available in LabVIEW, I decided that the fastest, most effective and most easily integrated means of analysing phase contrast images was to perform thresholding on a variance image derived from the phase contrast image[140]. Briefly, the value of each pixel of the variance image is obtained by calculating the variance over a disk of user-defined radius centred upon that pixel in the raw phase contrast image. The user can then choose a minimum variance threshold, to highlight regions enclosed by sharp edges in the phase contrast images, as well as a maximum threshold to avoid anomalous highlighting of pieces of debris. Area thresholding controls also help to prevent such anomalies by allowing the user to set the minimum size of highlighted area that is considered to be "cell" rather than debris. The resulting binary, thresholded images can then be used by the prefinding software to identify suitable fields of view in a similar manner to when intensity-based thresholding is used.

(a) (b)

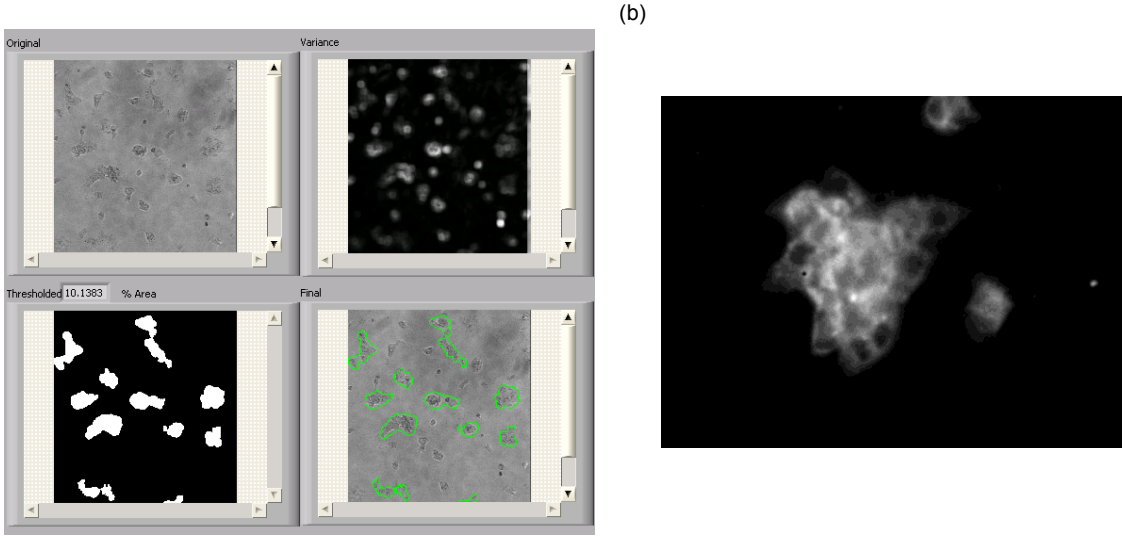

Figure 3-10 An illustration of the deployment of low magnification phase contrast cell prefind on the FLIM plate reader using MCF7 cells.
(a) A screenshot taken as the prefind operation is in progress, illustrating that the combination of controls available allow successful identification of cells in the presence of large scale variations in illumination and cell debris in this day-old live cell plate. (b) Exemplar resultant high magnification fluorescence (FLIM) field of view.

It is important that the user is aware of the contrast in the sample under investigation when considering using the phase contrast prefind modality. For example, for Cos7 cells the boundary delineated by the cell membrane is difficult to see even by eye under phase contrast illumination, and it is unlikely that the software will succeed in properly segmenting the prefind images. As well as considering whether this method is suitable for the particular sample, it is important for the user to be aware of the differences in phase contrast image quality between the centre of the well and the edges. The meniscus of the media, and the sharp edges of the chimney wells, interfere with the correct illumination of the sample from the bright field condenser above the plate. Therefore the phase contrast prefind is best employed for samples in which there are cells present in the centre of the wells, or indeed for samples prepared on microscope slides or coverslips.

Low magnification prefind

Along with the option to increase the number of stage positioning steps per autofocus step, the ability to search for cells using lower magnification objectives proved crucial in increasing the speed and the effectiveness of the prefind tool. A lower magnification objective enabled prefind images of correspondingly larger regions of the plate to be acquired, decreasing the time taken per unit area searched. One significant drawback of the current implementation of this method is that the ZDC autofocus unit is not capable of focussing when the magnification of the objective in place is less than 20x, because of the relatively poor light collection of such lenses. This means that the objective turret must be rotated to a higher magnification objective every time an autofocus step is required, adding significantly to the time taken for the low magnification search.

A brief outline of the process of the low magnification prefind is as follows: prior to starting the prefind process, the user chooses the low magnification objective, as well as the high magnification objective intended for use in the eventual FLIM acquisition. Initially, the stage is moved to the centre of the first well. If necessary, an autofocus step is carried out, followed by rotation of the nosepiece to engage the low magnification objective. A prefind image is then taken at the low magnification, and is processed according to the modality selected (intensity- or phase contrast-based). The resulting binary image is then passed to a VI that counts "particles" in the image, in this case the highlighted areas corresponding to cells. The output of this VI includes an area parameter: the regions are then sorted so that the largest fall at the top of the results array. Another output parameter, the "centre of mass" of each particle, is passed to a VI which removes particles that, on account of falling within a high magnification FOV centred on a particle higher in the list, would otherwise be measured twice. The remaining particle centres of mass are then passed through two small VIs that map low magnification image coordinates to high magnification image coordinates, and then image coordinates to stage coordinates: the resulting stage positions are such that each highlighted region will fall in the centre of the high magnification field of view when the FLIM data is eventually acquired. If the number of resulting FOVs is greater than the number requested by the user in the control "# FOVs", then only the first "# FOVs" fields are stored, and the stage is moved to the next well. If an insufficient number of fields have been found, then the stage is moved to the next FOV in the same well according to the search pattern chosen. A typical low magnification prefind run over a whole 96 well plate might take on the order of 30 minutes, dependent on transfection efficiency and seeding density.

In addition to the problem of switching objectives to engage the autofocus in the ZDC unit, the lateral offset between low and high magnification fields of view is a problem in this implementation. After consultation with Olympus representatives, no obvious optical solution could be found, and so it remains the case that a calibration tool is required to place regions found in the low magnification successfully in the centre of the high magnification field of view. This is simply a case of running a VI, which takes an image with each objective and requires the user to click on the same feature in each image. The offset values returned by the calibration only change if the objectives are moved to different positions on the nosepiece – for day-to-day running of the instrument, this calibration step is not required. Another minor inconvenience of running the low magnification prefind based on fluorescence intensity with M≤10 is that it is necessary that the condenser be flipped up out of the path. This is because of the background caused by reflections from the condenser, which reduce the contrast in the image and increase the likelihood of false positives in the FOVs output.

Prefind in two spectral channels

It is often assumed that presence in a cell of one of the plasmids transfected implies that the other plasmid has also been transfected into the cell, for example in intermolecular FRET experiments where the donor and acceptor plasmids are typically distinct but cotransfected. Empirically, this is not always the

case, and it certainly does not follow that high expression of the donor plasmid means that expression of the acceptor plasmid is also high. If cells containing satisfactory levels of both donor and acceptor fluorescence are reasonably ubiquitous then running a prefind search interrogating donor-wavelength fluorescence only is sufficient, though it is then useful to acquire acceptor-channel images in the final automated acquisition to allow thresholding based on acceptor levels to be performed during processing. However, if cells with sufficiently high levels of acceptor are relatively rare, then this is an inefficient use of imaging time as a large proportion of the fields of view imaged will be discarded during processing.

An alternative is to set thresholding levels in both donor and acceptor spectral channels and to apply these to prefind images in both channels. The resulting binary images are then combined ANDwise, and the resulting image is processed as normal based on the other prefind options chosen. This ensures that any region found in the search has appropriate levels of both fluorescent species, minimising the likelihood of imaging unsuitable FOVs. A drawback of this approach is that switching the position of the filter cube cassette twice per FOV interrogated significantly slows down the prefind process, even when the cubes are adjacent in the cassette.

Advanced prefind image analysis

CellProfiler is an open source software tool designed for use for biologists who wish to quantitatively measure phenotypes from thousands of images automatically[141]. Three separate motivations led to incorporation of CellProfiler as an option in the prefind routines. Firstly, as a pre-existing tool, many biologists concerned with microscopy will be familiar with the interface. Secondly, CellProfiler is equipped with a large number of image processing algorithms; it would be inefficient to rewrite these in LabVIEW. Thirdly, as an open source tool, CellProfiler is constantly being updated and additional functionality being added – by incorporating it into our software, we make use of a large community of developers working together to create a more flexible and powerful set of tools.

Modules for CellProfiler 2.0 are written in Python, based on code written by Dr. Volker Hilsenstein (EMBL, Germany) using socket communication. To improve the user interface, I rewrote the code in order that the CellProfiler module runs in a server mode. Since Labview can launch executables from the command line, and CellProfiler supports command line switches to run automatically with a pre-defined pipeline, designing the software in this manner allows the user to run CellProfiler from the prefind setup, and add modules to the pipeline in order to segment the current FOV as desired. Running the CellProfiler pipeline starts the socket server. When the user has set the prefind running from Labview, the prefind software connects to CellProfiler as a client in order that images can be sent from Labview to the CellProfiler pipeline, and object positions can be sent back to Labview for storage and conversion as appropriate.

In-line prefind/FLIM acquisition

Previously, it was intended that the prefind should be run prior to the FLIM acquisition, with user intervention in between. This mode, which is still the default, allows the user to set up acquisition parameters after the prefind has been performed and check that the fields of view found are acceptable. In cases for which imaging parameters are known beforehand, acquiring FLIM data in-line with the prefind, that is to say as soon as an acceptable FOV has been found, may save time, both by cutting down the total time required for autofocussing and by eliminating the need for user interface between finding cells and starting the acquisition.

3.2.3 Development of user interface

Further additions to the functionality of the instrument were made with the goal of increasing the user-friendliness of the software, and to facilitate collaborative research. In some cases, specific software release versions were generated on a case-by-case basis to provide a cleaned-up GUI on the final tab of main program front end: typically, it is possible to use the event-based nature of the main program to bundle common functions for a particular application in order that a less experienced user is faced with a less daunting array of controls. Further changes to the function of the program were made with expert users equally in mind, to improve the overall workflow and enable rapid, error-free configuration. The initialisation process, in particular the relatively time consuming step of stage calibration, was redesigned in order that this could be bypassed, or performed in the background while the user selects other hardware configuration options. Hardware and software was modified to provide feedback on whether the diffuser wheel was rotating at the beginning of a sequenced acquisition, as a stationary diffuser causes a fixed pattern to be overlaid on the illumination. In addition, important settings that cannot be checked automatically, including the possible presence of ND filters in the microscope illuminator and the fact that the HRI should be wrapped in blackout material to reduce the impact of ambient light on measurements, were highlighted in a message box prior to starting sequenced acquisitions; users can choose not to be reminded again of these settings in the current session. The scope of the "ABORT" control was widened to cover all time-consuming setup and acquisition steps, allowing the user to gracefully stop any experiment if settings had been misjudged. Gmail-based VIs were incorporated to provide notification emails upon completion of prefind and sequenced acquisition steps, and an address book VI provides functionality to change the recipient of notifications and add new users to the list of saved addresses. With significant input from Sunil Kumar, modifications were made such that the software should feed back more visually to the user the position of the current field with respect to the current well by drawing an outline of that field within a circle representing the well in a preview window. In addition, the option to automatically accumulate downsampled (4x) images in a montage of the entire plate was added: the user may then save the montage image, for example to give an overview of transfection quality across a whole plate. Finally, the simple addition of an "Are you sure?" dialog that appears after clicking the quit button prevents users from mistakenly closing the imaging session prematurely.

3.3 Preliminary HRI characterisation

The high rate imager (HRI, Kentech) is the enabling technology that allows FLIM experiments to be carried out on the automated plate reader. Under time gated operation, wafer-based fabrication allows standard model HRIs to provide (quoted) 10 lpmm^{-1} resolution across the 18 mm photocathode, permitting the acquisition of fluorescence lifetime data over all pixels in a field of view in parallel and thus enabling FLIM experiments to be conducted in multiwell plate formats on a practical time scale. The principles of operation of HRI instruments have been outlined in Chapter 2: section 2.4.3; here various parameters associated with the two different HRI units used in the course of this project are discussed. The characterisation experiments presented here act as preliminary work for an ongoing project within the Photonics group at Imperial College London that seeks to compare different HRI models with different design parameters.

Two different Kentech high rate imagers were used for the data presented in the remainder of this thesis: a blue-sensitive model that may be considered to be a "standard" HRI, and a prototype "single edge" model, the electronics behind which were designed to give a fast rising gate edge and a slower falling edge. These models are distinguished by differences in spectral sensitivity, spatial resolution, range of gate width and gate shape. The nominal differences in specification are presented in Table 3-2 for reference. Spectral sensitivity curves for the intensifier tubes, determined by the wavelength-dependent QE of the photocathode, are shown in Figure 3-11. Methods and results relating to the measurement of a number of these parameters are presented below, followed by a brief discussion on the relative strengths of the two devices.

Parameter	Single Edge HRI	Blue Sensitive HRI
HRI serial number	J0601161/2	J0404621
Intensifier tube serial number	0920264	0404906
Photocathode	S25	S20
Spectral sensitivity, peak wavelength (nm)	700	480
Spectral sensitivity, width (nm)*	500-800	400-560
Phosphor	P43	P43
Phosphor emission, peak wavelength (nm)	545	545
Phosphor lifetime (ms)**	1	1
Default gate width range (ps)	1800-6800	200-1000
Gating voltage (V)	32	24, 54

Table 3-2 A summary of manufacturer specifications for two HRIs used to collect data in this thesis. Information has been collated from private correspondence with Kentech Instruments Ltd, intensifier tube specification sheets[142,143] and product manuals[144]. *Width defined as the range of wavelengths for which sensitivity is greater than 40 mA/W. **Phosphor lifetime defined as the time taken for intensity to fall from 90% to 10% of original intensity[145].

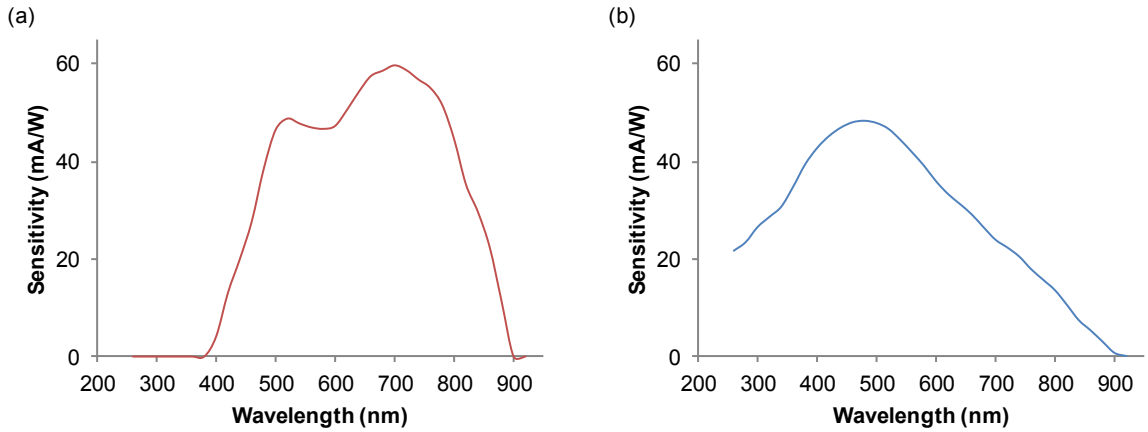

Figure 3-11 Spectral sensitivity curves for two HRIs used to collect data in this thesis.
(a) Spectral sensitivity for the single edge HRI[143]. (b) Spectral sensitivity for the blue-sensitive HRI[142].

3.3.1 Photon-digital number conversion factor

To allow judgments of acquisition strategies to be made with confidence based on typical rule-of-thumb indications for number of photons necessary to fit different models to lifetime data[146], it is useful to be able to convert between digital numbers (DN) recorded by a CCD camera, and photons incident on the photocathode of the HRI. In a simplified model of the HRI-camera detection system, the mean recorded signal in digital numbers ($\bar{N}_{DN}$) is related to the photons incident on the photocathode (N_{phot}) by the expression

$$\bar{N}_{DN} = kN_{phot} \qquad 3.2$$

where k comprises several factors relating to different stages of detection, including the microchannel plate gain, phosphor conversion efficiency, coupling optics transmission and CCD quantum efficiency.

The means of determining the value of k has been described elsewhere[104,147] and the equipment used is shown in Figure 3-12. Briefly, an LED source at 623 nm (Phlatlight CBT-40, Luminus) was used to uniformly illuminate the photocathode of each HRI, with a fixed 3.2 OD neutral density (ND) filter placed in front of the photocathode to reduce the incident flux to avoid damaging the photocathode, and ND filters of different densities used to vary the level of incident light on the photocathode. A combination of lens tubes and optical cage system components was used to ensure a common axis, and a combination of a rotating diffuser wheel, a diverging lens, and a long distance between this lens and the front face of the HRI ensured uniform illumination. Measurements were taken on different days. The driving current of the LED was set at the start of each day to a level that avoided saturation of the camera for the case of highest gain and lowest ND filter, and the LED left running for two hours before measurements were taken in order to allow the output illumination to stabilise. In addition to measurements with varying ND filter combinations, measurements were also taken with the HRI capped to generate background images that were subsequently used to account for fixed pattern CCD noise and

to calculate the standard deviation associated with CCD noise. Each HRI was characterised at three different gain voltages (650 V, 750 V and 850 V). A tool was written in LabVIEW and integrated into the acquisition software to take 100 repeat images at a range of integration times in the range 1-500 ms using shutter timing on-board the Hamamatsu ORCA ER-II.

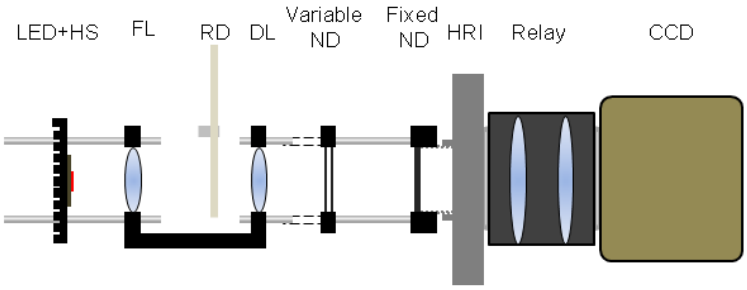

Figure 3-12 A schematic showing the experimental set up used to determine the relationship between photons detected by an HRI and the mean recorded signal in digital numbers.
HS: heatsink, FL: focusing lens, RD: rotating diffuser, DL: diverging lens, ND: neutral density filter.

An analysis software tool written in MATLAB was used to determine photon fluxes incident on the photocathode (photons pixel^{-1} s^{-1}) based on images taken at high gain with maximal ND filters: for this "photon counting" data, individual photon events can be distinguished in the acquired images, and fluxes calculated from the gradient of plots of the number of photon events against acquisition time generated by the software. In determining the digital number threshold above which pixels are determined to be associated with photon events a deviation was made from previously published methods[104], with an approach identified by Sean Warren being adopted instead. Using a CCD noise term σ_{CCD} inferred from measurements made with the HRI capped, an analytical expression for the intensity threshold t was derived such that the probability of false positives being counted as photon events in an image convolved with a kernel of radius r should fall below a given value p (derivation performed by Sean Warren and outlined in Appendix 1):

$$t = \sqrt{2} \cdot \sqrt{\pi r^2} \cdot \sigma_{\mathrm{CCD}} \cdot \mathrm{erf}^{-1}\left(1 - \frac{2p}{n_{pix}}\right) \qquad 3.3$$

The kernel size $r = 4$ was chosen empirically in order that separation between photon events should be maintained whilst ensuring that all DN counts in a cluster associated with a single photon event are included in the calculation. Based on 256×256-pixel central regions of the CCD[147], with $\sigma_{CCD} = 2.07$ DN by calculation and choosing $p = 0.001$, the appropriate threshold was determined to be $t = 81.3$ DN. A second MATLAB script was written to generate values of k from plots of mean detected signal against incident flux for each HRI at each gain voltage.

Figure 3-13 (a) shows an exemplar 256×256 region of a camera frame captured with high gain voltage and ND filter settings, illustrating the appearance of individual photon events, whilst the intermediate

image in the photon counting analysis script is presented in Figure 3-13 (b) . Using calculated photon fluxes for each ND filter used, values of k from plots of mean detected signal against incident flux for each HRI at each gain voltage were generated from the fitted gradients of mean recorded signal against detected photon plots as depicted in Figure 3-14 (a) and (b) for the single edge and blue sensitive HRI models, respectively. These values of k are presented in Table 3-3. In addition, it is possible to extract the counts per photons for the high gains by taking the maximal value of the convolved photon-counting data for each thresholded photon event. These values are plotted in histograms in Figure 3-14 (c) and (d), and mean values are shown in the final line of Table 3-3. There is fairly good agreement between the k-factors for 850 V measurements calculated from the two approaches: it is possible that discrepancies are linked to the method of extracting means from the histograms, rather than fitting appropriate probability distributions. Further improvements might be afforded by a different choice of ND filters to provide a more complete range of possible photon fluxes.

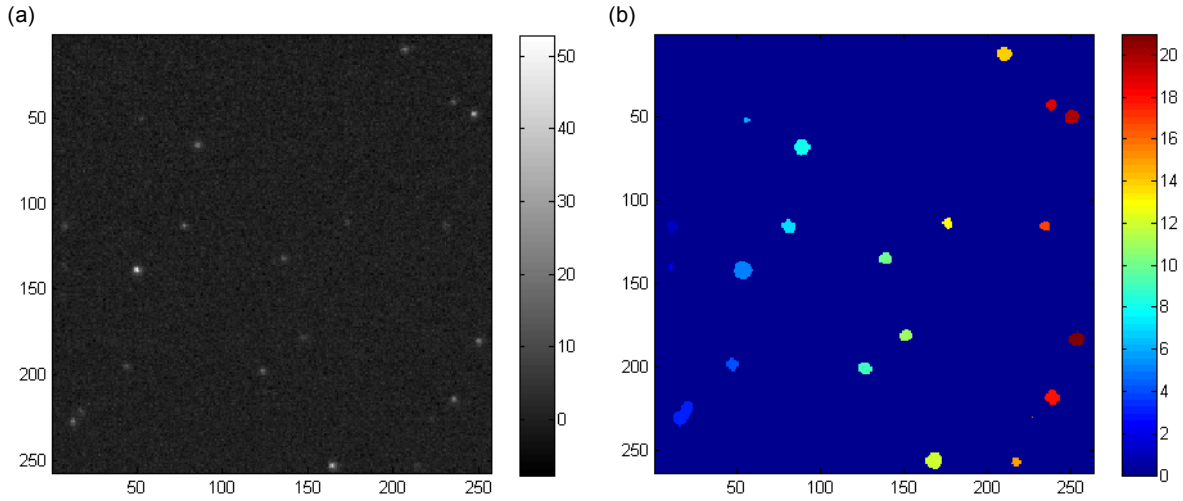

Figure 3-13 Exemplar regions from photon counting experiments to establish photon flux on the photocathode of an HRI.

(a) An exemplar background subtracted 256×256 region of an acquired image at high HRI gain and high ND filter settings, used for photon counting experiments. (b) An intermediate image generated by the MATLAB script used for analyzing photon counting data; coloured by photon event number.

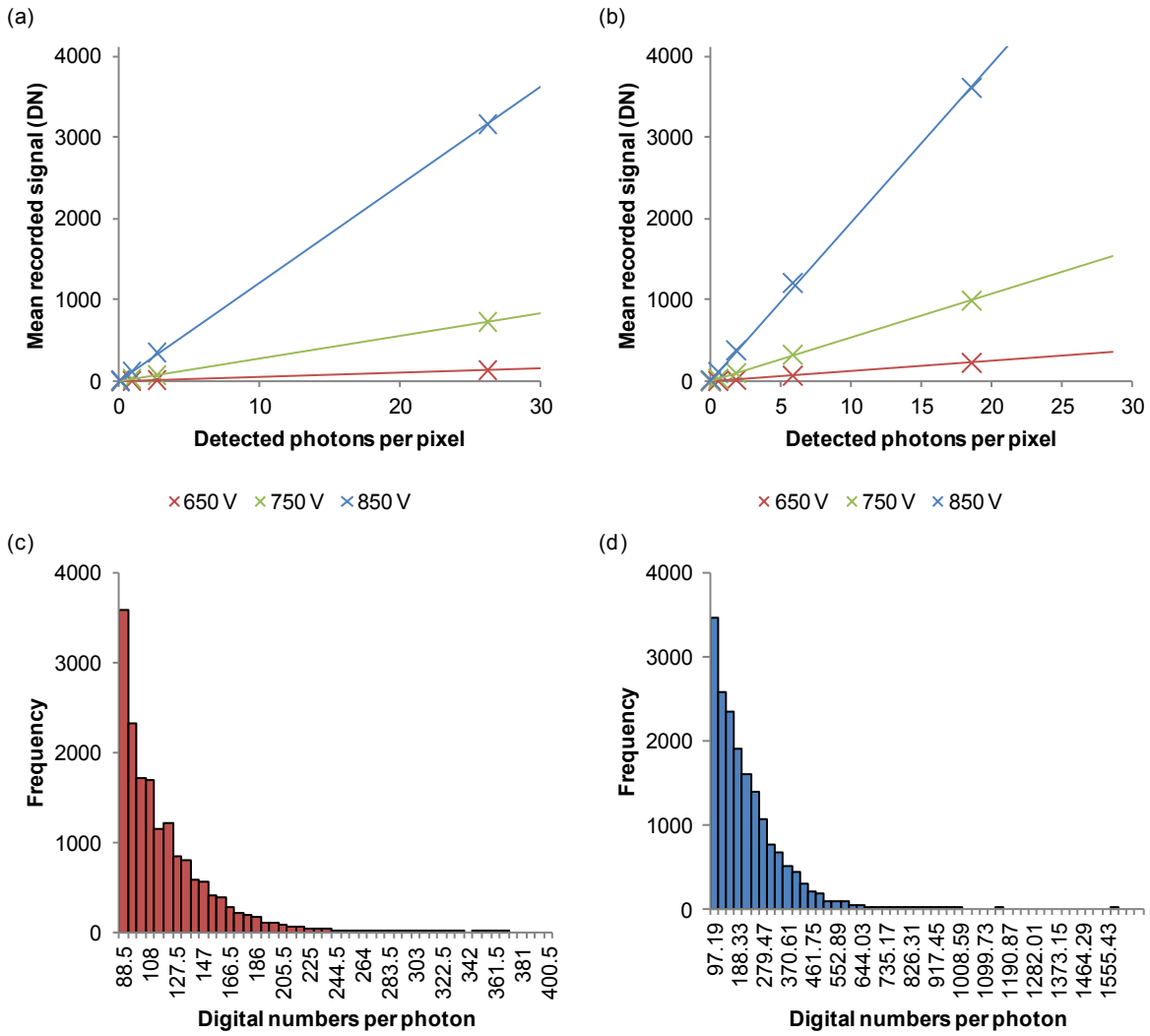

Figure 3-14 Results of experiments to determine conversion factor k between recorded signal in digital numbers, and detected photons.

(a) Mean recorded signal in digital numbers plotted against photon flux for three different gain settings for the single edge HRI. (b) Mean recorded signal in digital numbers plotted against photon flux for three different gain settings for the blue-sensitive HRI. (c) Histogram of measured digital numbers per photon event for 850 V gain for the single edge HRI. (d) Histogram of measured digital numbers per photon event for 850 V gain for the blue-sensitive HRI.

Gain setting (V)	*k*, Single Edge HRI	*k*, Blue Sensitive HRI
650	5.3 (4.9, 5.7)	12.3 (12.0, 12.5)
750	28.1 (23.3, 28.8)	53.7 (52.9, 54.42)
850	121.2 (118.7, 123.7)	195.2 (192, 198.3)
850*	116	228

Table 3-3 Calculated k-factors (and 95% confidence intervals on fitted parameters), showing the relationship between detected photons and recorded signal in digital numbers for incident radiation at 623 nm.

*850 V k-factor identified from photon-counting data.

3.3.2 Gate profiles and generation of library IRFs

A key difference between the single edge HRI and the blue-sensitive model is the ability to select wider gate widths by default, up to a maximum width of 6800 ps. However, the rise time of the gate profile, which contributes to the temporal resolution and precision of lifetime determination is typically <200 ps. To provide insight into the performance of these HRIs, gate profiles have been measured for both HRIs at a variety of wavelengths, gain settings and gate widths. Here, a profile generated from a "scatter" instrument response function at a single gain setting (750 V) and wavelength (supercontinuum source filtered to 525/50 nm) for 6000 ps or 1000 ps gates for the single edge and blue-sensitive HRIs, respectively, is presented. The equipment used to generate the data is shown in Figure 3-15: the combination of rotating diffuser, diverging lens and the distance to the HRI ensures a uniform illumination of the photocathode and a flat wavefront at the front of the HRI (calculated to be 0.47 ps deviation across the 18 mm photocathode). Automation of the experiment to generate gate profiles across conditions was afforded by a tool written in LabVIEW and integrated into the main acquisition program. 10 profiles were measured for each combination of settings; central 128×128 pixel regions were extracted and averaged over repeat measurements to generate the curves presented here. In addition, by means of a MATLAB script, the time at which each pixel reached 50% of its maximum brightness was determined; the resulting plots show the variation in gate opening and closing time across the face of the photocathode.

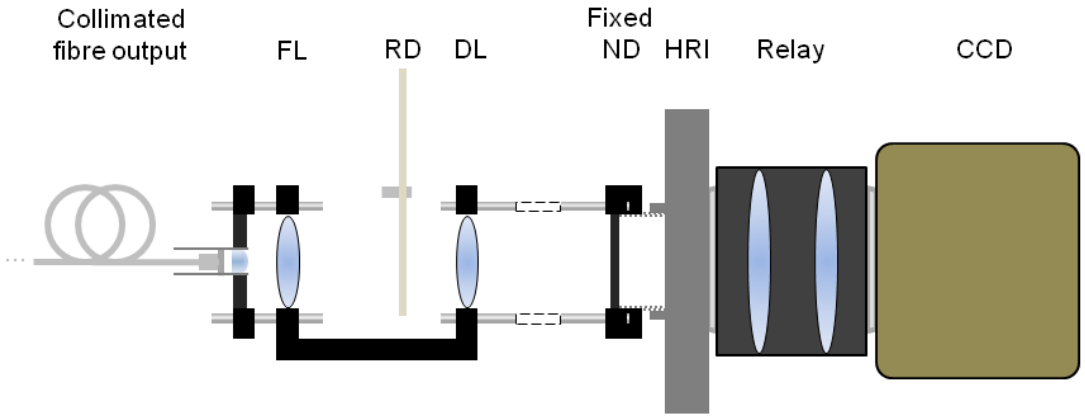

Figure 3-15 A schematic showing the experimental set up used to generate gate profiles for HRIs.
FL: focussing lens, RD: rotating diffuser, DL: diverging lens.

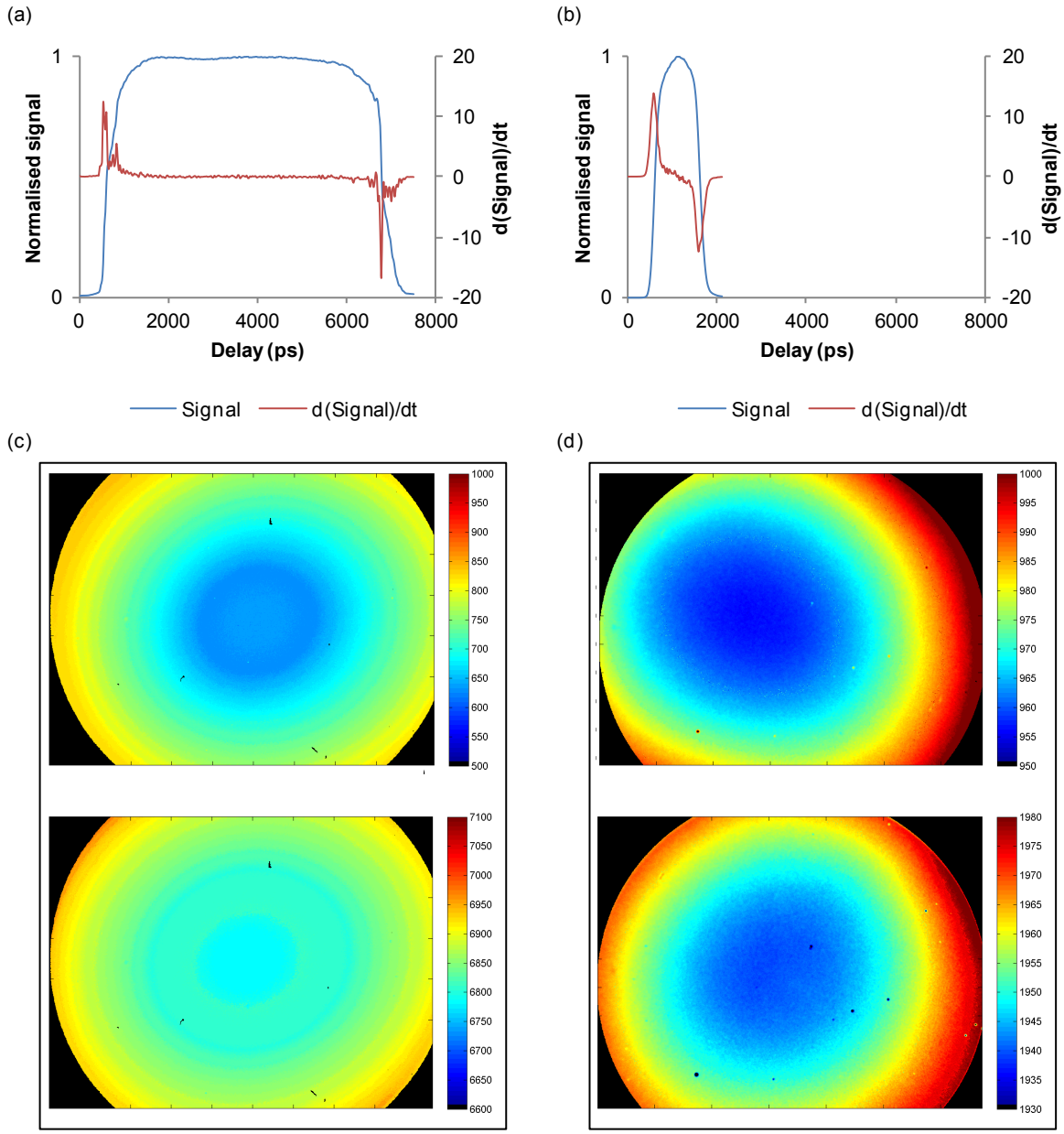

Figure 3-16 Exemplar gate profiles from the single edge and blue-sensitive model HRIs.
(a) Gate profile and derivative curve for single edge HRI, 750 V gain, 6000 ps nominal gate width. (b) Gate profile and derivative curve for blue-sensitive HRI, 750 V gain, 1000 ps nominal gate width.(c) Gate opening and closing xy-profiles for the single edge HRI; warmer colours representing later on/off times. (d) Gate opening and closing xy-profiles for the blue-sensitive HRI; warmer colours representing later on/off times. Note that there is a 10-fold change in colour scale between (c) and (d).

From the data presented in Figure 3-16 (a) and (b) above, and in particular looking at maxima and minima on derivative curves, it is established that the nominal gate widths set electronically with reference to a calibration reference table match the measured gate widths for the blue-sensitive HRI, whilst the gate on the single edge model is slightly wider (6250 ps) than the nominal value: this offset in gate duration is reflected across a range of nominal gate widths, and could potentially be calibrated for if desired. Figure 3-16 (c) and (d) show the presence of *irising* – a phenomenon whereby the propagation of the electrical gating signal across the photocathode causes different *xy*-positions across the field of view to exhibit

different opening and closing times. Noting the ten-fold difference in colour scale, it is clear that this phenomenon is more pronounced in the case of the single edge HRI. Following discussion with Kentech Instrument Ltd. and with reference to literature[148], it is concluded that the physical origin for this difference is linked to changes in the design between the two models, leading to different capacitive coupling between electronic components and the photocathode.

In addition to showing the measured gate width compared to nominal values, Figure 3-16 (a) and (b) illustrate differences in gate profile between the two HRIs under investigation, and particularly the similarity in the sharpness at the gate edges between the two models as evidenced by the derivative curves. This is despite the fact that the single edge model was designed to provide a faster on-time than standard models. The impact of gate sharpness on lifetime fitting will in future be investigated by simulation.

In addition to providing characterisation information, the traces generated by the process described above can be used to build a "library" of scatter IRF traces for use in subsequent experiments in which it is not always possible to satisfactorily measure the instrument response. Under the assumption that the shape of the IRF is not significantly changed by the microscope optics, but instead only the delay of the gate relative to the excitation pulse is altered by changing the optical path length, IRFs measured by the method described above can be used to fit FLIM data as long as the "t_0 shift" is correctly accounted for. This is achieved by measuring a monoexponential reference dye with fine delay sampling at the time of the experiment, and obtaining the best fit to this decay profile using a library IRF with matching HRI settings by altering the delay of the IRF only. Once the IRF has been correctly positioned with respect to the reference decay, it may be used to fit other experimental data.

3.3.3 Concluding remarks: current standards for HRI choice

The work presented in this section goes some way to providing a basis upon which a choice can be made regarding the most suitable HRI for any given experiment. Clearly spectral sensitivity must be considered based on the fluorescence emission of the sample being studied. Building on published studies of analogous systems[149] and using the determinant of the Fisher information matrix as a metric, Sean Warren has shown that in general, wider gates result in a more efficient use of photons in lifetime fitting. The single edge model offers the widest gates and hence the most favourable lifetime fitting performance. This factor, combined with its improved spatial resolution (illustrated in experiments being undertaken by Hugh Sparks), indicates that the single edge HRI is generally speaking the preferred option.

One relative drawback of the single edge HRI is seen in the manifestation of irising causing a shift in gate profile across the collected field of view, which can cause artefacts in fitting whereby lifetimes returned at the edge of the field are shorter than those in the centre. It is clear that the standard blue-sensitive HRI is less susceptible to this phenomenon than the single edge system, and therefore might be considered preferable based on this metric. However, with appropriate monoexponential reference dye controls, our

lifetime fitting software *FLIMfit* is now capable of accounting for a shift in instrument response across a field of view, rendering this factor largely irrelevant.

In future, it is intended that a wider survey of properties of all the HRI devices that exist in our laboratory should be carried out in order that the correct device might be chosen for any given application. This study is already in progress and is being conducted by Hugh Sparks. In addition to providing a more complete overview of HRI technology, the approach taken in this latest study to the elucidation of spatial resolution is preferable: by projecting wagon wheel resolution charts onto the front face of a range of HRIs, resolution might be explored at different gain settings. In addition, changes in gain at various stages of gate opening and closing are accessible by this alternative method as a pulsed laser source is being deployed in place of a continuous wave LED.

Further investigation of the effects of gate shape on lifetime fitting might be carried out in collaboration with Kentech Instruments Ltd. Currently, the form of distortions to the IRF generated in software are chosen largely to show similar behaviour to empirically observed optical response functions with minimal considerations of the actual optical response to changes in voltage across the photocathode. A physical model based on the exponential behaviour of electronic (approx. RC circuit) gating, combined with the optical behaviour of photocathodes in response to electrical gating[148], might feedback more meaningfully into the design process for future HRI models. In addition, spatial resolution might be improved for HRIs with short gates by application of a magnetic field along the axis of image propagation: with an appropriately chosen magnetic flux density, the Larmor radius of propagating electrons can be chosen to reduce the spread of electrons occurring between the MCP and the phosphor screen[150].

3.4 FLIM fitting software

The software used for analysis of FLIM data throughout this thesis is *FLIMfit* – a package developed in the Photonics group at Imperial College London, primarily by Sean Warren. *FLIMfit* implements a computationally efficient algorithm for global analysis of fluorescence lifetime data acquired on both time correlated single photon counting and time gated FLIM systems. Global analysis permits robust extraction of fluorescence lifetimes and fractional contributions in complex decay profiles by making assumptions regarding the invariance of lifetimes over a data (sub)set. Details of the computational methods used have been described elsewhere[78]. Employing *FLIMfit* allows fitting of large FLIM plate reader datasets to be conducted on relatively modest PCs on reasonable (sub-minute) timescales. The software enables the experimenter to account for time-varying fluorescent background, the instrument response function (as described in Chapter 2: section 2.4.3) and the effects of repeated excitation by a train of pulses, as well as offering significant flexibility in the choice of model to fit data to: some such models are illustrated in section 3.5 below. The segmentation algorithm that is used extensively in this thesis, and the complex-donor-profile FRET model that is used to determine FRETting donor fractions in *FLIMfit* for experiments in section 3.5 are discussed in more depth in the following two sections.

3.4.1 Segmentation

It is often important when analysing FLIM microscopy data to be able to distinguish between regions of fields of view corresponding to fluorescent cells, and those corresponding to background – regions of either growth substrate, or untransfected cells. *FLIMfit* is bundled with a built-in "segmentation manager", developed by Yuriy Alexsandrov and Sean Warren, which makes a number of segmentation algorithms and field of view filtering techniques available. In this thesis, the preferred segmentation algorithm is an implementation of a size-tuned nonlinear top-hat transform, referred to throughout as NTH segmentation[78,151]. In this implementation, a test image is generated by application of the transform

$$NTH(J|\varepsilon,k) = \frac{J \cdot \langle J \rangle_{\varepsilon}}{(\langle J \rangle_{k\varepsilon})^2} \qquad 3.4$$

on a pixelwise basis, where J is donor intensity integrated over FLIM gates, ε is the scale parameter relating to the objects of interest, k is a background scale parameter greater than one, and $\langle \cdots \rangle_x$ represents averaging over a square mask of width x. In the resulting transformed image, pixels are enhanced if they themselves are bright, the close vicinity (defined by ε) is bright, and the far vicinity (defined by $k\varepsilon$) is dim. This test image is then thresholded at a user defined fraction of maximal intensity to define a binary mask of foreground objects, which is smoothed by application of imdilate and imerode functions with structure element size given by a user defined smoothing factor. Finally, thresholded objects are filtered such that those smaller than a user defined size are discarded.

3.4.2 "FRET model" fitting

Though the continuing development of fluorescent proteins leads to increasing options of FPs that exhibit monoexponential decay profiles, there remains a significant subset of fluorescent constructs that make use of fluorophores with complex decay profiles, including many cyan fluorescent proteins. When FPs with monoexponential decay profiles are used as donors in FRET experiments, it is possible to infer information regarding the relative populations of free and FRETting donor constructs subject to the caveats outlined in Chapter 2: section 2.3.4. If, however, fluorescent molecules used as donors in a FRET system cannot be assumed to be monoexponential, it becomes challenging to interpret the results of a biexponential fitted model decay in a quantitative manner.

An attempt to account for biexponential donor decays in FRET experiments has been proposed[78] and implemented in *FLIMfit* by Sean Warren. The decay profile of a non-FRETting biexponential donor is described by

$$\tilde{F}_0(t) \propto \left(\beta_1 \exp\left(-t/\tau_1\right) + \beta_2 \exp\left(-t/\tau_2\right)\right). \qquad 3.5$$

Under assumptions that the complex decay behaviour of the donor is linked to the existence of two different chromophore conformation, that physical parameters κ^2, R and J as defined in equations 2.11 – 2.13 (Chapter 2: section 2.3.1) are equal for both conformations, and that conformations exist in a slow

equilibrium, the FRET efficiency of the second donor lifetime component may be related to that of the first, and an expression for the decay profile in the FRETting state found:

$$E_2 = \frac{\tau_2}{\tau_1} \cdot \frac{E_1}{1 - E_1\left(1 - \frac{\tau_2}{\tau_1}\right)} \quad \textbf{3.6}$$

$$\tilde{F}_1(t) \propto \left(\beta_1 \exp\left({}^{-t}/_{(1-E_1)\tau_1}\right) + \beta_2 \exp\left({}^{-t}/_{(1-E_2)\tau_2}\right)\right). \quad \textbf{3.7}$$

The model fitted to FRET data then depends on 5 parameters ($\tau_1, \tau_2, \beta_1, E_1, \gamma_1$):

$$I(t) = I_0\left(\gamma_0 \tilde{F}_0(t) + \gamma_1 \tilde{F}_1(t)\right), \quad \textbf{3.8}$$

where γ_0 is non-FRETting fraction, γ_1 is FRETting fraction and $\gamma_0 + \gamma_1 = 1$. Typically, data measured from donor-only samples are globally fitted to the model described in equation 3.5 and values for τ_1, τ_2 and β_1 are fixed; FRET efficiency E_1 is then fitted globally across the data and FRETting fraction γ_1 is fitted locally.

3.5 FRET construct test samples

In order to demonstrate the functionality and performance of the FLIM plate reader for FLIM-FRET cell biology experiments, it is desirable to generate standard, repeatable samples to be run. Whilst fluorescent dye mixtures can be employed to give an indication of the speed of acquisition in the case of spatially homogeneous samples, a more realistic test of the capabilities of the plate reader is accessed by generating and imaging plates of cells transfected with fluorescent constructs with different linker lengths. The work presented below highlights the strengths and limitations of analysis of FLIM-FRET data, and illustrates the speed of the plate reader when acquiring FLIM-FRET data from cells.

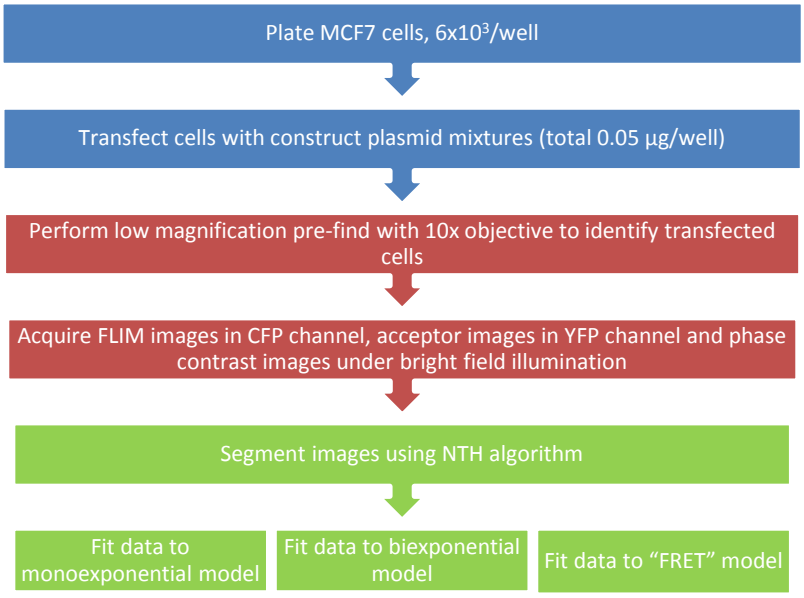

Figure 3-17 Flow chart summarizing the methods used for generation and analysis of FRET construct test samples.
Further details are found in sections 3.5.1-3.5.3

mCerulean-Venus constructs developed by the Vogel lab[152] were purchased from Addgene. These constructs, designed as "FRET standards", each comprise mCerulean and Venus fluorescent proteins separated by 5, 17, or 32 amino acids and are subsequently denoted C5V, C17V and C32V. Given the increasing average separation of fluorophores, it is expected that C5V will exhibit high FRET efficiency, C17V moderate FRET efficiency, and C32V relatively low FRET efficiency: as such, the constructs may be used as surrogates for single chain FRET sensors in different active/inactive conformations, or alternatively, to simulate donor construct-acceptor construct complexes in bimolecular FRET experiments, where different lengths of linker represent differences in binding geometry or construct design.

The lifetime reported for mCerulean in literature varies between publications and according to analysis methods; furthermore, the most appropriate model (mono- or biexponential) for fitting mCerulean decay profiles is a matter of contention. When characterising the FRET standard constructs, Koushik et al. report a monoexponential lifetime of 3.0 ns[152], whilst Rizzo et al. report a biexponential decay with lifetime values of 2.3 ns and 4.5 ns (relative contributions 0.38 and 0.62 respectively) in their original paper on the development of mCerulean[41]. Following initial experiments that resulted in fitted lifetimes measured on separate microscopes using different FLIM methods being found to be shorter than those reported in literature[41,152–154], a number of experiments were conducted using these FRET standards to investigate possible biological causes for discrepancies in absolute lifetime. Experiments were also undertaken to test the effect of different experimental conditions on the separability of lifetimes measured in cells transfected with mCerulean donor-only constructs from those from cells transfected with C32V, C17V and C5V FRET standards. These experiments can be used to inform on the limits of

dynamic range of FRET experiments, where mCerulean represents a negative control, and the FRET standards represent three different notional donor-acceptor complexes with progressively decreasing fluorophore separation R.

In experiments devised to investigate instrument speed and performance and the capability of fitting software to extract physical parameters relating to FRET experiments, C5V was transfected in different ratios with the donor fluorophore mCerulean across a plate to simulate notional mCerulean donor constructs binding in different ratios to notional mVenus acceptor constructs: this might be considered as a model for an idealised dose response read out by FLIM-FRET.

3.5.1 Methods: generating FRET constructs plates

For all FRET constructs plates, cells were seeded at 6×10^3 cells per well and incubated in growth media for 24 hours. Greiner μClear plates were used unless otherwise stated. Transfections were performed using XtremeGene HP (Roche) transfection reagent, following the manufacturer's instructions. In all cases, the *total* plasmid weight per well was chosen to be 0.05 μg; in cases where multiple constructs were transfected per well, plasmids were mixed in the relevant ratios before transfection. Cells were incubated with transfection mixtures for 24 hours prior to washing and submersion in imaging media (formulation in Table 3-4). In every plate, at least one well of cells was left untransfected for the purposes of making background fluorescence decay measurements. Fixed plates were generated by incubating samples at room temperature for fifteen minutes in 4% paraformaldehyde.

Component	Concentration
Hank's buffered salt solution	
L-glutamine	2 mM
Glucose	4.5 g/L
HEPES	10 mM

Table 3-4 Formulation of imaging media.

3.5.2 Methods: Imaging parameters

Images were acquired using a 40x long working distance phase contrast objective (LUCPLFLN 40x, Olympus). These FRET construct plates were imaged using a gating strategy with 5 gates after the peak and one preceding the peak. At each delay, images were acquired by accumulating 3 camera frames, each of which was integrated for 0.1 s. FLIM images were acquired using a CFP filterset (excitation: 438/24 nm, dichroic: 458 nm, emission: 483/32 nm). Acceptor intensity images were acquired using the FLIM detection arm and a YFP filter set (excitation: 500/24 nm, dichroic: 520 nm, emission: 542/27 nm); acceptor images were integrated for 0.5 s. Non-FLIM images were acquired under phase contrast illumination with integration time of 0.01 s. These parameters were used for all plates presented in the remainder of this chapter unless otherwise stated. Whilst early plates were set up to perform autofocus between every field of view, this was reduced to autofocus every three fields for later plates with no

apparent reduction in image quality, providing that autofocus was always performed when moving between wells.

3.5.3 Methods: Analysis of FRET constructs plates

Analysis of plates was performed in *FLIMfit*. Fluorescent cells were separated from well background within fields of view by application of NTH segmentation (described in section 3.4 above) with parameters outlined in Table 3-5: these were found to yield generally acceptable segmentation, even across different cell lines (section 3.5.4). Instrument response functions were generated by shifting the peak of "library" IRF functions, derived from past data generated in the study of HRI gate profiles (section 3.3.2) with respect to the peak of a decay acquired on the day of the experiment using a monoexponential lifetime dye, for example Coumarin 6. A time-varying background decay, associated to different degrees with growth substrate, cellular autofluorescence and media components, was included in the model.

Parameter	Value
Scale	300
Relative background scale	2
Thresholding	0.40
Smoothing	1
Minimum size	1000

Table 3-5 NTH segmentation parameters used for FRET construct plate analysis.

Biexponential fitting was performed globally leaving all parameters free to fit. For fitting a "FRET model", biexponential decays were fitted globally across columns with donor alone; these lifetimes, and the mean relative contributions, were fixed. The software was then deployed to fit data to yield a global FRET efficiency, and relative contributions of FRETting and non-FRETting species across all pixels in the dataset. For plates that aim to provide comparisons between conditions, in addition to absolute monoexponential lifetime values, Z' parameters (as defined in Chapter 2: section 2.5.1 above) were calculated to highlight the separability of fitted parameters for FRETting constructs from non-FRETting constructs using a familiar (conservative) assay quality parameter. Standard deviations calculated across repeat wells were used to calculate Z' values.

3.5.4 Comparison of cell lines

In order to confirm whether the cell line into which constructs are transfected might have an impact on the absolute lifetimes recorded, explaining the discrepancy observed between our measured lifetimes and those presented in literature, and to assess the effect of different cell lines with different morphologies on the strength of assays when simple analysis methods are applied to all cell lines equally, three lines were transfected with constructs. MCF7 cells are a breast cancer cell line with "cobblestone"-like morphology; COS7 cells are derived from African green monkey kidney cells and exhibit a fibroblast-like morphology,

thin cytoplasm regions and thick nuclear regions. HEK293T are derived from human embryonic kidney cells, and fall somewhere between COS7 and MCF7 in morphology. Phase contrast and CFP-channel intensity images for the three cell lines are shown in Figure 3-18. Cells were plated and transfected according to the method in section 3.5.1 above and following the pattern shown in Figure 3-19 (a).

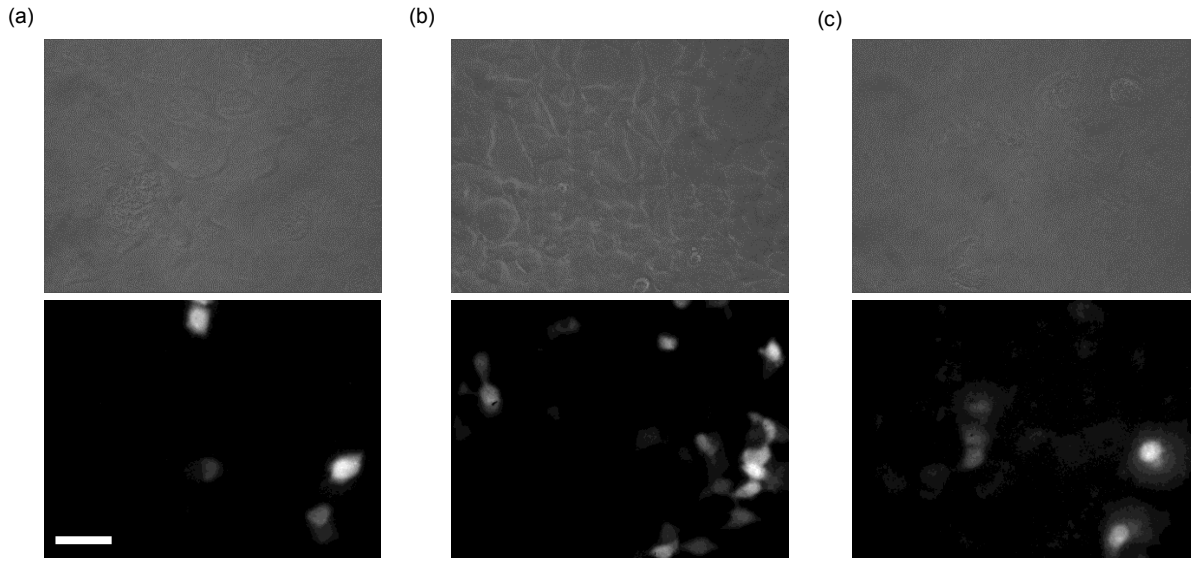

Figure 3-18 Exemplar phase contrast and mCerulean fluorescence intensity images for each of the three cell lines under investigation.
(a) MCF7 breast cancer cell line. (b) HEK293T human embryonic kidney-derived cell line. (c) COS7 African green monkey kidney-derived cell line. Scale bar 50 μm.

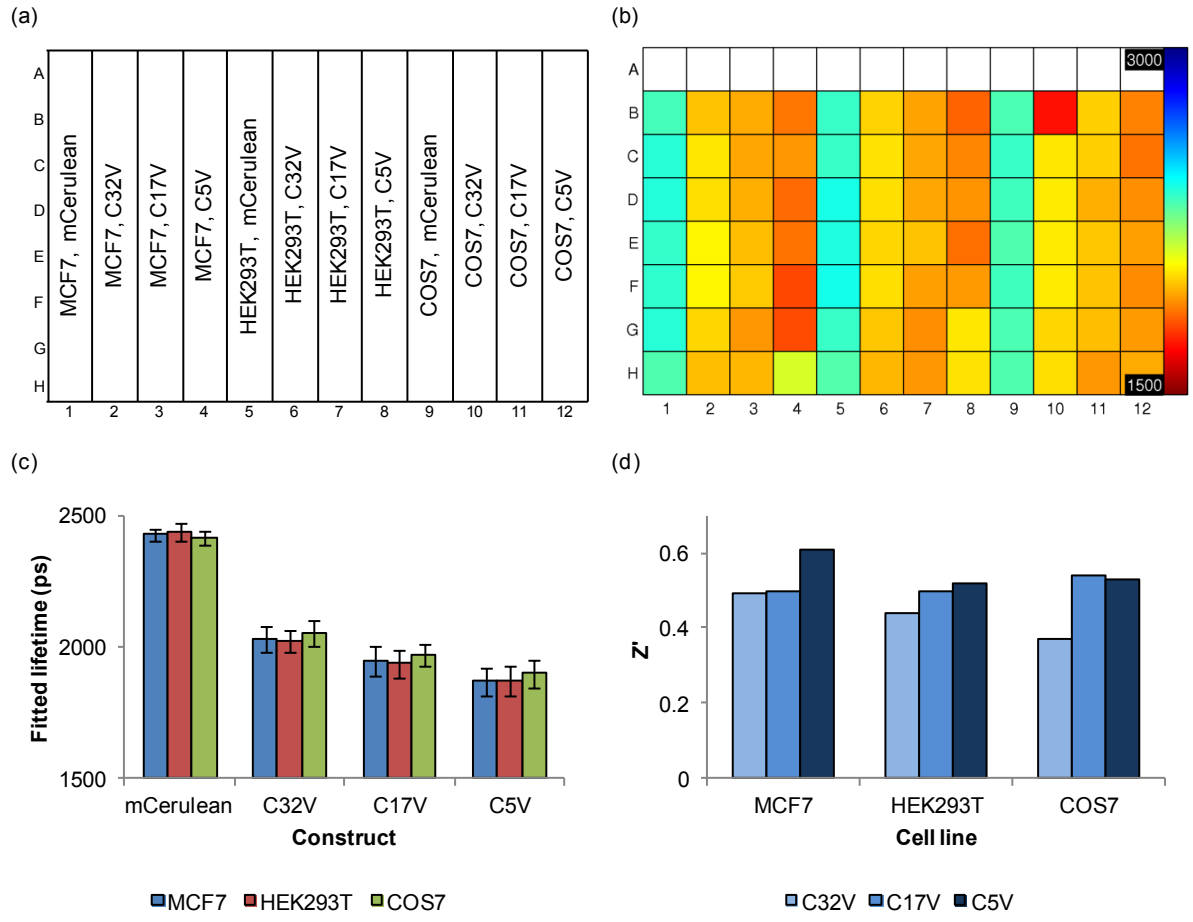

Figure 3-19 Results of experiment investigating FRET construct lifetime across three different cell lines.

(a) Plate layout. (b) Plate map showing fitted single lifetimes across all wells. (c) Fitted mCerulean lifetime by construct and cell line showing predicted decrease in lifetime with decreasing linker length and absence of difference in lifetime between cell lines. Error bars show standard errors calculated across repeat wells. (d) Z' assay parameter by construct and cell line.

The exemplar mCerulean fluorescence intensity images presented in Figure 3-18 serve to illustrate differences in patterns of expression between the cell lines: in particular, COS7 cells exhibit significantly more fluorescent signal in the nucleus than the cytoplasm under wide field imaging. These exemplar images also highlight two problems with the plate reader: firstly, phase contrast images presented here provide evidence that it is not always possible to infer any useful morphological data from bright field images, particularly for confluent cells or lines such as COS7, the cytoplasmic regions of which are thin. Furthermore, the importance of correct calibration of the low magnification prefind tool is underlined by the offset evident in the resulting high magnification FLIM images presented here, where the bright cells identified by the prefind algorithm are placed towards the bottom-right of the FLIM fields of view, rather than in the centre.

The lifetime data presented in Figure 3-19 (b) and (c) illustrate that there is no significant difference in absolute lifetimes measured for the mCerulean-mVenus FRET constructs when they are expressed in different cell lines. Figure 3-19 (d) illustrates that separability as defined by the Z' parameter generally

improves with increasing FRET efficiency as expected. The exception to this trend appears for COS7 cells when comparing Z' for C17V and C5V constructs, where the former condition appears to present an abnormally high Z' value. In an attempt to explain this discrepancy, the number of segmented pixels, the intensity, and the goodness-of-fit for the anomalous result was compared to mean values for these parameters for the rest of the plate. These parameters were identified as possible indications of anomalous expression of fluorescent constructs for this condition. None of the parameters deviated from the plate mean by more than 5%; closer investigation of intensity images across the dataset also failed to provide a possible explanation for this result.

3.5.5 Comparison of live cell and fixed cell imaging

To illustrate one source of potential differences in absolute lifetimes and assay strength parameter Z' between experiments and labs, two identical plates of MCF7 cells were generated. One plate was imaged when the cells were alive under supplemented HBSS at 37°C, and the other was imaged at room temperature following fixation in 4% PFA.

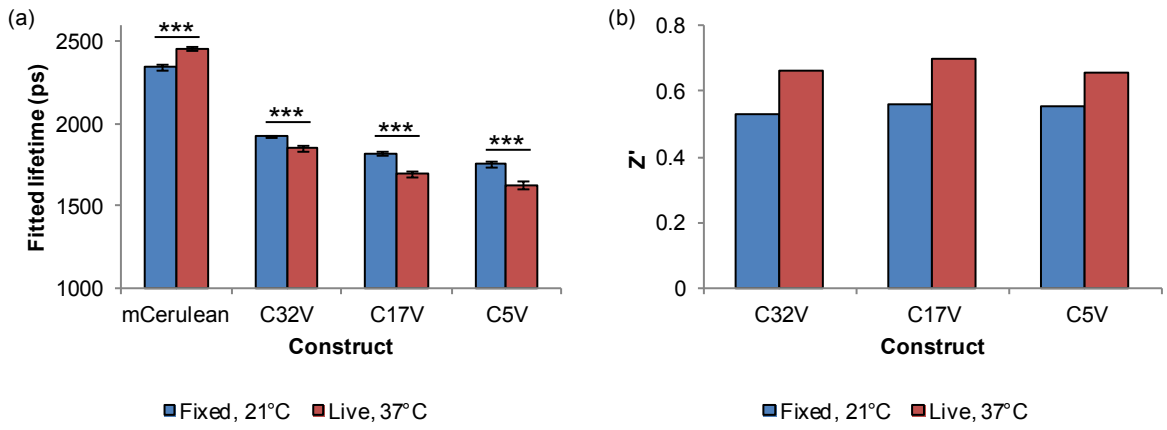

Figure 3-20 Results of experiment investigating FRET construct lifetime measured in live MCF7 cells at 37oC in comparison to fixed MCF7 cells measured at room temperature.
(a) Fitted lifetime by construct and cell condition showing predicted decrease in lifetime with decreasing linker length and absence of difference in lifetime between cell lines. Error bars show standard errors calculated across repeat wells. *** indicated differences significant at $p<0.001$, Student's t-test. (b) Z' assay parameter, calculated by construct and cell condition.

The data presented in Figure 3-20 indicates the combined effects of temperature and fixation on lifetime measurements with FRET constructs, even in the absence of changes to cell biology which might cause differences for FRET probes designed to read out cellular processes. In all cases there is a very significant difference in measured lifetime, indicated by Student's t-test ($p < 0.001$ for all comparisons). In addition, Figure 3-20 (b) shows that different imaging conditions might also have a marked effect on assay quality as measured by the Z' parameter. It is notable that changes in measured lifetime with temperature for fluorescent proteins exhibiting complex decay profiles have been widely reported: for some cyan fluorescent proteins, changes in lifetime on the order of -50 ps per degree temperature change have been measured[67,155]. Based on the data summarised in Figure 3-20 alone, it is difficult to draw any conclusions

regarding the exact origin of the differences observed between live and fixed cells, given the possible combination of factors at play including sample temperature and potential differences in sample refractive index: further study is required to separate possible causes of the observed changes in lifetime.

3.5.6 Comparison of growth substrate

Following discussion with high content imaging experts in the Advanced Light Microscopy Facility (ALMF) at the European Molecular Biology Laboratory (EMBL) in Heidelberg, the substrate on which cells are grown was identified as another possible source of error in the determination of FRET standard lifetime which might explain differences between observed lifetimes and literature lifetimes. Such changes may be attributed either to slightly different cell behaviour on different substrates, or to background fluorescence which might be expected to be more prevalent for plastic-bottomed plates. Cells were seeded according to methods above in either Greiner µClear® plastic bottomed plates, or ZellKontact 96 well glass bottomed plates. Imaging was performed at 37°C in live cells.

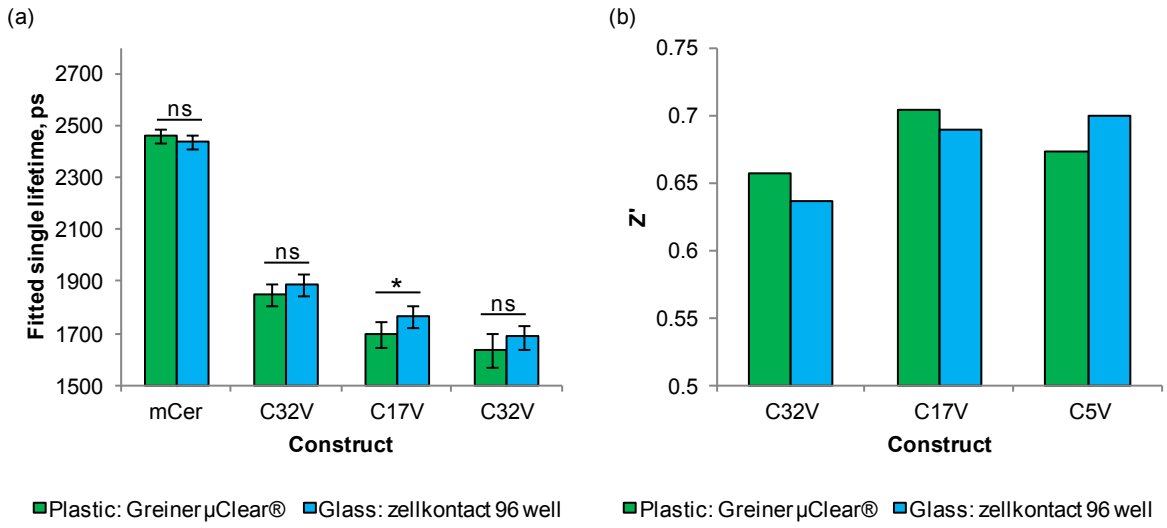

Figure 3-21 Results of experiment investigating FRET construct lifetime measured in live MCF7 cells plated on plastic in comparison to live MCF7 cells plated on glass measured at 37°C.
(a) Fitted lifetime by construct and growth substrate showing predicted decrease in lifetime with decreasing linker length and absence of difference in lifetime between cell lines. Error bars show standard errors calculated across repeat wells. * indicates differences significant at $p<0.05$, Student's t-test. (b) Z' assay parameter, calculated by construct and growth substrate.

Results presented in Figure 3-21 comparing the effect of growth substrate on lifetime illustrate that there is, for the most part, negligible differences in lifetime dependent on growth substrate. Crucially, measured lifetimes remain significantly different from reported literature values (>3.0 ns), but are consistent with all other measurements made in our lab.

3.5.7 Pseudo dose response: comparison of data models

In order to illustrate the performance of the plate reader, a FRET constructs plate was prepared on a Greiner µClear plastic-bottomed 96 well plate, and fixed before imaging at room temperature. Donor-

only mCerulean (mCer) constructs were transfected in different ratios with donor-acceptor fusion C5V. Throughout the following sections, the fraction of the plasmid mixture in transfection made up by mCer is designated F, referring to the fractional mCer plasmid weight, defined

$$F = \frac{\text{mCer plasmid weight}}{(\text{mCer plasmid weight}) + (\text{C5V plasmid weight})}. \qquad \textbf{3.9}$$

The plating strategy, showing decreasing ratio of mCer:C5V plasmid weight from left to right across the plate, is illustrated in Figure 3-22 (a). This layout was chosen to mimic an ideal bimolecular FRET system, whereby there is no interaction between donor and acceptor in column 1, and 100% donor-acceptor binding in column 12. In this regard, the plate of standards resembles an idealised FRET readout of a dose response: plates generated in this manner are therefore referred to as "pseudo-dose response" plates, although the relatively high FRET efficiency of the short linker FRET standard C5Vis not typical of biological experiments. Figure 3-22 (b) shows that there is an approximately linear relationship between the weight of C5V plasmid transfected and the expression of C5V protein as reported by intensity in the acceptor spectral channel. It should be noted that C5V plasmid has 1.6x as many base pairs as the donor only plasmid, and that there is no easy way to modulate expression levels beyond changing the weight of plasmid used in transfection. Biochemical methods such as Western blotting might give a clearer impression of the extent to which the ratio of expressed proteins follows the ratio of plasmids in the transfection mixture.

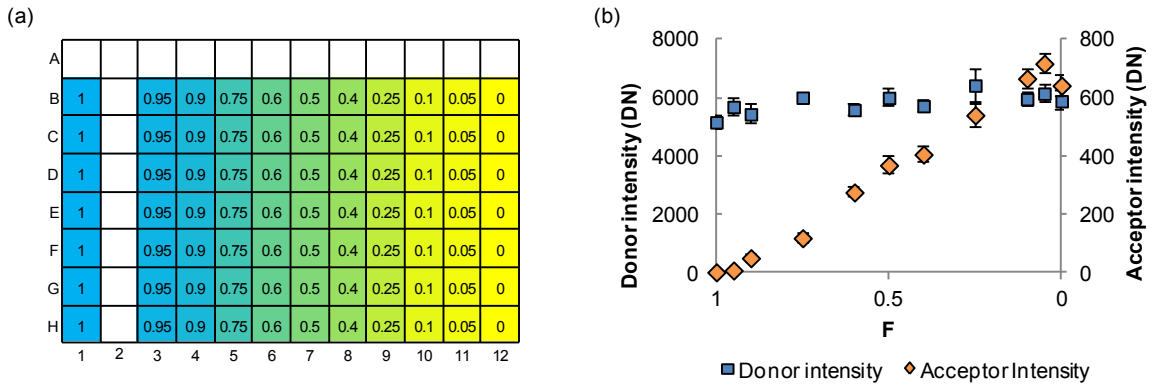

Figure 3-22 Illustration of plating strategy for a "pseudo-dose response" FRET constructs plate.
(a) Plate map showing the proportion of total plasmid weight in transfection mixes made up by mCerulean, from mCerulean-only in column 1 to C5V-only in column 12. (b) Resulting intensities in donor and acceptor spectral channels, acquired in-line with FLIM data, showing predicted trend in fluorescent signal originating from mVenus across columns associated with increasing FRETting construct expression.

Following imaging, analysis was performed as outlined in section 3.5.3 above. In the first instance, a monoexponential decay model was fitted pixelwise across the plate. The results of this fit are presented in Figure 3-23. As expected, there is a decrease in lifetime from the donor-only wells across the plate to the donor-acceptor fusion wells. An average value of goodness-of-fit parameter χ^2, scaled by the number of photons per digital number for the HRI settings used in the acquisition, was calculated in order to yield a

means of comparing different fitting methods applied to a single data set. For the monoexponential fit, $\chi^2_{\text{average}} = 1.81$.

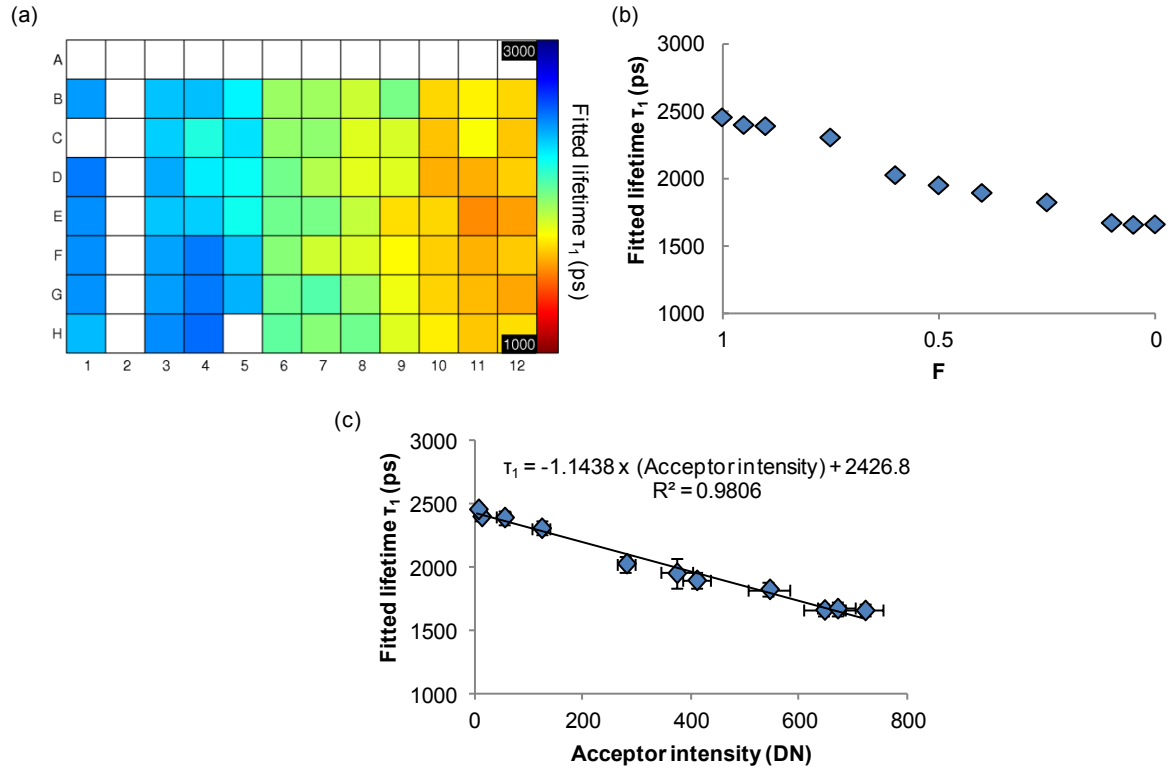

Figure 3-23 Results of a monoexponential fit to data acquired from a "pseudo-dose response" FRET constructs plate.

(a) False colour plate map showing variation in donor lifetimes returned from a monoexponential fit across all wells. (b) Fitted donor lifetime plotted against mCerulean:C5V plasmid weight, showing expected decrease in lifetime with increasing FRETting construct expression. Error bars show standard errors across repeat wells. (c) Fitted donor lifetime plotted against recorded acceptor intensity to illustrate linearity of fitted donor lifetime with FRETting construct expression using a monoexponential model.

Global biexponential fitting was then performed on the same data set, leaving all parameters free to fit. In this case, globally fit parameters were returned as shown in Table 3-6, and the contribution of the short lifetime component were found to change as outlined in Figure 3-24. Given that the fitted contribution of the short lifetime component runs between 0.42 and 0.71, this data serves to illustrate the difficulty of interpreting the results of a biexponential model imposed on a more complex system: it is impossible to simply assign FRETting fractions based solely upon the returned lifetime contributions.

Fitted parameter	Value
τ_1 (ps)	3726
τ_2 (ps)	954.7
Average scaled χ^2	1.27

Table 3-6 Global fit parameters and average χ2 resulting from a global fit of a biexponential model to data acquired from a "pseudo-dose response" FRET constructs plate.

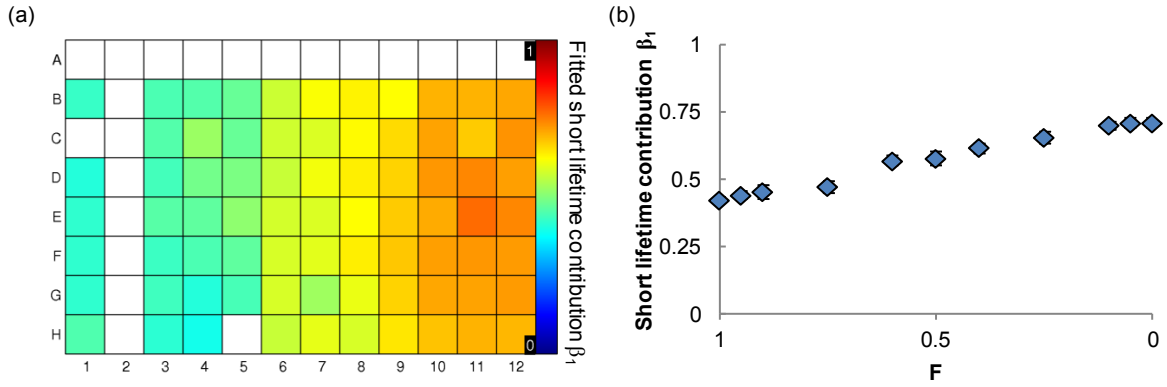

Figure 3-24 Results of a global biexponential fit to data acquired from a "pseudo-dose response" FRET constructs plate.
(a) False colour plate map showing variation in short donor lifetime components returned from a global biexponential fit, across all wells. (b) Fitted short donor lifetime component plotted against mCerulean:C5V plasmid weight. Error bars show standard errors across repeat wells.

Our data suggests that mCerulean exhibits a significantly complex decay profile, a finding in agreement with some studies and contrary to others. For this data, fitting a monoexponential decay pixelwise across donor-only images yields $\chi^2 = 1.87$ ($\tau_1 = 2489$ ps) on average, compared to $\chi^2 = 1.17$ ($\tau_1 = 4186$ ps, $\tau_2 = 1029$ ps, $\langle\beta_1\rangle = 0.50$) when a biexpoential model is fitted. Given these results, a FRET model accounting for biexponential donor decay profiles was used to fit the "pseudo-dose response" plate data following the method outlined in section 3.4.2 above. Resulting fit parameters are recorded in Table 3-7 – although absolute lifetime values do not reflect those reported in literature, the FRET efficiency calculated corresponds well with that reported elsewhere[152]. Figure 3-25 illustrates the trend in fitted FRETting fraction, γ_1 with plasmid ratio and acceptor intensity.

Fitted parameter	Value
τ_1 (ps)	4186
τ_2 (ps)	1029
β_1	0.50
E_1	0.43
Average scaled χ^2	1.11

Table 3-7 Global fit parameters and average χ2 resulting from a global fit of an "ECFP-FRET" model to data acquired from a "pseudo-dose response" FRET constructs plate.

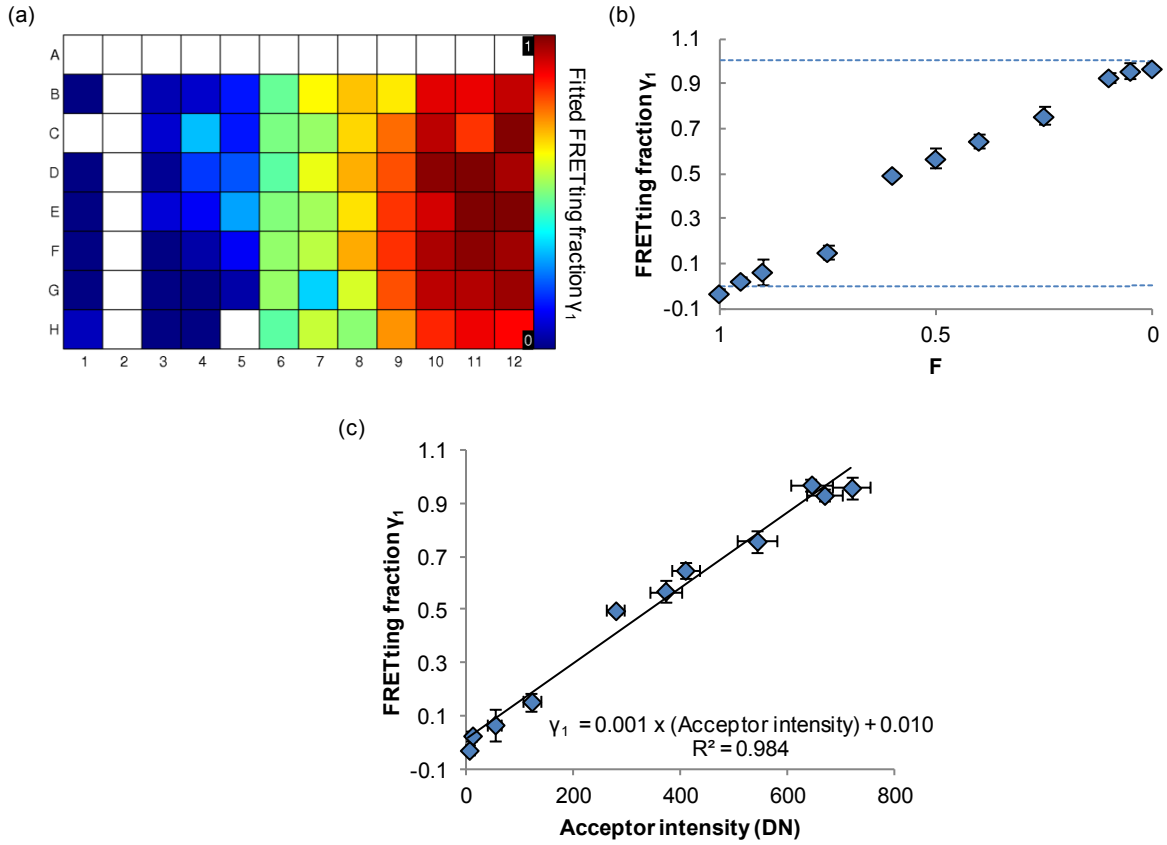

Figure 3-25 Results of fitting an "ECFP-FRET" model to data acquired from a "pseudo-dose response" FRET constructs plate.

(a) False colour plate map showing variation in donor FRETting fraction returned following fitting an "ECFP-FRET" model, across all wells. (b) Fitted donor FRETting fraction plotted against mCerulean:C5V plasmid weight, showing an approximately monotonic increase in "FRETting fraction" with increasing FRETting construct expression. Error bars show standard errors across repeat wells, dashed lines indicate $\gamma_1 = 0$ and $\gamma_1 = 1$. (c) Fitted donor FRETting fraction plotted against recorded acceptor intensity to illustrate linearity of fitted donor FRETting fraction with FRETting construct expression.

The three approaches to fitting FLIM-FRET data presented in the preceding section illustrate the importance of being aware of the limitations of models to which data is being fit, in even the simplest of

cases. Increasing the complexity of the model applied to reflect more closely the physical system under investigation can provide a greater level of understanding of that system in addition to a quantitatively better fit to data. With the caveat that behaviour of any FRET system will depend on the particular fluorophores employed, it is instructive to note that a simple monoexponential fit yields lifetimes that change linearly with expression of FRET constructs (Figure 3-23 (c)) – this suggests that should the experimenter have access to both negative (donor only) and positive (constituently active) controls in a bimolecular FRET experiment, it may be possible to infer binding fractions as well as FRET efficiencies from monoexponential fit results. The same is true of spectral FRET experiments. In the common case in which a positive control is either unavailable or time consuming to generate, a biexponential decay analysis of lifetime data is required to extract FRET efficiencies and fractions. Finally, if the donor fluorophore exhibits a biexponential decay profile, it is possible to extract FRET efficiencies and FRETting donor fractions by fitting data to the "ECFP-FRET" model described above, which yields FRET efficiencies that agree with literature values and FRETting fractions that correspond well to expected values based on transfection ratios and acceptor intensities. Further refinement of the model – perhaps accounting for the quasi-static regime affecting the effective distribution of κ^2 as described by researchers in the Vogel lab[81,82] – may yield further improvements in the simultaneous determination of the fraction of FRETting donor and FRET efficiency.

3.5.8 FRET construct plates for characterisation of instrument speed

Several of the changes to hardware and software that were made in the course of this project in order to increase the functionality of the plate reader had an impact on the maximum speed at which data can be acquired. These timing issues, along with potential improvements, are outlined in this section. Profiling of a sequenced acquisition was performed when running the plate outlined in section 3.5.7 above, chosen in part due to it being as a sample for which the acquisition was relatively complex, involving imaging in different spectral windows and in both FLIM and non-FLIM channels. A breakdown of the time spent imaging each field of view is presented in Figure 3-26 (a), whilst Figure 3-26 (b) illustrates how time is spent at each delay step in greater detail. From these diagrams it is clear that autofocus is a relatively time consuming step, taking on average ~3.5 seconds. For a total of 1.8 seconds camera integration time (number of delays × number of accumulated frames × integration time per frame), a FLIM sequence takes 8.4 seconds in total due mainly to lag associated with the microcontroller used to trigger the camera. Whilst filter wheel changes are relatively fast to execute, changing filter cube position using the Olympus automated filter cube cassette takes more than 900 ms for each change; similarly, the mechanical operation of switching between the FLIM and non-FLIM imaging pathways by the motorised repositioning of a mirror within the IX81 microscope frame takes one second per imaging path change. The average total time spent per field of view for this plate was 23.3 s, resulting in a total acquisition time of 3.8 hours during which 596 fields of view were imaged.

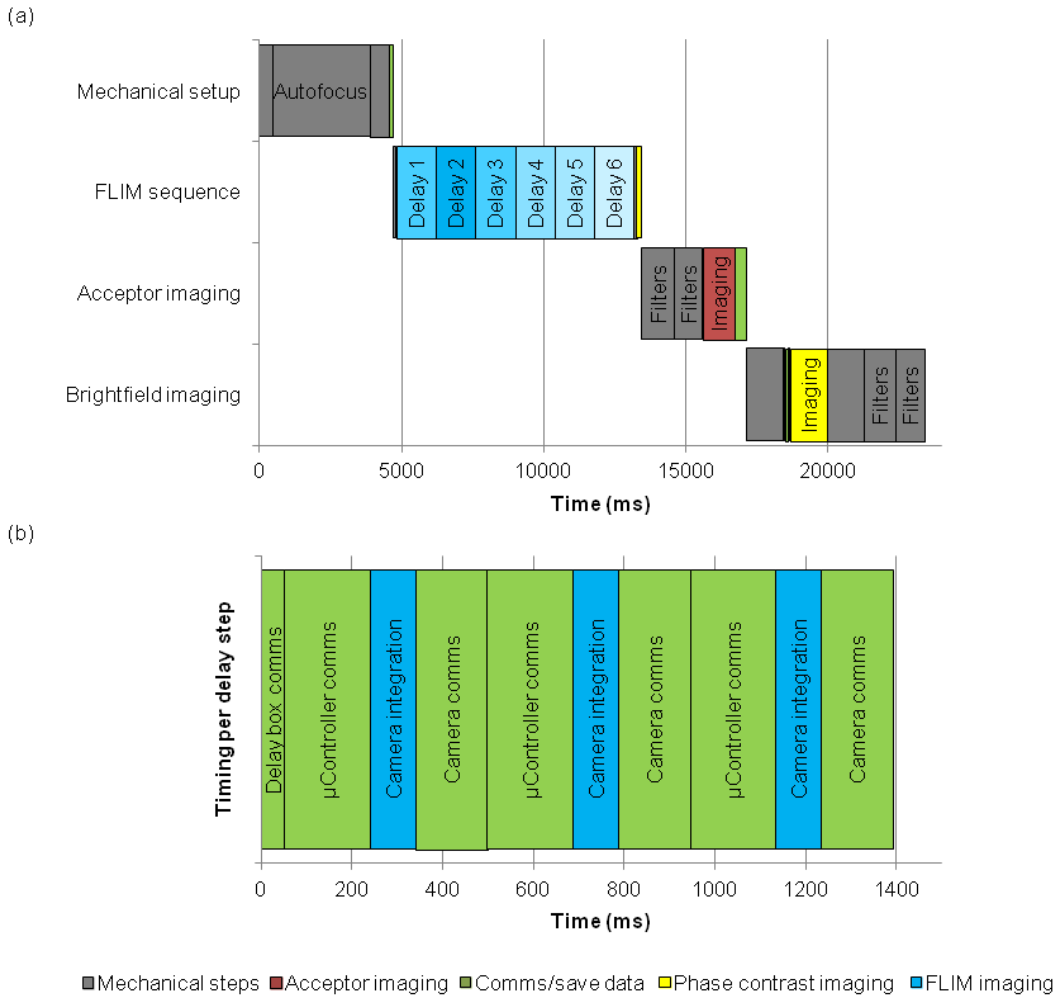

Figure 3-26 Charts showing breakdown of acquisition timing for acquisition of FRET construct plates. (a) Chart breaking acquisition of a single field of view down into component steps, which are then further subdivided. Time consuming steps are labeled. (b) Chart further subdividing each FLIM delay step from (a), highlighting the relatively short time spent integrating signal on the CCD when accumulating frames.

This acquisition, being a particularly complex case and involving imaging many fields of view per well, is an example of one of the slowest acquisitions that is likely to be undertaken using the FLIM plate reader. Acquisition time can be reduced in many ways depending on user preference; some potential means of increasing acquisition speed are summarised in Table 3-8 and discussed below.

Modification	Approx. time saving*	Notes
Image samples with an objective with M≠40	1-2 s/FOV	ZDC issue; see text
Autofocus every x FOV	$3.5 \times \left(\frac{x-1}{x}\right)$ s/FOV	Most easily implemented when objective in use has large depth of focus.
Trigger frame accumulation by sending N pulses from microcontroller for every command from PC	$180 \times (N-1)$ ms/delay step	
Update serial communications protocol to avoid dead time	50-500 ms/FOV	Time saving as yet untested.
Reduce number of repeat FOV per well (by Z FOV/well)	$23.3 \times Z$ s/well	
Save in multipage TIFF format	100 ms/FOV	Including metadata bundled with FLIM images.
Use wider gates, up to 6800 ps for single edge HRI	$\sim 0.1 \times \left(1 - \frac{1}{6.8}\right)$ s/delay step	
Sample decay with Y fewer gates	$1.4 \times Y$ s/FOV	Depends on complexity of decay

Table 3-8 Summary of means by which acquisition time may be decreased for FLIM plate reader experiments.

* Time saving based on data from Figure 3-26.

The time consuming autofocus step imposed by the Olympus ZDC autofocus unit may be approximately halved if higher or lower magnification objectives are used: for a 20x objective, autofocus typically takes 1950 ms; for a 100x objective, autofocus took on average 1147 ms. The exceptionally long autofocus time in the case summarised in Figure 3-26 is due to the ambiguity in assignment of the focal plane for 40x magnification air objectives, which necessitates an additional downwards movement of the objective turret before autofocussing in order that the lower, air-glass boundary of the plate is consistently found[156]; naturally, an additional upwards offset must be added to the turret position following autofocus to ensure that cells growing on the upper surface of the substrate are imaged, further adding to the autofocus time.

Modifications to the acquisition software, currently in the process of being fully implemented, can reduce the acquisition time per field of view. Elements of the acquisition software that make use of serial port communications, including setting delays and camera parameters, can be the source of dead time if the LabVIEW function "WaitForBytesAtPort" is used to determine whether a command has been successfully executed. It is preferable to instead make use of termination characters in communications protocols to avoid this dead time. In addition, newly written code for controlling camera parameters via an Arduino Uno reduces lag by streamlining the process of changing integration time, for example between FLIM and acceptor fluorescence imaging steps. Further reductions in time spent communicating with the microcontroller in cases in which frames are accumulated at each delay step might be achieved

by sending a predefined stream of pulses every time the PC sends a "grab frame(s)" signal to the microcontroller, rather than requiring communication between PC and microcontroller for every individual frame.

Finally, improvements in speed can be achieved by changing the experiment design. Whilst not generally desirable, removing in-line phase contrast or acceptor imaging steps significantly reduce acquisition time. Similarly, reducing the number of frames accumulated at each delay step reduces acquisition time at the expense of fewer photons being available for analysis. Alternatively, reducing the number of fields of view acquired per well will naturally reduce the total time spent acquiring data. To illustrate the effect of reducing the number of fields of view imaged on assay quality parameter Z' and standard error on the mean determined lifetime, MCF7 cells were plated on plastic plates and transfected with mCerulean and three FRET standards as described above. Acquisitions were carried out on live cells at 37°C, imaging 10 fields of view per well. In the analysis software, fields of view were incrementally deselected such that the number of fields of view analysed per well ran from 10 to 1: by deselecting fields of view in the reverse order that they were acquired, such an approach may be considered equivalent to acquiring only N fields.

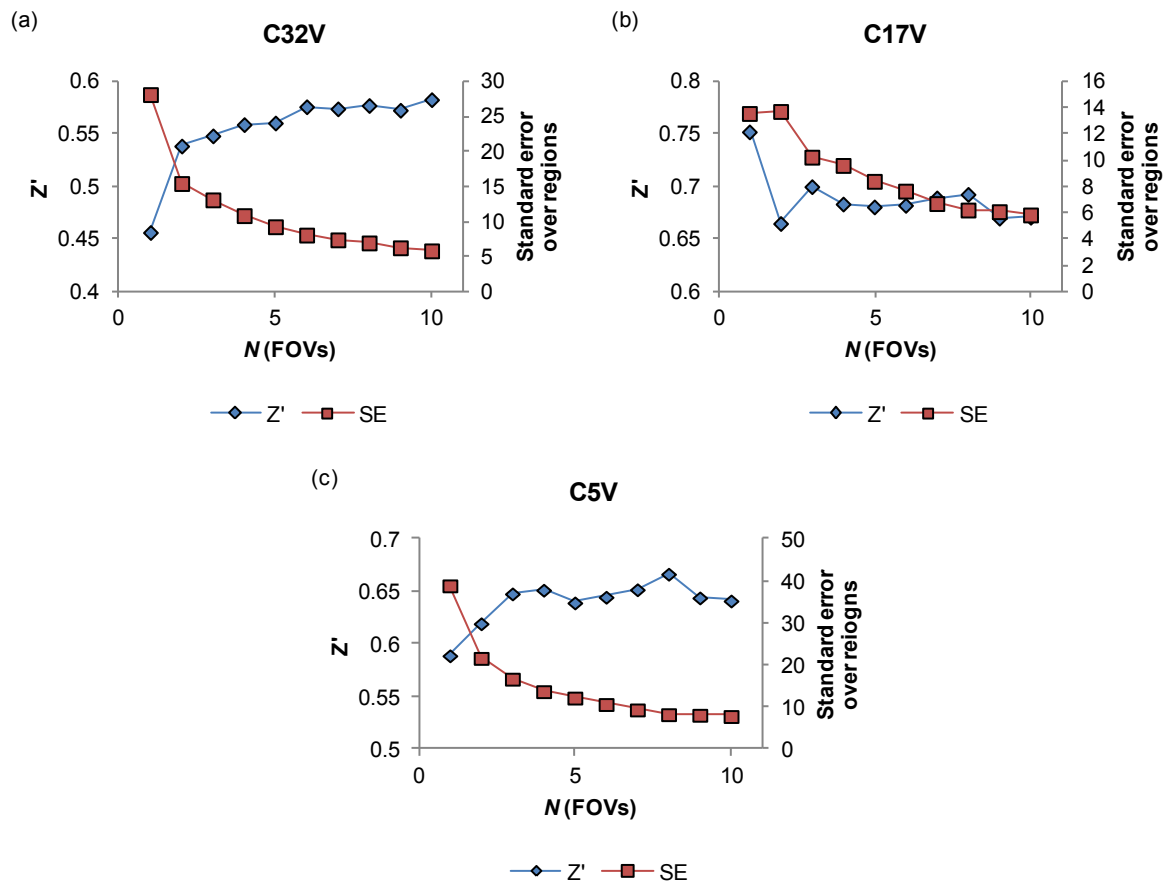

Figure 3-27 Plots of assay quality parameter Z' and standard error calculated cellwise against number of fields of view acquired.

(a) Z' calculated by comparison of results from N fields of view of live MCF7 cells plated on plastic, transfected with C32V and N fields of view of mCerulean only cells. (b) Z' calculated by comparison of results from N fields of view of live MCF7 cells plated on plastic, transfected with C17V and N fields of view of mCerulean only cells.

(c) Z' calculated by comparison of results from N fields of view of live MCF7 cells plated on plastic, transfected with C5V and N fields of view of mCerulean only cells.

In a broadly homogenous sample without significant subpopulations, for which pre-find tools have been run to guarantee the presence of fluorescent cells in every field of view and which does not suffer from fluorescent debris or artefacts, Figure 3-27 illustrates that the number of fields of view required per well/condition is much less than the conservative 8 FOV/well acquired in the experiment that was profiled for speed. Based on Figure 3-27 (a) and (c), four fields of view per well might seem a reasonable number, though the anomalous behaviour apparent for C17V in Figure 3-27 (b) indicates that caution must be exercised when making a judgement on the number of fields to acquire.

At the opposite extreme from the complex example profiled above, FLIM data for a plate of Coumarin 6 dye was imaged combining a number the factors identified in Table 3-8 to increase acquisition speed. For this acquisition it is possible to acquire a 96 well plate of dye samples in 9 minutes 23 seconds. The resulting lifetime plate maps from these plates are shown in Figure 3-28.

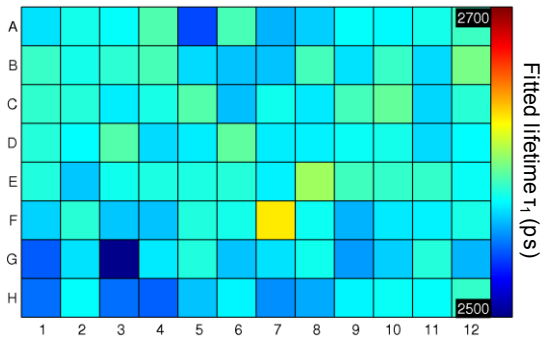

Figure 3-28 False colour lifetime plate map for a monoexponential fit to Coumarin 6 dye.

3.6 Summary

This chapter has outlined the development of an automated plate reading FLIM microscope, equipped for wide field time gated lifetime imaging. Both hardware and software aspects have been discussed, with particular focus placed upon the development of a prefind tool that improved the applicability of the microscope to a wide range of challenging samples. Preliminary experiments concerning the characterisation of the enabling technology for high speed time gated FLIM acquisitions – the high rate imager – have been presented. Finally, a series of experiments using FRET standards have been used to illustrate the application of the plate reader to measurements of FRET and the performance of the system in such applications.

3.7 Future development

In the continued development of the FLIM plate reader, there are a number of potentially fruitful directions for future work, from both hardware and software perspectives. A strength of the wide field imaging modality over sectioned imaging in the current implementation is increased flexibility with respect to acquiring data in multiple spectral windows. It is intended in the short term that the additions

might be made to the detection arm of the plate reader such that sectioned acquisitions may be performed automatically across a number of wavelengths. In the absence of a spinning disk unit equipped with automated emission and dichroic filter changers, this may be achieved by using a multipass dichroic mirror and an external automated filter wheel placed in an infinity-space region to be generated after the CSUX output. This will improve flexibility in optically sectioned imaging experiments, with particular application in interaction screening experiments (see Chapter 4: section 4.2).

Interest from collaborators in a range of experiments using automated stimulation has already been expressed. Without purchasing a commercial liquid handling system, it may still be possible to improve the current setup as outlined in section 3.1.4 above. Adding a small vibrating motor, typically used in mobile phones and powered by a button cell, and using low retention pipette tips, might improve the accuracy of delivery of the dispenser head. For increased speed of delivery in dose- and time-response experiments, it may be advisable to stimulate with a single volume of drug into wells containing different volumes of imaging media. Compared to the current situation, in which dose responses would typically be achieved by changing the dispensing volume between wells, such an approach would abrogate the need for multiple start-stop commands to be sent to the syringe pump.

In addition to improvements to hardware to increase the functionality of the instrument, it is intended that software control should be migrated to the μManager platform[157]. Such a move would have several benefits, not the least of which would be the availability of software as open-source code, which would represent a significant step towards the realisation of "OpenHCA-FLIM". In addition, adaptation of the existing μManager means that users will be presented with a familiar GUI when using the system, whilst integration into other data infrastructure including CellProfiler and OMERO will be more straightforward than in the current LabVIEW implementation. Finally, designing the software from scratch rather than on-the-fly should result in a cleaner source that will be more readily modifiable for future developers.

It is intended that further work should be carried out to fully characterise a range of HRI devices available in the Photonics group. This work, which is in progress and being carried out by Hugh Sparks, will include characterisation of spatial resolution and noise behaviour, and will seek to assess which HRI design is preferable for use in both high content and endoscopy-based applications of time gated FLIM. In parallel, it is expected that mathematical modelling and simulations will further direct future HRI choice and, through collaboration with Kentech Instruments, design parameters.

Chapter 4: Intermolecular FRET

The benefits of intermolecular FRET have been outlined in Chapter 2: section 2.3.2. Using intermolecular FRET constructs can provide increased dynamic range in FLIM-FRET experiments compared to intramolecular FRET sensors, and permit protein-protein interaction screens to be carried out in live cells. Making use of the automated FLIM plate reader, it is possible to correlate FRET changes associated with binding events to variations in treatment conditions in fixed or live cells, including in the presence of "biological noise" or in samples that exhibit sparse labelling. Both of these challenges were encountered in the course of experiments that I carried out to investigate changes in SUMO1 binding to FOXM1 in response to anthracycline treatment, outlined in the first part of this chapter.

A further advantage of intermolecular FLIM-FRET experiments is the capacity to investigate both FRET efficiency of a bound donor-acceptor construct complex, and the ratio of free-to-bound donors, by fitting a biexponential decay model to data. The results of biexponential fitting, in conjunction with intensity data linked to donor and acceptor concentrations, can inform on relative binding strengths of pairs of proteins in live cells. This method is discussed in the context of a protein-protein interaction screening experiment designed to determine which members of the RASSF-family of proteins interact with MST1; this series of experiments is reported in the second part of the chapter. Together, these experiments offer an insight into the capabilities of the FLIM plate reader in intermolecular FRET applications.

In this chapter,

- The biological context of a FOXM1-SUMOylation project is outlined together with the motivation for investigating this phenomenon using FLIM-FRET.
- Characterisation and optimisation experiments which address practical concerns surrounding measurement are presented.
- The use of the FLIM plate reader to investigate SUMO1 modification of FOXM1 in response to anthracycline time course treatments is demonstrated.
- A protein-protein interaction screen set up in to investigate RASSF-family interaction partners with MST1 in live cells is discussed.
- The results of the screen are presented. The benefits of the automated FLIM plate reader in this experiment and the possibility of extracting quantitative information on relative binding strength in different interactions are considered.

4.1 SUMOylation of FOXM1

The modification of the transcription factor FOXM1 by the small ubiquitin-like modifier protein SUMO1 is associated with changes in activity. Given the role that FOXM1 plays in breast cancer, particularly in the loss of sensitivity to anthracycline treatments, the spatiotemporal profile of FOXM1 SUMOylation is of interest in the context of elucidating the mechanisms by which drugs promote cell death in cancer cells, and how cells in drug-resistant tumours escape this fate.

In parallel with biochemical methods used in the Department of Surgery and Cancer at Imperial College London, we sought to investigate the dynamics of FOXM1 SUMOylation in response to anthracycline treatment. SUMOylation in general is known to be a highly dynamic process[158,159]. Furthermore, experiments performed in parallel suggest that SUMOylation is associated with a change in FOXM1 localisation. FRET microscopy gives spatiotemporal information on protein-protein interactions, potentially combining the localisation capabilities of fluorescence intensity imaging with the ability to probe protein-protein interactions normally provided by biochemical techniques following cell fractionation such as His tag purification, co-immunoprecipitation (CoIP) and Western blotting. Thus a robust FRET microscopy well plate experiment could confirm conclusions drawn from many separate biochemical experiments.

4.1.1 Biological context

Anthracyclines in cancer therapy

Breast cancer is the most common form of cancer in the UK: in 2011, breast-sited tumours made up 30.7% of all malignancies in females in England[160] and there were 41 826 new diagnoses of breast cancer (males and females). Furthermore, the age-standardised mortality rate for breast cancer in the UK over the period 2008-2010 was 25.3%[161], placing it second to lung cancer as the malignancy with the worst survival rate. Of all anticancer drugs, anthracyclines remain amongst the most commonly used[162], despite the fact that their mode of action is not fully understood. Two examples of anthracyclines used in chemotherapy are doxorubicin (trade name Adriamycin) and epirubicin (trade name Pharmorubicin), often employed as a part of adjuvant treatment. Though the efficacy of these two treatments is similar, epirubicin is considered to have a better safety profile since it has been shown to exhibit cardiotoxicity at higher doses than doxorubicin in clinical studies[163,164].

When performing experimental studies of the effects of anthracyclines, it is crucial to bear in mind the clinically relevant range of concentrations, and in particular the upper bound of concentration to which cells are exposed when a patient is undergoing treatment. This upper bound is 1-2 μM, reflecting the dose achieved immediately following a bolus administration to a patient of 15-90 mg/m^2 doxorubicin[165].

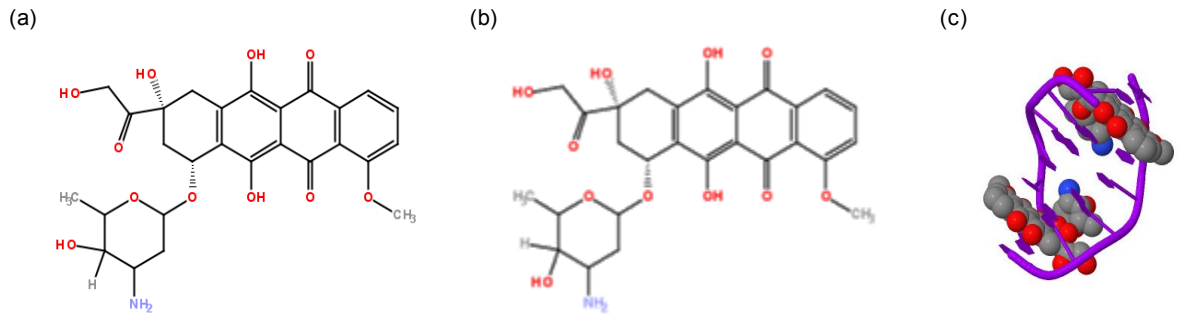

Figure 4-1 Chemical structures of (a) doxorubicin and (b) epirubicin. (c) X-ray diffraction structure of DNA-doxorubicin complex illustrating intercalation.
(a), (b) rendered in JChemPaint; (c) rendered in Jmol from PDB entry 1D12[166].

Doxorubicin and epirubicin are structurally similar, differing only in the orientation of a hydroxyl group in the hexapyranosyl sugar group – epirubicin is described as the 4'-epimer of doxorubicin (Figure 4-1 (a) and (b)). Structural data from X-ray crystallography[166] and spectroscopy[167] indicate that in common with all anthracyclines, both intercalate with DNA as shown in Figure 4-1 (c). There are several proposed mechanisms of cytotoxicity promoted by the anthracyclines. Following intercalation with DNA, anthracyclines can prevent DNA and RNA synthesis to induce cell death, though there is a lack of consensus in literature as to whether this effect is important at sufficiently low drug concentrations to be clinically relevant[165]. Another related mode of action is topoisomerase poisoning: anthracyclines can stabilise the DNA-topoisomerase IIA complex. Since topoisomerase IIA is implicated in changing DNA topology by cleaving and rejoining dsDNA, cleaved DNA cannot subsequently be rejoined, so double-strand breaks (DSBs) accumulate in a time-dependent manner[168]. The DNA damage induced by topoisomerase poisoning is followed by cell cycle arrest in G1 and G2[169] and eventually cell death. Such effects are apparent at clinically relevant concentrations.

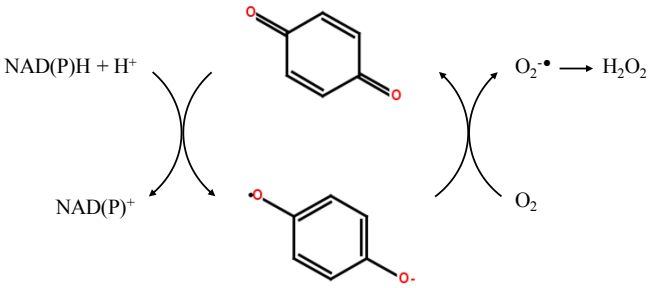

Figure 4-2 Schematic showing mechanism of ROS generation by anthracyclines.
One-electron cycling generates NAD and a semiquinone form of the third ring of the anthracycline (the remainder of the molecule has been omitted for clarity). This electron is subsequently donated to molecular oxygen to form free radicals including superoxide and hydrogen peroxide. Figure adapted from[170,171], rendered in JChemPaint.

Free radical reactive oxygen species (ROS) are generated by one-electron cycling of a quinone moiety present in doxorubicin. This process involves oxidation of NAD(P)H to NAD(P)+ as shown in Figure 4-2 and results in intracellular hydrogen peroxide and superoxide anion[170,172]. Such ROS can directly oxidise cell constituents and can cause DNA damage by modifying bases or by inducing single-strand

breaks. It has been argued that such direct modifications are unlikely to be found at clinically relevant concentrations of anthracyclines, but that the ROS generated by one-electron cycling instead induce cell death via alternative pathways[165,170].

Forkhead box protein M1and drug resistance

Forkhead box protein M1 (FOXM1, 89 kDa) is a transcription factor, the dysregulation of which is linked to aberrant cell behaviour relating to cell cycle progression and proliferation. If FOXM1 is depleted the progress of cells through the cell cycle is disrupted, and consequent mitotic abnormalities can result in aneuploidy or polyploidy[173]. Conversely, overexpression of FOXM1 is linked to tumorigenesis, angiogenesis and metastasis[174,175]. Elevated levels of FOXM1 are considered a marker for early cancer detection in a range of malignancies including (but not limited to) high-incidence, high mortality rate cancers of the lung, prostate, colon and breast. A variety of proteins have been implicated in the regulation of FOXM1 expression, including forkhead box class O (FOXO) transcription factors[176,177], estrogen receptor alpha (ERα)[178], p53 and Ataxia-telangiectasia mutated protein (ATM)[179]. In turn, as a transcription factor, FOXM1 regulates expression of a great number of proteins such as Stathmin[180], ERα[181], E-cadherin[182] and BRCA1-interacting protein (BRIP1)[168]. FOXM1 also plays a regulatory role in tissue repair and maintenance of pluripotency in stem cells[183,184].

In addition to tumorigenesis, progression and metastasis, FOXM1 plays a role in drug resistance in cancer cells. The mechanisms behind drug resistance in the context of refractory cancer - inoperable malignancies that are either inherently unresponsive to chemotherapy or become so in the course of treatment – is an active area of research. Correlations between FOXM1 expression and resistance to the taxane paclitaxel (trade name Taxol) have been demonstrated, and linked to the role played by FOXM1 in mediating stathmin expression[180]. Sensitivity to anti-EGFR/HER2 drugs such as trastuzumab (trade name Herceptin) or gefitinib (trade name Iressa) is associated with overexpression of FOXM1, as FOXO3a acts as a link between the EGFR/HER2-PI3K-PKB signalling pathway and expression of FOXM1[176]. The positive feedback relationship that has been shown to exist between estrogen receptor alpha (ERα) and FOXM1 expression[178,181], together with evidence showing that ERα and FOXM1 share binding sites across the genome[185], suggests that FOXM1 may contribute to resistance to endocrine treatments such as tamoxifen and fulvestrant (trade name Faslodex).

Anthracycline resistance has been shown to be closely linked to expression of the forkhead transcription factor FOXM1 in cell lines. Doxorubicin-resistant cell lines (MCF7-Dox^R), generated from wild type MCF7 by selection pressure under long term treatment with Doxorubicin to a final concentration of 17 μM, exhibit enhanced expression of FOXM1[179]. Sensitivity can be restored to resistant cell lines by depleting FOXM1 using siRNA, and modulation of FOXM1 expression in response to anthracycline treatment varies between resistant and sensitive cells[175]. A further link between FOXM1 activity and anthracycline resistance is indicated by previous and parallel research in the Lam laboratory, in which activity-related post-translational modifications to FOXM1, including phosphorylation[186,187] and

SUMOylation[188], were shown to occur in response to anthracycline treatment. The mechanisms by which this regulation occurs are currently not well understood.

Post-translational modifications and small ubiquitin-like modifier

In cellular signalling, post-translational modifications to proteins play myriad crucial roles. Of such modifications, a proportion involves the addition of small chemical groups – phosphorylation mediated by kinases and phosphatases modulate activity of many proteins, and acetylation (addition of an acetyl group) is implicated in transcriptional control[189,190]. Addition of hydrophobic moieties can regulate localisation to membranes or organelles, for example the modulation of membrane association of R-Ras by post-translational palmitoylation[191]. Alternatively, whole peptides or proteins can be added to other proteins post-translationally. Ubiquitination is one example of such a process, in which ubiquitin (Ub, 8.5kDa) is covalently attached to a substrate protein by E3 ubiquitin ligases following activation by E1 Ub-activating enzymes and conjugation by E2 Ub-conjugating enzymes. In proteasome degradation signalling, chains of Ub many monomers long (lysine 48-linked chain) are appended to proteins marking them for degradation[192]. Polyubiquitin chains have also been implicated in the cellular DNA damage response (DDR)[193].

The addition of small ubiquitin-like modifier (SUMO, 11 kDa) is another peptide post-translational modification, closely related to ubiquitination. There are four paralogues of SUMO proteins in humans. Herein we are mostly concerned with SUMO1, since parallel biochemical experiments did not show that SUMO2/3 interact with FOXM1, though it is noted that recent research has contradicted this finding[194]. The isopeptide bonding of SUMO1 to a target protein occurs at the SUMO-acceptor consensus site ΨKxE, where Ψ represents an aliphatic branched amino acid and x represents any amino acid[195]. SUMOylation is mediated by a relatively small set of enzymes. Similarly to ubiquitination, there is typically a three-step process of activation, conjugation and ligation by SUMOylation-specific E1, E2 and E3 proteins (Figure 4-3); conversely, deSUMOylation is performed by sentrin-specific proteases (SENP1-3, 5-7)[158]. Many proteins also contain a SUMO-interacting motif (SIM) which interacts non-covalently with SUMOylated proteins via a hydrophobic core, typically followed by phosphorylatable residues – one consensus sequence for this motif is V/I-x-V/I-V/I[196]. In such cases, SUMO might be considered to facilitate an increase in affinity between a SUMOylatable protein and its binding partner. Additionally, it has been proposed that the existence of SIMs on a protein gives rise to an alternative, SUMO-E3 ligase-independent mechanism by which SUMOylation might occur, particularly on non-consensus sites[159,197] (Figure 4-3). The sequence of FOXM1 indicates the presence of SIM motifs[198].

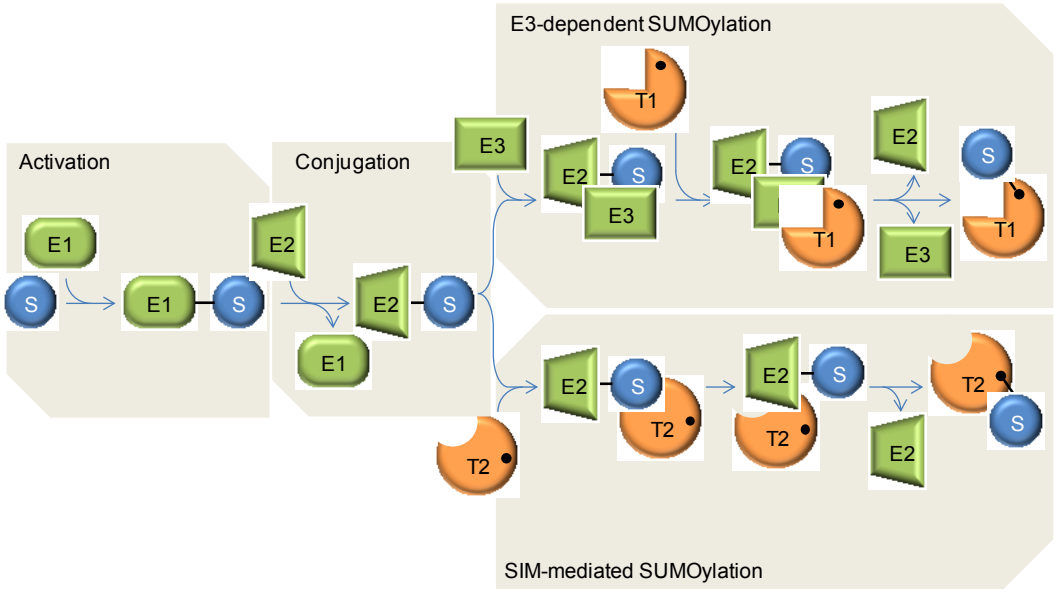

Figure 4-3 A schematic of the SUMOylation pathway
SUMO (S) is first activated by the E1 dimer (Aos1-Uba2) before being passed to the active site of enzyme E2 (Ubc9). In the case of E3-dependent SUMOylation, an E3 SUMO ligase (PIAS family protein, RanBP2 or others[159]) binds both the E2-S complex and the target T1, facilitating SUMOylation at the consensus site (●, ΨKxE). In SIM-mediated SUMOylation, the SUMO in the E2-S conjugate associates with the SUMO interaction motif on target T2. This is thought to increase the local concentration of E2-S, facilitating the conjugation of SUMO to the target at the consensus site. Figure adapted from[159].

Like ubiquitination, SUMOylation has been implicated in signalling processes relating to proteolytic degradation[199], as well as mitosis and cell cycle progression[200]. Crucially in the context of drug resistance, SUMOylation has been identified as having a role to play in DDR-related pathways. These include the base excision repair (BER) pathway in which individual base lesions are repaired. Studies have suggested that SUMOylation of the Thymine-DNA glycosylase (TDG) protein modulates binding to DNA[201] in BER, facilitating recycling of the enzyme. The role of SUMOylation of BRCA1 in response to DNA damage has been investigated by FLIM-FRET[202] in a study which showed that the activity of the BRCA1/BARD1 heterodimer increased upon SUMOylation. Other ubiquitin ligases RNF168 and HERC2 have also been shown to become SUMOylated in response to DNA DSBs[203].

Post translational modifications of FOXM1

Multiple studies have highlighted the role of post translational modifications in modulating the transcriptional activity of the transcription factor FOXM1. Nine sites have so far been identified at which phosphorylation can occur (Figure 4-4 (a)), mediated by different kinases in a multitude of pathways. Cyclin dependent kinases, implicated in cell cycle control, stabilise and activate FOXM1 as well as increasing interaction with co-activators, resulting in expression of genes expressed in the G1/S phase of the cell cycle[204]. Downstream of the known oncogene KRAS, Erk can phosphorylate FOXM1 and enhance activity by increasing localisation in the nucleus[205]. Alternatively, phosphorylation by CHK2 following DNA damage increases transcriptional activity of FOXM1 by stabilisation[186]. Increased FOXM1 transcriptional activity is reflected in the increased production of FOXM1 target gene products,

including DNA damage response proteins BRCA2, RAD51 and BRIP[205]. These processes are summarised in Figure 4-4 (b).

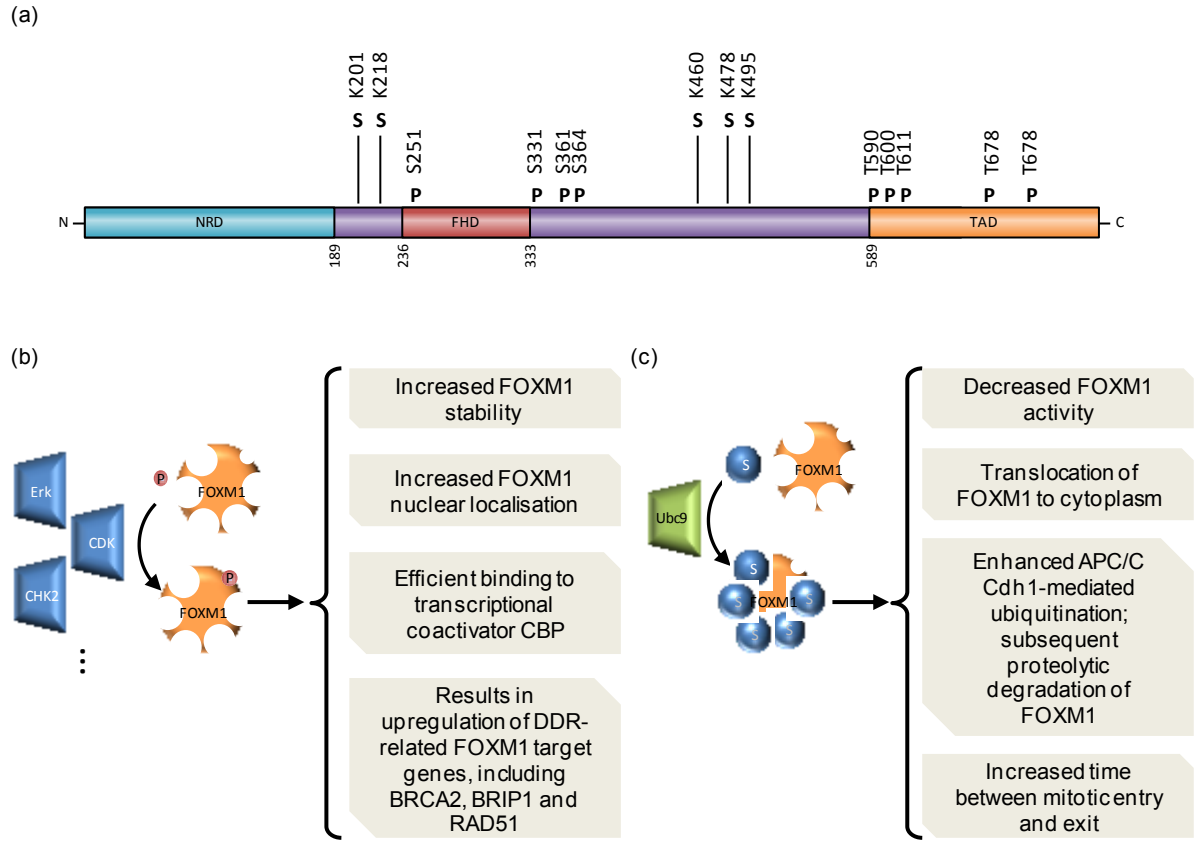

Figure 4-4 Summary of phosphorylation and SUMOylation post-translational modifications of FOXM1. (a) Phosphorylation and SUMOylation occurs at multiple sites on FOXM1. In this schematic, lysine residues in SUMOylation sites are marked, along with serine and theronine residues in phosphorylation sites[188,205]. (b) Summary of the effects on FOXM1 transcriptional activity caused by phosphorylation by kinases including Erk, CDK and CHK2. A single phosphorylation site is shown in the schematic for clarity. (c) Summary of the effects of SUMOylation, mediated by ligases including Ubc9, on FOXM1 transcriptional activity. NRD: N-terminal repressor domain, FHD: Forkhead DNA-binding domain, TAD: transactivation domain, CDK: cyclin-dependent kinase, Chk2: checkpoint kinase 2, APC/C Cdh1: Anaphase-promoting complex, complexed with activator protein Cdh1, **P**: phosphorylation site, **S**: SUMOylation site.

Five SUMO modification sites have been identified on the transcription factor FOXM1[188,194] (Figure 4-4 (a)). In light of the role played by SUMOylation in other DDR systems, the modification of FOXM1 activity in response to anthracycline treatment described above and a proposed link between the ability of cells to repair DNA damage and anthracycline resistance, it was speculated that SUMOylation might play a role in modulating FOXM1 activity. In order to examine this hypothesis, a series of biochemical experiments have been performed in the Department of Surgery and Cancer at Imperial College London, in parallel with the FLIM-FRET work presented in this chapter[188]. This work served to illustrate the inhibitory effect on FOXM1 activity conferred by SUMOylation, including promotion of translocation to the cytoplasm, and enhancement ubiquitination and degradation of FOXM1. In addition, treatment with epirubicin was shown to increase FOXM1 SUMOylation in MCF7 cells, highlighting the role of this modification in DNA damage response. Negative controls were carried out using a "non-SUMOylatable"

FOXM1 mutant, generated in the Lam lab by performing five lysine-to-arginine mutations at five SUMO-acceptor ΨKxE motifs present on FOXM1. The resulting mutant (FOXM15X(K>R) (K201R/K218R/K460R/K478R/K495R), hereafter denoted simply FOXM1mut) was shown to be unmodified by SUMO in Western blot analysis. Expression of FOXM1mut enhanced proliferation compared to the wild type FOXM1, was more efficient in conferring resistance to anthracycline treatment, and exhibited different subcellular localisation compared to the wild type[188]. These effects are summarised in Figure 4-4 (c).

Assay of FOXM1-SUMOylation in response to epirubicin treatment using FLIM-FRET

The small protein modification studied in this project is intrinsically intermolecular in nature, suggesting that intensity-based FRET techniques may provide a less robust measure of interaction than FLIM-FRET. Critically, as discussed in section 2.3.3, intensity-based methods typically yield "effective FRET efficiency" as an output parameter, whereas it is possible to extract information relating to both FRET efficiency and binding stoichiometry using FLIM. We therefore performed a series of experiments which sought to establish the dynamics of FOXM1 SUMOylation throughout a time course of drug treatment, using an automated multiwell plate reading FLIM microscope. The fluorescent constructs used in FLIM-FRET experiments are illustrated in Figure 4-5; both wild type and non-SUMOylatable FOXM1mut are labelled with eGFP at the N-terminal end to act as FRET donors, and SUMO1 is labelled with TagRFP-T (subsequently denoted TRT) to act as FRET acceptors. SUMO1-TRT is adapted from a fluorescent protein tagged SUMO1 construct gifted from the Ng lab (Richard Dimbleby Department of Cancer Research, King's College London, UK) using a TagRFP-T fluorescent protein gifted by Alex Sardini (Cellular Stress group, MRC Clinical Sciences Centre, Imperial College London). FOXM1-mCherry and SUMO-eGFP constructs were also available; however, the relative ubiquity of SUMO1 expression suggests that using SUMO-eGFP as a FRET donor would yield extremely small mean lifetime shifts due to the large excess free donor population.

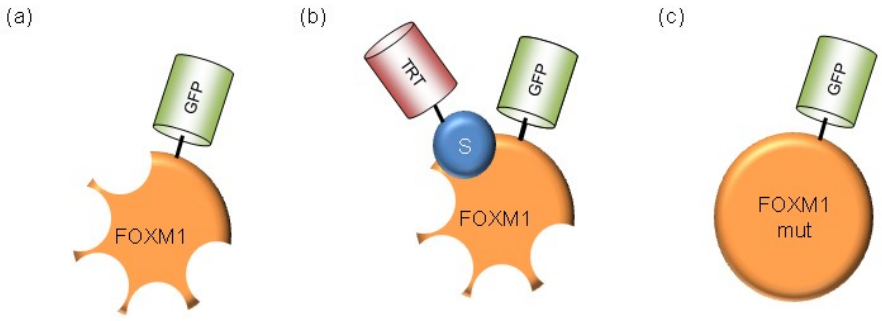

Figure 4-5 FOXM1-SUMOylation experiment fluorescent constructs
(a) Wild-type FOXM1-eGFP. (b) SUMO1-TagRFP-T, binding at a FOXM1 SUMOylation consensus site. (c) Non-SUMOylatable FOXM15x(K>R)-eGFP.

In the context of investigating the effects of anthracyclines in live cells using fluorescence techniques, it is necessary to realise that anthracyclines are themselves typically fluorescent. This property has been exploited in the direct observation of doxorubicin distribution within cells as well as in lifetime studies investigating changes in lifetime corresponding to release from poly(L-lysine adipamide) micelles and DNA binding events[206]. For the purposes of the FLIM-FRET experiments presented below, changes in fluorescence intensity or lifetime of directly-excited doxorubicin might confound interpretation of FRET signal or acceptor expression: this possibility is investigated in section 4.1.3 below.

Initially, an experiment was performed without extensive optimisation of conditions and without using automated HCA FLIM techniques. Following optimisation of transfection and drug treatment conditions, experiments were carried out in order to address concerns surrounding doxorubicin background fluorescence and non-specific association of donor and acceptor constructs. Finally, both live and fixed plates were used in experiments to investigate FOXM1-SUMOylation in response to a time course of anthracycline treatment.

4.1.2 Preliminary experiment: time course of doxorubicin treatment, TCSPC FLIM

Prior to implementing FOXM1-SUMOylation FLIM-FRET assays in an HCA format or optimising experimental conditions, an initial FLIM experiment was carried out on a Leica SP5 microscope equipped for TCPSC lifetime imaging[207]. Samples for this experiment were prepared at Hammersmith Hospital in conjunction with Mesayamas Kongsema.

Sample preparation

Glass coverslips were washed in ethanol and rinsed in PBS before being laid in wells of a six well plate. MCF7-WT cells were seeded at a density of 2×10^5 per well in standard growth media. 24 hours after seeding, cells were transfected with FOXM1-eGFP (donor only) or FOXM1-eGFP and SUMO1-TRT (donor + acceptor) using Fugene 6 in a 2:1 plasmid:transfection reagent ratio. 24 hours after transfection, a treatment time course using 1 μM doxorubicin was started. 24 hours after treatment was started, cells were rinsed in PBS and fixed by submerging in 4% paraformaldehyde (PFA) for 10 minutes at room temperature. Transfection and fixation was performed in the Hammersmith lab before the samples were transported to South Kensington for imaging.

Image acquisition and analysis

Low transfection efficiency meant that transfected cells were identified manually under Hg lamp illumination on the Leica SP5 microscope, then lifetime images were acquired using time correlated single photon counting. Photobleaching was judged not to be an issue as average counts per second did not decrease over the imaging period, which was set at 300s to allow for the dimness of the fluorescence whilst keeping incident power low.

Data was fitted in *FLIMfit* to a monoexponential decay model using DASPI as a reference IRF, including a fixed time varying background in the fit. The background fluorescence was measured from a region without cells.

Results

The results from this preliminary experiment are presented in Figure 4-6. These samples showed a decrease in lifetime between untreated and six hour time points that persisted to the 24 hour time point, evident in the false colour lifetime images of untreated, 6 h- and 24 h doxorubicin treated cells in Figure 4-6 (a-c) and in the cell-averaged lifetime plot in Figure 4-6 (d). Despite the relatively low number of cells, the measured lifetime changes associated with increase doxorubicin treatment time were found to be significant when averaged over segmented cells ($p < 0.005$, Dunnett's test).

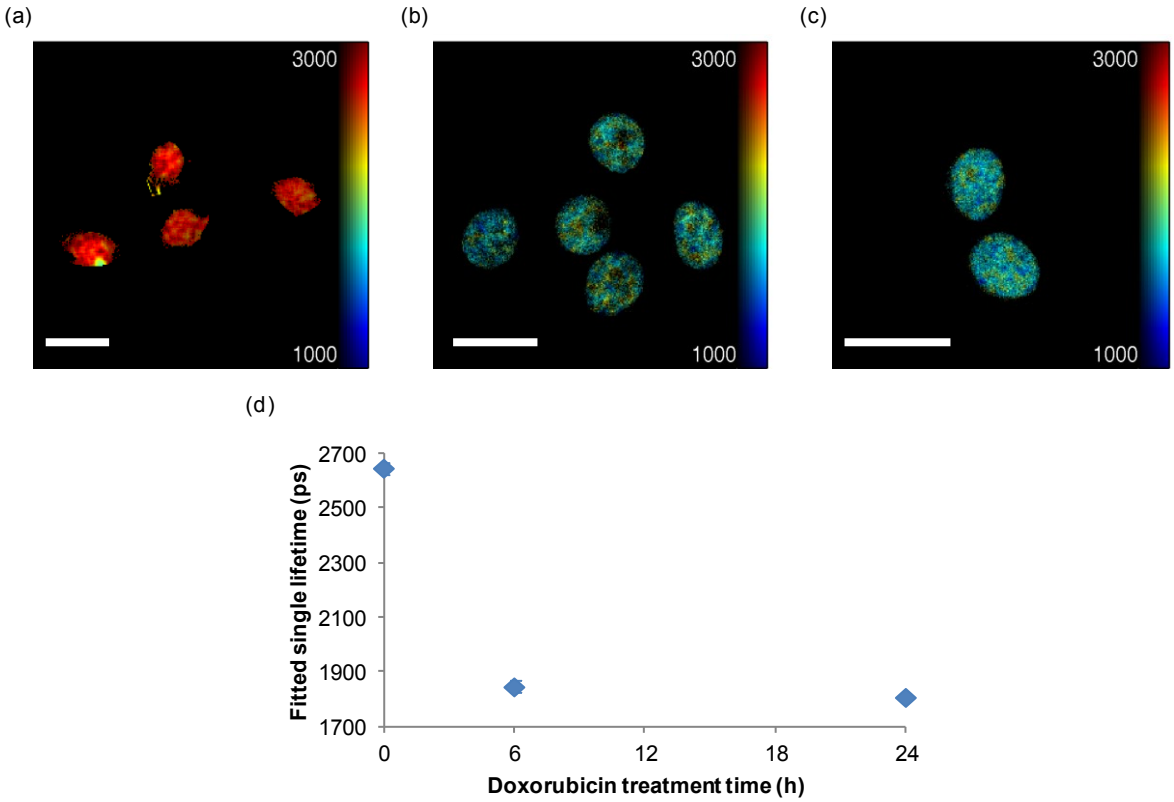

Figure 4-6 Results from preliminary experiment into FOXM1 SUMOylation measured by FLIM on a TCSPC system.

Intensity merged lifetime images generated from (a) untreated cells, (b) cells treated with 1 μM doxorubicin for 6 hours, (c) cells treated with 1 μM doxorubicin for 24 hours. Scale bars 50 μm. (d) Plot of lifetimes averaged over imaged cells. Error bars represent standard errors calculated over cells.

Discussion

Several points were noted from this preliminary experiment. Firstly, both the level of expression and the proportion of cells expressing labelled proteins were low, resulting in long acquisition times being required. It was therefore concluded that optimisation of the transfection technique should be carried out prior to running plate reader experiments. Furthermore, the translocation of FOXM1 upon SUMOylation evident from imaging experiments carried out elsewhere[188] was not observed in the small population of cells imaged here. Nevertheless, the magnitude of lifetime change measured encouraged us to pursue applying our automated FLIM plate reader to robustly establishing the spatiotemporal profile of FOXM1 SUMOylation following doxorubicin treatment.

4.1.3 Preliminary experiment: doxorubicin background fluorescence

Based on the work presented by Dai et al.[206], we were concerned that the presence of any background fluorescence from doxorubicin in fluorescence decays data might adversely affect our ability to measure and interpret changes in lifetime caused by FRET, given the reported change in doxorubicin fluorescence lifetime upon DNA binding. Measured spectra of 1 mM free doxorubicin in solution illustrate the potential for directly excited doxorubicin to be detected in the GFP channel (Figure 4-7). To establish whether background linked to doxorubicin might be prohibitive to GFP-based FRET experiments, a series of FLIM images were taken on the plate reader across a number of plates in which wells were seeded and treated according to the same time course as the experimental wells, but not transfected with either donor or acceptor fusion proteins.

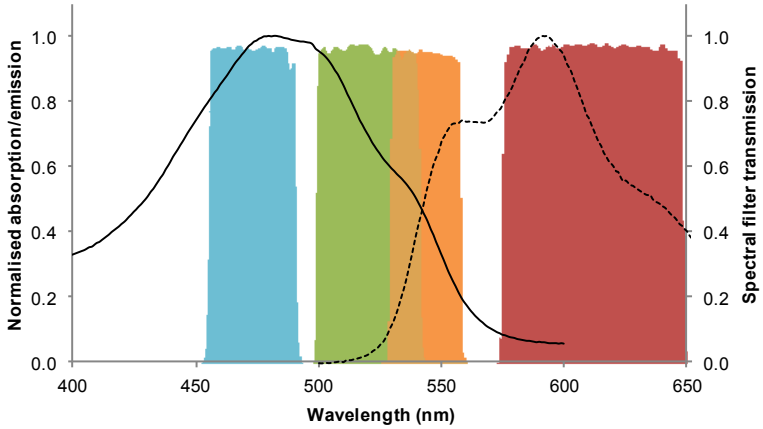

Figure 4-7 Absorption and emission spectra of doxorubicin, overlaid with transmission spectra of filters in the FLIM plate reader.

The absorption spectrum of 1 mM doxorubicin was measured using a UV3101-PC spectrophotometer (Shimadzu, Kyoto, Japan). The emission spectrum of 1 mM doxorubicin, excited at 488 nm, was measured using a RF5301-PC spectrofluorimeter (Shimadzu, Kyoto, Japan). Filter spectra were downloaded from the Semrock and Chroma websites[208,209].

Sample preparation

Following mycoplasma infection being found in cell cultures grown in both the Photonics and the Lam lab in the Department of Surgery and Cancer, a new cryovial of low passage MCF7 wild type cells were purchased from European Collection of Cell Cultures (ECACC) and assayed for mycoplasma infection using a MycoFluor mycoplasma detection kit (Molecular Probes, Oregon USA).

For background fluorescence measurements, cells were seeded at a density of 10^4per well on Greiner μClear plates in standard growth media and incubated for 48 hours at 37°C. 0.1 μM Doxorubicin was applied to wells 24 and 6 hours prior to removal of media. Growth media was replaced with glucose-supplemented HBSS (25 mM glucose to match growth media formulation) at 37°C before transferring the sample to the plate reader.

Image acquisition and analysis

8 fields of view per well were automatically selected spiralling out from the centre of the well. FLIM images were acquired across 7 gates per decay, in the GFP channel defined by the 472/30 - 495 - 520/35 filter cube, with each gate imaged using a single frame with 3 s integration time. Acceptor-channel fluorescence images were acquired at a single time delay with an integration time of 1 s through the 545/30 - 570 – 610/75 filter cube. Phase contrast images were acquired in line with FLIM and acceptor images to verify that fields of view contained cells.

For analysis, images were subjected to a 1000 DN integrated intensity threshold, and fitted to a monoexponential decay using a reference decay profile acquired from a 20 μM solution of Erythrosine B. All phase contrast images were checked manually to ensure that each field of view contained cells.

Results

Figure 4-8 shows a donor FLIM image and time-integrated donor intensity and acceptor intensity images from an exemplar field of view from the study of doxorubicin fluorescence in untransfected MCF7 cells, as well as plots showing the doxorubicin treatment time dependence of these three parameters. There is no significant change in integrated donor intensity over the 0.1 μM doxorubicin treatment time course as shown in Figure 4-8 (d). More pertinently, there is no significant change in lifetime across a typical 24 hour treatment time course when cells are treated with 0.1 μM doxorubicin, as illustrated in Figure 4-8 (b). There is also no contribution to intensity in the acceptor channel that varies with doxorubicin treatment, as shown in Figure 4-8 (f).

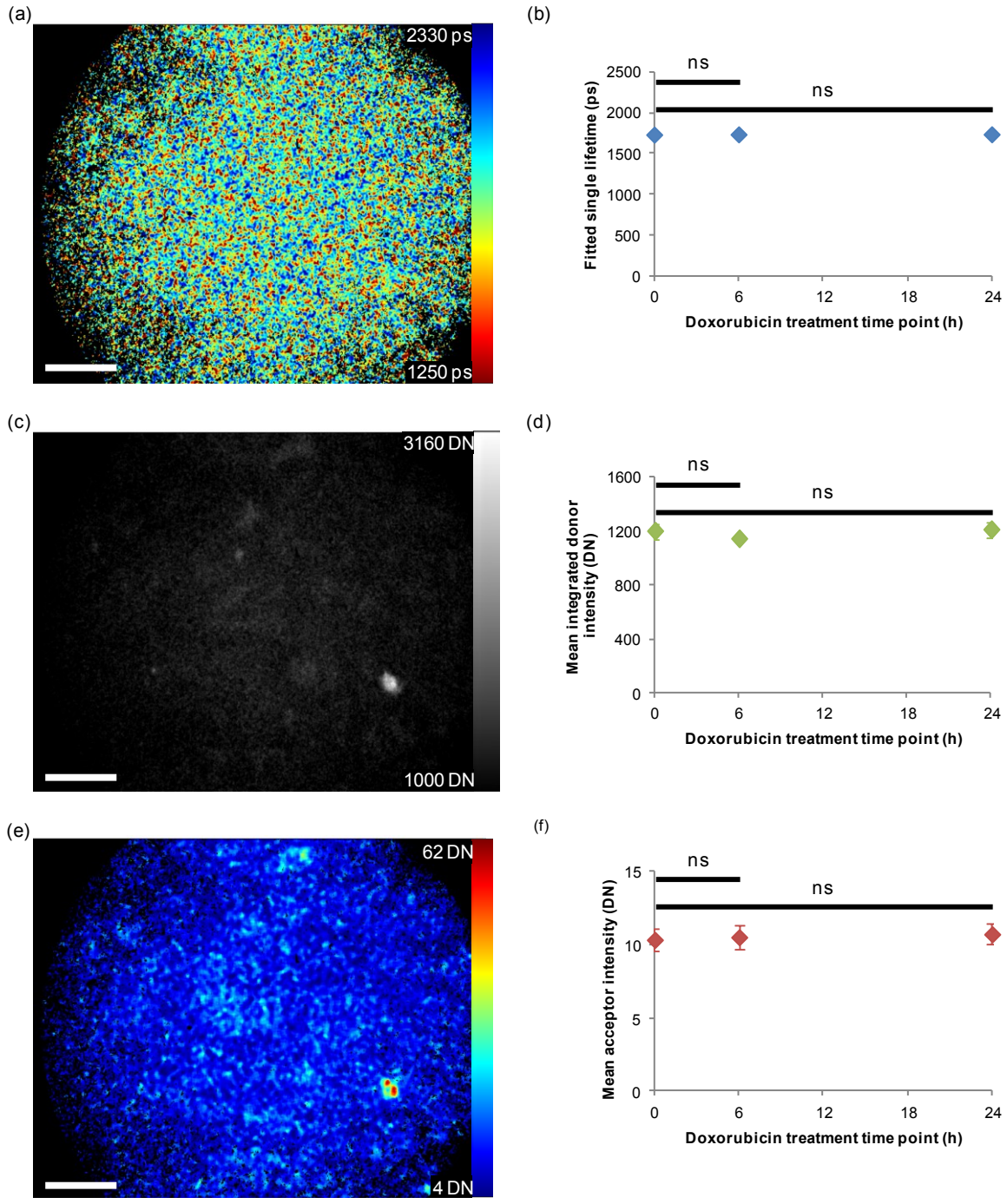

Figure 4-8 Results of experiment showing background effect of treating with doxorubicin in untransfected cells.

(a) Exemplar field of view showing pixelwise-fitted monoexponential lifetime data acquired from untreated cells. (b) Plot showing fitted donor-channel lifetime against doxorubicin treatment time, where error bars represent standard errors over repeat wells. (c) Exemplar field of view showing donor-channel integrated intensity image. (d) Plot showing integrated donor intensities against doxorubicin treatment time. (e) False colour map of acceptor-channel intensity image from an exemplar field of view. (f) Plot showing acceptor intensities against doxorubicin treatment time. All scale bars are 50 μm. No statistically significant differences were found using Dunnett's test.

Discussion

The data presented in Figure 4-8 suggest that there is no measurable doxorubicin fluorescence above background in the FLIM plate reader. This background might be composed of contributions from cellular autofluorescence, residual growth media components or the plastic growth substrate, in untransfected cells. It is particularly reassuring in the context of subsequent experiments that there is no significant change in fitted monoexponential lifetime over the treatment time course, even in this case where integration time has been increased by a factor of ~4 beyond those values used elsewhere, to permit the low levels of signal to be effectively fit on a pixelwise basis.

4.1.4 Preliminary experiment: optimisation of transfection conditions

In order to generate data capable of showing significant results despite the small lifetime shift observed, it was vital to increase the number of cells imaged per experiment. In parallel with the development of the low magnification prefind, time was spent to attempt to optimise the transfection protocol such that as many cells as possible expressed the fluorescent proteins at sufficiently high levels to be imaged. This was particularly an issue for the FOXM1-eGFP plasmid. Optimisation using XtremeGene HP to transfect cells on coverslips was carried out by Kongsema Mesayamas in the Department of Surgery and Cancer; it was found that appropriately scaled transfection parameters were suitable for 96 well plate experiments.

One potential additional issue that came to light through running optimised plates, as well as through other work in the Photonics group, was the effect of varying levels of acceptor expression on lifetime. This is of particular concern given the availability of SIM sites on FOXM1, since it may be that such non-covalent interactions of the SUMO-acceptor that occur independently of SUMOylation will cause lifetime to be modified in an acceptor concentration-dependent manner. Furthermore, through automated FLIM plate reader studies undertaken by Dr Anca Margineanu, the potential for association or hetero-dimerisation of donor and acceptor fluorescent proteins independently of biological association of the proteins of interest to which the FPs are fused was highlighted. Both of these effects were investigated.

Sample preparation

Cells were seeded at 10^4 per well in a single Greiner μClear plate in standard growth media and incubated for 24 hours. Transfection was carried out using XtremeGene HP (Roche, Basel, Switzerland) according to the manufacturer's protocols for MCF7 cells. The plate was laid out as illustrated in Figure 4-9, with different combinations of wild type and mutated FOXM1-eGFP constructs, SUMO1-TRT constructs, and "free" TRT protein. The ratio of transfection reagent volume to plasmid weight (2:1) is maintained across all conditions. Cells were incubated for a further 24 hours at 37°C before replacing growth media-transfection mixtures with glucose-supplemented HBSS at 37°C before transferring the sample to the plate reader.

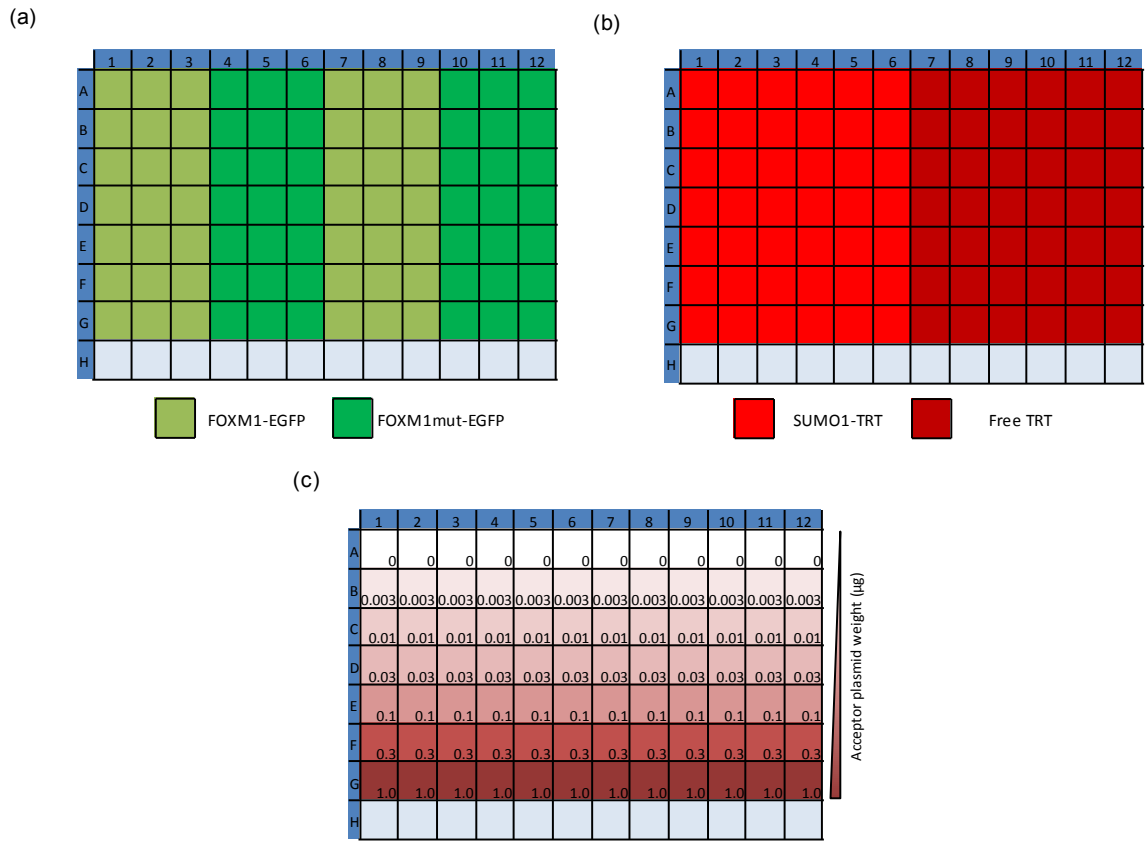

Figure 4-9 Illustration of plate layout and combinations of plasmids transfected to investigate effects of acceptor construct and free FP overexpression on FOXM1-eGFP lifetime.
(a) Donor construct layout. (b) Acceptor construct layout. (c) Acceptor construct plasmid weight per well layout.

Image acquisition and analysis

Cells expressing the FOXM1-eGFP construct were automatically identified using the low magnification prefind routine with a 10x objective and illumination provided by a Hg lamp in the spectral channel defined by the GFP filter cube (excitation: 472/30 nm, dichroic: 495 nm, emission: 520/35 nm). Subsequently, the illumination path was altered to allow excitation by the pulsed source, and FLIM images were acquired in the same spectral channel across 7 gates, with 3 0.5 s integrated frames summed at each time delay. Acceptor images were acquired using the "red" filter cube (excitation: 545/30 nm, dichroic: 570 nm, emission: 610/75 nm), with a single time delay being summed over 5 0.1 s exposures.

The NTH segmentation algorithm described in Chapter 3: section 3.4.1 was performed on integrated donor intensity images using the parameters outlined in Table 4-1, and a manual pass was made to eliminate fluorescent debris from analysis. A monoexponential model was fitted using a time-varying background measured from an HBSS-only well and a reference decay profile acquired from a 20 µM solution of Erythrosine B.

Parameter	Value
Scale	40
Relative background scale	2
Threshold	0.5
Smoothing	5
Minimum area	1000

Table 4-1 NTH segmentation parameters for automated segmentation of MCF7 expressing FOXM1-eGFP or FOXM1mut-eGFP.

Results

Figure 4-10 shows the results of increasing the plasmid weight of SUMO1-TRT or free TRT in transfection of MCF7 cells. The false colour lifetime plate map presented in Figure 4-10 (b) illustrates a dramatic decrease in fitted lifetime in rows in which 0.3 μg or 1.0 μg SUMO1-TRT is transfected. Inspection of images shows that in these wells, a large proportion of the "cells" identified by the prefind and segmentation algorithms are cell debris rather than whole cells. These rows are therefore omitted from further analysis, and other rows were checked manually for the presence of similar debris. The plots in Figure 4-10 (c-d) illustrate that there is a significant decrease ($p<0.005$, Tukey's test) in fitted lifetime when SUMO1-TRT is transfected at 0.1 μg/well for both FOXM1-eGFP and FOXM1mut-eGFP. In contrast, there is no significant decrease in fitted lifetime when free TRT is transfected alongside FOXM1-eGFP or FOXM1mut-eGFP, as shown in Figure 4-10 (e-f).

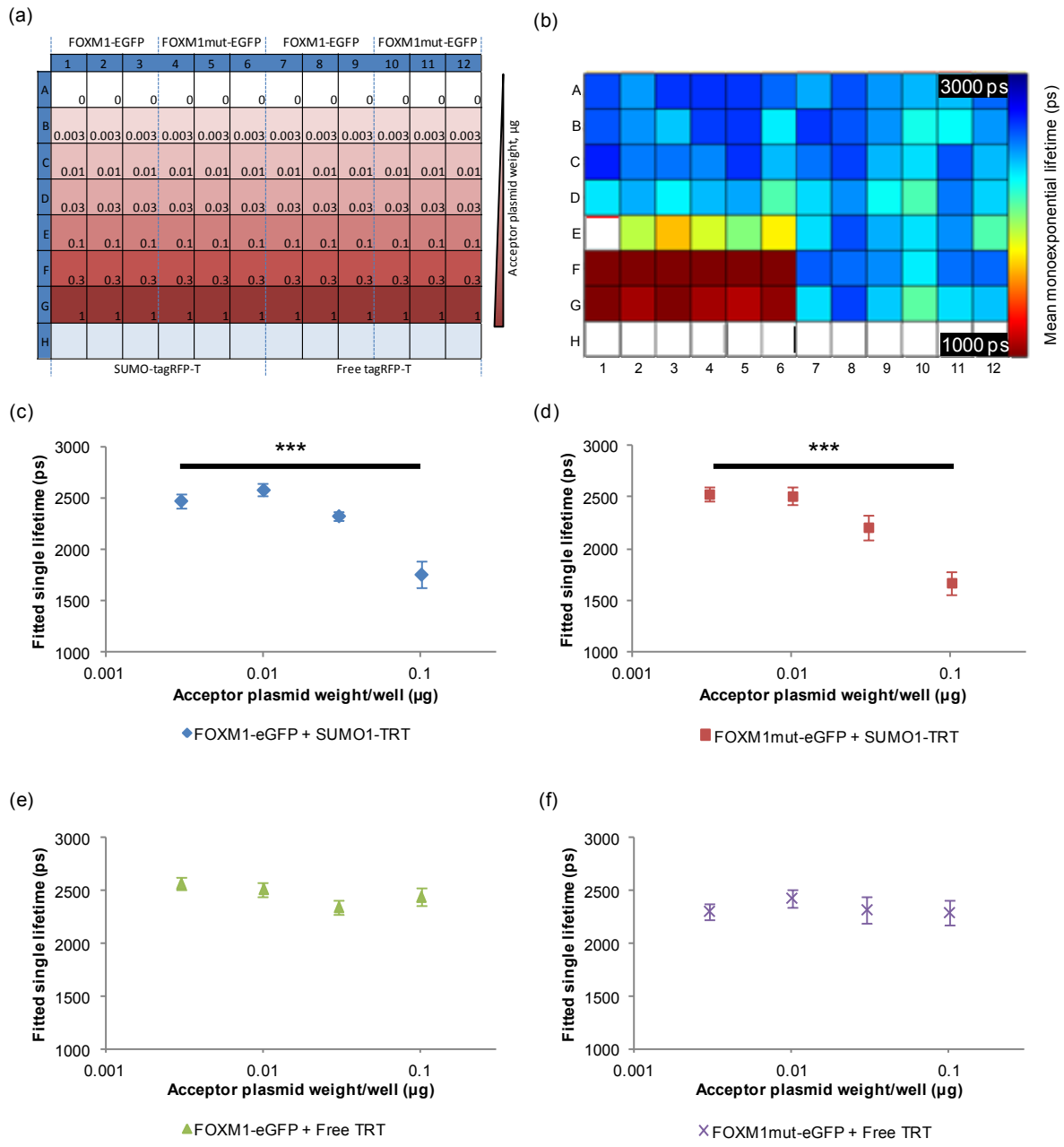

Figure 4-10 Results of experiment showing effects of increasing SUMO1-TRT expression in the absence of doxorubicin treatment.

(a) Plate layout, condensed from those outlined in Figure 4-9. (b) Plate map showing lifetime results of a monoexponential fit to data, averaged over fields of view per well. (c) Plot showing monoexponential fitted lifetime values based on FOXM1-eGFP signal against transfected SUMO1-TRT plasmid weight. (d) Plot showing monoexponential fitted lifetime values based on FOXM1mut-eGFP signal against transfected SUMO1-TRT plasmid weight. (e) Plot showing monoexponential fitted lifetime values based on FOXM1-eGFP signal against transfected free TRT plasmid weight. (f) Plot showing monoexponential fitted lifetime values based on FOXM1mut-eGFP signal against transfected free TRT plasmid weight. Error bars are shown as standard errors over repeat wells. Differences between conditions were assessed using Tukey's test, and are not significant unless otherwise marked.

Discussion

In parallel with work by Mesayamas Kongsema in the Department of Cancer and Surgery, we sought to identify the optimal transfection conditions that would result in sufficiently high expression of the

fluorescent FOXM1 constructs that robust FLIM data might be acquired on a reasonable time scale for high content analysis without overexpression of the transcription factor causing cells to die. In the course of the project it was concluded that transfecting 0.1 μg of donor construct plasmid per well with a transfection reagent:plasmid ratio of 2:1 (volume:weight) would reliably result in useful expression of the donor construct. Phase contrast imaging was typically used to ensure that cells did not appear to be damaged by overexpressing the transcription factor prior to carrying out experiments. It should also be noted that different transfection reagents (Lipofectamine, Fugene 6) and methods (electroporation) were tried in the course of the project, but in no case was there sufficient improvement in expression level or cell health to justify changing the established protocol using XtremeGene HP.

To address potential artefacts arising from non-specific interactions between donor fluorescent constructs (FOXM1-eGFP and FOXM1mut-eGFP) and acceptor fluorescent constructs, an experiment was undertaken in which the acceptor plasmid weight was varied, the results of which are presented in Figure 4-10. The presence of a large amount of fluorescent debris when SUMO1-TRT is transfected at concentrations greater than 0.1 μg/well indicates that high levels of expression of this construct is deleterious to cell health. The absence of this effect when free TRT is cotransfected at the same concentrations indicates that cytotoxity is associated with increased SUMO1-TRT plasmid weight, rather than with increased transfection reagent concentration. Lifetime was found to decrease significantly (Tukey's test) for wells transfected with 0.1 μg SUMO1-TRT for both wild type and mutated forms of FOXM1-eGFP. The absence of such a trend when free TRT was expressed provides evidence that there is no significant non-specific interaction between the two fluorescent proteins in this system. The fact that increasing SUMO1-TRT plasmid weight results in decreased lifetime when the construct is cotransfected with both the wild type and mutated FOXM1 constructs suggests that a non-specific or alternative association is occurring independently of the presence of the ΨKxE SUMOylation consensus site, perhaps indicating that SIM interactions are playing a role.

4.1.5 FOXM1-SUMOylation in response to anthracycline treatment time course

In parallel with biochemical and colocalisation assays relating to FOXM1 SUMOylation conducted in the Department of Surgery and Cancer, Imperial College London, HCA FLIM-FRET experiments were planned to investigate FOXM1-SUMOylation in the MCF7 breast cancer cell line in response to a time course of anthracycline treatment. Two plates of data acquired at different points during the course of the project are presented here; both datasets were acquired from live cells, and both experiments were performed using low passage number cells. Differences between the two plates relate to development of the instrument and software in the intervening period, and to the change in acceptor transfection protocol to reflect the findings of the optimisation studies explained above.

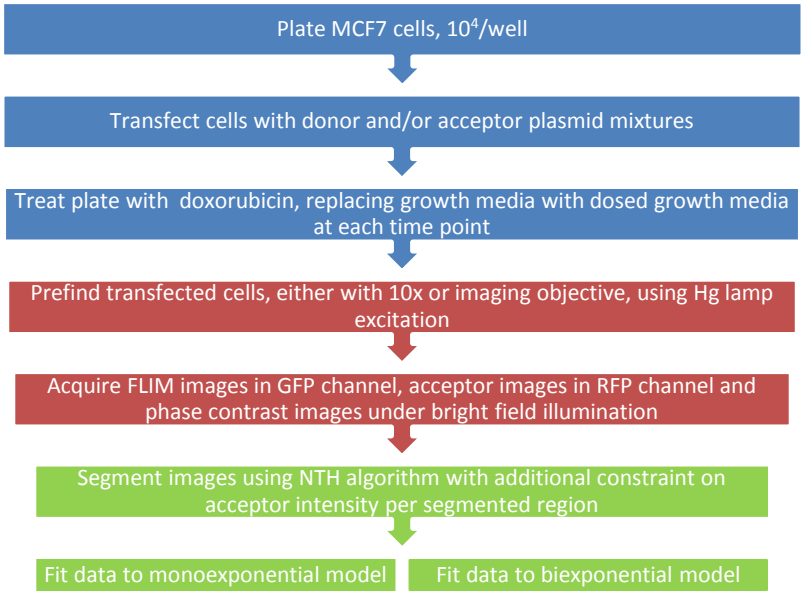

Figure 4-11 Flow chart summarizing the methods used for generation and analysis of FOXM1-SUMOylation assay samples.
Further details are found in the remainder of section 4.1.5.

Sample preparation

Plate 1: Cells were seeded at a density of 10^4 per well on Greiner μClear plates in standard growth media. Particular care was taken to ensure a single cell suspension, and the plate was tilted vigorously to ensure that cells were distributed evenly within wells. The sample was incubated for 24 h at 37°C. Based on results from experiments in the preceding section, transfections were carried out using XtremeGene HP according to the manufacturer's instructions with a transfection reagent:plasmid ratio of 2:1 (volume:weight). Donor constructs (FOXM1-eGFP, negative control FOXM1mut-eGFP or free eGFP) were transfected at 0.1 μg per well; SUMO1-TRT was transfected at 0.025 μg per well. The layout of donor-only and cotransfected wells within the plate is illustrated in Figure 4-12 (a-b). Cells were incubated with transfection mixtures for 24 h, after which media was replaced. Wells designated for 24 h treatment were treated at this point with 0.1 μM doxorubicin, freshly diluted in growth media from stock (3400 mM). 3 hours later (21 hours prior to end point), media in all wells was again replaced; this time, media

supplemented with doxorubicin was used for both 24 h and 21 h treatment wells. This process was repeated for 8 h, 6 h, 4 h and 2 h treatment wells (16 h, 18 h, 20 h and 22 h after starting treatment, respectively). The layout of doxorubicin-treated wells is illustrated in Figure 4-12 (c). Two hours after the final treatment was administered, all media was removed and replaced with glucose-supplemented HBSS at 37°C. The sample was then transferred to the microscope incubator.

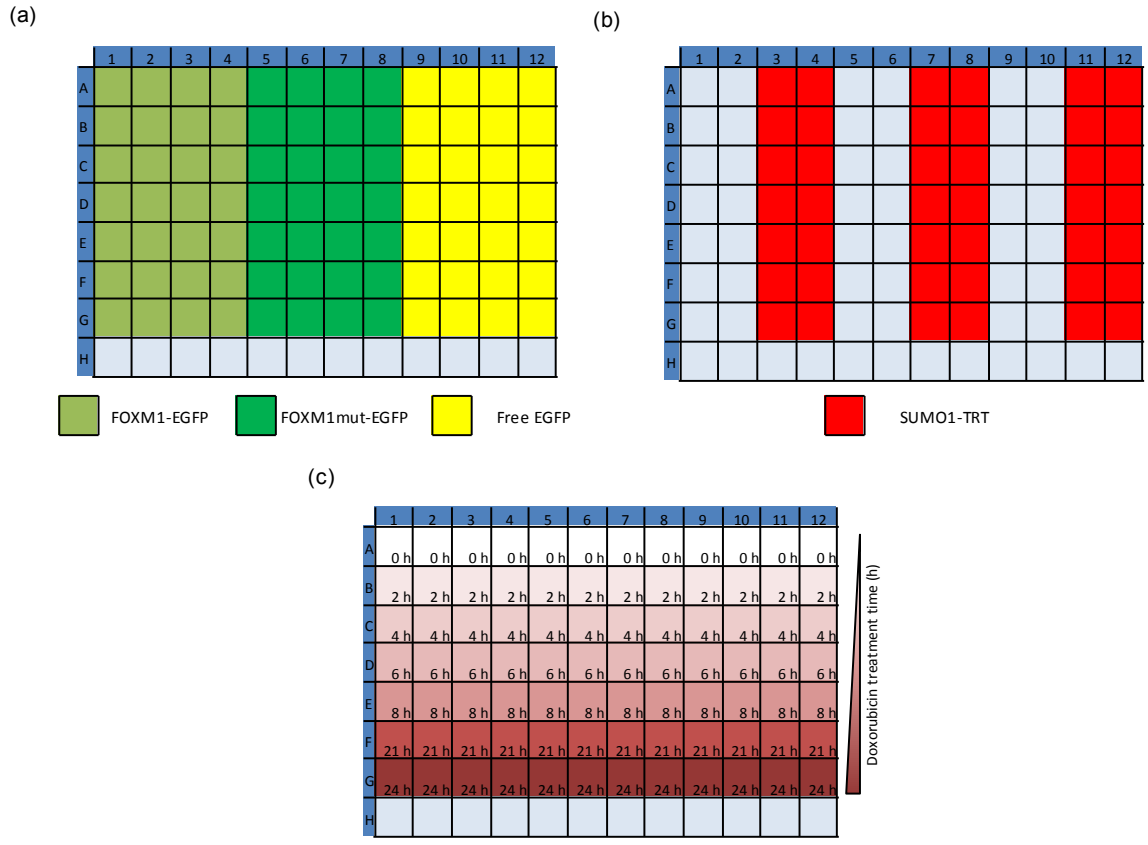

Figure 4-12 Plating strategy (plate 1) for experiment investigating FOXM1-SUMOylation in response to doxorubicin treatment.
(a) Donor construct layout. (b) Acceptor construct layout. (c) Doxorubicin treatment time layout.

Plate 2: Cells were seeded at a density of 10^4 per well on Greiner μClear plates in standard growth media. Particular care was taken to ensure a single cell suspension, and the plate was tilted vigorously to ensure that cells were distributed evenly within wells. The sample was incubated for 24 h at 37°C. Based on results from experiments in the preceding section, transfections were carried out using XtremeGene HP according to the manufacturer's instructions with a transfection reagent:plasmid ratio of 2:1 (volume:weight). Donor constructs (FOXM1-eGFP and negative control FOXM1mut-eGFP) were transfected at 0.1 μg per well; SUMO1-TRT was transfected at 0.01 μg per well. The layout of donor-only and cotransfected wells within the plate is illustrated in Figure 4-13 (a-b). Cells were incubated with transfection mixtures for 24 h, after which media was replaced. Wells designated for 24 h treatment were treated at this point with 0.1 μM or 1.0 μM doxorubicin, freshly diluted in growth media from stock (3400 mM). 16 hours later (8 hours prior to end point), media in all wells was again replaced; this time, media

supplemented with doxorubicin was used for both 24 h and 8 h treatment wells. This process was repeated for 6 h and 3 h treatment wells, 18 h and 21 h respectively after starting treatment. The layout of doxorubicin-treated wells is illustrated in Figure 4-13 (c-d). After another 6 h, all media was removed and replaced with glucose-supplemented HBSS at 37°C. The sample was then transferred to the microscope incubator.

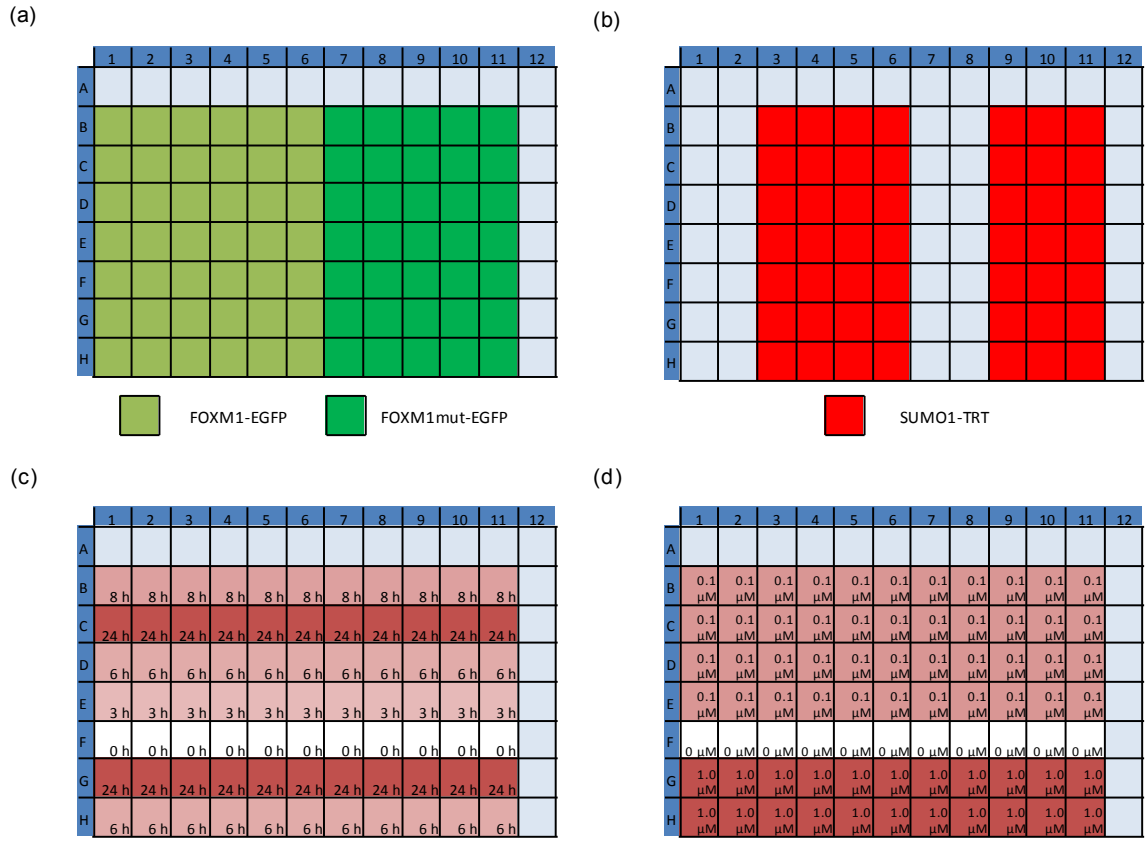

Figure 4-13 Plating strategy (plate 2) for experiment investigating FOXM1-SUMOylation in response to doxorubicin treatment.
(a) Donor construct layout. (b) Acceptor construct layout. (c) Doxorubicin treatment time layout. (d) Doxorubicin treatment dose layout.

Image acquisition and analysis

Plate 1: Fields of view that were sufficiently populated with cells expressing donor constructs were identified using a coverage-based prefind method with a 40x long working distance objective (LUCPlanFLN 40x/0.6) and Hg lamp illumination through the GFP filter cube (excitation: 472/30 nm, dichroic: 495 nm, emission: 520/35 nm). Four fields of view per well were identified by this method. Automated FLIM data was acquired with the same long working distance 40x objective in the same spectral channel across 7 gates, at each of which the camera was exposed for 0.8 s. Unlike all other work in this section, this experiment was performed using an HRI that supported wide gates; here, 3000 ps gates were used. SUMO1-TRT was imaged in the spectral channel defined by the "red" filter cube (excitation: 545/30 nm, dichroic: 570 nm, emission: 610/75 nm); a single exposure of 0.02 s was acquired

at a single time delay chosen to lie at the peak of the decay profile. In total, the automated acquisition took 72 minutes. A time-varying background decay was measured from a well of untransfected cells using the same acquisition parameters as the automated experiment, and a reference decay profile was obtained from a well containing 25 μM Erythrosine B.

Plate 2: Cells expressing donor constructs were identified using the low magnification prefind algorithm with a 10x objective under Hg lamp illumination using the GFP filter cube (excitation: 472/30 nm, dichroic: 495 nm, emission: 520/35 nm). 10 fields of view per well were sought in 77 wells; the prefind operation took 24.8 minutes to complete, finding a total of 747 fields of view. Automated FLIM data was acquired using a 40x long working distance objective (LUCPlanFLN 40x/0.6) in the same spectral channel across 7 gates, at each of which 3 frames integrated for 0.25 s each were summed. SUMO1-TRT was imaged in the spectral channel defined by the "red" filter cube (excitation: 545/30 nm, dichroic: 570 nm, emission: 610/75 nm); 3 frames integrated for 0.05 s each were summed at a single time delay chosen to lie at the peak of the decay profile. Phase contrast images were also acquired as part of the automated acquisition sequence. In total, the automated acquisition took 259 minutes. A time-varying background decay was measured from a well of untransfected cells using the same acquisition parameters as the automated experiment, and a reference decay profile was obtained from a well containing 20 μM Erythrosine B.

NTH segmentation was applied to integrated donor intensity images from both plates, using parameters outlined in Table 4-2. In addition, for wells in which acceptor constructs were cotransfected, an additional constraint was imposed such that the minimum level of acceptor upper quartile per segmented region should be 500 DN in order to exclude cells with low expression of SUMO1-TRT from analysis. Wells treated with 1 μM doxorubicin were omitted from analysis due to the impact of fluorescent cell debris present after 24 hours of treatment at this dose.

Parameter	Value
Scale	40
Relative background scale	2
Threshold	0.5
Smoothing	5
Minimum area	1000

Table 4-2 NTH segmentation parameters for automated segmentation of MCF7 expressing FOXM1-eGFP or FOXM1mut-eGFP.

In the first instance, a monoexponential model was fit to data, using the measured time-varying background and reference decay profiles. Subsequently, the global fitting capabilities of *FLIMfit* were used to fit a biexponential model to data, fitting globally by donor construct.

Results

Plate 1: Lifetimes resulting from a monoexponential fit to data acquired from the first experimental plate are given in Figure 4-14. Figure 4-14 (a) illustrates the distribution of monoexponential lifetimes averaged

per well across fitted wells, whilst Figure 4-14 (b) is included to provide an insight into the heterogeneity of measured cell lifetimes within time points for FOXM1-eGFP + SUMO-TRT wells. Plots of donor lifetime against doxorubicin treatment time for each transfection condition are presented in Figure 4-14 (c-f). Significance of deviations from zero treatment time point are assessed using Dunnett's test: only in the case when wild type FOXM1-eGFP is cotransfected with SUMO1-TRT (Figure 4-14 (d)) is there a significant deviation from the zero time point with treatment. In this case, the fitted lifetime is found to decrease significantly for treatments between 6 and 8 h, followed by a return towards the zero time point value by 21 h post-treatment.

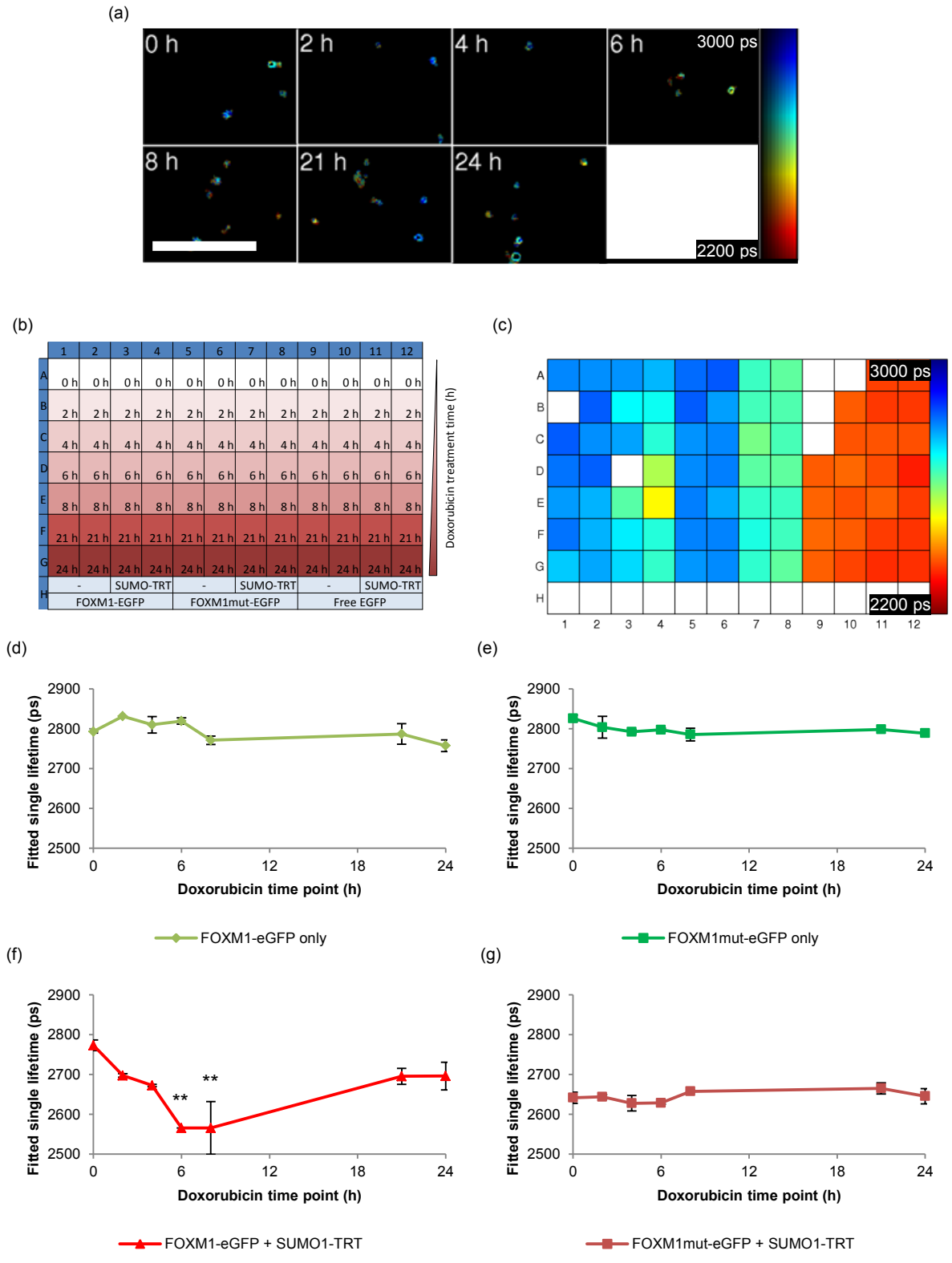

Figure 4-14 Results of monoexponential fit to data from the first plate experiment designed to investigate FOXM1-SUMOylation in response to doxorubicin treatment.

(Figure on previous page) (a) Gallery image from *FLIMfit* illustrating heterogeneity of lifetimes within doses for cells expressing both FOXM1-eGFP and SUMO1-TRT constructs. Scale bar 200 μm. (b) Plate map showing layout of conditions, summarising Figure 4-12. (c) Plate map showing lifetime results of a monoexponential fit to data, averaged over fields of view per well. (d) Fitted lifetime plotted against doxorubicin treatment time in cells expressing FOXM1-eGFP only. (e) Fitted lifetime plotted against doxorubicin treatment time in cells expressing FOXM1mut-eGFP only. (f) Fitted lifetime plotted against doxorubicin treatment time in cells expressing FOXM1-eGFP and SUMO1-TRT. (g) Fitted lifetime plotted against doxorubicin treatment time in cells expressing FOXM1mut-eGFP and SUMO1-TRT. All error bars show standard errors across repeat wells. Stars show significance of difference from zero time point condition, established using Dunnett's test.

Globally fitting all FOXM1-eGFP wells and all FOXM1mut-eGFP wells separately was found to yield lifetime parameters outlined in Table 4-3. Figure 4-15 shows the corresponding short ("FRETting") lifetime component contributions for wells containing both donor and acceptor constructs. Once again, significant deviation from the untreated case is only seen in the wild type FOXM1-eGFP case at 6 h and 8 h doxorubicin treatment (Dunnett's test).

Donor construct	FOXM1-eGFP	FOXM1mut-eGFP
τ_1	2770	2800
τ_2	2034	2134
Implied FRET efficiency, E	0.27	0.24

Table 4-3 Globally fit lifetime parameters from bioexponential model fit to data from the first plate experiment designed to investigate FOXM1-SUMOylation in response to doxorubicin treatment.

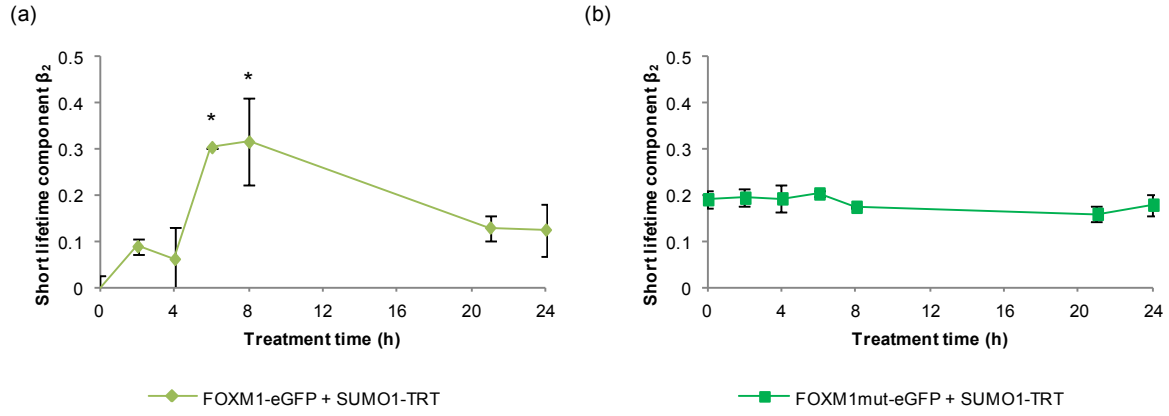

Figure 4-15 Results of a global fit of a biexponential model to data from the first plate experiment designed to investigate FOXM1-SUMOylation in response to doxorubicin treatment.
(a) Fitted short lifetime contribution plotted against doxorubicin treatment time in cells expressing FOXM1-eGFP and SUMO1-TRT. (b) Fitted short lifetime contribution plotted against doxorubicin treatment time in cells expressing FOXM1mut-eGFP and SUMO1-TRT. Error bars represent standard errors over repeat wells; significance assessed using Dunnett's test.

Plate 2: For comparison, lifetimes resulting from a monoexponential fit to data acquired from the second experimental plate are given in Figure 4-16. Figure 4-16 (a) illustrates the distribution of monoexponential lifetimes averaged per well across fitted wells, whilst Figure 4-16 (b) is included to provide an insight into the heterogeneity of measured cell lifetimes within time points for FOXM1-eGFP + SUMO-TRT wells. Plots of donor lifetime against doxorubicin treatment time for each transfection condition are presented in Figure 4-16 (c-f). The significance of deviations from zero treatment time point is assessed using Dunnett's test: only in the case when wild type FOXM1-eGFP is cotransfected with SUMO1-TRT (Figure 4-16 (d)) is there a significant deviation from the zero time point with treatment. In this case,

fitted lifetime is found to decrease significantly for treatments between 3 and 8 h, followed by a return towards the zero time point value by 24 h post-treatment.

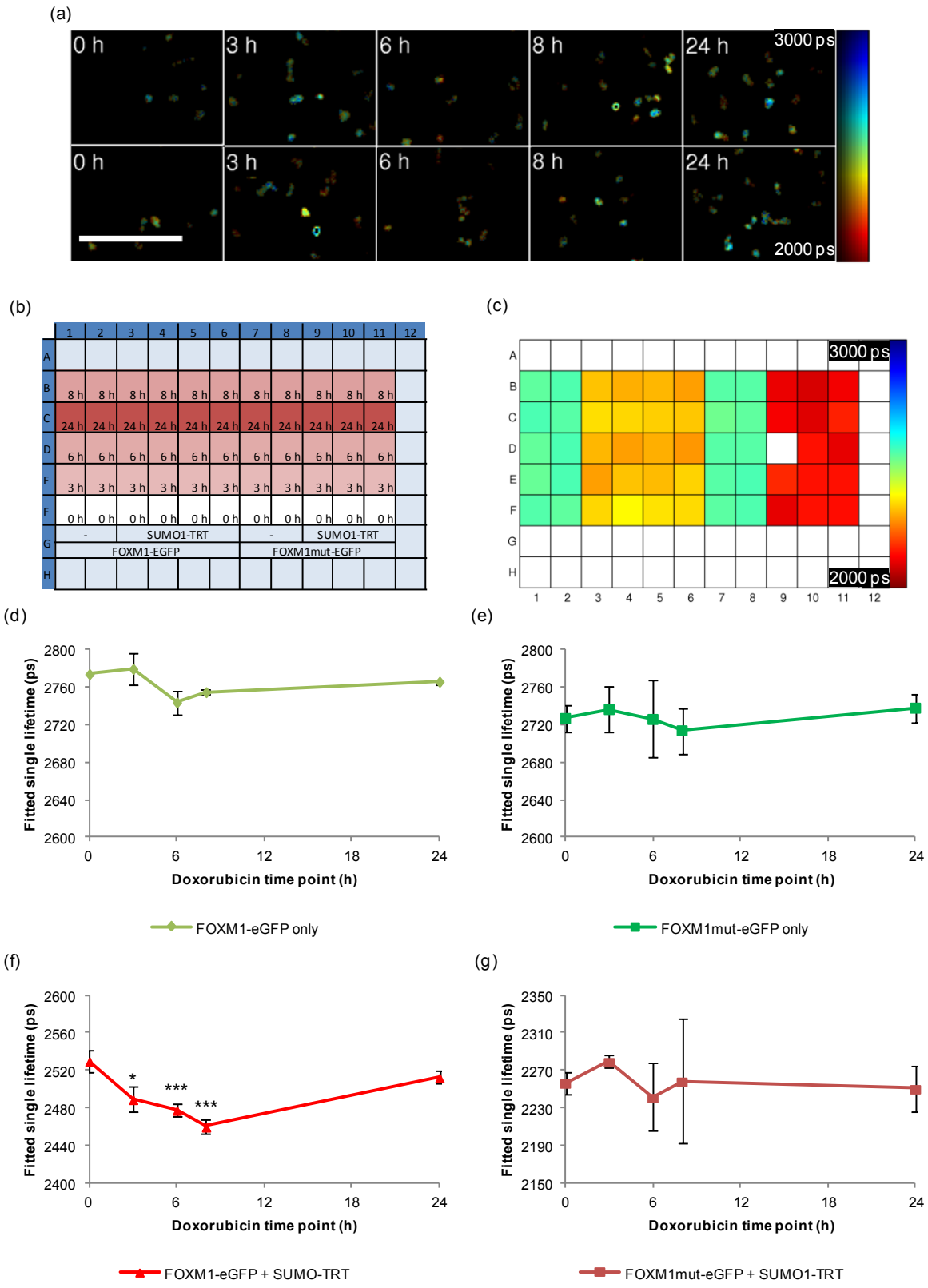

Figure 4-16 Results of monoexponential fit to data from the second plate experiment designed to investigate FOXM1-SUMOylation in response to doxorubicin treatment.

(Figure on previous page) (a) Gallery image from *FLIMfit* illustrating heterogeneity of lifetimes within doses for cells expressing both FOXM1-eGFP and SUMO1-TRT constructs. Scale bar 200 μm. (b) Plate map showing layout of conditions, summarising Figure 4-13. (c) Plate map showing lifetime results of a monoexponential fit to data, averaged over fields of view per well. (c) Fitted lifetime plotted against doxorubicin treatment time in cells expressing FOXM1-eGFP only. (d) Fitted lifetime plotted against doxorubicin treatment time in cells expressing FOXM1mut-eGFP only. (e) Fitted lifetime plotted against doxorubicin treatment time in cells expressing FOXM1-eGFP and SUMO1-TRT. (f) Fitted lifetime plotted against doxorubicin treatment time in cells expressing FOXM1mut-eGFP and SUMO1-TRT. All error bars show standard errors across repeat wells. Stars show significance of difference from zero time point condition, established using Dunnett's test.

Discussion

As a result of these high content experiments, some doubt is cast on the magnitude of the changes observed in the preliminary experiment carried out on the Leica SP5 TCSPC system (section 4.1.2). In particular, given that the lifetimes associated with weak cell autofluorescence in Figure 4-8 are not dissimilar to those measured for cells analysed in Figure 4-6 (b) and (c), it is possible that cells that were for some reason more autofluorescent than neighbours were misidentified as expressing the donor construct due to the non-optimal Hg lamp filter set present in the SP5 system for manual identification of imaging targets.

It is well established that GFP and eGFP exhibit altered lifetime dependent on environmental factors including pH[210], refractive index[211] and binding to other cellular proteins[212], and that this can lead to different measured values for intracellular eGFP lifetimes when the FP is included in protein constructs. Nevertheless, it is notable in all experiments undertaken using the FOXM1-eGFP constructs that donor-only lifetime tends to fall towards the upper end of the range of values that might be considered reasonable. To ensure that this long measured lifetime was not an artefact of the instrument or of the biological protocol, wells in the first measured doxorubicin time course plate were transfected with free eGFP in place of either of the FOXM1 constructs, along with SUMO1-TRT where appropriate. The lifetimes evident in the final four columns of the monoexponential FLIM plate map shown in Figure 4-14 (c) provide evidence that the instrument is returning the correct lifetime values: the mean lifetime across these wells is 2367 ps, which is in a more familiar range for eGFP lifetime.

It must be noted that changes made to the instrument and acquisition software in the intervening time between the acquisitions presented in this section preclude a direct comparison between absolute lifetime values returned from the two plates. Nevertheless, trends in lifetime are reflected between the plates, with the recorded FLIM data from wells in which wild type FOXM1-eGFP is cotransfected with SUMO-TRT serving to back up expectations based on biochemical experiments; that is, there is significant decrease in measured lifetime when cells have been exposed to doxorubicin treatment for between 3 and 8 hours, which is lost at longer treatment times. CoIP assays conducted in parallel have confirmed that FOXM1-SUMOylation occurs by 6 hours, resulting in the formation of higher-order complexes[188]. SUMOylation of FOXM1 has been shown to accelerate degradation of the transcription factor[188]; this process of degradation may explain the decrease in FOXM1-SUMO1 interaction evident at 21 and 24 hour time points in the FLIM-FRET assays. Furthermore, caspase-mediated cleavage of the N-terminus of FOXM1[213] may act to reduce FRET signal between the donor and acceptor fluorescent proteins if

apoptosis is induced by anthracycline treatment over these timescales[168]. The results of a biexponential fit to the lifetime data from plate 1 presented in Table 4-3 and Figure 4-15 must be interpreted with caution: given that wild-type FOXM1 might be SUMOylated on multiple sites and that both wild-type and mutated FOXM1 may interact with the acceptor construct via multiple SUMO1 interaction motifs, leading to more complex decay profiles originating from a range of possible FRET efficiencies for interacting constructs.

The changes in intracellular localisation of FOXM1-eGFP upon SUMOylation in response to anthracycline treatment that were observed in the colocalisation studies carried out in the Department of Surgery and Cancer were not evident in this study. It is possible that the prefind algorithm may skew results by preferentially selecting brighter cells associated with higher concentrations of FOXM1-eGFP found in the nucleus rather than the more diffuse signal exhibited by lower concentrations of FOX1-eGFP in the cytoplasm.

In Figure 4-14 (b) and Figure 4-16 (b), which present FLIM fields of view at different treatment time points from wells in which FOXM1-eGFP and SUMO1-TRT have been cotransfected for each of the two plates, it is evident that in both cases there was significant heterogeneity in fitted lifetimes across cells within fields of view as well as within treatment conditions. That the data may be resolved to the corresponding plots in Figure 4-14 (e) and Figure 4-16 (e) respectively illustrates the benefits of increasing sample numbers to generate statistically significant results in the presence of biological noise, noting that this required less than five hours of imaging time (747 fields of view).

The analysis of the interactions occurring between FOXM1 and SUMO1 using FLIM-FRET becomes even more challenging when the possible role played by non-covalent SUMO-interacting motifs is considered. In both plates the non-SUMOylatable mutant FOXM1 construct does not show a change in lifetime when DNA damage is incurred by anthracycline treatment across a time course, as expected. However, a higher base line level of interaction between mutated FOXM1 and SUMO1 compared to wild-type FOXM1 and SUMO1 is suggested by the observed difference between conditions in which FOXM1mut-eGFP is transfected with and without SUMO1-TRT. This is particularly evident comparing columns 7 and 8 to columns 9-11 in Figure 4-16 (c). It is seems likely, based on these results and those shown in Figure 4-10 above, that there is some DNA damage response-independent mechanism by which SUMO-associated proteins – in this case, SUMO1-TRT – might be recruited to SIM sites on FOXM1. It is, however, not obvious why the FOXM1mut construct should be more susceptible than the wild-type protein to such a process. One hypothesis is that SIM-mediated interactions occur more often when cells have been exposed to stresses; if impurities in the FOXM1mut-eGFP plasmid cause the transfection of this construct to be more deleterious to cell health than transfection of the wild type construct, this might go some way to explaining the results seen across the analyses outlined in the previous section.

4.1.6 Summary

The investigation of FOXM1 SUMOylation by FLIM-FRET proved to be a challenging project, due mainly to difficulties in establishing a reliable protocol that provided sufficient signal from the donor constructs without causing the living cells undue harm. The complicated nature of the interaction of FOXM1 with SUMO, and specifically the presence of interaction sites other than those removed in the "non-SUMOylatable" FOXM15X(K>R) construct, contribute to making the interpretation of FLIM-FRET results relating to this biological system more challenging than in many other FRET experiments. The capability of the automated FLIM plate reader to provide statistically significant results was key to the eventual success of the project, as was the parallel development of cell prefind algorithms that enables even samples that fail to express constructs well to yield useful data. The ability to acquire images in multiple spectral channels in the course of an automated acquisition allows potential pitfalls linked to unfavourable acceptor stoichiometry to be avoided and the number of cells assayed in the duration of a practical experiment overcomes the noise inherent in the biological signal, permitting statistically robust conclusions to be drawn.

4.1.7 Future work

To further complement biochemical assays carried out in the Department of Surgery and Cancer, it might be instructive to replicate the assays presented here in cell lines such as MCF7-Dox^R that exhibit resistance to anthracycline treatments. Such experiments were in fact attempted towards the end of the project. Unfortunately, the resistant cell line is more challenging to manipulate, and it is significantly more difficult to attain useful levels of exogenous fluorescent construct expression in these cells. Therefore, further work would be needed to optimise the transfection of FOXM1-eGFP constructs in 96 well plates for these cells before this avenue could be explored.

A further alternative that would require only minimal alteration to existing protocols would be to extend the study of FOXM1 SUMOylation to DNA damage-causing drugs beyond the anthracyclines: SUMOylation in response to treatment with cisplatin and taxanes could be investigated, and investigations of the dynamics of FOXM1 SUMOylation following DNA damage induced by exposure to ultraviolet or radioactive sources would also be achievable. Since FOXM1 has also been shown to be SUMOylated in response to mitotic checkpoint drugs such as nocodazole, this would be another class of compounds for which elucidation of FOXM1 SUMOylation dynamics might prove useful.

Finally, the role played by FOXM1 SUMOylation in the wider context of DNA damage response signalling pathways might be investigated. Fluorescent ubiquitin and RNF168 constructs are easily accessible within the lab; preliminary experiments show that RNF168-eGFP is significantly easier to transfect into MCF7 cells than FOXM1-eGFP, forming bright, punctuate loci in the nucleus. Since many constructs, including those in our lab, can be prepared as FRET pairs with different fluorescent proteins acting as FRET donors/acceptors, it should be possible to prepare constructs that could be measured in different spectral regions and in so doing introduce the option to multiplex more than one signalling

event in the DNA damage response pathway. Thus the dynamic interplay between interaction events associated with DDR could be read out on the automated FLIM plate reader.

In parallel with work to further elucidate the dynamics of FOXM1 SUMOylation, it is intended that FLIM-FRET be employed to investigate autoinhibition of FOXM1 activity by the N-terminal repressor domain in response to SUMOylation, and in particular the hypothesis that the activity of the transactivation domain is reduced by the N-terminal domain looping. By cloning an acceptor fluorophore to the C-terminus of FOXM1, the dynamics of conformational changes in the transcription factor that may be associated with inhibition of the C-terminal transactivation domain will be accessible, with and without overexpression of SUMO1 or Ubc9, in transcription factors with and without mutations of SUMO consensus binding sites.

4.2 RASSF family-MST1 interaction screen

One of the original goals for the automated FLIM plate reader was to screen libraries of proteins for interaction pairs using FLIM-FRET. In conjunction with Jia Chan and Dr. Matilda Katan at the Department of Structural and Molecular Biology, University College London, and Dr. Anca Margineanu at Imperial College London, a project was undertaken to show the potential of the instrument in this area. A family of interaction candidates, the RASSF family proteins, were screened against MST1. This work acts to confirm biochemical experiments performed by Jia Chan in the Department of Structural and Molecular Biology at UCL. In addition to identifying the proteins that interact with MST1, some degree of quantitative data on binding affinities can also be gleaned from the FLIM measurements.

4.2.1 MST1 and the RASSF-family proteins: biological context

Ras-Association Domain (RASSF) family proteins are implicated in a range of cellular processes including regulation of apoptosis, microtubule stabilisation, DNA damage response and tumour suppression[214]. The majority of RASSF family proteins are silenced in tumours, with the exception of RASSF7, which has been shown to be upregulated in certain malignancies[215]. The regulatory activity of RASSF proteins is achieved through their role as scaffold proteins – though they lack any enzymatic activity, such proteins act by bringing other proteins together in order that they might fulfil their functions. All RASSF proteins share the Ras association (RA) domain through which they can interact with K-Ras or Ran[216]. Beyond this, however, the RASSF family has significant diversity in both structure and function. RASSF1A and 5 contain the protein kinase C conserved region, or C1 domain, which has been shown to mediate Ras-RASSF interaction by occlusion of the RA domain. The classical RASSF proteins 1-6 exhibit the Salvador-RASSF-Hippo (SARAH) domain. This domain is shared with the mammalian sterile 20-like proteins (MST1/2), and mediates the heterodimerisation of RASSFs with MST1 or other classical family members[217]. The N-terminal RASSF proteins lack the SARAH domain and instead have coiled-coil or unstructured domains at the C terminal end. RASSF1 proteins have a site that can be phosphorylated by ATM, which serves to activate them[216]. The different structures of RASSF family proteins are summarised in Figure 4-17.

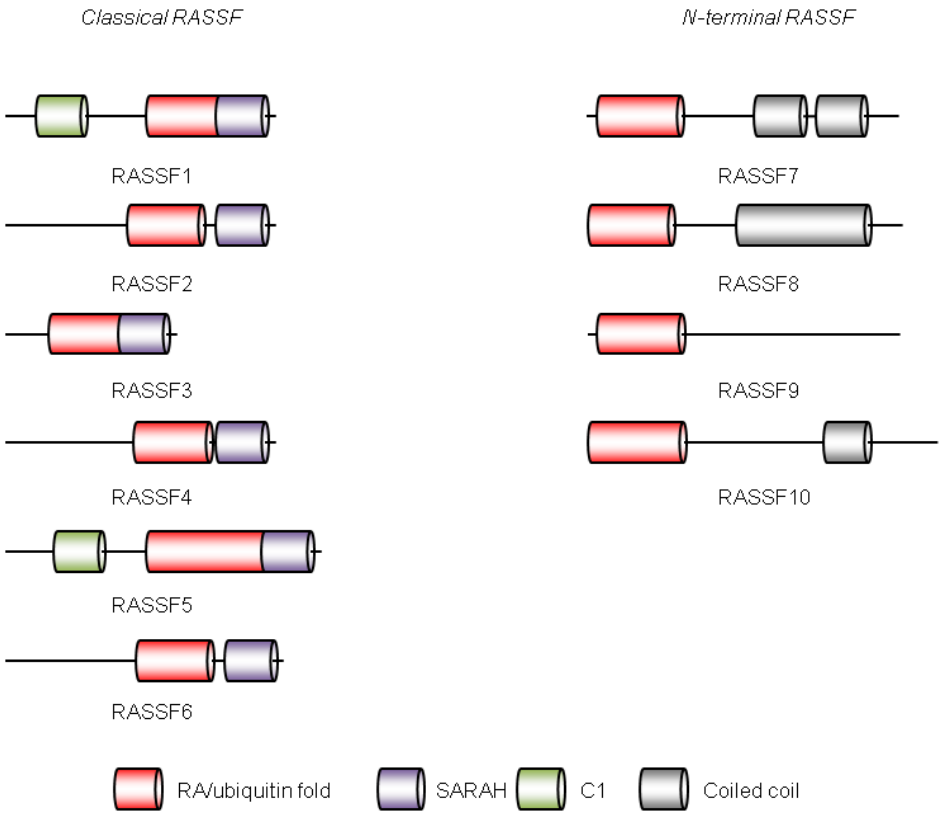

Figure 4-17 An overview of RASSF family protein structures.
Adapted from Sherwood et al.[215]

Mammalian sterile 20-like kinase (MST) proteins promote apoptosis and act as proliferation and tumour suppressors in conjunction with RASSF proteins. MST1 has been shown to regulate activity of the FOXO transcription factors, interact with histones H2B and H2AX, and effect the activity of the "guardian of the genome", p53[218].

Based purely on the structures of the RASSF proteins summarised in Figure 4-17 above, it is expected that the classical RASSF proteins should interact with MST1 via dimerization of the SARAH domains, whilst the N-terminal RASSF proteins will not bind to MST1. We sought to test this hypothesis using the FLIM plate reader to image cells transfected with genetically encoded fluorescent fusion RASSF and MST1 proteins, and in so doing illustrate the strengths of high content FLIM-FRET imaging in the context of protein-protein interaction screening. The potential effect of overexpression of exogenous KRas in modulating MST1 binding to RASSF-family proteins was also investigated.

4.2.2 Sample preparation

Samples were prepared by Dr Anca Margineanu and Jia Chan. Following previous optimisation experiments, two plates were planned, with 30 different transfection conditions in each plate. In the first plate, each RASSF family member-eGFP plasmid was transfected alone (rows A and H), with full length-MST1-mCherry (rows B-D) and with both full length-MST1-mCherry and unlabelled KRas (rows E-G).

In the second plate, each RASSF-eGFP was again transfected alone (rows A and H), with a truncated SARAH-mCherry acceptor construct (rows B-D) and a SARAH-deficient MST1 mutant, denoted MST1Δ-mCherry (rows E-G). Schematic representation of the constructs used is found in Figure 4-18; full plate layouts are illustrated in Figure 4-19.

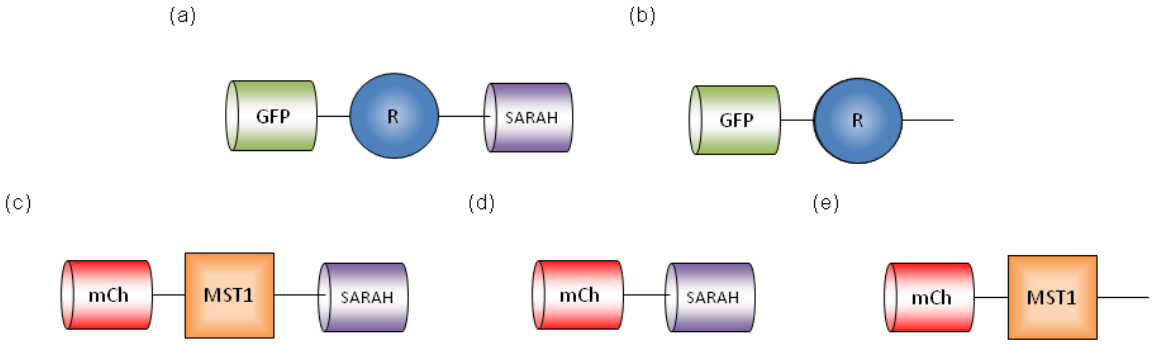

Figure 4-18 Schematic representation of the fluorescent constructs used in the RASSF-MST1 interaction screen.
(a) Classical RASSF-eGFP (RASSF1-6); (b) N-terminal RASSF-eGFP (RASSF7-10); (c) Full length MST1-mCherry; (d) Truncated SARAH-mCherry; (e) MST1Δ-mCherry. R represents subunits of RASSF family proteins other than the SARAH domain.

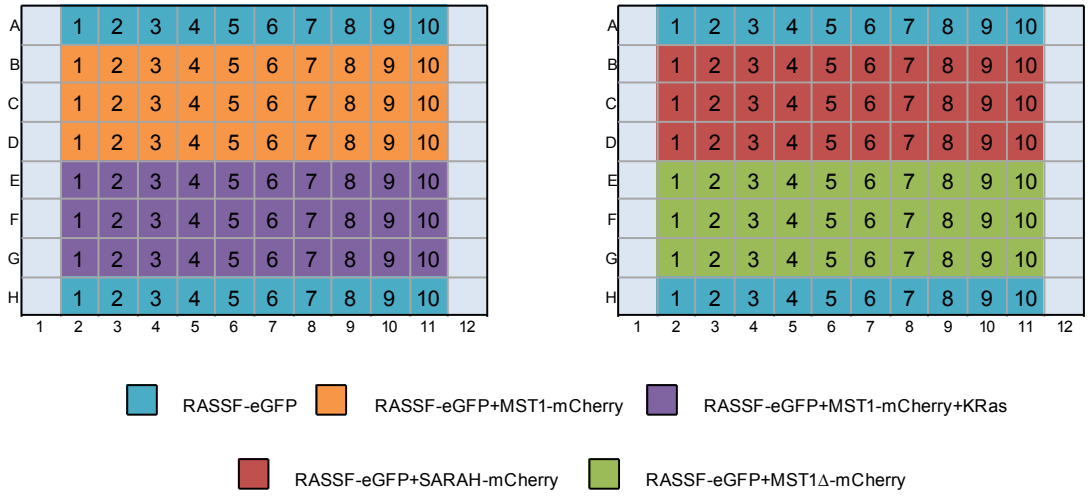

Figure 4-19 Plate layouts for RASSF-family MST1 interaction screen experiments
Numbers in each well indicate RASSF family member.

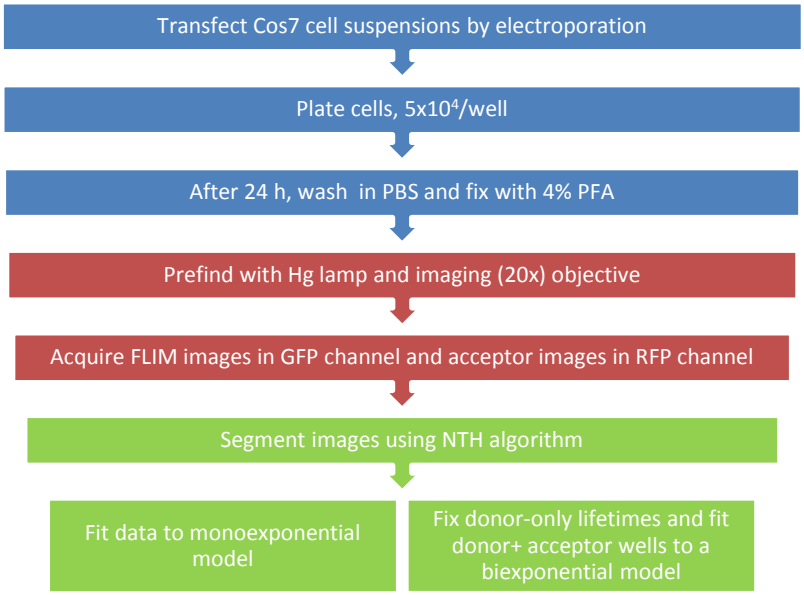

Figure 4-20 Flow chart summarizing the methods used for generation and analysis of RASSF family interaction screen assay samples.
Further details are found in sections 4.2.2 and 4.2.3.

For both plates, transfections were carried out over the course of an afternoon by electroporation (Nucleofector 2b, Lonza), Cos7 cells having previously been expanded to sufficient numbers over a matter of weeks in T175 flasks. Cells were suspended in 100 µl of electroporation buffer (see Table 4-4 for formulation) in batches of 1×10^6 cells, after which 4 µg of each plasmid was added to each cell suspension. Transfection mixtures were transferred to electroporation cuvettes (Mirus Bio) and electroporated using standard settings for the Cos7 cell line. Following transfection, cells were plated at 5×10^4 cells per well of a 96 well plate and incubated in standard growth media for 24 hours. Cells were washed and fixed in 4% paraformaldehyde, then washed again and submerged in PBS. Plates were transferred to the FLIM plate reader, where imaging was performed at room temperature.

Component	Concentration
MilliQ	
KCl	8 mM
NaCl	8 mM
$MgSO_4$	0.88 mM
Na_2HPO_4	2.97 mM
NaH_2PO_4	1.06 mM

Table 4-4 Table showing constituents of buffer for electroporation of Cos7 cells.

4.2.3 Image acquisition and analysis

To maximise the number of cells acquired per field of view, a 20x objective (Olympus UPlanFl 20x/0.5) was chosen to image ten fields of view per well; a prefind was performed using the imaging objective and mercury lamp illumination to ensure that every field of view in the FLIM acquisition sequence had a high degree of coverage. For data presented here, images were acquired in the wide field modality. FLIM images were acquired across 6 gates per decay in the channel defined by the GFP filter cube (excitation: 472/30 nm, dichroic: 495 nm, emission: 520/35 nm). To maximise dynamic range while minimising saturation, integration time was set to 0.2 seconds and five frames were accumulated per delay. Acceptor images were acquired at a single delay time chosen to fall at the peak of the signal decay, using the "red" filter cube (excitation: 545/30 nm, dichroic: 570 nm, emission: 610/75 nm). Four acceptor images were accumulated per FOV with integration time of 0.4 seconds in the case of the first plate, and 0.5 seconds in the case of the second. In total, acquisition times for the plates were 317 and 319 minutes, respectively. A time varying background decay was measured from a well containing PBS only, and a reference decay profile was acquired from a well of 20 μM erythrosine.

Multiple approaches were taken to fitting the datasets acquired in this experiment. A monoexponential fit was performed, taking account of time varying background and using the erythrosine reference with a tail fitted value of 180 ps reference lifetime. For this, and all subsequent analyses, images are segmented according to a two-scale NTH algorithm with parameters outlined in Table 4-5. Using *FLIMfit*, lifetime values were fitted on a cellwise basis; results are presented as averages over cells per condition.

Parameter	Value
Scale 1	100
Relative background scale 1	2
Scale 2	200
Relative background scale 2	2
Thresholding	0.99
Smoothing	1
Minimum size	1000

Table 4-5 Segmentation parameters for two-scale NTH segmentation algorithm used in RASSF-famliy protein screen.

Variations in relative donor and acceptor expression levels between cells might lead to differences in measured lifetime values that do not reflect differences in relative interaction strength, nor changes in FRET efficiency caused by different arrangements of fluorescent proteins in the bound complex. The capability of the FLIM plate reader to acquire images in multiple spectral channels is used to construct correlation plots of lifetime against acceptor:donor intensity ratio for each condition, in order to allow qualitative assessment of this effect.

Biexponential fluorescence decay models were then fitted to data, using methods informed by the results of monoexponential fitting. Here, donor-only lifetimes (τ_1) were fitted globally for each RASSF family

member in the absence of acceptor constructs, and then fixed for analyses of donor+acceptor conditions. A shift parameter t_0 was obtained for each RASSF-family construct by running a minimisation routine in *FLIMfit* to account for a drift that was apparent across this plate (see Chapter 3: section 3.1.1). Such an approach results in a pair of lifetimes for each condition, the shorter of which is considered to be the "FRETting" donor lifetime (τ_2). From these lifetimes, FRET efficiencies corresponding to each interaction were determined according to equation 4.1:

$$E = 1 - \frac{\tau_2}{\tau_1} \qquad \textbf{4.1}$$

The other fitted parameter in the model is the short lifetime ("FRETting") contribution per cell: these contributions were averaged over cells per condition.

4.2.4 Results

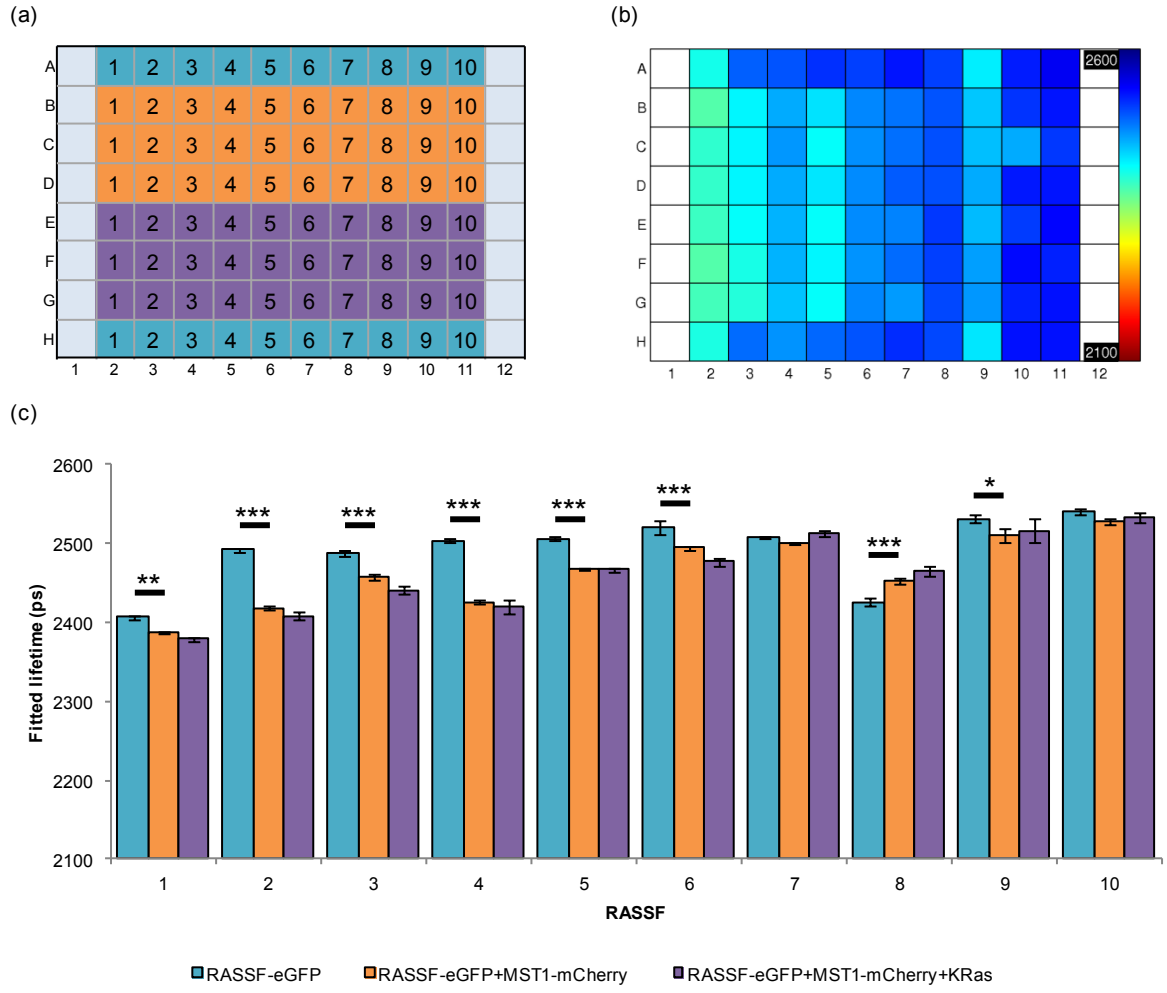

Figure 4-21 Results of monoexponential fits for first RASSF plate containing donor only, donor + acceptor, and donor + acceptor + KRas constructs.

(a) Plate layout for RASSF-MST1 screen consisting of RASSF-eGFP (blue), RASSF-eGFP+MST1-mCherry (orange) and RASSF-eGFP+MST1-mCherry+KRas (purple) for each of the ten RASSF family members. (b) Plate map showing monoexponential fit results for this plate. (c) Monoexponential fit results presented as average fitted lifetimes by condition; error bars representing standard errors across segmented cells. Significance of difference between RASSF-eGFP and RASSF-eGFP+MST1-mCherry for each family member protein is indicated for each RASSF protein and are calculated using Tukey's honestly significant difference test. Differences that are not significant are left unmarked.

Figure 4-21 shows results of a monoexponential fit to data acquired from a plate screening for interactions between RASSF-family proteins and full length MST1, laid out as shown in Figure 4-21 (a) and acquired under wide field illumination. Figure 4-21 (b) illustrates the variation in fitted monoexponential lifetime across the plate with differing conditions when results are combined wellwise and displayed as a false-colour lifetime plate map; Figure 4-21 (c) shows monoexponential lifetimes averaged over segmented cells and combined per condition. All classical RASSF proteins show a statistically significant decrease in lifetime when cotransfected with MST1 acceptor constructs compared to conditions in which RASSF-eGFP is transfected alone, indicative of an increase in FRET linked to the

occurrence of interactions (Tukey's honestly significant difference test, $p<0.01$). No classical RASSF family members exhibit a significant decrease in lifetime upon cotransfection with acceptor constructs, though RASSF8 shows a difference in the opposite sense to that expected. When KRas is transfected along with both donor and acceptor proteins, there is a statistically significant decrease in lifetime for RASSF3 and RASSF6 only.

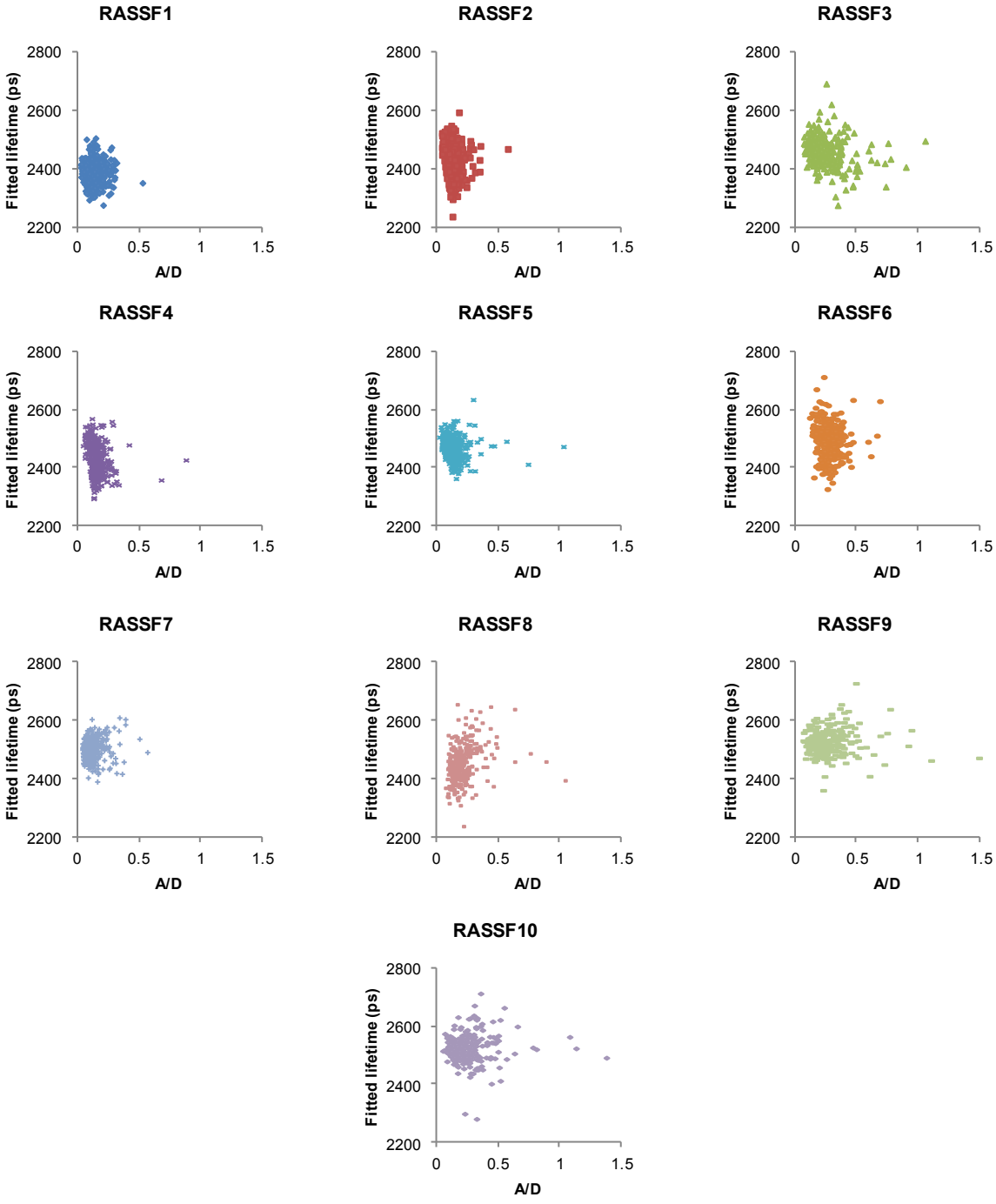

Figure 4-22 Plots illustrating correlation between ratio of measured acceptor:donor intensities, and fitted donor lifetime for cells from wells in which RASSF-family protein-eGFP fusions are cotransfected with MST1-mCherry.

Supplementary to Figure 4-21, lifetimes for cells from wells in which RASSF-eGFP constructs were coexpressed with MST1-mCherry are presented cellwise in correlation plots against the ratio of acceptor to donor intensities in Figure 4-22. Qualitatively, there appears to be no correlation between fitted lifetime and the acceptor:donor expression ratio for N-terminal RASSF family members. By inspection, there does appear to be a slight negative correlation between relative acceptor expression and fitted lifetime for classical RASSF family members.

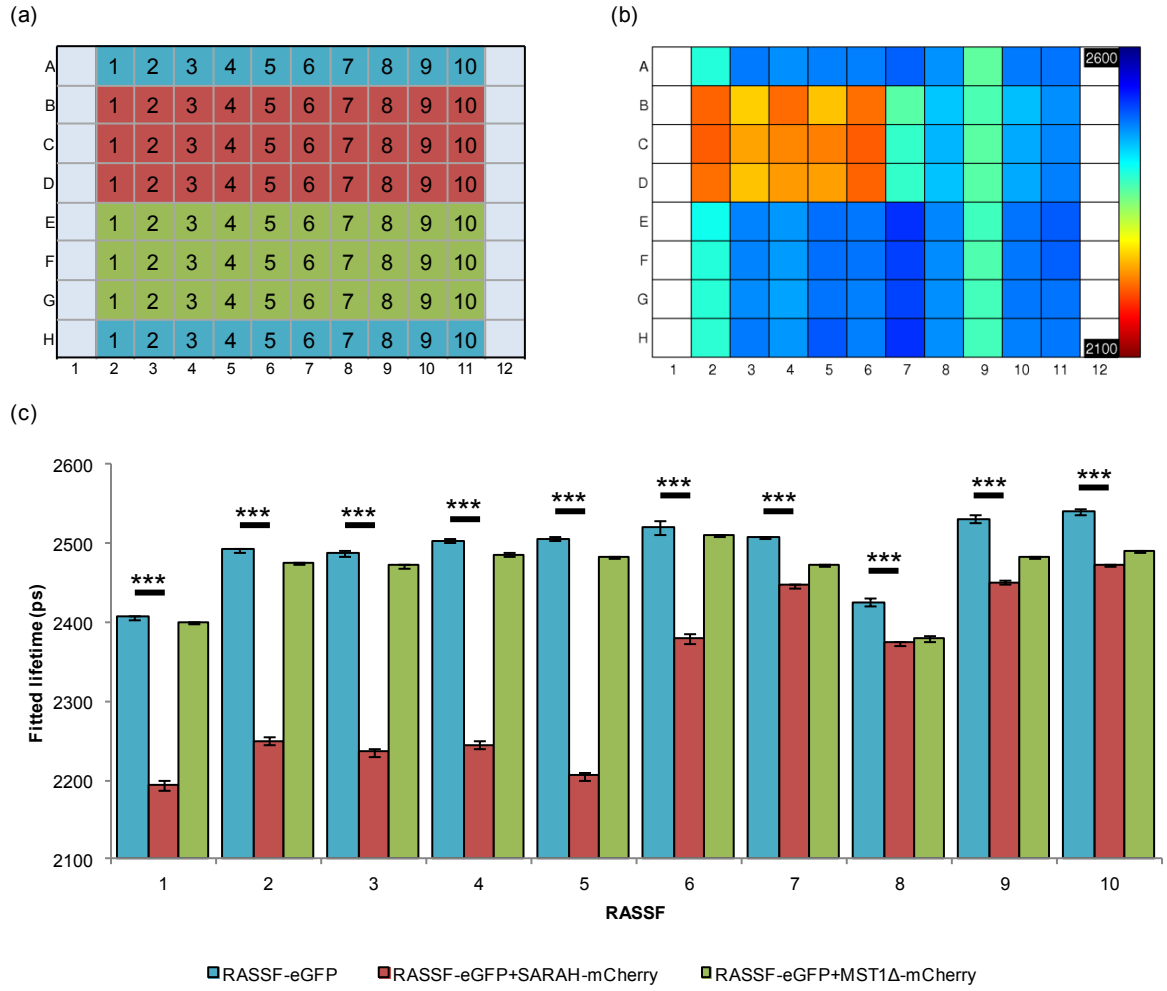

Figure 4-23 Results of monoexponential fits for second RASSF plate containing donor only, donor + truncated acceptor, and donor + negative control mutated acceptor constructs.
(a) Plate layout for RASSF-MST1 screen consisting of RASSF-eGFP (blue), RASSF-eGFP+SARAH-mCherry (red) and RASSF-eGFP+MST1Δ-mCherry (green) for each of the ten RASSF family members. (b) Plate map showing monoexponential fit results for this plate. (c) Monoexponential fit results presented as average fitted lifetimes by condition; error bars representing standard errors across segmented cells. Significance of difference between RASSF-eGFP and RASSF-eGFP+SARAH-mCherry for each family member protein is indicated for each RASSF protein and are calculated using Tukey's honestly significant difference test. Differences that are not significant are left unmarked.

Results of monoexponential fits to the second plate are shown in Figure 4-23. This plate is intended to screen for interactions with a truncated acceptor protein consisting only of the putative RASSF binding domain SARAH, as well as to investigate the effects on interactions of deleting the SARAH domain from the acceptor protein, and is laid out as illustrated in Figure 4-23(a). Figure 4-23 (b) illustrates the variation

in fitted monoexponential lifetime across the plate with differing conditions when results are combined wellwise and displayed as a false-colour lifetime plate map for which the same colour scale has been employed as in Figure 4-21 (b) to facilitate comparison between these plates. Figure 4-23 (c) shows monoexponential lifetimes averaged over segmented cells and combined per condition. Compared to full length MST1 binding, there is a relatively large decrease in lifetime when classical RASSF donor constructs are co-transfected with truncated acceptors compared to the donor-only case, indicated in Figure 4-23 (b) by the presence of warm colours in wells corresponding to these conditions. It is noted that there is a smaller but still statistically significant decrease in lifetime when non-classical RASSF constructs are co-transfected with the truncated acceptor ($p < 0.005$). For most classical RASSF constructs, no significant difference was observed in lifetime between conditions with donor only, and those in which donor was co-transfected with the SARAH-deficient mutant MST1Δ; the exception was RASSF5 which showed a difference ($p = 0.05$). Unexpectedly, there was in general a much more significant difference in lifetime between donor only and donor/MST1Δ cases for non-classical N terminal RASSF proteins ($p < 0.005$).

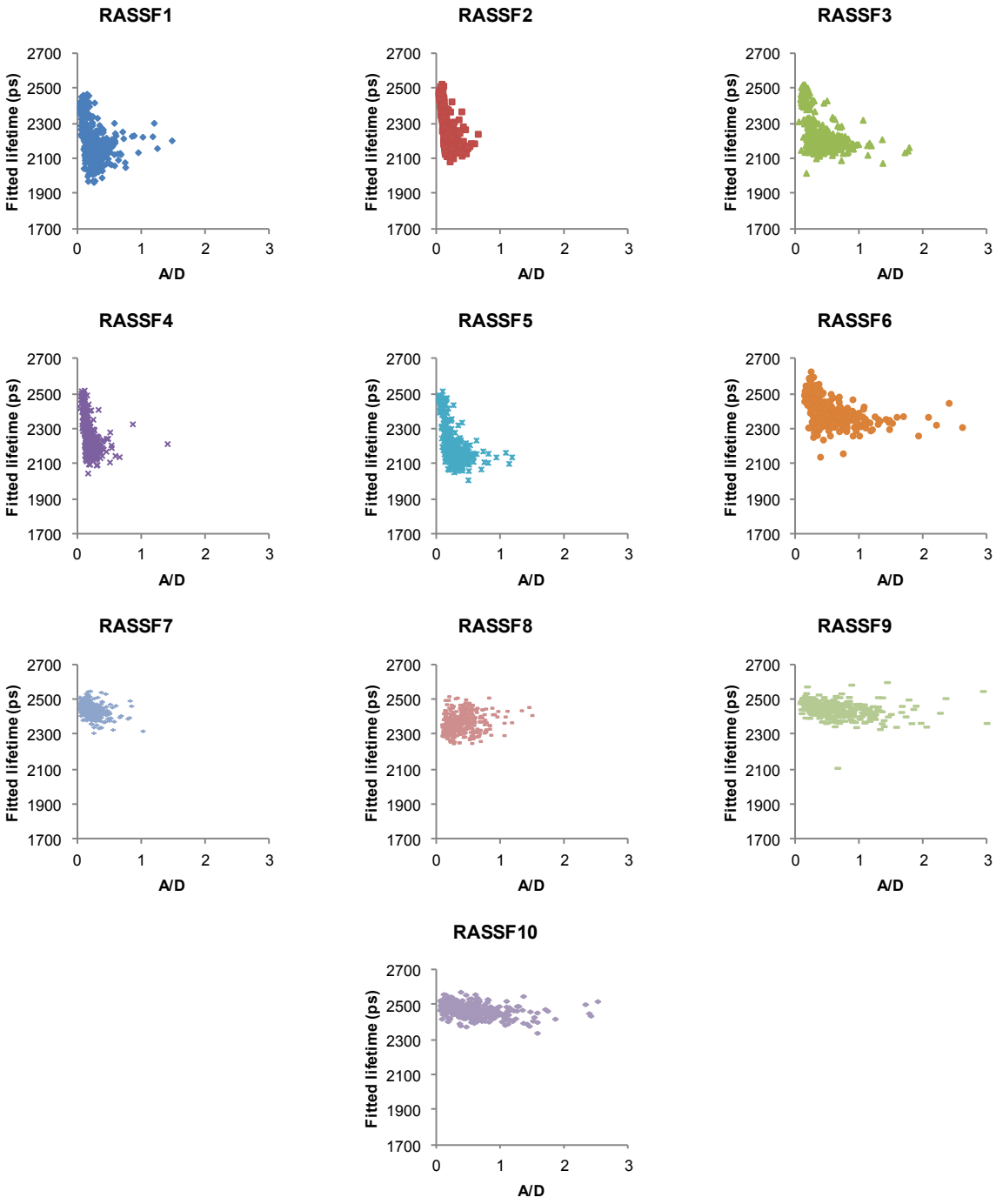

Figure 4-24 Plots illustrating correlation between ratio of measured acceptor:donor intensities, and fitted donor lifetime for cells from wells in which RASSF-family protein-eGFP fusions are cotransfected with truncated acceptor construct SARAH-mCherry.

Supplementary to Figure 4-23, Figure 4-24 shows correlation plots relating the ratio of acceptor to donor intensity to lifetimes yielded by fitting to a monoexponential model for cells from wells in which RASSF-eGFP constructs were coexpressed with the truncated acceptor SARAH-mCherry, presented cellwise. Qualitatively, there appears to be no correlation between fitted lifetime and the acceptor:donor expression ratio for N-terminal RASSF family members. By contrast, the presence of an apparent correlation

between relative acceptor expression and fitted lifetime for classical RASSF family members provides further evidence for interactions between this set of proteins and MST1.

A biexponential model was fitted to the subset of data corresponding to conditions in which the particular RASSF family member and MST1 are expected to interact, based on biochemical and *in silico* experiments. Here, long lifetimes are fixed per condition to mean monoexponential lifetime derived from corresponding donor-only wells, short lifetimes are fitted globally over all cells in a condition, and lifetime contributions are fitted cellwise following segmentation, as outlined as outlined in section 4.2.3 above. The results of this analysis on cells coexpressing classical RASSF family members and MST1 acquired from the first plate are summarised in Table 4-6 and Figure 4-25, where $<\beta_{FRET}>$ represents the short lifetime contribution averaged over cells per condition, and FRET efficiency E is calculated using equation 4.1. The same analysis is applied to cells coexpressing classical RASSF family members and the truncated SARAH-mCherry acceptor construct, acquired from the second plate; these results are summarised in Table 4-7 and Figure 4-26.

RASSF	Interaction partner	t_0 (ps)	τ_1 (ps)	τ_2 (ps)	E	$<\beta_{FRET}>$
1	MST1	41.31	2393	1515	0.37	0.06
2	MST1	51.7	2484	2008	0.19	0.21
3	MST1	65.3	2465	1516	0.39	0.08
4	MST1	68.21	2496	1393	0.44	0.12
5	MST1	70.1	2497	1579	0.37	0.10
6	MST1	70.8	2517	1244	0.51	0.08

Table 4-6 Summary of biexponential fit results for different classical RASSF family proteins in cells cotransfected with MST1-mCherry.

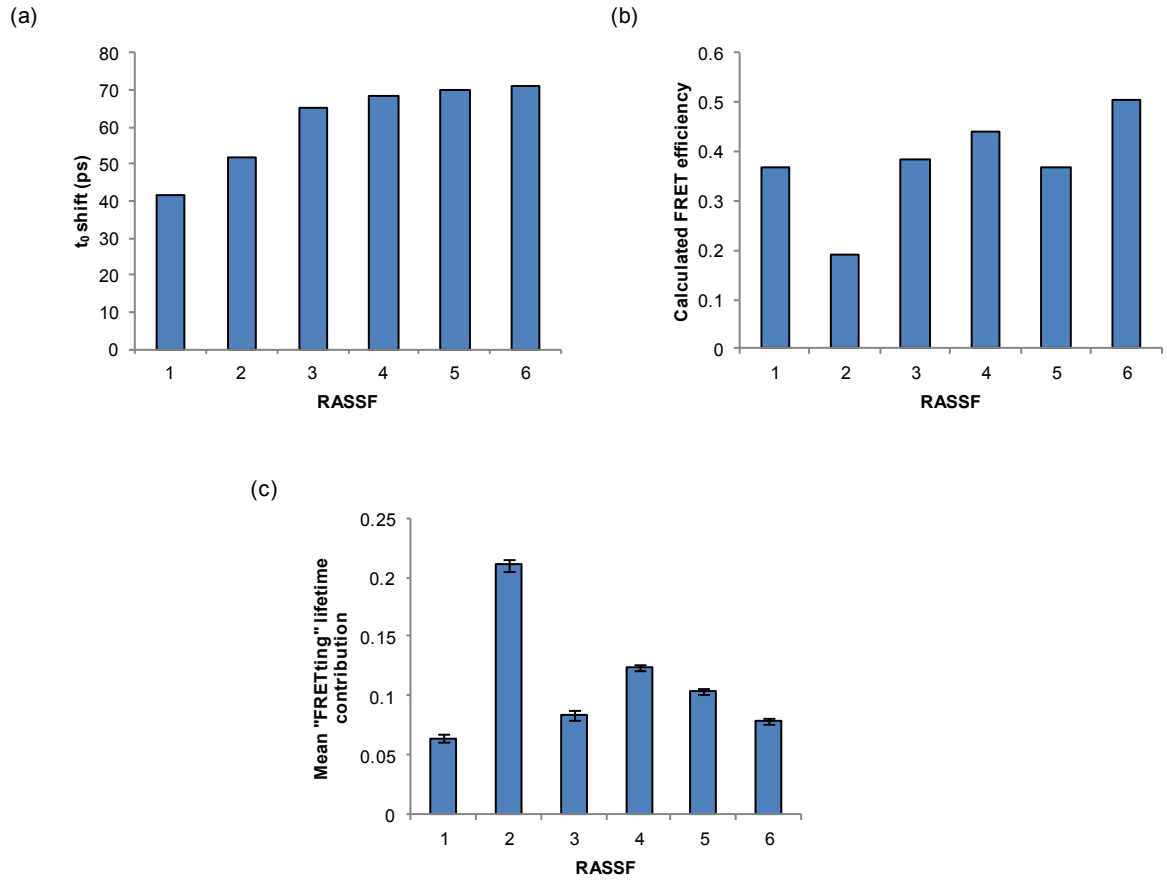

Figure 4-25 Results from biexponential fit to data acquired from cells cotransfected with classical RASSF-eGFP proteins and full length MST1-mCherry constructs.

(a) t_0 shift calculated by minimisation routine in FLIMfit, run using a monoexponential decay fit to donor-only wells. (b) FRET efficiency calculated from globally fitted lifetimes. (c) Short lifetime contributions; error bars represent standard errors calculated across segmented cells.

RASSF	Interaction partner	t_0 (ps)	τ_1 (ps)	τ_2 (ps)	E	$<\beta_{FRET}>$
1	SARAH	45.3	2406	1477	0.39	0.1788
2	SARAH	39.5	2492	1615	0.35	0.2101
3	SARAH	41.5	2487	1519	0.39	0.2212
4	SARAH	35.52	2503	1526	0.39	0.2141
5	SARAH	41.75	2506	1372	0.45	0.2404
6	SARAH	30.77	2521	1081	0.57	0.1379

Table 4-7 Summary of biexponential fit results for different classical RASSF family proteins in cells cotransfected with SARAH-mCherry.

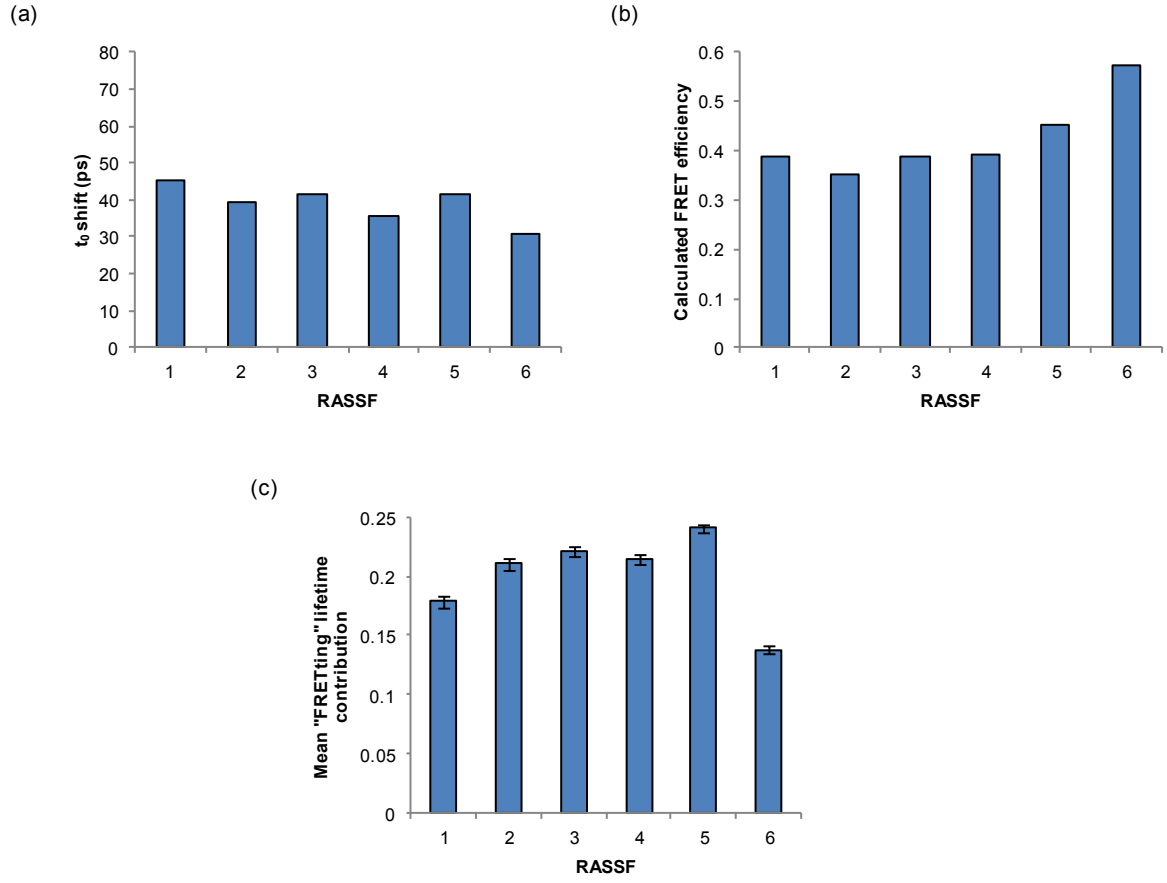

Figure 4-26 Results from biexponential fit to data acquired from cells cotransfected with classical RASSF-eGFP proteins and truncated SARAH-mCherry constructs.
(a) t_0 shift calculated by minimisation routine in FLIMfit, run using a monoexponential decay fit to donor-only wells. (b) FRET efficiency calculated from globally fitted lifetimes. (c) Short lifetime contributions; error bars represent standard errors calculated across segmented cells.

4.2.5 Discussion

The results in Figure 4-21 highlight the possibility of using simple monoexponential analyses to screen for protein-protein interactions. These results illustrate that even with small changes in measured lifetime, the number of cells interrogated leads to statistically significant differences between donor only and donor-acceptor for all the classical RASSF proteins. The anomalous result for RASSF8, for which donor only cells exhibit a shorter lifetime than those expressing both donor and acceptor proteins, is difficult to explain. By inspection, fluorescent protein expression in cells expressing RASSF8 only is more localised in

the nucleus than is the case for other members of the RASSF family. Furthermore, this effect is less evident when cells are cotransfected with RASSF8-eGFP and MST1-mCherry (Figure 4-27). It is not clear why the distribution of the protein should change in this way; however, this change in local environment of the donor construct upon cotransfection of MST1-mCherry may provide some explanation for the increase in lifetime observed.

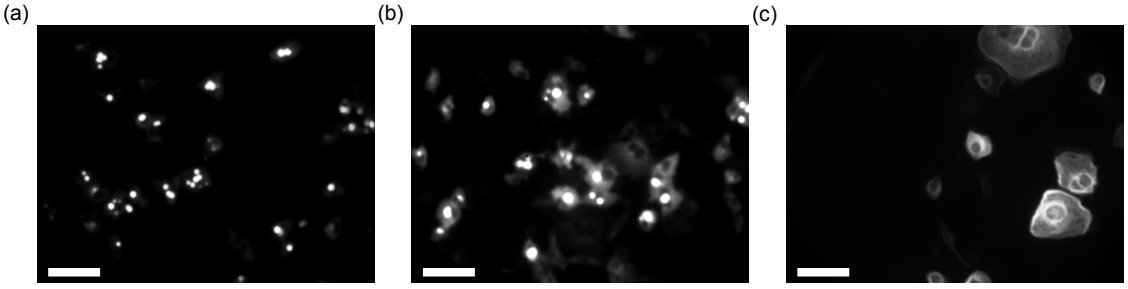

Figure 4-27 Exemplar donor channel integrated intensity images for RASSF-family proteins to illustrate anomalous fluorescence distribution for cells expressing RASSF8 alone.
(a) RASSF8-eGFP only. (b) RASSF8-eGFP+MST1-mCherry. (c) RASSF1-eGFP only. Scale bars 50 μm.

These data also indicate that the presence of K-Ras may play role in MST1 binding: significant differences in lifetime between RASSF+MST1 and RASSF+MST1+KRas cells are exhibited in the cases of RASSF3 and RASSF6. It has been proposed that conformational changes induced by binding at the RA domain might promote SARAH-mediated interactions in RASSF-family proteins. In the specific case of RASSF5 (also known as Nore1), it has been shown that Ras association does not affect RASSF5-MST1 heterodimerisation[219], in agreement with our findings.

Figure 4-23 illustrates the enhanced change of lifetime upon binding the truncated acceptor protein SARAH-mCherry compared to binding to the full length MST1 protein, as well as confirming the importance of the SARAH domain by illustrating a failure to interact when this domain is removed. It is noted, however, that the differences in the case of N-terminal RASSF members between donor only cells and cotransfected donor/SARAH-mCherry cells are, in fact, statistically significant ($p<0.05$). One possible explanation for this might be non-specific interactions between fluorescent proteins in the constructs, though preliminary experiments conducted by Dr Anca Margineanu showed no evidence of interactions when RASSF-eGFP constructs were cotransfected with plasmids for the expression of mCherry alone. The differences seen may be evidence of a high false positive rate that is typical of interaction screening methods in which proteins of interest are overexpressed[220]. Obtaining endogenous expression levels whilst maintaining signal levels required for robust FLIM is a significant challenge, but one which the FLIM plate reader, combined with global fitting techniques implemented in *FLIMfit*, is relatively well placed to address. In this case, conclusions regarding the presence or absence of interactions are made possible by considering intensity ratios in addition to lifetime results, as well as by parallel biochemical and *in silico* experiments[221].

The plots in Figure 4-22 and Figure 4-24 allow an assessment to be made as to the correlation between the ratio of acceptor:donor intensities and fitted lifetime values on a cellwise basis. The lack of apparent correlation in the case of N-terminal RASSF family members confounds the interpretation outlined above by indicating that there is no concentration-dependent, SARAH-independent, non-specific association between RASSF-family-eGFP donor constructs and SARAH/MST1-mCherry acceptor constructs. The negative correlation that is evident for classical RASSF family member constructs, particularly when cotransfected with the truncated SARAH-mCherry acceptor, indicate that lifetime parameters alone are not sufficient to assess relative binding attributes; rather, it is necessary to consider the effects of the relative expression of donor and acceptor constructs.

4.2.6 Summary

The study of RASSF-family interactions with MST1 presented here illustrated the potential value of the automated FLIM plate reader in screening for protein-protein interactions. Simple monoexponential analysis of FLIM-FRET plate data showed interaction partners for full length MST1 protein and the truncated SARAH domain that broadly followed expectations based on *in silico* predictions and biochemical experiments. The potential for FLIM-FRET data acquired using the automated FLIM plate reader to be used to generate quantitative data relating to interaction binding strength was recognised relatively late in the course of the project and so is yet to be thoroughly investigated beyond the initial work outlined here. Nevertheless, relative expression of donor and acceptor constructs – and the potential capability of the automated FLIM plate reader to measure these parameters as part of an automated data acquisition sequence – could be useful in assessing qualitatively the relative strength of protein-protein interactions. As such, this work will direct future development of the instrument for fully automated optically sectioned imaging as well as future applications to protein-protein interaction screening by intermolecular FRET.

4.2.7 Future work

In the course of analysing the data acquired for the study of RASSF-family interactions presented here, issues came to light concerning temporal drift of the excitation pulse with respect to the acquisition gates (see Chapter 3: section 3.1.1) and errors linked to the calibration of the delay generator (see Chapter 3: section 3.1.2). Having addressed these problems by switching to a single mode optical fibre and applying a newly measured calibration table to allow accurate delay generation, it is intended that the experiment should be repeated in order that data can be analysed without the necessity of fitting t_0 for each RASSF member. Optimisation of the transfection protocol using transfection reagents in place of electroporation, which has been demonstrated since the nominal end of the project, would mitigate the need for expanding cell cultures to high volumes to meet the requirements on cell numbers per electroporation cuvette. This approach will result in the repeat experiment taking significantly less time to conduct than the original series of experiments, as well as reducing the cost of the assay significantly.

When conducting a repeat experiment, it is intended that imaging should be conducted at higher resolution. At the expense of the number of cells assayed, using a higher magnification objective would lend the dual benefits of greater light collection efficiency and increased ability to make inferences regarding intracellular distribution of different RASSF family members: for example, clear differences are apparent by eye between microtubule-associating RASSF1[222]and other family members. In order to make the most of an improvement in resolution afforded by changing the imaging objective, a higher resolution HRI would be desirable. In addition to increasing the spatial information contained in images, using an HRI with an automatically selectable DC (non-gated) mode would allow acceptor images to be acquired more quickly, reducing the overall time taken to acquire plate data.

In the course of analysing lifetime data in the RASSF family interaction screen experiments, the potential for using plate reader data to calculate quantitative values relating to binding affinities was considered. Taking the dissociation constant $K_d = \frac{[D_{free}][A_{free}]}{[DA]}$, using measured values for donor- and acceptor-channel fluorescence intensity along with fitted values for fractional short lifetime component (β_2) and FRET efficiency (E), it is possible to relate dissociation constant to experimental parameters that can be acquired using the FLIM plate reader. The ability of such an approach to return absolute quantitative values for binding strengths between interacting protein pairs is subject to approximations of the linearity of β_2 with bound fraction, is potentially compromised by fluorescent constructs being much more highly expressed than the endogenous proteins they model, and requires calibration measurements to be taken to allow intensity measurements to be related to concentrations of fluorescent constructs. In the case of the data presented in this thesis, only relative values of protein interaction strength might be obtained using this approach due to the widefield imaging modality employed: in such a configuration, variations in measured intensity may be equally due to changes in sample thickness as to changes in fluorophore concentration. Given these reservations, this approach to ascertaining binding strengths in live cells has not been presented here. However, by adapting the instrument to use a Nipkow disk unit for optical sectioning and considering the relationship between short lifetime fraction and bound fraction using mCherry-EGFP fluorescent fusion constructs, it is envisioned that such an experiment will be conducted as part of ongoing work using the FLIM plate reader. In future, it would be instructive to apply the instrument to the study of binding in live cells of a protein pair that has been more completely characterised *in vitro* to confirm the validity of results whilst exploring the sensitivity and specificity of this approach.

Whether or not the FLIM plate reader can practically be used to obtain absolute quantitative dissociation constant data for protein-protein interactions, it is clear that it can be effective in screening for interaction partners. Potential future applications could involve screening for proteins that interact with Aurora kinases during mitosis: the abilities of FLIM-FRET to resolve spatiotemporal aspects of binding events in addition to simply screening for their existence means that the automated FLIM plate reader is well suited to such studies. Furthermore, since cell lines have been developed expressing fluorescent fusions of these

proteins at endogenous levels, it may be possible to screen for interactions without the high false-positive rate typically associated with screens in which proteins of interest are necessarily overexpressed.

Chapter 5: Automated FLIM–FRET of Raichu biosensors

As outlined in Chapter 2: section 2.3.2, FRET biosensors are single molecule probes comprising donor and acceptor fluorophores along with linker domains and biologically active regions. Such biosensors may report on changes in environment via induced changes in the spatial arrangement of donor and acceptor fluorophores, which is measured as a change in FRET efficiency. The family of *Ra*s and *i*nteracting protein *ch*imeric *u*nit (Raichu) biosensors developed in the Matsuda lab (Institute for Integrated Cell-Material Sciences, Kyoto University, Japan) instead report on the activation of small GTPases, an important family of proteins in cellular signalling cascades. These FRET biosensors exhibit the advantages common to all well-designed unimolecular probes – they are relatively simple to load into cells, show no significant adverse effects linked to overexpression causing interference with endogenous cellular signalling cascades and do not suffer from low signal-to-noise that might be linked to unfavourable stoichiometry between donor and acceptor constructs. Furthermore, by careful design the developers of the probes have minimised the impact of the drawbacks inherent in intramolecular FRET constructs discussed previously: most critically, the Raichu FRET probes are capable of reading out small GTPase activity with acceptable dynamic range[223,224].

In collaborative projects set up as part of EuroBioimaging and Imperial College London Kickstart programmes, we were particularly interested in the spatio-temporal activation profiles of two members of the Rho-family GTPases at cell-cell junctions in keratinocytes, RhoA and Rac1, which are not easily accessible by standard biochemical methods. Making use of the relevant Raichu probes, FLIM-FRET can be applied to addressing this challenge, and the FLIM plate reader enables a range of different conditions to be explored. Such experiments benefit from the automation of the plate reader in terms of switching between spectral detection windows as well as the cell finding algorithm. Following proof-of-principle experiments and establishment of protocols reported here, it is hoped that the plate reading FLIM microscope may be used in screening experiments to investigate the effects of different experimental conditions – for example, ectopic expression of different proteins – on small GTPase activation profiles.

In this chapter,

- The role of the small GTPase RhoA in the formation and maintenance of adherens junctions is introduced.
- Experiments measuring RhoA activation read out by FRET on the FLIM plate reader are presented.
- The activation of the small GTPase Rac1 mediated by the GTPase activating protein CdGAP at the adherens junction is explored using FLIM-FRET.

- The development of a manual segmentation utility for use with touch screen tablets and smart phones is discussed.

5.1 Spatio-temporal profiles of RhoA small GTPase activation in response to calcium stimulation for the formation of adherens junction

5.1.1 Biological context

Small GTPases (Ras superfamily GTPases) play roles in a myriad of cellular signalling pathways, including those linked to control of cell morphology, motility and mitosis. Small GTPases function by hydrolysing guanosine triphosphate (GTP) to guanosine diphosphate (GDP); the terminal phosphate of GTP induces a conformational change of the small GTPase, rendering it active by allowing it to interact with its effectors. Conversely, when GTP is hydrolysed to GDP, interactions between the GTPase and its effectors are not possible, and the GTPase is considered inactive. Small GTPase activity is modulated by guanine-nucleotide exchange factors (GEFs) and GTPase activating proteins (GAPs). GEFs bind small GTPases and cause a conformational change that allows GDP to dissociate; free GTP may then bind the GTPase to activate it. GAPs inactivate GTPase signalling by enhancing the hydrolysis of GTP to GDP. The interplay of GEFs and GAPs, which themselves are regulated by other proteins, allow fine tuning of GTPase signalling in the cell environment.

Ras homologous (Rho)-family GTPases represent a branch of the Ras superfamily GTPases. 20 members of the family have been identified to date, with diverse cellular functions[225–227]. In particular, aberrant expression and activity of Rho-family GTPases has been implicated in tumorigenesis and metastasis[225,227]. RhoA is one of the most extensively characterised proteins in the family, with multiple known effectors and regulators. It has been shown to play a role in generation of contractile force in conjunction with its effector Rho-associated protein kinase (ROCK), and in endocytosis via its effector protein kinase N1 (PKN). It has also been established that RhoA plays a role in the assembly and stabilisation of cell-cell junctions[228,229] in epithelial cells. It is this function that is of interest to our collaborators in the cell-cell adhesion signalling group in the National Heart and Lung Institute at Imperial College London, with whom a set of FLIM-FRET experiments was conceived to be undertaken as a proof-of-concept study for the EuroBioimaging research infrastructure project.

Keratinocytes are epithelial cells that make up the vast majority of cells in the epidermis, providing structure and acting as a barrier between organisms and their environment. In physiological conditions, keratinocytes in layers are polarised cells; that is, they exhibit different domains associated with basal, lateral and apical domains (Figure 5-1 (a)). Junctions at lateral membranes between keratinocytes are required to maintain epithelial integrity under mechanical stresses; junctions must also be dynamic in order that cells can respond properly during development, renewal and wound repair. Adherens junctions between keratinocytes fulfil crucial roles both mechanically, by providing a means for cells to form connections, and as foci for signalling events linked to cytoskeletal reorganisation. Dysregulation of adherens junctions is linked to epithelial tumour progression and metastasis[230], as well as to dermatological conditions such as pemphigus[231] and juvenile macular dystrophy[232,233].

The structure of the adherens junction at lateral membranes is presented in Figure 5-1 (b) and (c). Cadherins ("calcium-dependent adhesion" proteins) are membrane-spanning proteins, the extracellular domains of which are made up of a number of subunits with three calcium-binding pockets between each. Calcium binding has been shown to cause conformational changes in extracellular subunits of N-cadherin and calcium depletion is linked to a decrease in transjunctional interactions between cadherin dimers[234] – this behaviour is known as the "calcium switch" for modulation of junction formation. Keratinocytes grown in low calcium conditions do not form cell-cell contacts; increasing calcium to physiological concentrations results in junction formation and epithelial polarisation, typically within 30 minutes of stimulation[235]. The catenins β-catenin and p120 bind to the intracellular cadherin domain, whilst α-catenin links F-actin cytoskeletal filaments to the junction complex[236].

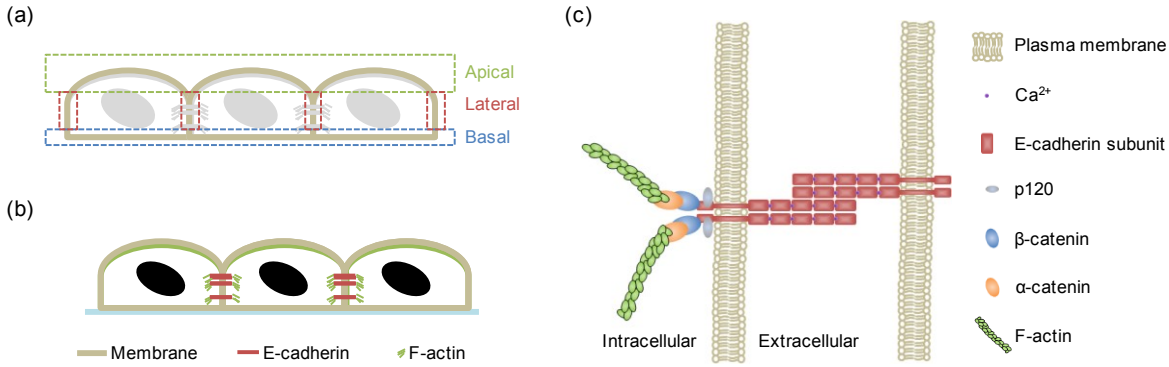

Figure 5-1 Schematic overview of polarised epithelial cells and adherens junction structures
(a) Crude identification of apical, lateral and basal membrane regions in polarised epithelial cells. (b) Schematic representation of adherens junction formation at lateral membranes in a keratinocyte monolayer. Adapted from Kalaji et al.[235] (c) Schematic representation of a structural model of the components in an adherens junction.

In addition to these structural roles, all of the catenins have been shown to perform functions in distinct signalling networks: for example, β-catenin accumulation in the cytosol and nucleus is modulated in the canonical Wnt signalling pathway, dysregulation of which is linked to pathological outcomes including bone disease and cancer[237]. Cadherins may also act as signalling receptors that respond to adhesion, modulating the activity of Rho-family GTPases[238]. Since the Rho-family GTPases, and particularly RhoA, are themselves implicated in regulation of assembly, remodelling and maturation of junctions[228], this functional interaction can be described as reciprocal.

In the RhoA-based FLIM-FRET experiments devised by our collaborators, we sought to establish the spatio-temporal activation profile of RhoA following "calcium switch" activation of junction formation using the Raichu-RhoA biosensor developed in the Matsuda lab[223,224]. The probe shares the same basic design common to all of the Raichu probes, whereby activation of the small GTPase promotes binding to the corresponding binding domain. In the case of the Raichu-RhoA, the sensor region is human RhoA and the ligand region is the RhoA-binding domain of protein kinase N1 (PKN-RBD). When GTP binds to the RhoA region, the small GTPase is activated allowing binding between the sensor and ligand domains. These binding events bring the donor and acceptor fluorophores into closer proximity, causing

FRET to occur. As intimated previously, RhoA-GEF proteins act to promote RhoA activity by liberating hydrolysed GDP from the probe, whilst RhoA-GAP proteins enhance the hydrolysis of the bound GTP, inactivating the probe: this behaviour is summarised in Figure 5-2. The native RhoA C-terminal CAAX (cysteine-aliphatic AA-aliphatic AA-any AA) region is replaced in the probe used here for a Ki-Ras4B CAAX motif, in order to promote delivery of the probe to plasma membrane rather than to intracellular membranes where endogenous RhoA is more often found: since our experiments are concerned with RhoA activation at cell-cell junctions, this modification reduces background signal. The version of the probe gifted to our collaborators from the Ng lab (Richard Dimbleby Department of Cancer Research, King's College London, UK) has been modified from the original Raichu-RhoA sensor by replacing CFP and YFP with GFP and mRFP as the donor and acceptor fluorescent proteins, respectively[239]. In addition, a dominant negative form of the probe with a reduced affinity to guanine nucleotides, achieved by substitution of Asn for Thr at position 1237 (Raichu-RhoA T19N)[224], was used as a negative control.

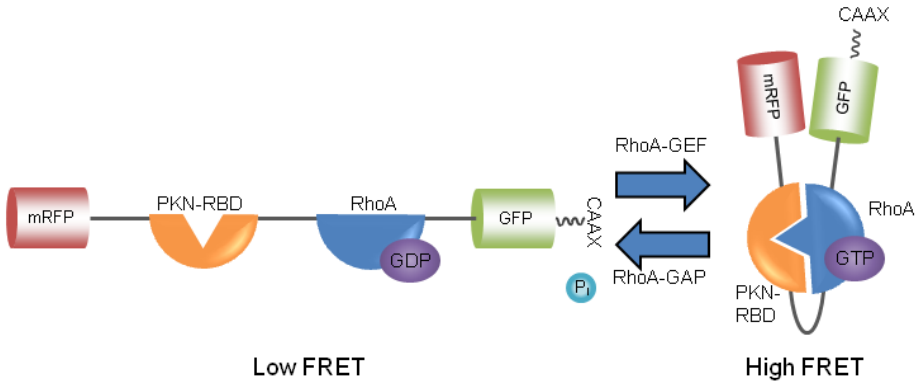

Figure 5-2 Schematic of Raichu-RhoA FRET biosensor for RhoA activation mediated by RhoA-GEFs and RhoA-GAPs.
PKN: protein kinase N1, CAAX: Ki-Ras4B CAAX motif allowing modification for membrane association, P_i: inorganic phosphate.

5.1.2 Sample preparation

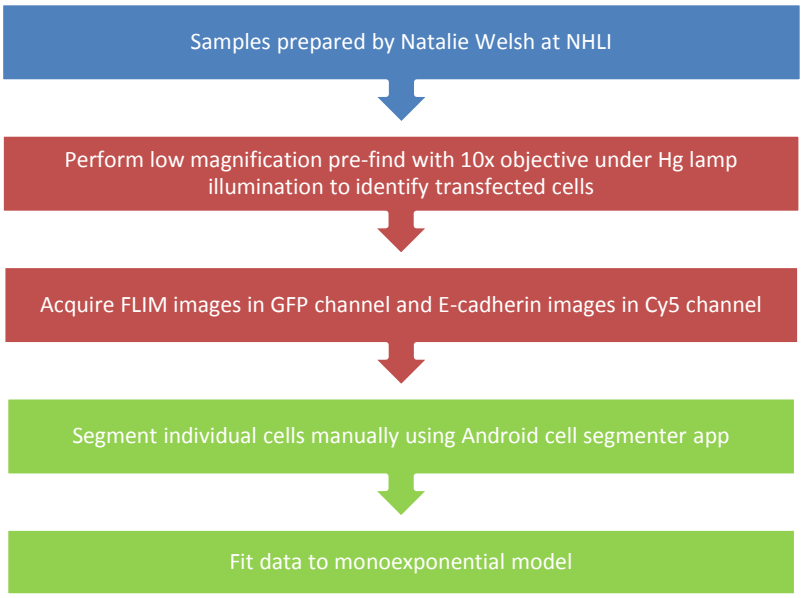

Figure 5-3 Flow chart summarizing the methods used for generation and analysis of RhoA small GTPase activation samples.
Further details are found in sections 5.1.2-5.1.3.

Samples were prepared by Natalie Welsh in the cell-cell adhesion signalling group at the National Heart and Lung Institute, Imperial College London. Human keratinocytes isolated from neonatal foreskin (strain SF, passages 3-6) were maintained on mitomycin-C (Sigma, Dorset, UK) treated J2 mouse fibroblasts in standard medium (Dulbecco's Modified Eagle Medium (DMEM) DMEM:F12 BioWittaker, Lonza, Germany) supplemented with 1.8mM $CaCl_2$, 10% foetal calf serum (FCS), 5mM glutamine, 100 units/ml penicillin, 100µg/ml streptomycin, 5µg/ml insulin, 10ng/ml epidermal growth factor (EGF), 0.5µg/ml hydrocortisone (all Sigma) and 0.1nM cholera toxin (Quadratech Diagnostics Ltd, Surrey, UK) as described elsewhere[240–243]. Low calcium medium (approximately 0.1mM $CaCl_2$) had the same formulation as standard medium but contained FCS pre-treated with Chelex-100 resin (BioRad, Hemel Hempstead, UK) to deplete divalent calcium ions[242]. Cells to be grown in low calcium were seeded in standard medium and switched to low calcium when approximately 20 cells per colony were seen. Cells were seeded on 96 well plates (Corning Incorporated, Corning, NY) at a density of 2.2×10^3 cells per well. Cells were maintained at 37°C, 5% CO_2. J2 mouse fibroblasts were maintained in medium consisting of Dulbecco's modified medium (DMEM, Sigma-Aldrich), 10% DCS (Sera Laboratories International Ltd, West Sussex, UK) and 5mM L-glutamine (Sigma-Aldrich).

Transfections were performed using plasmid DNA diluted in Effectene buffer (Qiagen) and Enhancer added at a ratio of 1:8 Enhancer. 1 µg/well DNA plasmid encoding the EGFP-mRFP-modified version of the Raichu 1240[224] construct illustrated in Figure 5-2 was used per well. Control wells were transfected using a plasmid encoding a dominant negative form of the probe subject to a single point mutation (T19N) that cannot be activated and therefore remains always in the low FRET conformation. Samples

were vortexed and incubated for 5 minutes at room temperature. Effectene transfection reagent was added at a ratio of 1:25 Effectene and tubes vortexed prior to 5 minutes' incubation at room temperature. Low calcium medium was used to dilute the final plasmid DNA mixture which was subsequently added to cells. Media was changed after 4 hours.

Immunofluorescence techniques were employed to probe for E-cadherin translocation upon cell-cell junction formation induced by adding calcium ions to a final concentration of 1.8 mM[229]. At different times following induction of junction formation by the calcium switch, cells were fixed with 3% paraformaldehyde (PFA) in phosphate-buffered saline (PBS) for 10 minutes at RT then washed 3 times in PBS. Cells were then simultaneously permeablised and blocked with 0.1% Triton X-100 (Sigma-Aldrich) diluted in 10% FCS-PBS solution, for 10 minutes at RT. Cells were then washed 3 times in PBS before staining. Samples were incubated with primary antibody against E-cadherin (mouse, gifted by M. Takeichi (NCCRI, Tokyo, Japan)) diluted in 10% FCS (final concentration) in PBS for 30 minutes in the dark at RT. Samples were washed nine times in PBS before incubation for 30 minutes in the dark at RT with secondary antibody (Cy5-conjugated anti-mouse (Jackson Immuno labs)). Cells were washed a further nine times in PBS then 3 times in water before addition of Mowiol mounting media. Samples were imaged at room temperature.

5.1.3 Image acquisition and analysis

Cells expressing Raichu-RhoA were found using the low magnification prefind algorithm (10x magnification) under mercury lamp illumination via the GFP filterset. In early plates with low expression of Raichu-RhoA, it was necessary to develop and apply a rolling background subtraction to aid cell identification. This method was replaced by the incorporation of CellProfiler into the acquisition software for advanced cell prefinding but, after optimisation of transfection, the simplest intensity thresholding method was sufficient to identify cells expressing the probe.

Imaging was carried out at 40x magnification (LUCPFLN 40x, Olympus). FLIM data was acquired in the GFP spectral channel across six time gates integrated for 1.2 seconds each. A 1.2 second exposure at a single time gate was acquired with Cy5 filters to assess E-cadherin localisation and phase contrast images were acquired in order that cells could be verified to have grown in a monolayer. 360 fields of view were acquired across 60 wells, leading to a total acquisition time of 84 minutes. A well seeded with untransfected keratinocytes was imaged using the same acquisition parameters as the FLIM experiment to measure the time-varying fluorescent background and a well of 20 μM Erythrosine was imaged to provide a reference decay profile.

Manual cell segmentation was employed, simultaneously providing lateral membrane segmentation and allowing our collaborators to reject unhealthy cells. A custom segmentation program was written in Java for Android to allow segmentation to be performed by drawing around cells with a finger or stylus on a tablet or mobile phone, with standard swipe and pinch gestures being used to pan and zoom the image. It

was intended that such a tool should be less tedious to use and more accurate in generating cell outlines than using a mouse to draw freehand in the segmentation manager incorporated into *FLIMfit*. For samples such as those investigated here, where "acceptable" cells vary significantly in size and shape and the presence of bright fibroblasts can confound automated segmentation (Figure 5-4), such an approach is simpler to implement and more robust than automated segmentation methods, though is only practical over relatively small data sets.

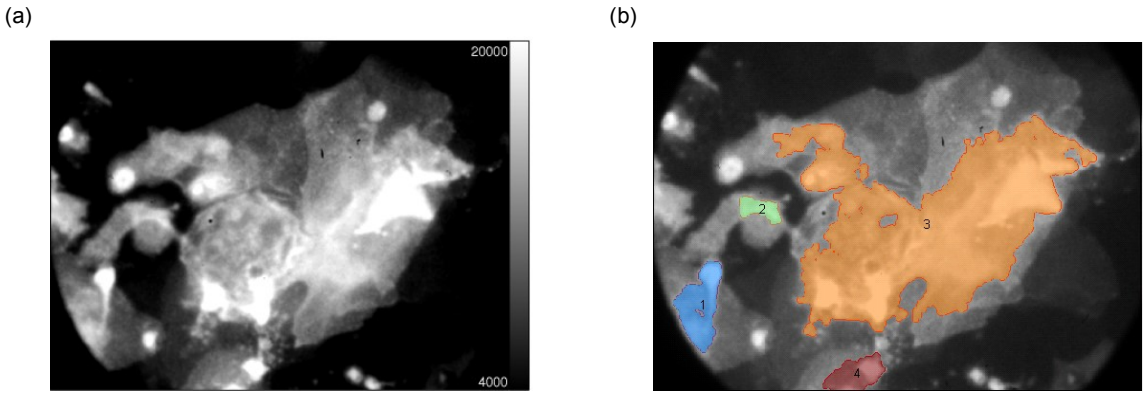

Figure 5-4 The effects of bright fibroblasts on automated segmentation of keratinocyte samples
(a) An exemplar integrated fluorescence intensity image showing large fibroblasts, cocultured with keratinocytes, expressing FRET biosensors at high levels. (b) Resulting erroneous segmentation using NTH algorithms with parameters outlined in Table 5-1 below.

Currently, mobile tablet devices or smartphones are interfaced with a host PC over a wireless internet connection using simple TCP socket-based communication implemented in Java. For speed in development, a front end was written in MATLAB to interface with the Java back end. The MATLAB GUI allows control of which images to send to the device, whether to segment a given gated image or an integrated intensity image, and whether to save cell outlines or full cell masks as TIFF mask files. Example screenshots from the segmentation app run on a mobile device (Figure 5-5 (a)) and from the MATLAB GUI run on a host PC (Figure 5-5 (b)) are presented below. Figure 5-6 illustrates the resulting segmentation employed for the Raichu-RhoA experiment: integrated intensity images (Figure 5-6 (a)) are used as a basis for manual cell segmentation (Figure 5-6 (b)). Then a lateral membrane, defined by our collaborators to be 6 pixels wide, is formed using an erode operation followed by a subtraction in MATLAB, resulting in masks as shown in Figure 5-6 (c). Finally, "cytosol" masks are generated in MATLAB by combining whole cell and lateral membrane masks in a NAND operation (Figure 5-6 (d)).

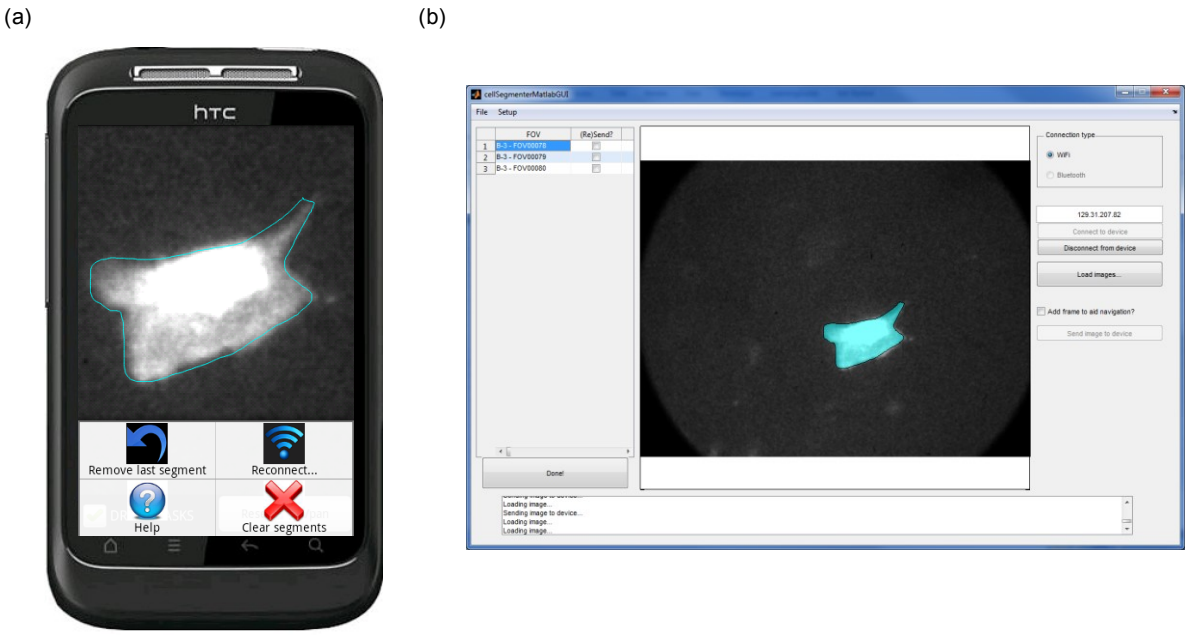

Figure 5-5 Illustration of implementation of manual cell segmentation tools.
(a) A screenshot showing implementation of manual cell segmentation presented overlaid on a HTC Wildfire S device, the device used as a test at the lower end of performance of compatible Android systems. Images can be panned and zoomed using standard swipe and pinch gestures. This screenshot was obtained with the options menu activated. (b) A screenshot showing corresponding field of view displayed on host machine in a MATLAB-based front end, with resulting whole cell mask overlaid on integrated intensity image.

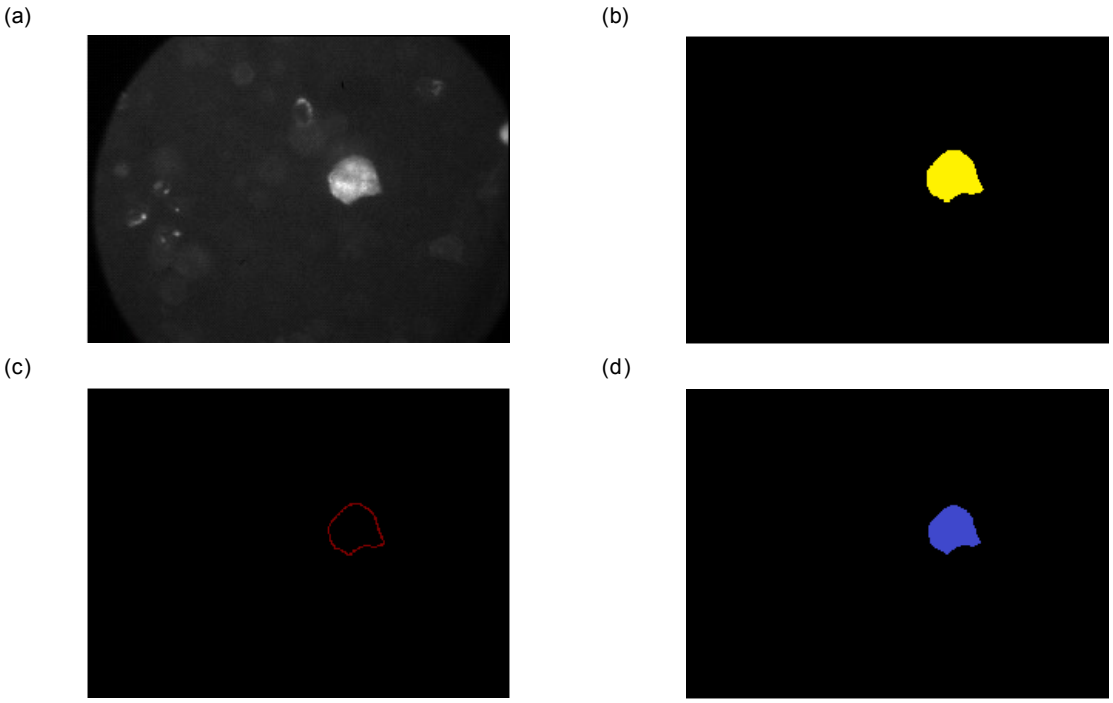

Figure 5-6 Overview of segmentation of cells and subcellular regions used for analysis of RhoA calcium switch data.
(a) Integrated intensity image of a keratinocyte expressing Raichu-RhoA, GFP channel. (b) Manually segmented cell mask. (c) "Lateral membrane" cell mask generated by eroding whole cell mask with a 3 pixel disk structure element followed by subtraction. (d) "Cytosol" cell mask generated by NAND operation on whole cell and "lateral membrane" masks.

Segmented data was fitted pixelwise to a monoexponential lifetime model in *FLIMfit* using the measured reference decay profile and time varying background. Mean lifetimes and standard errors were calculated cellwise and presented by condition.

5.1.4 Results

Results of monoexponential fits to "lateral membrane" segmented data are shown in Figure 5-7, where plots on the left of the figure refer to data acquired from cells expressing the dominant negative form of the Raichu-RhoA probe and represent a negative control, and plots on the right of the figure refer to cells transfected with wild type Raichu-RhoA. Figure 5-7 (a) and (b) show false colour lifetime maps of exemplar fields of view across calcium treatment time points, as well as from wells treated with serum as a positive control, for dominant negative and wild type Raichu-RhoA, respectively. Figure 5-7 (c) and (d) show comparisons between monoexponential lifetimes averaged over untreated and serum treated cells. For the wild type RhoA probe, serum treated cells exhibit a decrease in lifetime that is significant at $p < 0.05$ (Student's t-test). Taking the serum treatment of wild type probe data as a positive control measurement and untreated cells expressing the dominant negative probe as a negative control, the Z' parameter (defined in Chapter 2: section 2.5.1) associated with this assay is $Z' = -5.84$: by conventional criteria, this assay is not considered to be useful. Figure 5-7 (e) and (f) show lifetime changes in response to the calcium switch time course experiment for dominant negative and wild type Raichu-RhoA respectively. There is no significant change in lifetime across the time course for the dominant negative construct; the wild type probe shows a significant decrease in measured lifetime 60 minutes post-treatment ($p < 0.05$ compared to zero time point, Dunnett's test).

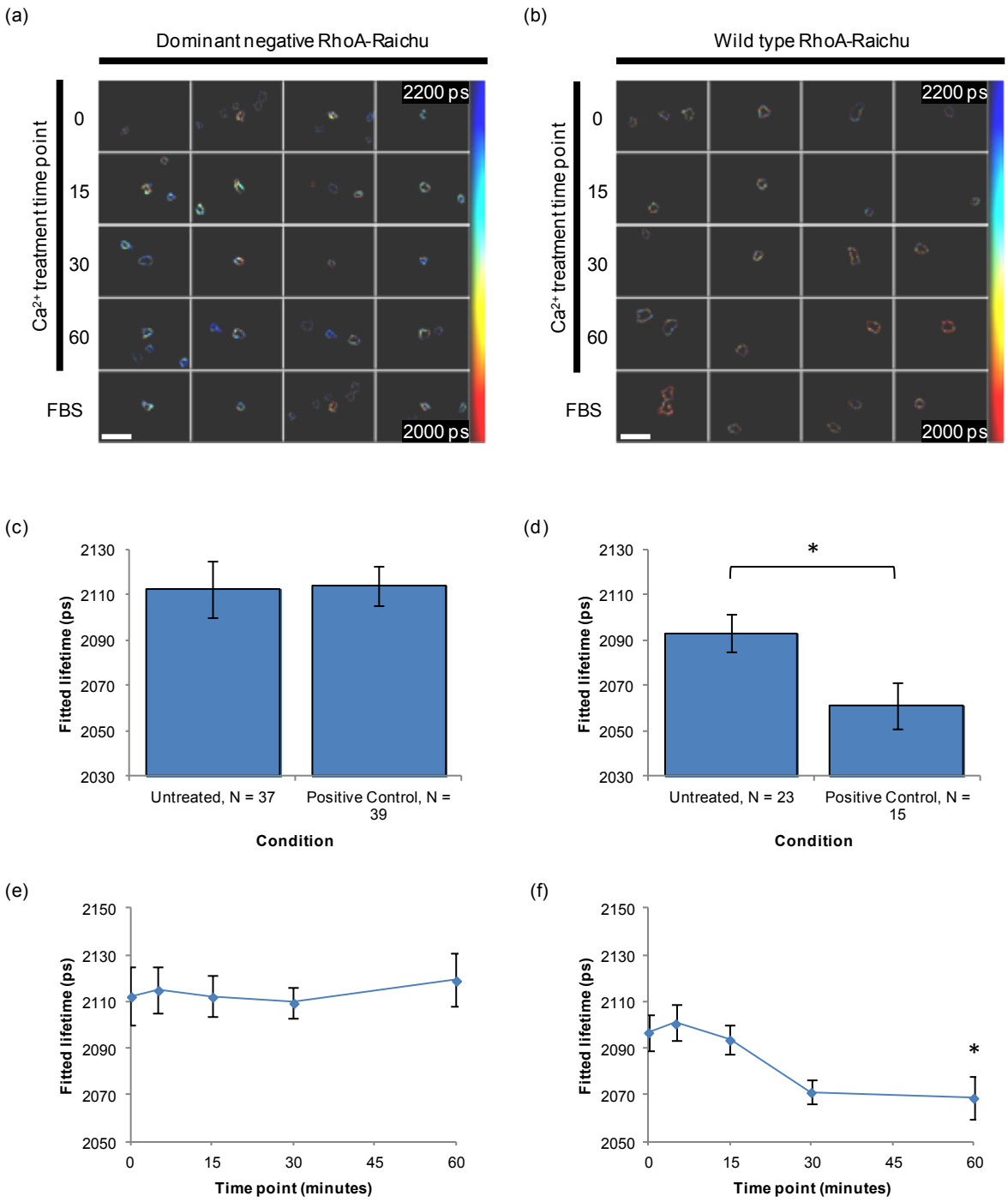

Figure 5-7 Results of experiment investigating RhoA activation in response to a calcium switch, lateral membrane segmentation applied.

(a) False colour map showing monoexponential lifetime fit results for typical fields of view in cells expressing the dominant negative form of Raichu-RhoA at different calcium treatment times, and 5 minute serum stimulation. (b) False colour map showing monoexponential lifetime fit results for typical fields of view in cells expressing the wild type form of Raichu-RhoA at different calcium treatment times, and 5 minute serum stimulation. Scale bar = 100 µm. (c) Monoexponential lifetimes averaged over cells to compare untreated and positive control (FBS) lifetimes for dominant negative Raichu-RhoA. (d) Monoexponential lifetimes averaged over cells to compare untreated and positive control (FBS) lifetimes for wild type Raichu-RhoA ($p < 0.05$, Student's t-test). (e) Monoexponential lifetimes averaged over cells to show response to calcium switch treatment time course for dominant negative Raichu-RhoA. (f) Monoexponential lifetimes averaged over cells to show response to calcium switch treatment time course for wild type Raichu-RhoA. Significance of difference from zero time point calculated using Dunnett's test.

Further analysis was carried out on the same dataset, segmented to include the cytosol of each cell but exclude the lateral membrane region: these results are summarised in Figure 5-8. It is evident that the positive control condition (5 minutes serum stimulation) results in a significant decrease in lifetime across the cytosol, indicative of RhoA being activated before recruitment to junctions. Furthermore, analysis of similarly segmented regions in the calcium switch experiment show a transient decrease in lifetime, albeit non-significant ($p = 0.21$, Dunnett's test) five minutes post-stimulation. This is followed by a statistically significant decrease in lifetime by 60 minutes ($p < 0.05$, Dunnett's test). The calculated Z' parameter for this analysis is $Z' = -4.46$; again, this assay would not be considered useful by conventional criteria set out in Chapter 2: section 2.5.1.

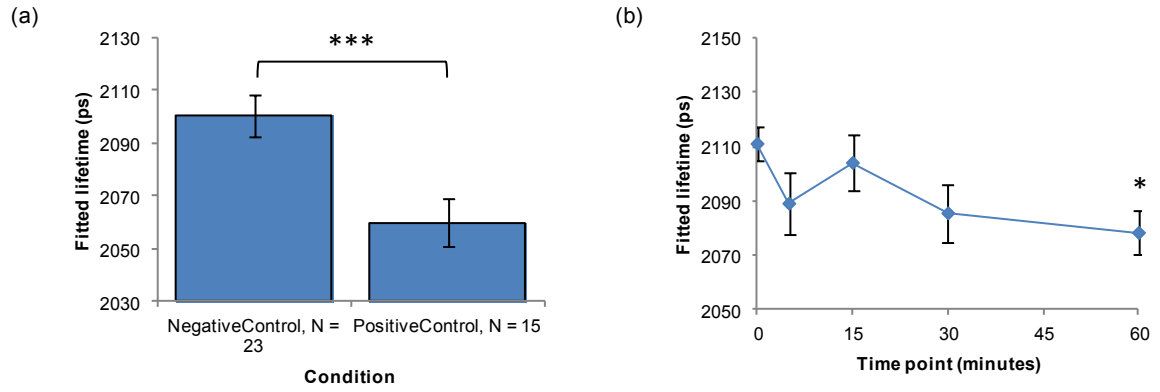

Figure 5-8 Results of experiment investigating RhoA activation in response to a calcium switch, cytosol segmentation applied.
(a) Monoexponential lifetimes averaged over cells to compare untreated and positive control (FBS) lifetimes for wild type Raichu-RhoA ($p < 0.005$, Student's t-test). (b) Monoexponential lifetimes averaged over cells to show response to calcium switch treatment time course for wild type Raichu-RhoA. Significance of difference from zero time point calculated using Dunnett's test.

5.1.5 Discussion

The data presented in Figure 5-7 shows that there is a statistically significant decrease in lifetime at the lateral membrane in cells transfected with the wild type Raichu-RhoA probe upon treatment with FBS, when averages are taken over all cells per condition. The dynamic range of the probe under this comparison is nevertheless very small – the change in lifetime is on the order or 30 ps. Previously published work and private correspondence has indicated that FRETting lifetime of the probe is as low as 1.6-1.7 ns in migrating CCRF-CEM (T lymphoblast) cells[239], though this discrepancy may be due simply to differences in mechanism of RhoA activation between the cases studied. Furthermore, the spatial distribution of RhoA activation in cells following serum activation was unknown at the start of the experiment. Since Figure 5-8(a) serves to confirm that RhoA is activated more generally in the cytoplasm as well as at the lateral membrane under this positive control condition, it is likely that the dynamic range established by this method in conjunction with automated membrane segmentation is greater than that

which might be expected to be evident when stimulation is achieved by calcium switch, where activation is expected primarily at cell-cell junctions.

It was intended that E-cadherin immunofluorescence staining should be used to highlight cell-cell junction formation, providing both spatial and temporal context to the RhoA activation experiments in relation to junction formation. Ideally, images from the Cy5 channel of the microscope could be used to generate segmentation masks for Raichu-RhoA FLIM images, potentially increasing the dynamic range of the experiment. Unfortunately this aspect of the experiment did not produce the useful junction staining seen when applied in other cases by our collaborators; therefore it was not possible to confirm that junctions were formed in response to calcium treatment. This may be attributed to the relatively late passage number of keratinocytes used in these experiments. In addition, human primary keratinocytes are notoriously difficult to culture and manipulate, especially after being subjected to low calcium conditions necessary for this experiment. An alternative method of confirming junction formation may be to study RhoA translocation to the membrane by intensity imaging. Unfortunately, this effect is typically evidenced by a relatively small increase in intensity over a small number of pixels at locations that are typically only identified by comparison with E-cadherin immunofluorescence images[229]. Such changes are difficult to quantify in automated well plate datasets. Here, comparing intensity in membrane-masked regions normalised to intensity in the cytoplasm region enclosed across conditions showed no significant change (data not shown).

Despite these difficulties, a significant change in RhoA activity is observable by FLIM-FRET 60 minutes after the calcium switch experiment is started. This increase in activity is in agreement with findings in murine keratinocytes, which have been reported to show no clear increase in activity until 60 minutes post-stimulation[244]. It is notable that in biochemical pulldown assays for activated RhoA (probing for GTP●RhoA) performed in the human keratinocytes used here by Natalie Welsh, a sharp transient increase in activity is seen 5 minutes post-stimulation[229] (Figure 5-9 (b)). The small (non-significant) decrease in lifetime at 5 minutes observed when the cytoplasmic regions are segmented (Figure 5-8 (b)) may be related to this phenomenon as the pull down assay affords no spatial resolution of RhoA activation.

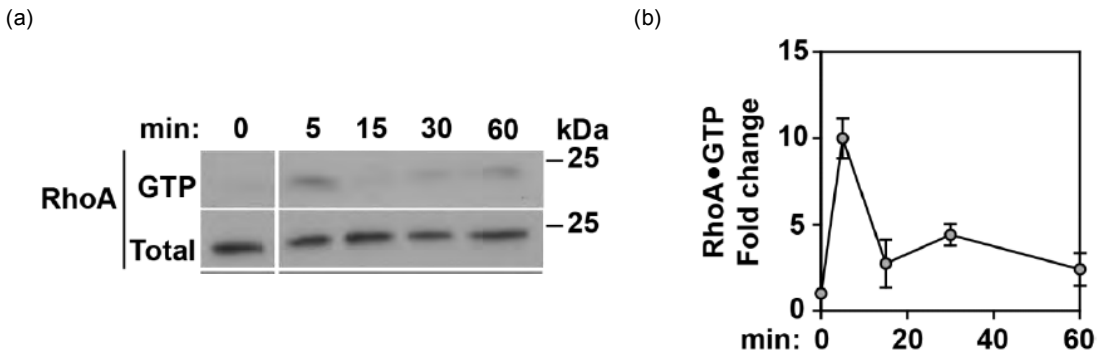

Figure 5-9 Results of biochemical experiments carried out in parallel with FLIM experiments by Natalie Welsh in the National Heart and Lung Institute, Imperial College London.
(a) A Western blot illustrating the increase in GTP-RhoA (i.e. activated RhoA) following stimulation with 1.8 mM Ca^{2+}. (b) Data from (a) presented as a fold-change in activated RhoA against time since stimulation. Figure adapted from Natalie Welsh's PhD thesis[229].

5.2 Localisation of Rac1 small GTPase activation modulated by CdGAP

5.2.1 Biological context

Rac1 is another Rho-family small GTPase, and like RhoA it is one of the better characterised proteins in the family. Rac1 is ubiquitously and constitutively expressed throughout mammalian tissue types. RAC1 is described as a pleiotropic gene, reflecting the diverse roles played by Rac1 in cells: it has been shown to be crucial in neurite growth[245], mitosis and cell cycle progression[246], whilst a splice variant Rac1b that exhibits prolonged signalling activity has been implicated in lung, colorectal and breast cancer development[247]. In addition, Rac1 has been established to play a role in the regulation of cell-cell adherens junctions: activated Rac has been shown to be critical in recruitment of actin at adhesive sites in the early stages of junction formation[248] and has further impact on junctions by regulating the endocytosis of E-cadherin[248–250].

More than 30 Rac1 effectors have been identified, associated with different cellular functions. Amongst these is IQGAP, notable for its role in regulation of E-cadherin endocytosis[249] and its function as a RhoGAP[251]. P21 protein (Cdc42/Rac)-activated kinase 1 (PAK) is another effector, which is crucial in contact inhibition of proliferation[252] and epithelial cell polarisation[253]. There are also a great number of GEFs and GAPs that regulate the activity of Rac1, many of which have been found to play roles in adherens junction formation and maintenance[228]. Recently the role of CdGAP, known to be critical in the signalling pathway that results in tight junction disassembly following treatment with hepatocyte growth factor[254], has been identified by biochemical means as a GAP for Rac1 that acts as a regulator of cell-cell contact maintenance[255]. In a collaboration with the cell-cell adhesion signalling group at the National Heart and Lung Institute, Imperial College London, we explored the potential of FLIM-FRET measurements to elucidate information on the local regulation of Rac1 activity by CdGAP in the context of adherens junction formation in keratinocytes.

This was addressed using a Raichu probe similar to that used in section 5.1 above. In the Raichu-Rac originally developed in the Matsuda lab[224], the sensor region is Rac1 and the ligand region is the Cdc42/Rac interacting binding domain of the Rac1 effector PAK described above. As with Raichu-RhoA, a C-terminal K-Ras CAAX motif is included in the probe to promote plasma membrane binding in order to improve signal-to-noise, and the plasmid gifted from the Ng lab (Richard Dimbleby Department of Cancer Research, King's College London, UK) used GFP and mRFP as donor and acceptor fluorophores[256], as illustrated in Figure 5-10. Experiments were planned to investigate the spatial distribution of Rac1 activity, measured using the Raichu-Rac FRET biosensor, in response to overexpression of CdGAP. CdGAP is expresses using the pRK5-myc vector; as a control, an empty pRK5-myc vector was used[255].

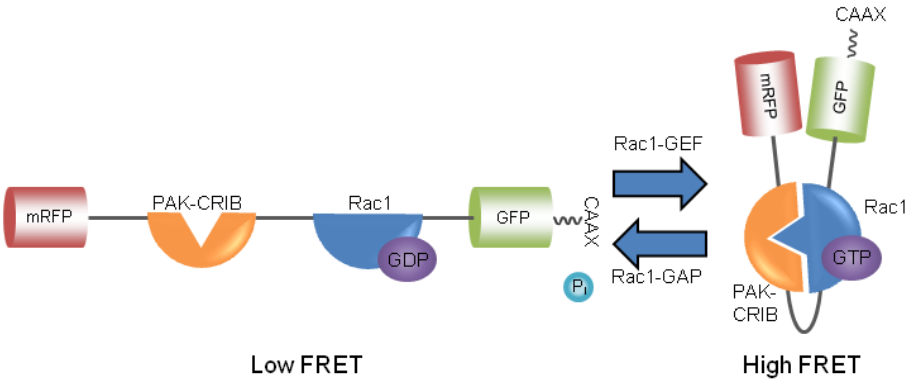

Figure 5-10 Schematic of Raichu-Rac1 FRET biosensor for Rac1 activation mediated by Rac1-GEFs and Rac1-GAPs.
PAK-CRIB: Cdc42/Rac interacting binding domain of P21 protein (Cdc42/Rac)-activated kinase 1, CAAX: Ki-Ras4B CAAX motif allowing modification for membrane association, P_i: inorganic phosphate

5.2.2 Sample preparation

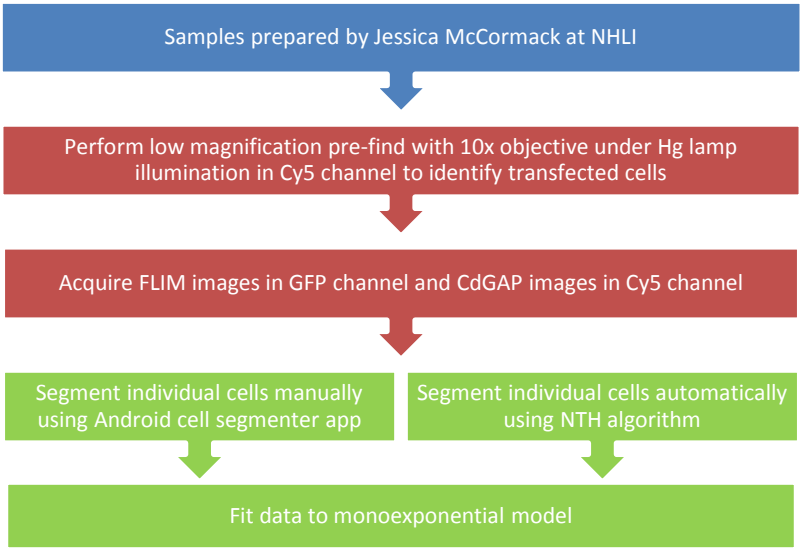

Figure 5-11 Flow chart summarizing the methods used for generation and analysis of Rac1 small GTPase activation samples.
Further details are found in sections 5.2.2-5.2.3.

Cells were cultured as outlined in section 5.1.2. Samples were prepared by Jessica McCormack in the cell-cell adhesion signalling group at the National Heart and Lung Institute, Imperial College London. In the Rac1 experiment described here, a variety of transfection conditions were tried on a single plate to optimise expression level and cell viability at the expense of number of wells per condition (Figure 5-12). Transfections were performed using plasmid DNA diluted in Effectene buffer (Qiagen) and Enhancer added at a ratio of 1:8 Enhancer. Samples were vortexed and incubated for 5 minutes at room temperature. Effectene transfection reagent was added at a ratio of 1:25 Effectene and tubes vortexed prior to 5 minutes' incubation at room temperature. Standard medium was used to dilute the final plasmid DNA mixture which was subsequently added to cells. Media was changed after 4 hours.

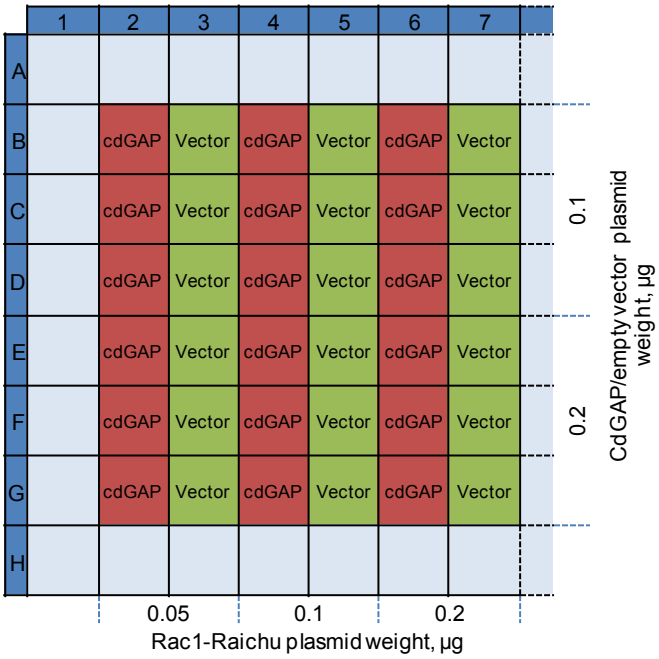

Figure 5-12 Plate map showing transfection conditions across 36 wells for Rac1 experiment
Wells are transfected with Raichu-Rac1 probe and either CdGAP or an empty pRK5-myc vector.

In order that CdGAP levels could be assayed, cells were permeablised using 0.1% Triton X-100 in 10% FCS for 10 minutes at room temperature following fixation with 3% PFA (10 minutes, room temperature). Samples were incubated with primary and secondary antibodies (myc A14 (rabbit, Santa Cruz) and anti-rabbit Cy5 (Jackson Immuno labs)) in 10% FCS-PBS sequentially for 30-60 minutes, followed by nine washes in PBS and three washes in water after each incubation. Each well of the 96-well plates was covered with 150 µl Mowiol before imaging at room temperature.

5.2.3 Image acquisition and analysis

Prior to acquisition of FLIM data, the sample was observed under fluorescent illumination from the mercury lamp through the eyepieces of the microscope. It was found that the majority of cells that fluoresced under Cy5 excitation also exhibited GFP (Raichu) signal. On this basis, the low magnification

cell prefind step was performed only in the Cy5 channel to increase speed, reduce photodamage to cells and to reduce photobleaching of the FLIM donor.

Imaging was carried out at 40x magnification (LUCPFLN 40x, Olympus). FLIM data was acquired in the GFP spectral channel (excitation: 472/30 nm, dichroic: 495 nm, emission: 520/35 nm), with six gates spaced throughout the decay being integrated for 0.5 seconds. A single 0.5 second integration time snapshot per field of view was acquired using Cy5 filters (excitation: 620/60 nm, dichroic: 660 nm, emission: 700/75 nm) in order that expression of CdGAP could be assessed during data analysis. Phase contrast images were also taken at each field of view. 325 fields of view were acquired across 36 wells, leading to a final acquisition time of 70 minutes. A well seeded with untransfected keratinocytes was imaged using the same acquisition parameters as the FLIM experiment to measure the time-varying fluorescent background and a well of 20 μM erythrosine was imaged to provide a reference decay profile.

Prior to fitting FLIM data, fields of view were browsed by our collaborators in a "quality control" process. In the first instance, this served to assess the expression level and cell health across different transfection conditions, leading to one condition (0.05 μg/well Raichu plasmid, 0.2 μg/well CdGAP/empty vector plasmid) being chosen for further investigation. Within this dataset, two approaches were taken to segment cells for fitting. For manual segmentation, the CellSegmenter app (see section 5.1.3) was used to trace the outlines of cells in integrated FLIM images, before it was confirmed by inspection that the chosen cells also exhibited fluorescence in the myc-Cy5 channel. "Lateral membrane" masks were generated from manually assigned masks by erosion and subtraction; our collaborators chose the membrane width parameter to be 3 pixels by inspection. When automated cell segmentation was used instead, cells were first segmented using integrated FLIM intensity images using the NTH algorithms implemented in *FLIMfit* with the parameters outlined in Table 4-2; then resegmented using Cy5-channel images. A MATLAB script was used to reject any cells falling in the acquired fields of view that did not exhibit both GFP and myc-Cy5 signal by a pixelwise AND operation followed by size thresholding.

Parameter	Value
Scale	500
Relative background scale	3
Threshold	0.9
Smoothing	5
Minimum area	1000

Table 5-1 NTH segmentation parameters for automated segmentation of keratinocytes expressing Racihu-Rac1

Data was fitted pixelwise to a monoexponential lifetime model in *FLIMfit* using the measured reference decay profile and time varying background. Mean lifetimes and standard errors were calculated cellwise and presented by condition.

5.2.4 Results

Results of a monoexponential fit to manually segmented lifetime data is shown in Figure 5-13. Exemplar false colour maps showing fitted lifetime images of entire cells, with (lower 8 panels) and without (upper 8 panels) CdGAP overexpression, are presented in Figure 5-13 (a). The fitted lifetime data is presented by condition in Figure 5-13 (b), illustrating the significant increase ($p < 0.0001$, Student's t-test) in lifetime observed across the whole cell when CdGAP is overexpressed. False colour maps showing lifetime in a 3-pixel wide region around the edge of segmented areas are shown in Figure 5-13 (c); lifetime data from images processed in this way is summarised in Figure 5-13 (d). Again, there is a significant increase ($p < 0.0001$, Student's t-test) in fitted lifetime when CdGAP is overexpressed.

For comparison, lifetime data resulting when an automated cell segmentation approach was adopted are also presented. As expected, automated segmentation results in a greater number of "cell" regions being identified (for CdGAP overexpressing cells, N=61 compared to N=16 in manual segmentation case), highlighting the fact that our collaborators were much more discerning in choosing appropriate cells than the automated segmentation algorithm. False colour lifetime maps for the same fields of view as those shown for manual segmentation are presented in Figure 5-14 (a) and lifetime data is summarised in Figure 5-14 (b). As for manually segmented data, there is a significant increase in fitted lifetime in cells overexpressing CdGAP ($p < 0.0001$, Student's t-test).

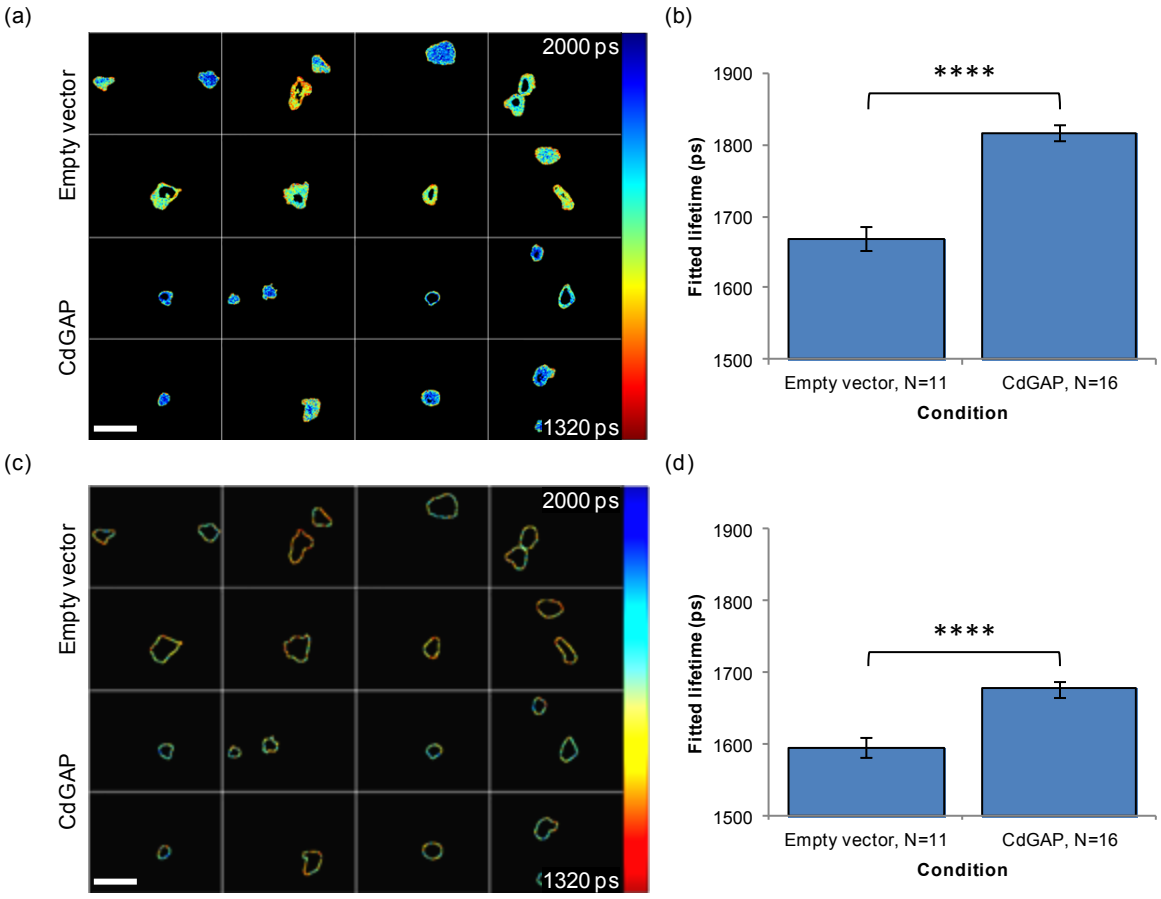

Figure 5-13 Results of experiment investigating Rac1 activation mediated by cdGAP overexpression with manual cell segmentation.

(a) False colour plots showing monoexponential lifetime fit results for typical fields of view in cells with and without overexpression of CdGAP, whole cell analysis. Scale bar = 100 μm. (b) Bar chart summarising monoexponential lifetimes averaged over N manually segmented cells per condition. Error bars show standard errors calculated over N cells per condition. Significance of difference $p < 0.0001$, Student's T-test. (c) False colour plots showing monoexponential lifetime fit results for typical fields of view in cells with and without overexpression of CdGAP, "membrane-only" analysis. Scale bar = 100 μm. (d) Bar chart summarising monoexponential lifetimes averaged over N manually segmented cell membranes per condition. Significance of difference $p < 0.0001$, Student's T-test.

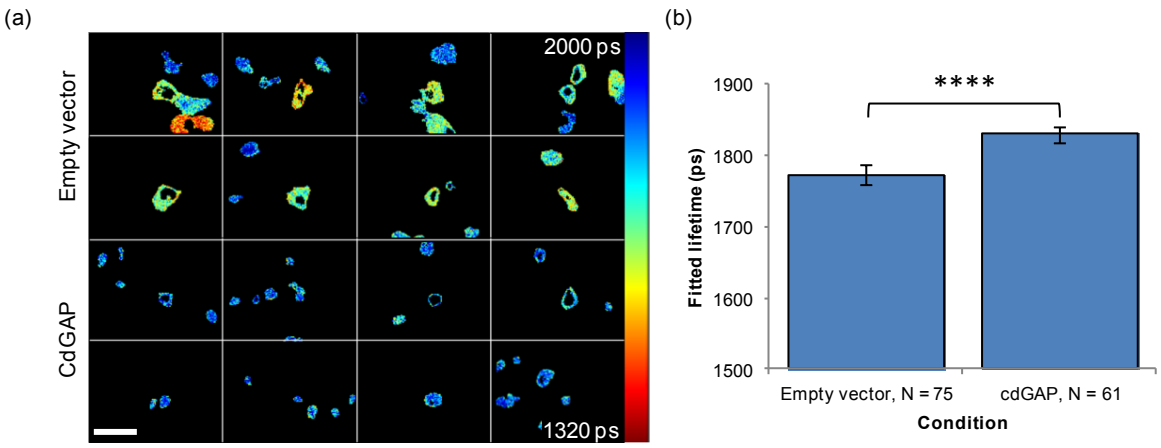

Figure 5-14 Results of experiment investigating Rac1 activation mediated by CdGAP overexpression with automated cell segmentation.

(a) False colour plots showing monoexponential lifetime fit results for typical fields of view in cells with and without overexpression of CdGAP. Scale bar = 100 μm. (b) Bar chart summarising monoexponential lifetimes averaged over N manually segmented cells per condition. Error bars show standard errors calculated over N cells per condition. Significance of difference $p < 0.0001$, Student's T-test.

5.2.5 Discussion

From Figure 5-13 (b) and (d) and Figure 5-14 (b), a very significant increase in monoexponential fitted lifetime reflecting a decrease in Rac1 activity upon CdGAP overexpression is evident across all segmentation methods. This is in accordance with expected results based on biochemical methods[255] as well as the simple model presented above whereby GAP reduces Rac1 activity. Comparing empty vector conditions in Figure 5-13 (b) and (d), it is apparent that lifetimes averaged across membranes are shorter than those averaged over whole cells, indicating that Rac1 is more likely to be active at the membrane than in the cytosol[257]. Taken together, these figures illustrate that Rac1 activity is reduced by expression of CdGAP both globally and locally at lateral membranes in keratinocytes[255].

It is instructive to reflect on the differences in lifetime results generated by the different segmentation methods employed. For keratinocyte samples, there was significant variation in cell size and shape within the set of cells deemed "acceptable" by manual quality control, leading to difficulties in successfully automating the segmentation process. This is compounded by the presence of fibroblasts that were cocultured to increase the longevity and proliferation of keratinocytes, and which express the fluorescent constructs at high levels (as shown in Figure 5-4 above). This effect may explain the differences observed comparing Figure 5-13 (b) and Figure 5-14 (b). The average change in lifetime associated with manually segmented whole cells is approximately four times greater than that observed in the case of in the automated segmentation, indicative of the inclusion of non-responding, unhealthy cells or subregions of bright fibroblasts by the automated segmentation algorithm. Accurate segmentation is especially critical when lateral membrane masks are generated, since missegmented pixels make up a greater proportion of the masked area compared to the case in which the whole cell is segmented. In the case observed here, where cells are in a confluent monolayer, poor segmentation may include more of the internal cell area

than desired, and may impact results by decreasing the dynamic range in observations of a probe that is activated primarily at the lateral membrane. On these grounds, following inspection of segmentation masks generated for whole regions, no attempt was made to adapt these masks to generate lateral membrane masks.

5.3 Summary

The results included in this section further illustrate the ability of the FLIM plate reader to generate statistically significant results utilising FLIM of FRET biosensors in the face of small lifetime changes and biological noise. While Z' analysis of the RhoA experiment indicates that this technique may not have sufficient separation between positive and negative controls to be useful in a screening context, it has nevertheless proved possible to gain insight into the spatio-temporal activation profile of RhoA in calcium switch modulation of adherens junction formation. In a parallel project, the FLIM plate reader has been successfully deployed in a study of Rac1 activation in response to overexpression of CdGAP, adding to the understanding of the spatial profile of Rac1 modulation by this GTPase activating protein. For both studies, the FLIM plate reader has been demonstrated to be a potentially useful tool to be used by our collaborators alongside biochemical methods[255]. Finally, a manual cell segmentation app has been developed in order to increase segmentation accuracy and decrease time expended when it is decided that automated segmentation does not perform sufficiently robustly to be used for region-of-interest analysis of small- to medium-sized data sets.

5.4 Future work

Due in part to the relatively short running time of the Kickstart and EuroBioimaging projects, progress in both studies presented here was stopped before all the goals of the initial proposals were achieved. In both cases, knowledge gained during the study – particularly in terms of optimisation of sample conditions and generation of manual segmentation masks – could be applied to confirm the findings presented here and further investigate GTPase signalling during cell-cell junction formation. In particular, it may be productive to revisit RhoA experiments with a newly optimised E-cadherin staining protocol in order that segmentation might be performed to investigate RhoA activation specifically at sites of junction formation. Without immunofluorescence staining of E-cadherin, which requires fixation and permeablisation of samples, it may also be possible to take advantage of the incubator and automated liquid handling attached to the FLIM plate reader to attempt live cell time lapse imaging of RhoA activation in response to stimulation with $CaCl_2$.

As outlined in the original project proposal for the EuroBioimaging study, having established a protocol for probing activation of small GTPases in the context of cell-cell junction formation in keratinocytes, it may prove productive to investigate the effect of overexpression of different GAP and GEF proteins in a single plate screen experiment, probing activity of either RhoA or Rac1. This work could be extended multiplexing more than one biosensor to gain a fuller understanding of the interplay of signalling

molecules at adherens junctions. Whilst the work included here is undertaken with the target of investigating the basic biology of junction formation, future studies might be used to characterise potential treatments for dermatological conditions.

From an instrumentation perspective, it should be relatively simple to port the manual cell segmentation host-side software to Python for inclusion in a CellProfiler plugin, at which point the whole software project could be made available as an open-source tool: an intermediate step would be to rewrite the front end in Java, removing the need for a MATLAB licence for development of this aspect. Interfacing between the host PC and the touch screen device using WiFi Direct would improve security at the expense of compatibility with versions of Android older than Ice Cream Sandwich. Another alternative that offers increased security at the expense of data transfer rate would be to use Bluetooth protocols. Improvement in segmentation performance and speed might be afforded by approaching a semi-manual technique: it might be possible to assess the intensity gradient perpendicular to a manually drawn outline and use this information to draw an accurate mask more quickly. Alternatively, the manual cell segmentation tool outlined here might be used to generate a training set over a small subset of data for a machine learning algorithm, which might then be applied to generate automated masks over a much larger dataset.

Chapter 6: Autofluorescence

In previous chapters, the potential of high content FLIM assays has been explored through the development of a fully automated plate reading microscope, and by its application to experiments reading out biologically relevant parameters through fluorescence lifetime imaging. In the studies presented thus far, all experiments have used visible wavelengths to excite exogenous fluorophores, and have read out biological parameters by measuring fluorescence of fluorescent protein constructs. By contrast, the aim of this element of my PhD project was to investigate the feasibility of deploying an automated plate reading FLIM microscope to measure lifetimes of endogenous fluorescence signals from biological samples by adapting it for use with UV-wavelength excitation.

Cellular autofluorescence is a familiar phenomenon to many biologists making fluorescence measurements. Background originating from endogenous fluorophores can be difficult to distinguish from signal if fluorescent protein expression or staining is weak. On the other hand, cellular autofluorescence can itself be used to report on biologically relevant phenomena. In particular, imaging of the endogenous fluorescence associated with metabolites can yield information on the metabolic state of the cell whilst removing the necessity to introduce exogenous fluorophores to the sample. Alternatively, as structural proteins are a source of tissue autofluorescence, lifetime imaging of tissue samples can inform on degradation of such proteins in the progression of disease. Both of these aspects of autofluorescence lifetime imaging have been explored using the FLIM plate reader in the course of my PhD project.

In this chapter,

- The roles played by endogenous fluorescent species in metabolism and disease are summarised.
- Specifics of instrument design, experimental methods and data analysis relating to UV-wavelength excitation experiments are discussed.
- Cell-based assays using known metabolic modulators and anti-cancer drugs are presented to illustrate the potential for using autofluorescence lifetime to read out metabolic state in the context of high content analysis assays.
- Experiments investigating the possibility of using autofluorescence lifetime to discriminate between cell lines exhibiting different drug sensitivities are presented.
- The applicability of the FLIM plate reader as a tool to validate results from a study using autofluorescence lifetime to monitor the progression of osteoarthritis is considered.

6.1 Biological background to cell autofluorescence imaging

In studies of cellular autofluorescence, the source of signal is generally considered to be one or more fluorescent species associated with metabolism. These include reduced nicotinamide adenine dinucleotide, flavins and reduced nicotinamide adenine dinucleotide phosphate. This section aims to provide context for the experiments carried out using the plate reader by offering a summary of the roles played by these species in cellular metabolism. The importance of cellular metabolism in the context of studies of disease is highlighted. Finally in this section, means by which cells can be driven to different metabolic states for the purposes of investigating their effects on fluorescence parameters are outlined.

6.1.1 Reduced nicotinamide adenine dinucleotide

The particular metabolite that is most commonly imaged in fluorescence studies is the coenzyme reduced nicotinamide adenine dinucleotide (NADH). The oxidised form of the molecule (NAD^+) plays roles in cell signalling, notably as a substrate for the poly(ADP-ribose) polymerase (PARP) protein family, and is implicated in regulation of structure and function around the genome as well as involvement in apoptotic and necrotic cell death pathways[258,259]. The classical role of NADH/NAD^+ in cells is, however, in redox reactions, specifically those associated with metabolism. Since aberrant metabolism is a hallmark of cancer (section 6.1.4) and other disease states, there is significant interest across the life sciences in understanding mechanisms by which dysregulation of elements of cellular respiration pathways might occur.

The process of cellular respiration that converts nutrients such as glucose to adenosine triphosphate (ATP), sometimes known as "the energy currency of the cell", involves multiple pathways. Oxidation and reduction reactions involving NADH are crucial steps in these pathways; thus the redox state, localisation and binding state of this coenzyme are linked to the metabolic behaviour of the cell. Figure 6-1 presents an overview of glucose metabolism to ATP in animal cells, with particular focus being placed on the role of NADH in each process[260]. For completeness, the equations relating to chemical reactions involved in different pathways involved in glucose metabolism are presented in Table 6-1. Elements of Figure 6-1 are discussed briefly below, stressing in particular the steps at which NAD/NADH binding occurs, in order to present a background to the experiments performed during this project.

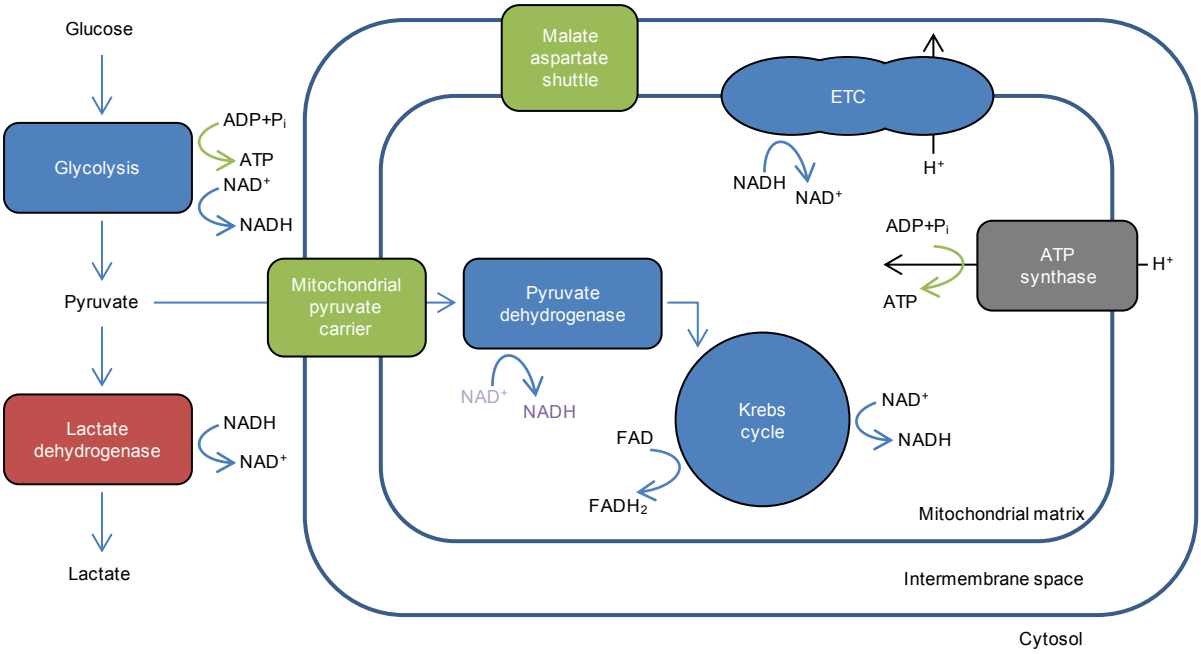

Figure 6-1 Schematic of major metabolic pathways involving NADH.
ADP – adenosine diphosphate; Pi – inorganic phosphate; NAD – nicotinamide adenine dinucleotide; FAD – flavin adenine dinucleotide; ETC – electron transport chain. Note that $FADH_2$ oxidation by Complex II of the electron transport chain is omitted for the sake of clarity. Note also that stoichiometry has been ignored here for clarity; see Table 6-1 for details.

Process	Equation
Glycolysis	$Glucose+2P_i+2ADP+2NAD^+ \longrightarrow 2Pyruvate+2ATP+2NADH+2H^++2H_2O$
Lactate dehydrogenase	$Pyruvate+NADH+H^+ \leftrightarrow L\text{-}lactate+NAD^+$
Pyruvate dehydrogenase	$Pyruvate+CoA+ NAD^+ \longrightarrow acetyl\ CoA+CO_2+NADH$
Krebs cycle	$Acetyl\ CoA+3NAD^++FAD+GDP+P_i+2H_2O \longrightarrow 2CO_2+3NADH+FADH_2+GTP+2H^++CoA$
ETC	$2NADH+O_2+2H^+ \longrightarrow 2H_2O+2NAD^+$
ATP synthase	$ADP+P_i+H^+ \longrightarrow ATP+H_2O$

Table 6-1 Chemical equations showing substrates and products at key stages in cellular respiration.

Glycolysis forms the first step of ATP generation from molecular glucose, and occurs in the cytosol of cells. Since it requires no oxygen, it is referred to as an anaerobic process. For each molecule of glucose that undergoes glycolysis, there is a yield of 2 ATP and 2 NADH molecules, meaning that glycolysis alone therefore provides relatively little useful energy. Glycolysis is a 10 step process utilising ten different enzymes: in the context of NADH studies, step six is the most relevant, as it is at this stage that NADH is produced from NAD^+ in a reaction mediated by glyceraldehyde 3-phosphate dehydrogenase.

In the absence of oxygen, anaerobic respiration continues and pyruvate is broken down in the cytosol into lactate. The enzyme lactate dehydrogenase (LDH) catalyses this fermentation, during which NAD^+ is regenerated by oxidation of NADH, allowing glycolysis to continue. This reaction is reversible, meaning that pyruvate and NADH can be generated from lactate and NAD^+ when oxygen is readily available, for example in cells in the heart. The fact that LDH is highly active means that an equilibrium is established between the substrates (pyruvate and lactate) and free nucleotides (NAD^+ and NADH); the existence of such an equilibrium has been used previously to investigate the ratio of free NAD^+ to NADH using lactate and pyruvate concentrations as a surrogate measurement[261], though recently published work has illustrated the care that must be taken with this approach[262]. LDH-NADH binding has been studied using fluorescence spectral, lifetime and polarisation measurements[263–265].

If oxygen is present, pyruvate generated from glycolysis may be used to generate further ATP in the mitochondria. Ionic pyruvate is transported across the inner mitochondrial membrane by mitochondrial pyruvate carrier protein (MPC)[266] where it is decarboxylated by the pyruvate dehydrogenase complex. This complex comprises 96 subunits in total, with three distinct enzymes represented in different ratios. NADH is generated from NAD^+ by the third enzyme in the process, dihydrolipoyl dehydrogenase.

Acetyl coenzyme A (acteyl CoA) is the other product of the pyruvate dehydrogenase complex, and is the substrate for entry into the citric acid cycle, also known as the Krebs cycle. This 8-step process generates three NADH molecules per acetyl CoA. NAD^+ reduction is mediated at three steps by isocitrate dehydrogenase, the α-ketoglutarate dehydrogenase complex and mitochondrial malate dehydrogenase (mMDH). Like LDH, fluorescence techniques have been used to investigate properties of NADH binding to mMDH[264,267], and we have used this protein to make *in vitro* measurements in the plate reader (section 6.5.3).

Malate dehydrogenase is also present in the complex of proteins that makes up the malate-aspartate shuttle[268]. Since the inner mitochondrial membrane is impermeable to NADH, this system of proteins acts first to form malate from NADH and oxaloacetate. Malate is passed across the membrane by an antiporter; a second malate dehydrogenase in the mitochondrial matrix then generates NADH and oxaloacetate from malate and NAD^+. In this way, NADH generated from glycolysis may effectively be passed into the matrix of the mitochondria in order to maximise the ATP output from respiration.

Oxidative phosphorylation is the final step in aerobic respiration in animal cells. In the electron transport chain (ETC), electrons are first donated by NADH, produced in earlier in the respiration process, to NADH dehydrogenase (also known as complex I). Electrons are passed down the ETC, facilitated by reduction of ubiquinone and cytochrome c, to the final protein in the chain, cytochrome c oxidase (complex IV). Here, oxygen acts as the sink for the electrons as it is reduced to water. The free energy released by successive electron transfer steps is effectively converted to a chemical potential, as proton pumping occurring at each stage of the ETC builds up an electrochemical gradient across the inner

mitochondrial membrane between the mitochondrial matrix and the intermembrane space. The oxidation of NADH is then coupled to phosphorylation of ADP to ATP by complex V, or ATP synthase: the proton motive force is used to provide the free energy for the unfavourable reaction $ADP + P_i \rightarrow ATP$. Enhancement of NADH fluorescence intensity and lifetime upon binding to complex I has been investigated previously[269,270]. Proteins involved in oxidative phosphorylation are targets for treatments that are typically employed to modulated the metabolic signature of cells, and that have therefore been employed in the validation of lifetime as a readout for metabolic state. The metabolic modulators used in this thesis are described in section 6.1.5.

6.1.2 Flavins

Though not examined in these studies, flavin adenine dinucleotide (FAD) is another important metabolite in an imaging context, since different forms of flavoproteins exhibit different fluorescent properties. Lipoamide dehydrogenase (LipDH)-bound FAD is crucial as an intermediary in the generation of NADH, both in the pyruvate dehydrogenase complex and in the α-ketoglutarate dehydrogenase complex that reduces NAD^+ to NADH in the Krebs cycle. $FADH_2$ generated in the Krebs cycle as succinate is oxidated to fumarate and remains associated to the succinate dehydrogenase protein, which is found at the inner mitochondrial membrane[271]; this protein is also known as electron transport chain Complex II, as the subsequent reduction of the associated $FADH_2$ back to FAD donates electrons to carriers in the ETC. In addition to pathways relating to glucose metabolism, flavoproteins are involved in β-oxidation, in which fatty acids are metabolised to acetyl-CoA and the donation of electrons to the ETC is mediated by FAD and electron transfer flavoprotein. It is notable that in investigations as to the origin of FAD fluorescence, 50% of fluorescent signal was attributed LipDH-associated FAD, 25% was tentatively linked to electron transfer flavoprotein-associated FAD, and another 25% was found to be discrete from the respiratory chain: Complex II-bound FAD was found to contribute negligibly to overall fluorescent signal[272]. Despite the complexity relating to the origin of FAD fluorescence in metabolic pathways, it has nevertheless been a useful tool in examining cell metabolism as outlined in section 6.2 below.

6.1.3 Nicotinamide adenine dinucleotide phosphate

NADPH is a closely related compound to NADH, differing only in chemical structure by the addition of a phosphate group on the ribose ring. As such, the fluorescent properties of NADPH are similar to those of NADH as discussed in section 6.2 below, and so the role played by NADPH in the cell is relevant to studies of cellular autofluorescence. NADPH is generated though the pentose phosphate pathway in which ribose 5-phosphate, which is required for nucleic acid synthesis, is also a product. NADPH is also formed following the series of reactions governing transfer of oxaloacetate from the cytosol to the mitochondria in the process of fatty acid synthesis. NADPH plays a further role in the generation of fatty acids, as 14 molecules are oxidised to form palmitate, which is a precursor for all other fatty acid formation. NADPH is recognised as an important factor in cellular response to oxidative stress: it is key to the generation of reduced glutathione, which is, in turn, a mediator of reactive oxidative species by the

action of glutathione peroxidase. NADPH also reactivates catalase after it binds H_2O_2, recovering its activity for further disposal of hydrogen peroxide[273]. The roles of reactive oxygen species as modulated by NADPH in pathways linked to disease are discussed briefly in the following section.

6.1.4 Cellular metabolism, redox state and disease

Since the work of Otto Heinrich Warburg in the 1920s, the role of cellular metabolism in cancer has been recognised[274]. The Warburg effect describes the shift in energy generation pathways from oxidative phosphorylation preferred in normal cells to glycolysis prevalent in tumour cells. There are many reviews, including those of Vander Heiden et al.[275] and Cairns et al.[276], that discuss this effect and seek to put it in context within the wider scope of cancer cell signalling. In contrast, shifts towards greater dependence than normal on oxidative phosphorylation (the "inverse-Warburg effect") have been observed in the development of Alzheimer's disease[277]. As discussed in section 6.1.1, NADH binds to different enzymes according to energy generation mechanism; therefore NADH binding is closely linked to the Warburg effect. It follows that the ability to read out NADH binding state may inform on the progression of cancer via the Warburg effect.

The *redox state* (or *redox environment*) of a cell typically refers to the ratio of oxidised-to-reduced species in one or more redox couples, for example NAD^+:NADH, FAD:FADH, or glutathione disulphide:glutathione[278]. The presence of reactive oxygen species in cells is linked to redox state and in particular the ratio of NADH to NAD^+[279]. High levels of NADH correspond to an oxygen-reducing environment in which reactive oxygen species population increases[280]: such changes have been linked to apoptotic cell death[281]. Dysregulation of pathways linked to the generation or scavenging of reactive oxygen species associated with aberrant redox state has been associated with type II diabetes[282], fibrosis[283] and cancer. In the latter case, the mechanisms for the pathological outcome have been attributed to DNA damage and disruption of gene regulation[284].

6.1.5 Means of modulating metabolic state *in vitro*

In order that attempts can be made to associate measured changes induced in cells by treatments with drugs of interest with cellular mechanisms, cells may be driven towards different metabolic states by chemical stimulation. Compounds are identified that enhance or inhibit oxidative phosphorylation, inhibit glycolysis, and induce apoptosis or necrosis and are described here.

Rotenone

Rotenone is a compound that is a known poison of NADH dehydrogenase, also known as Complex I in the electron transport chain (ETC), upon which it acts by preventing the transfer of electrons to ubiquinone[285]. By interrupting the progression of the ETC, rotenone effectively inhibits oxidative phosphorylation. Inhibition of the progression of the ETC prevents the oxidation of NADH to NAD^+; since the citric acid cycle may still be producing NADH, this has the effect of increasing the concentration of (free) NADH in mitochondria. This provides an alternative to cyanide compounds used

in many other studies as a means of disrupting the ETC by competing at the oxygen binding site of Complex IV.

FCCP

Carbonyl cyanide 4-(trifluoromethoxy)phenylhydrazone (FCCP) is widely used in metabolic studies to uncouple ATP synthesis from the electron transport chain. FCCP is an ionophore – a molecule capable of transferring ions across lipid membranes – that acts to disrupt the H^+ gradient across the mitochondrial membrane established by the electron transport chain. This is said to "uncouple oxidation from phosphorylation"[286] and increase the rate of NADH oxidation in the ETC in order to re-establish the gradient. This in turn causes a shift away from the reduced form in the NADH:NAD equilibrium, which is linked to an increase in the bound fraction of NADH.

2-deoxyglucose

2-deoxyglucose (2DG) is a glucose analogue in which a hydroxyl group is replaced by a hydrogen. This modification prevents 2DG from undergoing glycolysis. Since 2DG acts as a competitive inhibitor that replaces glucose in the glycolysis pathway, treating cells with 2DG effectively inhibits glycolysis. In addition, treatment with 2DG partially inhibits oxidative phosphorylation since this pathway is partially glycolytic-dependent[287], though the ability of the Kreb's cycle to run on the products of amino acid and fatty acid metabolism means that oxidative phosphorylation can continue. Reflecting this, studies measuring the concentrations of lactate and pyruvate in cells have shown that treatment with 2DG results in a decrease in the free NADH to NAD^+ ratio in primary fibroblasts[288]. Since tumour cells are typically more dependent on glycolysis than non-cancerous cells, 2DG has been investigated as a potential anti-cancer therapy[289].

Staurosporine

Apoptosis is of interest in the study of cancer and cancer therapies: dysregulation of programmed cell death can result in carcinogenesis and in resistance to treatments that act by inducing apoptosis. Therefore, the ability to detect apoptosis non-invasively in its early stages is relevant in the context of drug screening and basic oncology. Mitochondria are known to play a crucial role in apoptosis. In particular, mitochondrial permeability transition results in the breakdown of the mitochondrial membrane potential that is crucial for the progression of oxidative phosphorylation. Staurosporine (STS) is commonly used in cell biology studies as a means of inducing caspase-3-mediated apoptosis, achieved by its action as an ATP-competitive protein kinase inhibitor[290].

Hydrogen peroxide

Hydrogen peroxide (H_2O_2) is a reactive oxygen species that is a product of oxidative phosphorylation: if electrons are "leaked" from the electron transport chain, aberrant transfer to molecular oxygen results in the formation of superoxide which can then be converted to H_2O_2 by superoxide dismutases. Elevated levels of intracellular H_2O_2 are linked to necrosis (crudely, premature cell death); treating cells with H_2O_2

can be used to induce necrosis by oxidative stress. It has also been reported that exposure to H_2O_2 at lower doses can result in apoptotic cell death[291]. As in apoptosis, the mitochondrial membrane has been reported to undergo a permeability transition as necrosis progresses[292]; this is linked to the characteristic mitochondrial swelling in necrosis as water influx into mitochondria increases. The permeability transition is also linked to depletion of ATP and NADH.

6.2 Fluorescence as a means of studying metabolism

As outlined in section 6.1.4, examining the redox state – reported by the balance between NADH and NAD^+ – of the cell can inform on pathologies and abnormal cell function[293]. Biochemical methods, including measurements of pyruvate and lactate mentioned previously, have the drawback of using cell extracts and therefore are not suitable for reading out dynamic changes in live cells. Various fluorescence techniques have be used to report on redox state, including those using exogenous fluorescent biosensors[294]. We concentrate, however, on imaging of endogenous fluorescence associated with metabolism.

NADH is fluorescent under ultra-violet excitation, with excitation and emission peaks around 340 nm and 450 nm respectively (Figure 6-2). Despite low brightness and concentration of NADH in many cell types, it is nevertheless possible to use the coenzyme as an endogenous fluorophore both in single photon and 2-photon excitation microscopy. In contrast, the oxidised form of the coenzyme, NAD^+, is non-fluorescent at these wavelengths. NAD^+ does, however, share an absorption peak with NADH at shorter wavelengths (~250 nm): it is therefore possible to calculate the ratio between reduced and oxidised coenzyme by measuring absorption spectra and calculating the ratio of absorbance values at 250 nm and 340 nm[295,296]. However, this is impractical in cell specimens, due to the presence of other molecular species which absorb at similar wavelengths in the ultraviolet[297]. Another means of gauging the redox ratio by optical methods was proposed by Chance in 1979[298], and is based on the fact that unlike NADH, it is the reduced form of $FADH_2$ that is non-fluorescent whilst FAD has a fluorescence signal with excitation and emission peaks around 450 nm and 550 nm respectively: therefore, flavoprotein and NADH fluorescence signals react oppositely to changes in redox state. Defining optical redox ratio[299] as $I_{FAD}/I_{FAD} + I_{NADH}$, ratiometric measurements of redox-related fluorescence emission can be made with a single wavelength of excitation light (two photon), which helps to minimise the complicating effects of excitation fluctuation, sample scattering, fluorophore concentration and absorption of either excitation or emission light by other endogenous fluorophores[300]. Subsequent published work has shown correlation between changes in redox ratio and cell metabolism, and linked such changes to various pathologies[149,301–303]. Despite the many potential applications of optical redox ratio in studies of cell metabolism, it should be noted that differences in NADH quantum yield and emission spectrum are induced upon binding and can potentially complicate interpretation of such measurements[304].

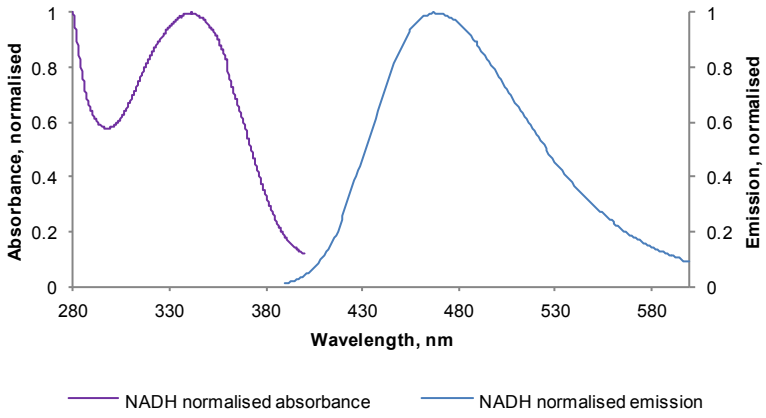

Figure 6-2 Measured NADH absorption and emission spectra
Spectra measured from 50 μM solutions of NADH in MilliQ pure water. Absorption spectrum measured using a spectrophotometer (UV3101-PC, Shimadzu); emission spectrum measured using a spectrofluorimeter (RF-5301 PC, Shimadzu).

Another relevant reporter on cell metabolism is the pattern of NADH binding – the ratio of free to protein-bound NADH, and which proteins NADH is bound to[305,306]. It has previously been established that protein binding causes a shift in the emission peak of NADH[297,307]; thus spectrally-resolved measurements can provide insight into the ratio of free to bound NADH. Similarly, it is possible to use fluorescence lifetime imaging to infer the binding state of cellular NADH, since it is well known that protein binding generally increases the fluorescence lifetime[5]. This change is generally attributed to the presence of an adeneine moiety in close proximity to the fluorescent reduced nicotinamide group that acts as a quencher when NADH is in a folded conformation[308], as is the case for a large proportion of molecules free in solution. When NADH binds to a protein, however, it is typically in an extended conformation, leading to decreased quenching and longer measured lifetime. In general, two or more NADH-associated decay components are observed within pixels in a cell image: crudely, these might be separated into free (short lifetime) NADH and protein bound (long lifetime) NADH components. In practice, there are found to be at least two components in free NADH lifetime decays that are associated with folded and extended NADH[264] and so the "bound" NADH decays depend on the population of binding partners and can therefore be complex. Despite the possible complexity of fitting and interpreting NADH lifetime data, the use of a biexponential decay model is often found to be useful; furthermore, FLIM renders measurements inherently ratiometric and thus less susceptible to laser fluctuations, scattering and spectrally-varying attenuation in the instrument or sample.

As stated in the previous section, NADPH is closely related to NADH in structure and hence fluorescence spectra, and is also involved in many disease pathways for which the study of NADH might be of interest. It is therefore a concern that the presence of this closely related coenzyme in cells might confound interpretation of readings in both FLIM and intensity-based readouts of metabolism in which only the effects of NADH on autofluorescence are considered. Previous investigations have, however, shown that in certain cell types NADPH is at least five times less abundant than NADH[309]. Combined

with the lower quantum yield of NADPH compared to NADH, this signal has therefore previously not been considered significant in many studies in literature[304]. A paper published recently by the Duchen group adopts a contrary standpoint[310]; the consequences of this work are discussed in section 0 below0 below.

Experiments in which metabolism is modulated in a predictable fashion have shown correlation between redox state and NADH binding without necessarily offering mechanistic explanations for the association. In some cases it may be sufficient to suggest that increasing the total concentration of NADH while keeping the number of available binding proteins constant will simultaneously increase the proportion of unbound NADH and the ratio NADH/NAD^+, for example if an NADH-generating step such as glycolysis runs unusually quickly, or an NADH sink step such as oxidative phosphorylation is inhibited. Alternatively, protein-bound NADH can be considered an intermediate in the generation of free NAD^+ from free NADH; thus the more significant the bound component of NADH, the lower the redox ratio of the cell. It has also been suggested that the most significant modification of NADH lifetime occurs as a consequence of binding complex I in the electron transport chain[270], such that increased NADH binding is associated with enhanced oxidative phosphorylation[305] or a shift away from glycolysis. There is some conflict in literature on the matter of the degree to which NADH lifetime and redox ratio imaging correlate: this had previously been illustrated[311], but Walsh *et al.* recently performed experiments in which no correlation between redox ratio and NADH lifetime was found to exist[312]. It is not unreasonable to suggest that though the two measurements probe related processes, they cannot be considered to read out exactly the same cellular parameters.

6.3 Application of FLIM to NADH imaging

It is evident from work cited in the preceding sections that there is significant complexity inherent in NADH binding in cells that makes a mechanistic interpretation of NADH lifetime data challenging. Nevertheless, there has been a significant body of work illustrating correlation between various metabolic events and NADH lifetime since Lakowicz first demonstrated FLIM of NADH in 1992[267]. Fluorescence lifetime of NADH in cells has been shown to decrease in the presence of high levels of extracellular glucose[313], upon serum starvation, and upon reaching confluence for certain cell types[314]. Direct inhibition of oxidative phosphorylation by poisoning of ETC elements[305] or by inducing hypoxia shows a shortening of mean NADH lifetime associated with an increase in the free fraction of NADH. Conversely, treatment with mitochondrial uncouplers that increase the activity of the ETC by decoupling oxidation from phosphorylation have been shown to result in an increase in NADH lifetime[265], as does treatment with an inhibitor of the glycolytic pathway, deoxygluocose[315,316]. In the context of reading out cytotoxicity by lifetime measurements, it has been shown that inducing apoptosis in cells using staurosporine results in an increase in lifetime[317,318].

Of particular interest in the context of translating NADH lifetime imaging from the lab to the clinic are studies showing differences in measured lifetimes between cancerous and non-cancerous cells and tissues,

in which shortening of fluorescence lifetime is linked to a shift towards glycolytic metabolism – the "Warburg effect"[299]. It should be noted, however, that changes in lifetime have subsequently been shown to depend on the classification of the cancer cells examined, potentially complicating the use of NADH lifetime as a diagnostic tool[312]. NADH lifetime has also been shown to be affected as cells enter apoptosis triggered by treatment with staurosporine[305,318,319]. Once again, however, caution must be exercised due to the potentially complex nature of changes in NADH binding profiles. Recently, the metabolic changes associated with stem cell differentiation have been investigated by measuring NADH lifetime in an attempt to monitor stem cell differentiation by non-destructive means[320–322].

To date, cellular NADH lifetime imaging experiments have almost exclusively been carried out using two-photon excitation of NADH fluorescence. Such experiments benefit from optical sectioning inherent to the technique, providing less out-of-focus blur compared to wide field imaging and meaning that areas of the sample outside the focal plane are not subjected to phototoxic effects[320]. Moreover, using time correlated photon counting to measure lifetimes means that such experiments are highly photon efficient. However, the need to scan the excitation spot sequentially across pixels in an image and the nonlinear relationship between excitation power and photobleaching/photodamage lead to such techniques having limited applications in studies where higher throughput is desirable. In the development of the automated FLIM plate reader discussed below for use in NADH imaging studies, we have demonstrated that high content NADH imaging is feasible: thus assays that are typically performed in high content formats, including drug screens and dose response studies in the context of cytotoxity, may be deployed using NADH lifetime as a potential output parameter.

6.4 UV-specific instrument development

For certain aspects of the design of the FLIM plate reader, design decisions were made with autofluorescence applications in mind. The imaging objective (Olympus LUCPLFLN 40x, NA 0.6) was chosen in part for its advertised suitability for use with UV excitation. Of the GOI units available in the lab, an HRI with an S20 cathode was chosen for sensitivity in the blue spectral region corresponding to the NADH emission peak for autofluorescence studies. For wide field imaging, a multimode fibre with UV transmitting properties was chosen (M67L02, Thorlabs), and the diffuser wheel UVT substrate was also picked for compatibility with autofluorescence studies. A light path for coupling UV wavelengths into the optical fibre was constructed making use of an asphere suitable for transmission at short wavelengths (A397TM-A, Thorlabs), in contrast to the case for the visible light path in which a 20x 0.5 NA microscope objective is employed.

Early experiments were conducted using a Mira 900F (Coherent) Ti:Sapphire laser source pumped by a Verdi (Coherent) diode-pumped solid state laser, with the infra-red output being frequency doubled using a 5-050 Ultrafast SHG/THG unit (Inrad). Later in the project, a MaiTai HP (SpectraPhysics) Ti:Sapphire system became available – this was preferred as an excitation source for subsequent experiments as alignment procedures are comparatively simple when changing from visible wavelengths employed by

other users of the lab bench to UV excitation. Essentially, the MaiTai is capable of automatically maximising power output and ensuring mode locking for a given selected output wavelength. The only realignment that must be done when making significant changes to excitation wavelength is in the frequency doubler (3980 Frequency doubler/pulse picker) to ensure that the crystal remains at the optimal angle for SHG and that collimation of the output is maintained. A generalised schematic showing the light path in the FLIM plate reader for UV-wavelength studies is shown in Figure 6-3.

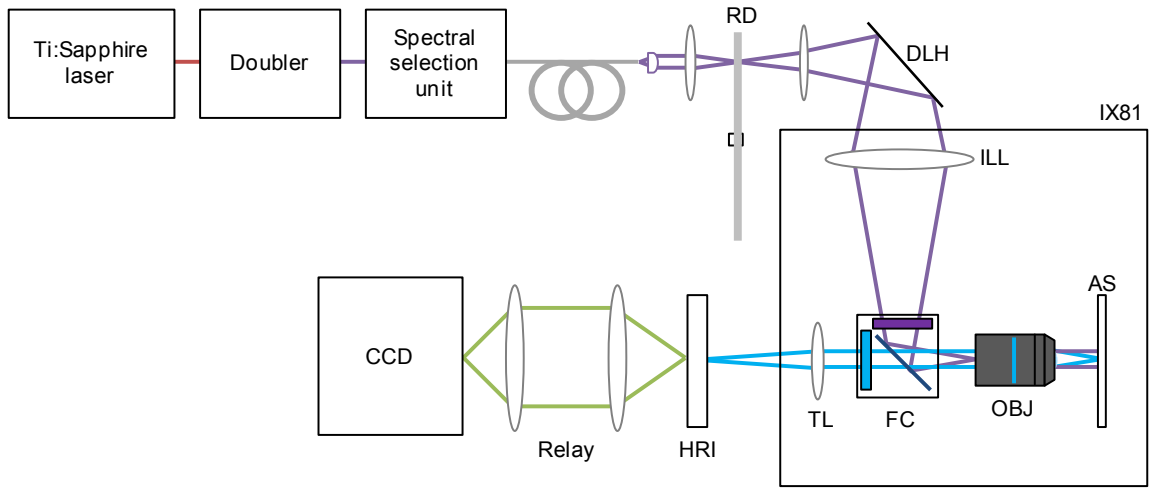

Figure 6-3 Schematic showing the optical path for wide filed time gated FLIM acquisitions using UV-wavelength excitation on the FLIM plate reader.
RD: rotating diffuser, DLH: dual lamp house unit mirror, FC: filter cube, OBJ: objective, AS: automated stage, TL: microscope tube lens, HRI: high rate imager.

6.5 Characterisation and solution-based experiments

6.5.1 Fitting UV-excited FLIM data

In order to accurately fit complex decay models, it is necessary to measure either an instrument response function directly using a scattering object, or a reference dye with known lifetime which may be combined with the model function via reference reconvolution[107]. The former course is impractical using the plate reader: the filterset, chosen to minimise excitation light leakage in normal operation, does not transmit sufficient signal for a scatter IRF to be recorded, and it is not practical to remove the barrier filter from the filter cube in the course of an experiment without seriously disrupting the imaging arm. One solution might be to use one position of the filter cube cassette for a beam splitter that would enable a scatter IRF to be taken more easily (allowing for possible shifts due to different filters between experiment data and IRF); however, the use of the plate reader with a wide variety of fluorophores and the need to retain one empty cassette position for sectioned imaging precludes this option. It is therefore desirable to account for the instrument response using a reference dye.

Lakowicz et al. have suggested a range of short lifetime reference dyes excitable at UV wavelengths[5]. Of these, few are commercially available. DCS (4-[(E)-2-[4-(dimethylamino)phenyl]ethenyl]benzonitrile, MolPort) was acquired and tested but was found to be difficult to dissolve in solvents that were

compatible with plastic walled plates. Other researchers have used 2-[4-(dimethylamino)styryl]-1-methylpyridinium iodide (DASPI) excited at 360 nm to record an IRF, using the fact that the lifetime of this dye is shorter than the response of the detection system to justify treating the resulting decay as a scatter IRF[265]. It was found that DASPI was an impractical dye for recording instrument responses on the plate reader: at concentrations low enough to avoid inner filter effects, the required acquisition time was extremely long per delay step, leading to IRF acquisition times of more than ten minutes. Furthermore, the lifetime of DASPI is sensitive to environment and the decay was found to not be reliably monoexponential.

DAPI (4',6-diamidino-2-phenylindole) is a compound commonly used in biology labs as a DNA stain. Its ubiquity, low cost, brightness and favourable excitation/emission spectra led us to examine the possibility of using solutions of DAPI to acquire reference fluorescence lifetime measurements. However, investigation showed that DAPI did not exhibit a monoexponential decay and that this significantly undermines its use as a reference for lifetime fitting. Furthermore, spectrally resolved lifetime measurements acquired using the spectrofluorimeter showed significant variation in both long and short lifetimes as well as the fractional contribution of long lifetime across the emission spectral window employed in plate reader studies.

As an alternative to DAPI, Stilbene 3 was investigated as a possible reference dye. Stilbene 3 is commonly used as a laser dye, producing light around 430 nm when pumped at 355 nm. Its spectral properties mean that the reference measurement can be undertaken without changing filter sets. Unlike DASPI, it is very bright, meaning that less time is spent collecting the reference decay during experiments, and unlike DAPI it is found to be monoexponential across a range of wavelengths as illustrated by lifetime and goodness-of-fit plots in Figure 6-4. It is noted, however, that the reference lifetime ($\tau = 1240$ ps) is longer than the short component of cellular autofluorescence decays; the suitability of using reference reconvolution in such circumstances was briefly investigated by simulation, as previous work within the Photonics group has suggested that a reference dye with lifetime shorter than the short component of the data is necessary for robust fitting.

A MATLAB script is used to generate biexponential "data" by convolving a top hat "gate" with decays parameterised by the lifetimes outlined in Table 6-2 and lifetime contributions varying across images as presented in Figure 6-5 (a). A "reference" decay is then generated by convolving the same top hat with an exponential described by $\tau \approx 1200$ ps. All simulations include Poisson noise. The output parameters resulting from using this "reference" to fit the "data" imagewise are shown in Figure 6-5; the variation in fitted contributions across the image are presented in Figure 6-5 (b) along with the absolute difference between output and input parameters (Figure 6-5 (c)) and the fractional error, defined as $\frac{|\beta_{in} - \beta_{out}|}{\beta_{in}}$ (Figure 6-5 (d)). The consistency between input and fitted lifetimes shown in Figure 6-5 and the broad agreement between input and output fitted contributions shown in Figure 6-5 is taken as sufficient

evidence to suggest that this approach is valid. The availability of measured "library" scatter IRF data enables an alternative approach similar to that adopted in section 4.2, whereby a scatter IRF is temporally aligned with a measured monoexponential decay profile – in this case, measured using Stilbene 3 – and the shifted scatter IRF is then used to fit decays measured from biological samples. This method has not been used in the analysis presented below.

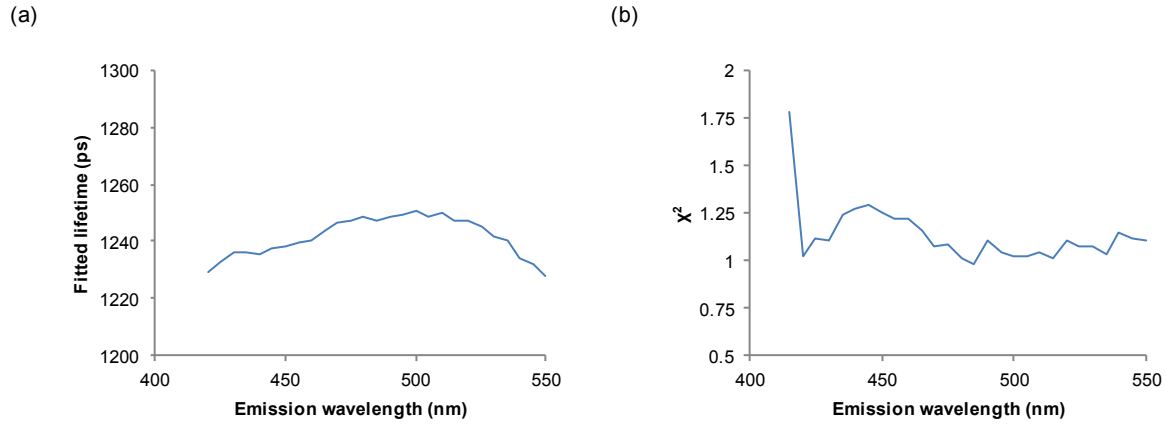

Figure 6-4 Stilbene fluorescence lifetime data acquired under 370 nm excitation across a range of emission wavelengths using the spectrofluorimeter.
(a) Fitted monoexponential lifetime. (b) χ^2 showing quality of monoexponential fit.

	Input (simulation) parameters			Output (fit) parameters			
Case	**τ_{long} (ps)**	**τ_{short} (ps)**	**τ_{ref} (ps)**	**τ_{long} (ps)**	**τ_{short} (ps)**	**Mean(β_{long})**	**Mean(χ^2)**
A	4000	400	1200	3997	402.1	0.50	0.948
B	850	350	1200	849.0	352.0	0.50	0.953

Table 6-2 Simulation and resulting fit parameters for long lifetime reference dye.
Input values are chosen to be similar to those measured in cellular autofluorescence (A) and solution-based mMDH (B) lifetime studies, illustrating the validity of fitting with a long monoexponential reference decay. Lifetime outputs are fitted globally across images; contribution and χ^2 parameters are returned pixelwise and are therefore presented as mean values.

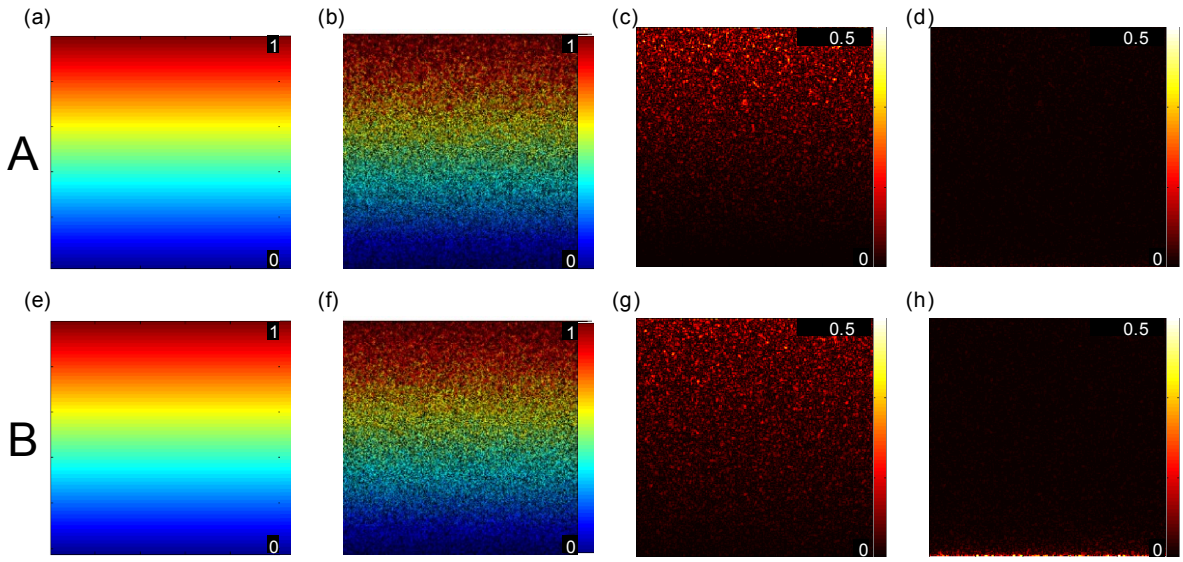

Figure 6-5 Simulated data illustrating lifetime fitting performance using a long lifetime reference dye. Data in cases A and B are simulated according to corresponding parameters in Table 6-2, where parameters approximate those in cellular autofluorescence and solution-based NADH measurements respectively. (a) Input β_1 for simulated data to be fit with long lifetime reference. (b) Output β_1 returned from fitting to data with cellular autofluorescence parameters. (c) Absolute difference between input and outputβ_1 for data with cellular autofluorescence parameters. (d) Fractional error on fitted β_1 for data with cellular autofluorescence parameters. (e) Input β_1 for simulated data to be fit with long lifetime reference. (f) Output β_1 returned from fitting to data with NADH solution parameters. (g) Absolute difference between input and outputβ_1 for data with NADH solution parameters. (h) Fractional error on fitted β_1 for data with NADH solution parameters.

6.5.2 Background fluorescence characterisation

In contrast to multiphoton microscopy of NADH, which is inherently optically sectioned, wide field single photon excitation measurements of NADH autofluorescence lifetime are prone to background fluorescence. This might arise from UV excitation of fluorescence in the microscope optics, sample holders (e.g. multiwell plates, cover slips etc.) and various components of cell culture media. Though *FLIMfit* can account for a time varying background in fitted models in order to account for such background signal, it is nevertheless generally preferable to minimise fluorescent background. To this end, characterisation of sources of background was carried out under typical imaging conditions.

Under pulsed UV wide field illumination at power levels typical of cell imaging experiments (~100 µW after imaging objective), time-gated FLIM image sequences were acquired from three different wells in different types of multiwell plates. These were chosen with different base thicknesses and materials, as outlined in Table 6-3. In addition, three coverslips were selected from a pack of 100 for investigation. Subsequently, different media formulations were made up. These include standard MCF7 growth media with and without FBS; HBSS and HBSS-based imaging media containing 10mM HEPES, 2 mM glutamine and 4.5 g/L glucose; and a selection of relevant compounds at typical dosage concentrations, made up in HBSS-based imaging media. 50 µl of each formulation was pipetted into three wells of a Matriplate 384 multiwell plate, and FLIM sequences are again acquired under typical conditions. Data was loaded into *FLIMfit* and integrated intensities in digital numbers were exported and plotted by condition.

Product name	Supplier	Base material	Base thickness (µM)
Cover glass	VWR	Borosilicate glass	160
Imaging plate CG	ZellKontakt	Borosilicate glass	145
Matriplate microplate	GE Healthcare	Borosilicate glass	720
µClear 96 well	Greiner BioOne	µClear® film	190
Nunc 384 optical bottom	Thermo Fisher	Polystyrene/polymer	250

Table 6-3 Sample holder parameters

The resulting integrated fluorescence intensities from the background characterisation experiments are presented in Figure 6-6. In Figure 6-6 (a), an overview of the measured integrated intensity of selected sample holders described in Table 6-3 is presented: plastic-bottomed well plates exhibit approximately eight times as much fluorescence under UV excitation as glass bottomed plates. This background signal is around 40% of the signal expected from a typical MCF7 cell sample. Figure 6-6 (b) illustrates the integrated fluorescence intensity originating from different components of cell culture media, and drug treatments. Standard deviations across repeat wells are shown as error bars.

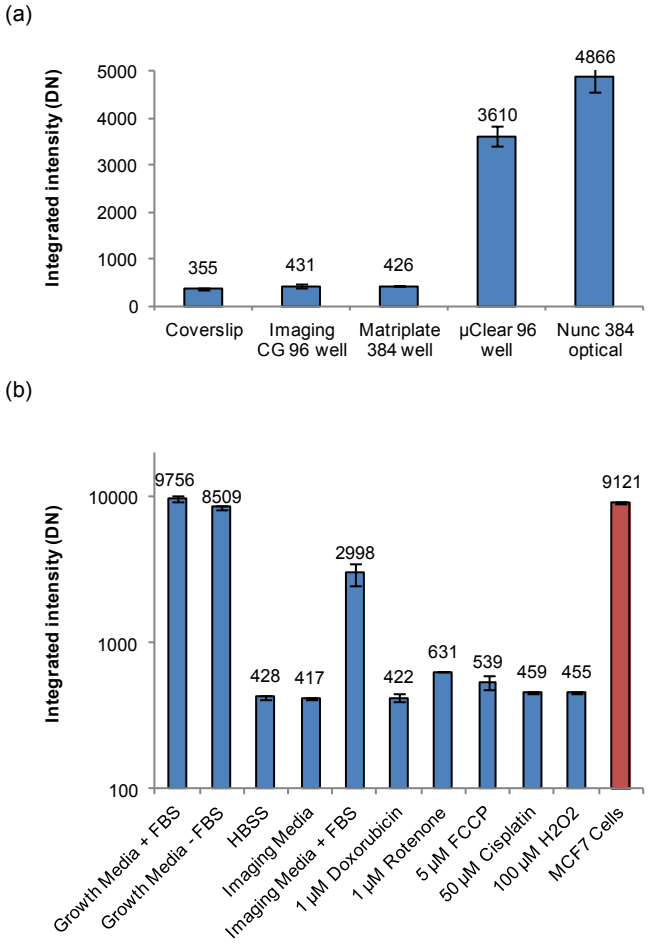

Figure 6-6 Background fluorescence contributions under UV excitation.

(a) Comparison of relative contributions from different potential sources of background fluorescence. (a) Integrated fluorescence intensity in units of camera digital numbers (DN) originating from a range of sample holders. (b) Comparison of background signal from media components and treatment compounds. Blue bars show integrated intensity originating from media components, including signal from Matriplate 384 well; red bar shows integrated intensity from MCF7 cells for comparison. Error bars show standard deviation across repeat wells[323].

Well plates with plastic bottoms are preferred in visible wavelength plate reader studies, as cells grown on plastic substrates tend to exhibit improved morphology and adhesion and, in our hands, show superior expression of transfected protein constructs. However, these results illustrate clearly the necessity to use glass as a growth substrate in UV-wavelength studies. In addition, the impact of phenol red and FBS in standard growth media on fluorescent background is shown. As a result, all subsequent UV-wavelength plate reader experiments were carried out using imaging media as described above, in glass-bottomed plates. Nipkow spinning disk systems may be used with the FLIM plate reader in visible-wavelength experiments for which optical sectioning is required. However, the manufacturer of the confocal spinning disk unit (Yokogawa) does not recommend the use of such systems with pulsed UV excitation light, precluding the adoption of this technique for reducing fluorescent background originating from outside the focal plane.

6.5.3 NADH binding in solution

As described in section 6.3, changes in autofluorescence lifetime observed in live cells are ascribed primarily to binding between NADH and partner proteins. Solution-based NADH binding experiments were set up in order that lifetime might be varied across samples in a predictable manner, allowing repeatability of measurements across a plate to be investigated in a means analogous to dye-based experiments presented in literature[76].

Mitochondrial malate dehydrogenase (mMDH) was purchased as a lyophilised powder (Merck Millipore) and made up in PBS (without calcium and magnesium) on the day of experiments. NADH was similarly made up in PBS, and the absorption of each stock solution was measured in a spectrophotometer (UV3101-PC, Shimadzu). Concentration was calculated from absorption spectra using Beer's law and literature extinction coefficient values (mMDH: 7.2×10^4 M^{-1} cm^{-1} at 280 nm[264], NADH: 6220 M^{-1} cm^{-1} at 360 nm[324]). The ratios of mMDH to NADH in the repeatability experiment were constrained by the volume of solutions required (> 50 µl per well in a 96 well plate), the weight of mMDH available and the concentration of NADH desirable for adequate signal levels as determined by spectrofluorimeter experiments carried out by colleagues. The final concentrations of mMDH used in each well are presented in Figure 6-7 (a). Final concentrations were achieved by diluting stock solutions in PBS in different ratios. Data was acquired in 646 seconds, imaging a single field of view per well.

Fitted results are presented as mean lifetimes in Figure 6-7 (b-d); standard deviations over repeat wells are shown to be less than 2.5 ps across the plate, indicating a high degree of repeatability in the measurements. The relatively high values for standard deviations for conditions 0 µM and 12.1 µM mMDH are attributed to data from wells G8 and G9 respectively, and, although no evidence could be found to support discarding these wells prior to fitting, their spatial proximity suggests some minor fault or contamination in these wells.

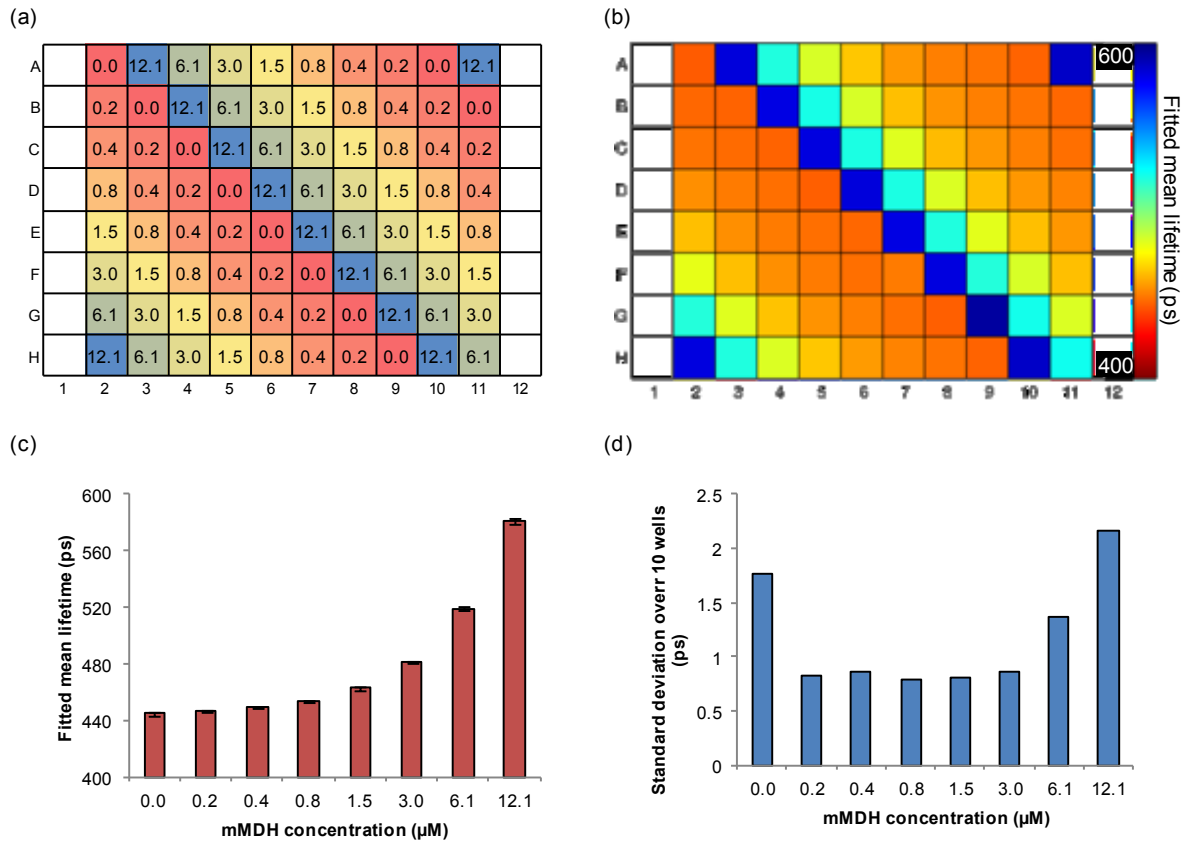

Figure 6-7 Results of experiment investigating repeatability of lifetime measurements across wells.
(a) Map showing plating strategy for NADH-mMDH measurements for lifetime repeatability; numbers associated with wells represent mMDH concentrations in µM. (b) Plate map showing fitted mean lifetime from this plate. (c) Plot showing fitted mean lifetime averaged over repeat wells, error bars showing standard deviations across repeat wells. (d) Standard deviations across repeat wells, rescaled for clarity.

Despite challenges that precluded establishing quantitative binding data from solution measurements made on the FLIM plate reader – including the effects of a background signal of unknown origin that was present in measurements made using multiple instruments –this series of experiments nevertheless serves to validate the repeatability of measurements made using UV-wavelength excitation measurements with the system.

6.6 Cell-based assays

Initial cell-based assays, including control time courses and metabolic modulation experiments were undertaken using cardiomyocytes. These cells were chosen as a starting point for autofluorescence imaging because of their bright fluorescence under UV illumination, caused in part by the large number of mitochondria present in heart cells. Additionally, since anti-cancer therapies including anthracyclines and herceptin can be linked to cardiotoxicity, the ability to examine changes in the metabolic state of cardiomyocytes in response to drug treatment represents a potentially useful application in the drug discovery pipeline. However, limited access to cardiomyocytes and the potential for artefacts linked to

beating to complicate analysis resulted in the majority of experiments aimed at measuring metabolic response and cytotoxicity being carried out in the breast cancer cell line, MCF7.

6.6.1 MCF7 cells: control plate

Having established a formulation for imaging media that exhibited low autofluorescence (section 6.5.2), an experiment was devised in order to confirm that measured lifetimes of control cells across a 96 well plate did not vary over the duration of a typical measurement. This was necessary to establish that autofluorescence of live cells do not present a change in lifetime caused by prolonged exposure to buffered imaging media. Furthermore, the design of the experiment allows possible spatial correlation of measured lifetime (i.e. edge effects) to be investigated.

A 96 well plate was seeded with MCF7 at 1×10^4 cells per well and incubated for 24 hours in growth media before aspirating, washing and replacing the growth media with imaging media. The plate was transferred to the incubated microscope stage and left to sit for ~30 minutes before FLIM data was acquired over 90 minutes. Lifetime data was fitted imagewise by standard methods, and mean lifetime was chosen as the parameter to analyse with respect to acquisition time and spatial position. In this experiment, the aim was to test for equivalence rather than difference, meaning that the standard statistical tests used elsewhere in this thesis were not appropriate. Rather, confidence intervals were calculated and compared to a tolerance parameter Δ. In the case of comparisons across acquisition time, a linear fit was performed on a plot mean lifetime versus acquisition time and 95% confidence intervals on the slope were constructed:

$$95\%\ C.I. = \ m \pm s_m t_{\alpha=0.05} \qquad \textbf{6.1}$$

where m is the fitted slope, s_m is the standard error on the fitted slope, and $t_{\alpha=0.05}$ is the 0.95 quantile of a t-distribution with the right number of degrees of freedom. These confidence intervals are compared to a tolerance parameter $\Delta = \pm 0.5$ ps/minute, which represents the "explainable trend" in the equivalence test[325]. Similarly, for spatial comparisons, confidence intervals on pairwise differences of rowwise or columnwise means $(\mu_i - \mu_j)$ are constructed based on a Tukey-Kramer corrected Z-statistic $q_{k,N-k,1-\alpha}$:

$$95\%\ C.I. = \ (\mu_i - \mu_j) \pm q_{k,N-k,\alpha=0.05} \sqrt{\left(\frac{MSE}{2}\right)\left(\frac{1}{n_i} + \frac{1}{n_j}\right)} \qquad \textbf{6.2}$$

where k is the number of samples, N is the total sample size, MSE is the mean square error returned from ANOVA analysis, and n is the size of each individual sample with mean μ. These confidence intervals are compared to a tolerance parameter $\Delta = \pm 50$ ps, which represents the "explainable difference" between pairs of samples in the equivalence test[326,327]. The motivation for choosing the values of Δ as shown is discussed below. Additionally, for data plotted by acquisition time, the homogeneity of variances across four equal "windows" of the acquisition period was investigated using the Brown-Forsythe test for equal variances. All statistical tests were carried out in MATLAB[328] and Microsoft Excel.

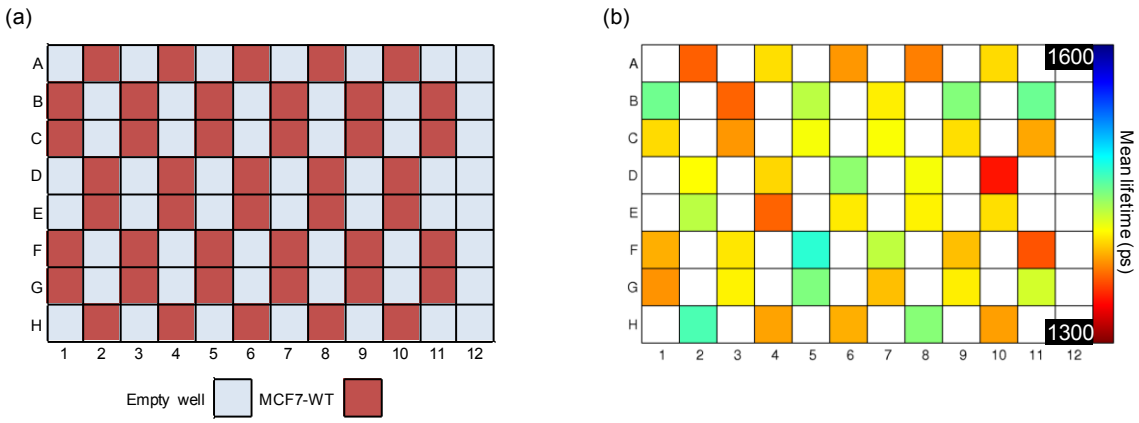

Figure 6-8 Plate maps showing spatial distribution of fitted lifetime for untreated MCF7 plate.
(a) Map showing plating of MCF7-WT cell samples in the 96 well plate. (b) Fitted mean lifetime map.

Results from fitting the lifetime data across the plate are presented as false colour plate map in: there is no obvious evidence of edge effects in the fitted lifetime map. The mean lifetimes of the fields of view collated in these maps are plotted as a function of time since the start of the experiment in Figure 6-9 (a). A linear fit performed in Excel to determine the slope, m, of any monotonic trend in lifetime with acquisition time returned $m = -0.981$ ps/minute. The residuals from this fit were plotted on a normal quantile plot, and visually determined to follow a normal distribution, which validates the use of confidence intervals based on the *t* distribution. 95% confidence intervals on the fitted slope were calculated to be $(-0.445, 0.249)$ ps/minute; this interval falls entirely within the equivalence region defined by $\Delta = \pm 0.5$ ps/minute. Futhermore, Brown-Forsythe's test gives no indication of any change in variance across four partitions spaced equally across the data ($p = 0.9$). Plots of mean lifetime averaged over column and row are shown in Figure 6-9 (b) and (c) respectively. In both cases, error bars represent standard deviations in order to show variability within the data. When 95% confidence intervals for differences between pairs of columns were constructed, all paired difference confidence intervals fell within tolerance parameters. Similarly, When 95% confidence intervals for differences between pairs of rows were constructed, all fell within tolerance.

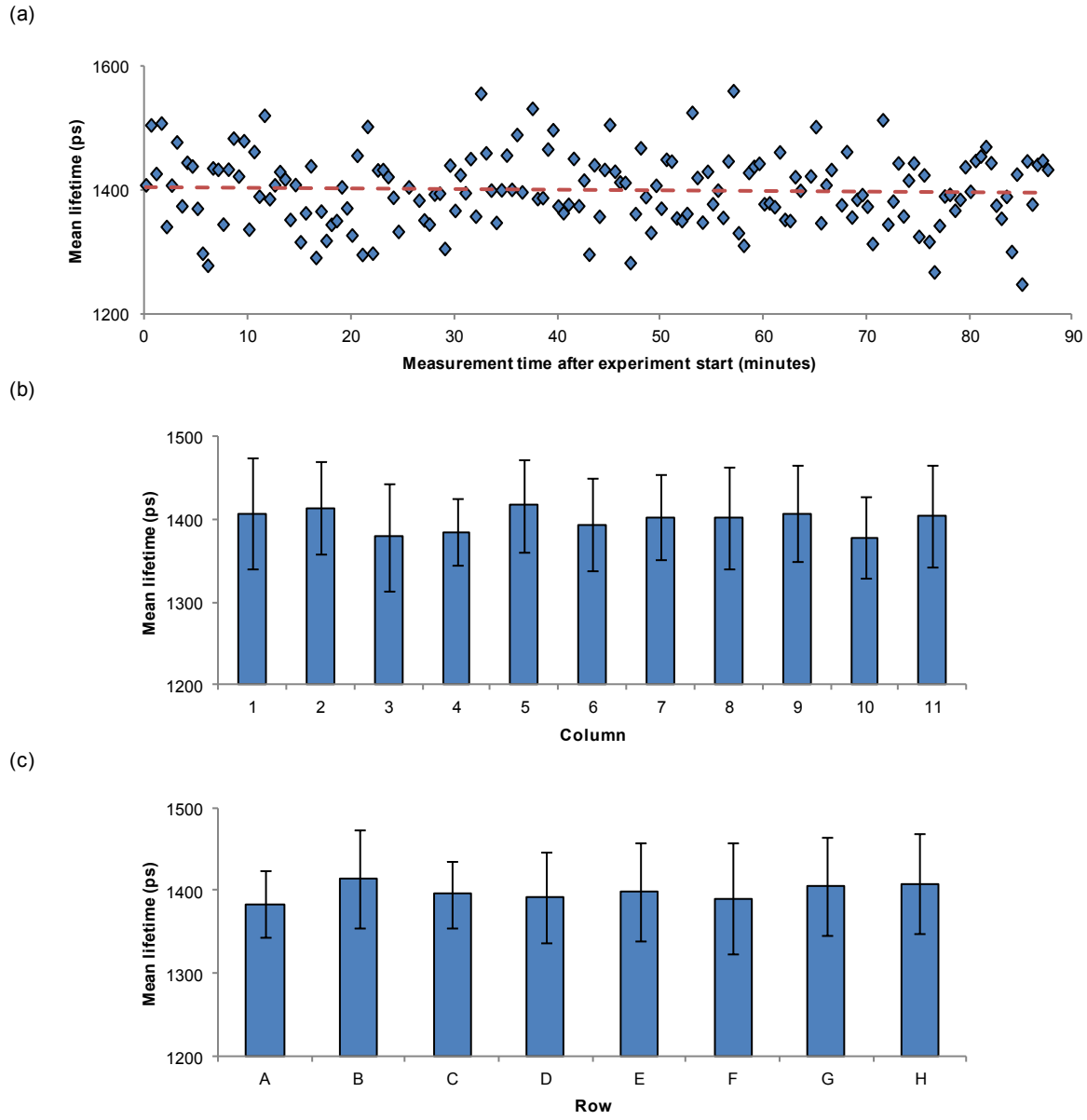

Figure 6-9 Untreated MCF7 plate mean lifetimes.
(a)Fitted mean lifetime plotted by time after acquisition start. (b) Fitted mean lifetime plotted by column, error bars show standard deviations over wells. (c) Fitted mean lifetime plotted by row, error bars show standard deviations over wells.

Results from this plate of untreated MCF7 cells are used to give a degree of confidence that cells investigated across a sequenced acquisition can be considered to have the same basal fluorescence lifetime. Employing equivalence testing requires judgement to be made regarding acceptable tolerance parameters for differences between measured values. In the case of assessing variations with acquisition time, the value for Δ was chosen based on the assumption that the most significant cause of a trend is likely to be drift associated with the instrument response (see Chapter 3: section 3.1.1). Making the approximation that such drift would result in a linear change in measured mean lifetime, a worst-case

value of $\Delta = \pm 0.5$ ps/minute was chosen. When considering the explainable difference between measurements at different spatial positions across the plate, the effect of temperature is considered: private correspondence with colleagues investigating NADH lifetime in the context of myocardial ischaemia suggests that changes of 25-50 ps per degree difference in temperature may be a reasonable approximation. Calibration measurements made using a thermocouple suggest that there is likely to be a 1-2^{o}C gradient across the length of a 96 well plate when the microscope incubator is at an equilibrium temperature; further variations in temperature are likely to be induced by opening access doors to adjust the microscope. The choice of the value $\Delta = \pm 50$ ps was made based on these considerations, and the fact that drift is likely also to impact on differences between measurements separated in space due to the acquisition method.

Despite the degree of ambiguity inherent in choosing parameters for equivalence tests, the results presented here suggest that there is no evidence that measured mean lifetimes change across a 96 well plate independently of treatment, or are induced to change with increasing time spent in imaging buffer on the microscope: the equivalence of measurements made at different acquisition times and spatial positions has been confirmed at 95% confidence level. Particularly, the absence of a trend in measured mean lifetime associated with increased time spent in imaging media obviates the need to investigate carbonate-buffered imaging media solutions in tandem with a CO_2-enriched imaging environment, which would add an extra layer of practical complexity. The possibility that NADH lifetime might vary significantly with temperature is worthy of investigation in cells as opposed to in tissue or in solution; such a study has not been completed in this project.

6.6.2 MCF7 cells: Viability study

A preliminary investigation was conducted in order to establish that the UV excited fluorescence imaging process did not lead to cell death caused by phototoxicity. Such an experiment is required to confirm that NADH lifetime imaging with UV excitation on the wide field plate reader is not a destructive, end-point method and can be deployed in moderate- to long-term time course experiments without the imaging process affecting the metabolism of the cells being studied.

MCF7 cells were split 1:3 one day prior to seeding on a glass bottomed 96 well plate in standard growth media at a density of 10^4 cells per well. 24 hours post-seeding, growth media was aspirated and replaced with imaging media following washing with DPBS. The sample was imaged over a 135-minute period to approximate the duration of a typical multiwell plate experiment. Typical imaging parameters (0.1 mW excitation power at sample for 10 seconds) were used with each field of view being imaged twice. After imaging, cell death was quantified in four wells that had been imaged with UV excitation, four wells that had not been imaged and four wells that had not been imaged but had been "partially heat-shocked". This quantification was performed using an erythrosine vital dye exclusion assay following the protocol for adherent cells outlined in Krause *et al.*[16] Briefly, erythrosine B was prepared at 5 μg/ml in growth media, in which cells were then incubated at room temperature for 2 minutes before washing three times with

imaging media. The sample was then returned to the plate reader. Fluorescence excitation was switched from the pulsed UV laser source to a mercury lamp in order that staining could be assessed using standard epifluorescence intensity, acquired through the non-FLIM imaging path, using a 10x magnification objective (UPlan Apo 10x/0.40) and the "red" filter cube (excitation: 545/30 nm, dichroic: 570 nm, emission: 610/75 nm). Bright field images were acquired of each field of view interrogated to find the proportion of stained cells. Analysis was performed in ImageJ. Fluorescence images were thresholded and overlaid on phase contrast images in order to determine the fraction of cells that had been stained. Counting of cells was performed manually. Results from imaged and heat shocked cells were compared to control results using Dunnett's test, implemented in MATLAB[329].

To confirm the effectiveness of the staining method, cells were subjected to "partial heat-shock" as a positive control, following Krause *et al.*[16]: cells were submersed in 60°C PBS for 10 seconds, then 0°C PBS for 5 seconds before staining. PBS was heated to 60°C using a water bath. Low temperature PBS was thawed from frozen immediately prior to the experiment. Temperatures were checked (to within 2°C) using a thermocouple. PBS was introduced to wells by pipetting down the side of wells to minimise mechanical disruption of cell adhesion. All measurements were made at 37°C, in imaging media.

Results of this experiment are shown in Figure 6-10, where thresholded fluorescence images have been overlaid on exemplar bright field images from wells in which the cells were not exposed to pulsed UV excitation (Figure 6-10 (a)), wells which were exposed to excitation light under the imaging conditions outlined above (Figure 6-10 (b)), and wells in which no imaging was performed but cells were subjected to partial heat shock (Figure 6-10 (c)). The proportion of stained cells was not significantly greater in the case in which cells had been exposed to UV excitation in the course of a FLIM imaging sequence than in the case of unimaged cells. Cells in wells exposed to the positive control "partial heat shock" condition exhibited a significant increase in staining fraction over both imaged and non-imaged conditions (Figure 6-10 (d)).

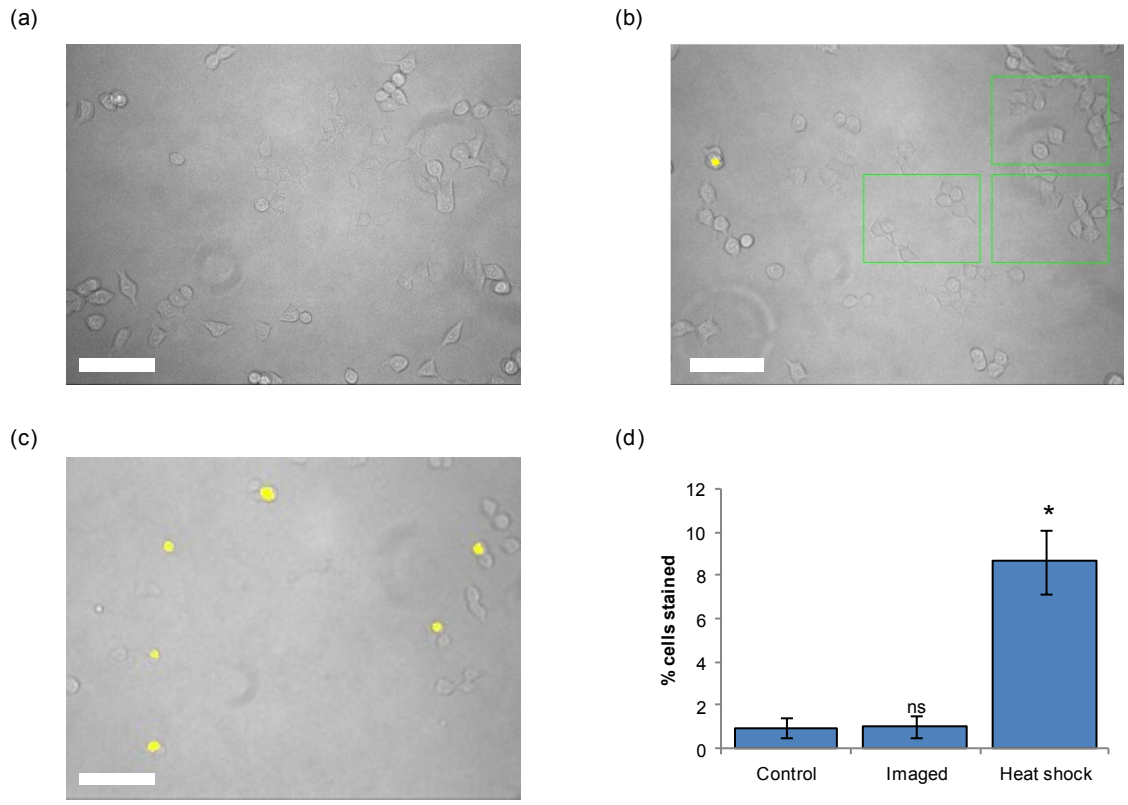

Figure 6-10 Results of vital dye exclusion assay following UV-excited FLIM imaging sequence.
(a) Exemplar bright field with overlaid thresholded fluorescence image from a well that was not used in FLIM sequence. (b) Exemplar bright field with overlaid thresholded fluorescence image from a well that was imaged. Thresholded pixels from the corresponding fluorescent image are overlaid in yellow, fields of view used in FLIM sequence shown with green rectangles. (c) Exemplar bright field with overlaid threholded fluorescence image from a well that was subjected to partial heat shock treatment. Thresholded pixels from the corresponding fluorescence image are overlaid in yellow. Scale bars 200 μm. (d) Plot showing proportion of imaged cells exhibiting erythrosine fluorescence following staining; error bars show standard errors calculated over repeat wells.

It is noted that the positive control shows a much lower level of staining than that shown in kidney cells and fibroblasts by Krause *et al.*, suggesting that the protocol is perhaps not optimal for MCF7 cells. The situation may be further complicated by the relative lack of adhesion of MCF7 to glass bottomed plates which leads to cells being washed away in the course of administering the heat shock and staining treatment. In addition, the vital dye exclusion assay probes for cells with compromised membrane integrity, showing cell death, rather than any more subtle effects linked to phototoxicity. Whilst a vital dye exclusion assay was employed for practical reasons, a more complete selection of cytotoxity assays – perhaps including the MTT colorimetric assay which has been applied in studies of phototoxicity[330], or commercially available fluorescence-based assays such as the ApoTox-Glo (Promega) triplex assay for viability, cytotoxicity and apoptosis – may be useful for future work.

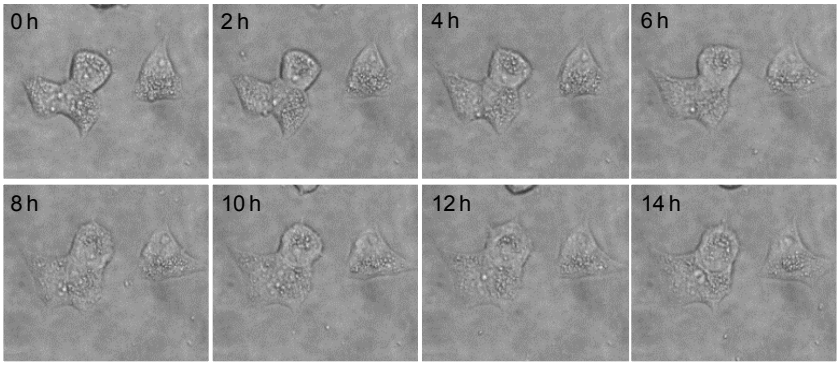

Figure 6-11 Exemplar bright field images interleaved with a long-term course of FLIM measurements of BT474 cells for investigation of morphology.

Separately, BT474 cells were imaged every 2 hours over a 16 hour time course, phase contrast imaging being interleaved with typical autofluorescence imaging in order to determine changes in morphology which might indicate cell damage. Figure 6-11 shows time lapse phase contrast imaging across this period; no adverse effects of imaging over this period caused either by prolonged exposure to imaging media or by repeated exposure to pulsed UV excitation are apparent from changes in cell morphology.

6.6.3 MCF7 cells: Metabolic modulation experiments

Initial studies into measuring changes in NADH lifetime in response to biochemical stimulus were carried out using metabolic modulators. Of these, rotenone and FCCP have clearly defined mechanistic roles that contribute to changes in the expected ratio of free:bound NADH while varying levels of glucose, addition of deoxyglucose or hydrogen peroxide are expected to change the metabolic state of the cells in a more biologically relevant manner.

Rotenone

Rotenone is used as modulator to inhibit the progression of the electron transport chain. As described previously, this is considered to increase the proportion of free NADH in cells. It has previously been shown that, as expected based on the model outlined above, the mean fluorescence lifetime of NADH decreases upon rotenone treatment: this behaviour is primarily attributed across literature sources to a shift in the ratio of free to bound NADH in the cell, even in cases in which the individual lifetime components are also shown to change.

Rotenone (Sigma Aldrich) was prepared in ethanol (1mM) and further diluted in imaging media to a final concentration of 2 μM. Ethanol was also added in a ratio 1:500 to imaging media to make control stimulation media. Cells had been seeded 24 hours prior to starting measurements at 1×10^4 cells per well a glass bottomed plate. Cells were washed and immersed in 100 μl of imaging media before transferring to the plate reader stage, which was incubated at 37°C. Rotenone and control stimulation media were both maintained at 37°C in a water bath prior to the experiment, before filling 20 ml syringes

that were transferred to a syringe pump positioned inside the incubator prior to starting time course experiments.

Two experiments, stimulating with imaging media only or with rotenone, were performed in separate wells. In each case, a time course was set up to image fields of view ten times at 10 second intervals, with a stimulation step set to add 100 µl of liquid to wells that was programmed to fall immediately prior to the fourth time point. The time resolution was chosen in an attempt to investigate the dynamics of the change in NADH lifetime following rotenone treatment. Six wells were selected so that six repeats of such time courses would be carried out per automated acquisition. The first automated run was performed adding imaging media only to prevent carrying rotenone over in the dispensing equipment into the control experiment. Data were analysed both globally and image wise.

Component	τ (ps)
1	3586
2	459.5

Table 6-4 Globally fitted lifetime results from rotenone time course experiment.

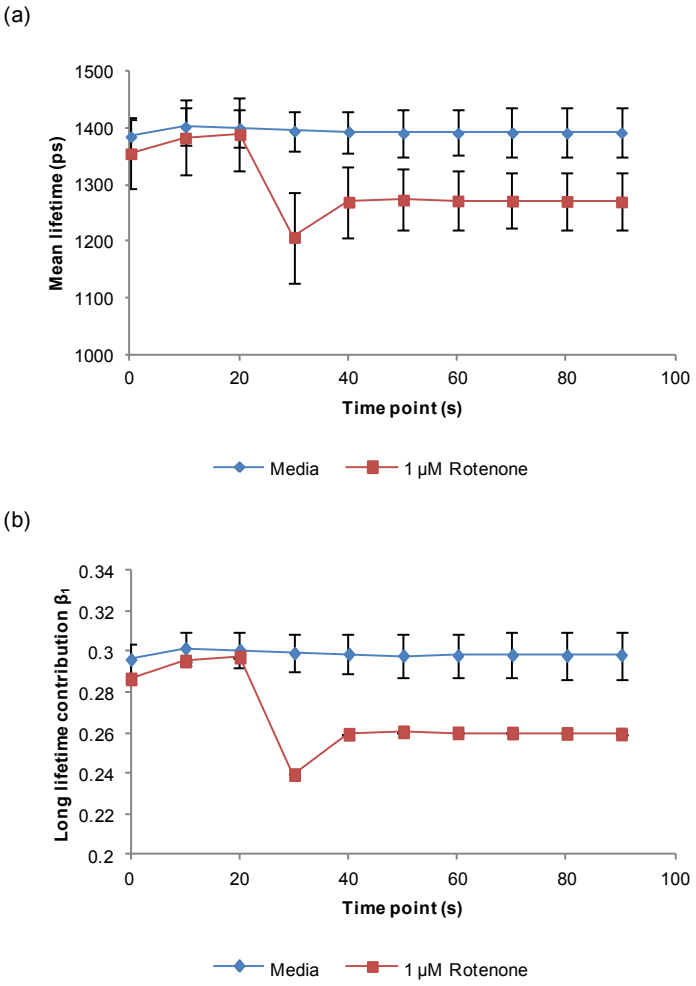

Figure 6-12 Global fit results from automated rotenone time course experiment in which stimulation with control media or 1 µM rotenone occurs immediately before the fourth time point.
(a) Fitted mean lifetime. (b) Fitted long lifetime fraction.

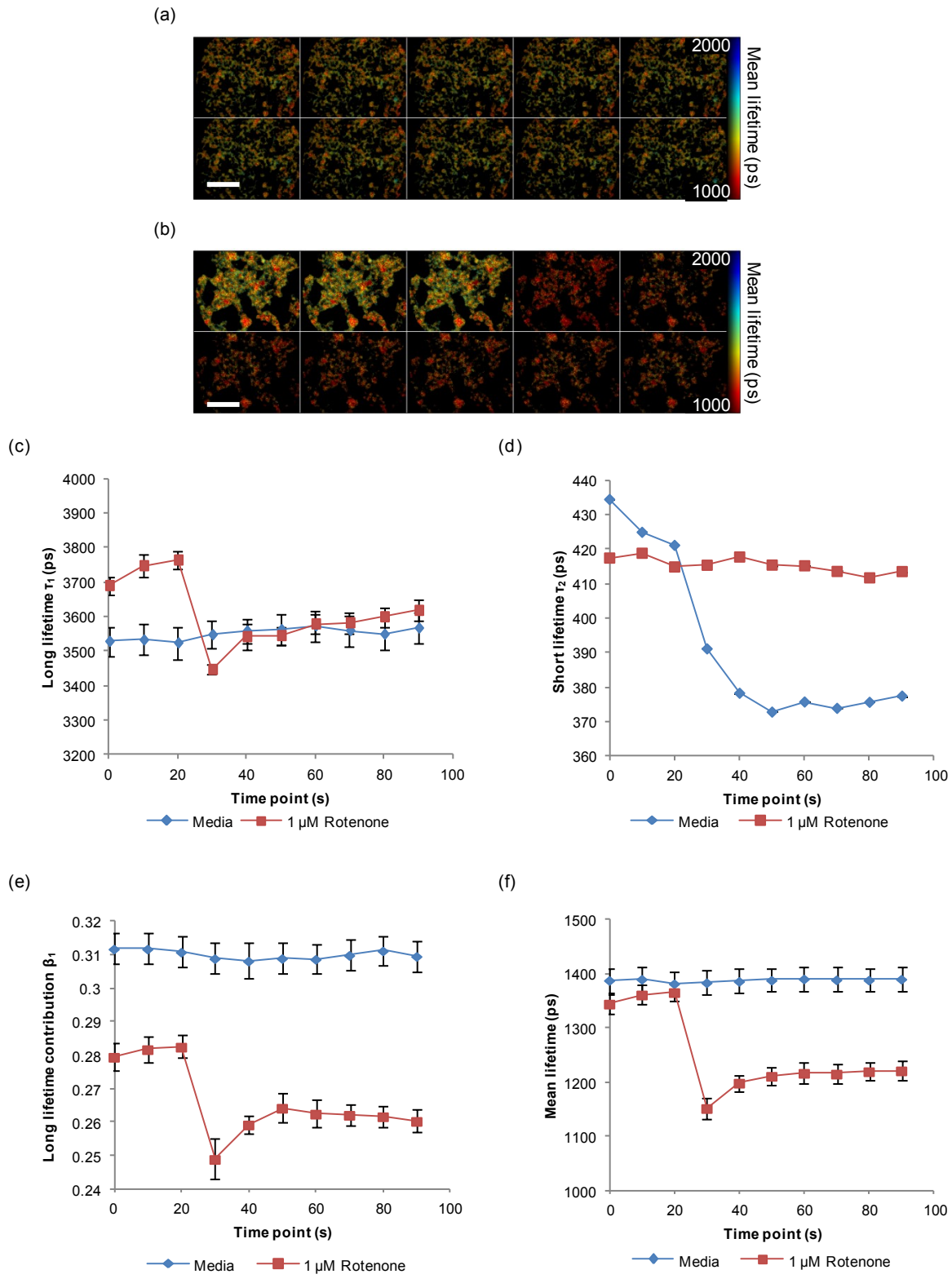

Figure 6-13 Imagewise fit results from an automated rotenone time course experiment.
Stimulation with control media or 1 µM rotenone occurs immediately before the fourth time point. (a) Fitted mean lifetime images for cells stimulated with media alone. (b) Fitted mean lifetime images for cells stimulated with 1 µM rotenone. Scale bar = 100 µm. (c) Fitted long lifetime plotted against time course time point. (d) Fitted short lifetime. (e) Fitted long lifetime contribution. (f) Fitted mean lifetime. Error bars represent standard errors calculated across repeat wells.

Globally fitting lifetimes across the dataset yields mean lifetimes and fractional contributions as shown in Figure 6-12 (a) and (b), respectively, with lifetimes given in Table 6-4. Fitted parameters show the expected behaviour based on the simple model outlined above: that is, an increase in the ratio of free:bound NADH in the cell upon rotenone treatment with no change in mean lifetime when cells are treated with control media. Imagewise fitting provides evidence of statistically significant changes in both bound (Figure 6-13 (c)) and free (Figure 6-13 (d)) NADH lifetime under rotenone treatment, contributing alongside a change in the ratio between long and short fractional contributions (Figure 6-13 (e)) to a decrease in mean lifetime (Figure 6-13 (f)) upon rotenone treatment.

From the results in Figure 6-13 (a) and (c), there is a clear difference between rotenone-treated and control cells' long lifetime component and long lifetime contribution *before* stimulation. This might be attributed to a failure to satisfactorily control temperature differences when switching from control media to rotenone stimulation: despite keeping all solutions at 37°C, opening the incubator to swap the syringes containing solutions may have caused temperature fluctuations. This might be overcome by using a two-channel dispensing system, daisychaining two of the current KDS syringe pumps, or simply allowing temperature to stabilise after switching stimulation syringes.

The fact that both fitted lifetime components exhibit changes upon rotenone stimulation suggests that a simple model, in which the only molecular change upon rotenone treatment is the ratio of free:bound NADH, is not sufficient to describe the system. As discussed in Zheng *et al.*[265], treatment with rotenone induces mitochondrial swelling, possibly causing both viscosity and refractive index changes in the environment of free NADH. The measured long lifetime will depend on the particular population of proteins that NADH may be bound to; though rotenone binds to the ubiquinone binding site on Complex I and so will not directly influence NADH binding, it is nevertheless possible that the inhibition of the electron transport chain in oxidative phosphorylation may cause a shift in the pool of proteins binding NADH. Crucially, these findings agree broadly with those reported for ETC inhibitors previously[265,312–314], validating the use of the plate reader as a means of reading out changes in cellular autofluorescence lifetime originating from changes in NADH binding.

FCCP

The ionophore carbonyl cyanide 4-(trifluoromethoxy)phenylhydrazone (FCCP) uncouples ATP synthesis from the ETC. In simple models, treating cells with FCCP results in an increase in bound fraction of NADH. Such a change would manifest itself as an increase in the long lifetime fractional component in FLIM data. Adding FCCP to cells is therefore another means of predictably changing NADH autofluorescence lifetime in order to confirm that the instrument is sensitive to such changes.

FCCP experiments were performed on the same plate containing MCF7 cells as the rotenone experiments above. FCCP was prepared in ethanol (1mM) and further diluted in imaging media; the same control stimulation media as the rotenone experiments was used. Unlike the rotenone experiment,

stimulations here were made manually by micropipette. In this case, four wells were selected per condition, and imaging occurred every 60 seconds over a ten minute period. Once again, cells were stimulated immediately before the fourth time point.

Component	τ (ps)
1	3505
2	414.3

Table 6-5 Globally fitted lifetime results from FCCP time course experiment.

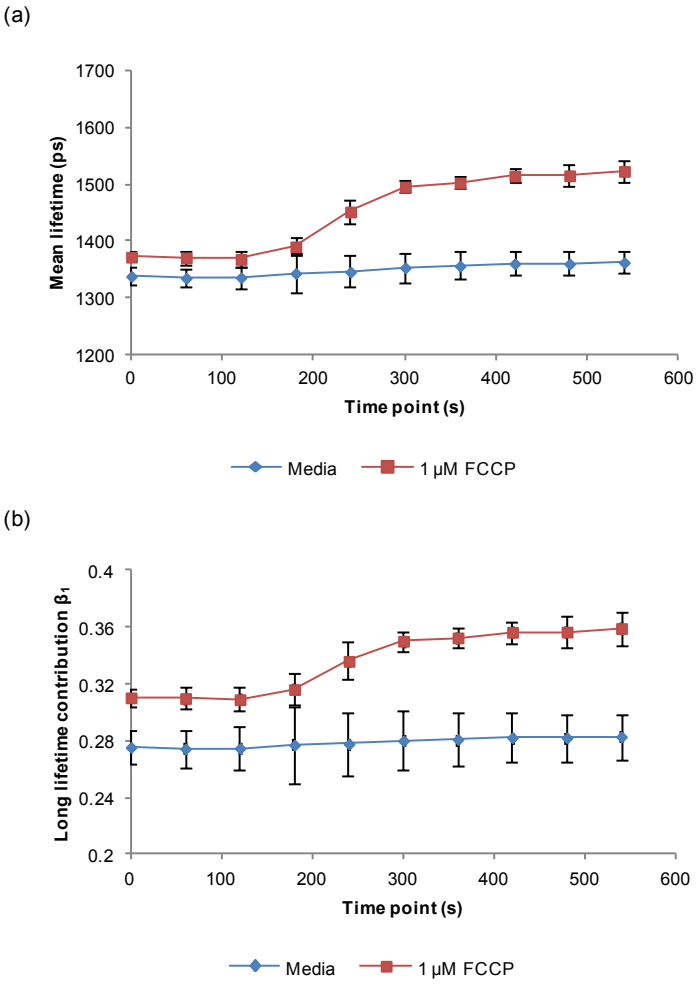

Figure 6-14 Global fit results from a manual FCCP time course experiment.
(a) Fitted mean lifetime. (b) Fitted long lifetime fraction.

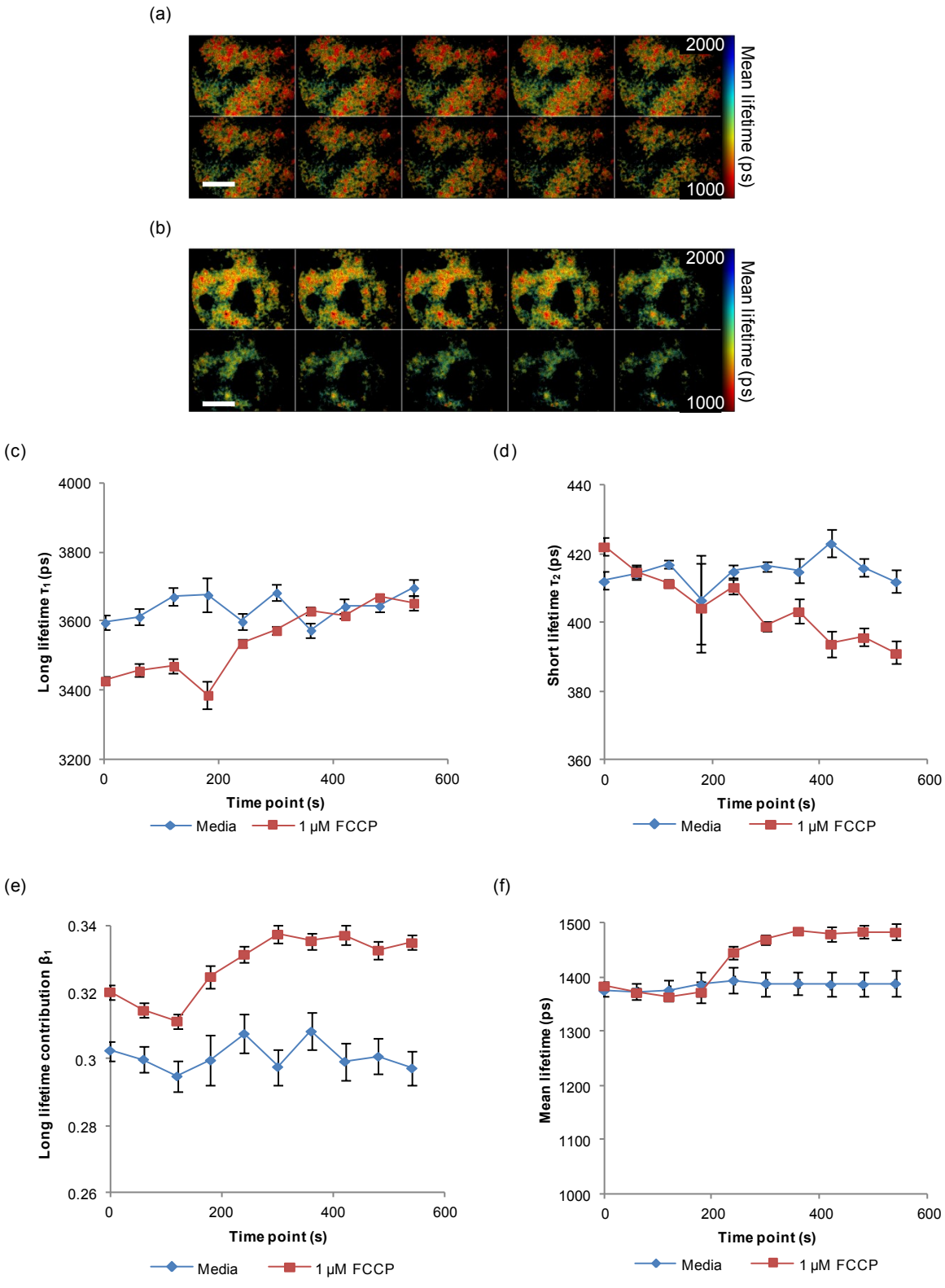

Figure 6-15 Imagewise fit results from a manual FCCP time course experiment in which stimulation with control media or 1 µM FCCP occurs immediately before the fourth time point.

(a) Fitted mean lifetime images for cells stimulated with media alone. (b) Fitted mean lifetime images for cells stimulated with 1 µM FCCP. Scale bar = 100 µm. (c) Fitted long lifetime against time course time point. (d) Fitted short lifetime. (e) Fitted long lifetime contribution. (f) Fitted mean lifetime. Error bars represent standard errors calculated across repeat wells.

Once again, fitting globally across all data yields the expected behaviour based on an increase in NADH oxidation in the ETC (Figure 6-14): the mean fitted lifetime increases, reflecting an increase in the long lifetime component across the time series following stimulation, in agreement with trends highlighted elsewhere when mitochondrial uncouplers are used[265]. Imagewise fits exhibit an increase in the fitted long lifetime following stimulation in addition to an increase in the fitted long contribution (Figure 6-15). Again, this might be attributed to a change in the population of NADH protein binding partners, though we have no clear idea of the mechanism that might underlie such a change. Again, conformation of results to predicted changes in mean lifetime indicate that the plate reader may be used to measure NADH binding by autofluorescence lifetime. It was noted that there was a difference in pre-stimulation lifetimes parameters between the media- and drug-stimulated cases. Given that the four wells selected per condition were chosen by position in the plate to facilitate manual stimulation, it is possible that some contamination of either the media- or drug-stimulated wells might contribute to this difference.

Staurosporine

STS has also been used to trigger apoptosis in cellular autofluorescence lifetime studies[318]. The potential for STS to be used to further confirm the utility of the plate reader in reading out metabolic state by fluorescence lifetime was investigated; however, it was found that STS introduced a significant background signal (signal-to-noise approximately 1) that could not be easily removed from the cellular autofluorescence, either by washing post-treatment or in software processing. Furthermore, the measured lifetime of STS in solution was found to match the reported (and measured) "cell" lifetimes following STS treatment, casting further doubt on the suitability of STS as a modulator in this context. Spectral measurements suggest that STS signal might be suppressed by use of appropriate filters, for example the 440/60 nm filter that was used in subsequent experiments as standard protocol. Unfortunately, practical constraints of time prevented pursuit of this avenue.

2-deoxyglucose

Previously published work has illustrated that treating BKEz-7 endothelial cells derived from calf aorta with 2-deoxyglucose (2DG) results in an increase in effective lifetime measured by rapid lifetime determination methods[315]. This corresponds to expected behaviour based on biochemical experiments that have shown a decrease in the NADH:NAD^+ ratio in fibroblasts[287]. An experiment was set up to treat MCF7 cells with 2DG to measure the effects of inhibiting glycolysis in this breast cancer cell line.

MCF7 cells were seeded at 1×10^4 in a glass bottomed plate in standard growth media and incubated for 24 hours. Growth media was aspirated and replaced with 100 μl imaging media before transferring the plate to the microscope stage for imaging at 37°C. 2DG solution was made up in imaging media at 20 mM. Six wells were selected with four fields of view per well, and a time course was set up to image each field every 300 seconds over a 40 minute period. 100 μl of 2DG solution was manually pipetted into wells immediately prior to the fourth time point in the series. Data were fitted image wise, statistical significance was assessed using Tukey's test for multiple comparisons.

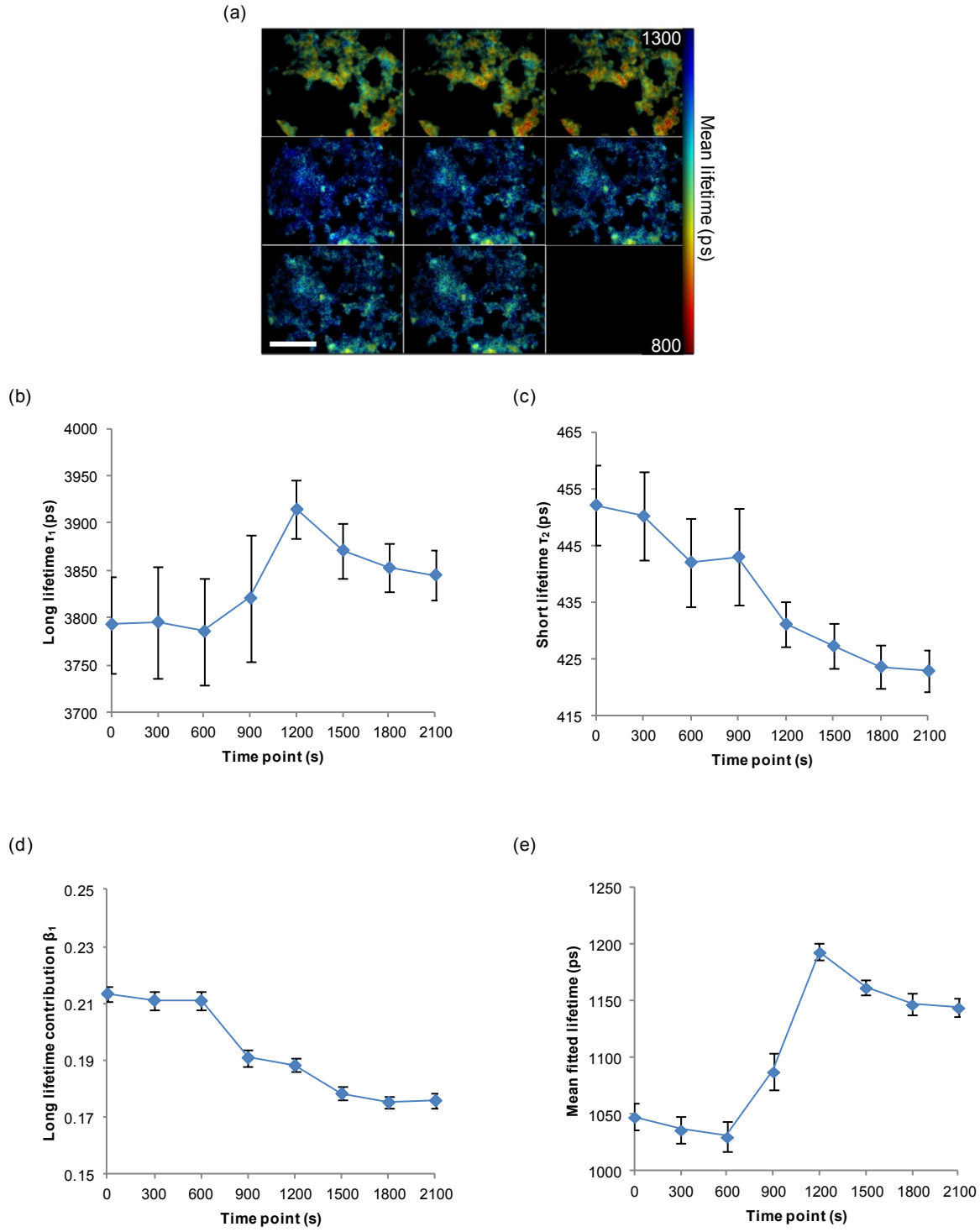

Figure 6-16 Imagewise fit results from a manual 2-deoxyglucose time course experiment in which stimulation with 10 mM 2DG is made immediately after the third time point.
(a) Fitted mean lifetime images. Scale bar = 100 μm. (b) Fitted long lifetime plotted against time course time point. (c) Fitted short lifetime. (d) Fitted long lifetime fractional contribution. (e) Fitted mean lifetime. Error bars represent standard errors calculated across repeat wells.

Results from this experiment are presented in Figure 6-16. Mean lifetime images from an exemplar field of view are presented in Figure 6-16 (a). It is evident from the images in Figure 6-16 (a) that the manual

stimulation of the plate has resulted in an *x,y*-offset being introduced. Plots of fitted lifetime parameters against time course time point show that treatment with 10 mM 2DG causes an increase in long lifetime (Figure 6-16 (b), $p < 0.0005$), and a decrease in the fractional contribution of this lifetime (Figure 6-16 (d), $p < 0.0005$), where significance of change is judged based on the difference between three pre-stimulation points and the final four post-stimulation points. The net result on mean lifetime is an increase following stimulation (Figure 6-16 (e), $p < 0.0005$). The observed decrease in the short lifetime component is not significant at $p = 0.05$.

The mean lifetime results presented in Figure 6-16 exhibit expected behaviour based on lifetime studies using RLD analysis[315]. Imagewise double fitting, however, highlights the possibility that such changes are due to increases in the long lifetime component rather than a shift towards bound NADH as suggested by previously published biochemical data[287]. This discrepancy may reflect the difference between the relatively short 2DG treatment time used in this experiment (following Schneckenburger et al.[315]) compared to the three hour incubation used in the study in which NADH:NAD^+ ratio was studied by biochemical means. Previously published biexponential analysis of NADH autofluorescence lifetime by Wang et al.[317], in which normal skin fibroblast cells were treated with 2 mM 2DG for an undefined period of time, showed no significant change in any fitted parameters. Further experimentation, possibly increasing the length of the experimental time course or inhibiting glycolysis by 3-bromopyruvate, may shed more light on the effects of 2DG treatment both for use in the lab and as a potential cancer therapy. In addition, controlling for changes in osmotic pressure caused by the addition of 10 mM 2DG, for example using mannitol in a solution for a control stimulation time course, may further elucidate the processes behind the observed changes in lifetime.

H_2O_2: dose response plate experiment

It has previously been reported that differences in autofluorescence lifetime response may be used to distinguish between apoptotic and necrotic cell death[318]. Furthermore, different doses of hydrogen peroxide have been shown to result in different mechanisms of cell death (apoptotic or necrotic death)[291]. A plate was therefore run in order to test for dose-dependent lifetime response to hydrogen peroxide (H_2O_2).

It was noted from literature that response might well be cell line-dependent; on the basis that the MCF7 line has been used throughout our plate reader studies of cellular autofluorescence, these cells were seeded at 1×10^4 in a glass bottomed plate. Cells were incubated for 24 hours in standard growth media which was replaced one hour before imaging with growth media supplemented with H_2O_2 at a range of concentrations up to 3000 μM. Prior to imaging, growth media was aspirated, cells were washed and buffered imaging media was added to all wells. Ten fields per well were imaged under standard imaging conditions.

Component	τ (ps)
1	3968
2	416.0

Table 6-6 Globally fitted lifetime results from hydrogen peroxide response experiment.

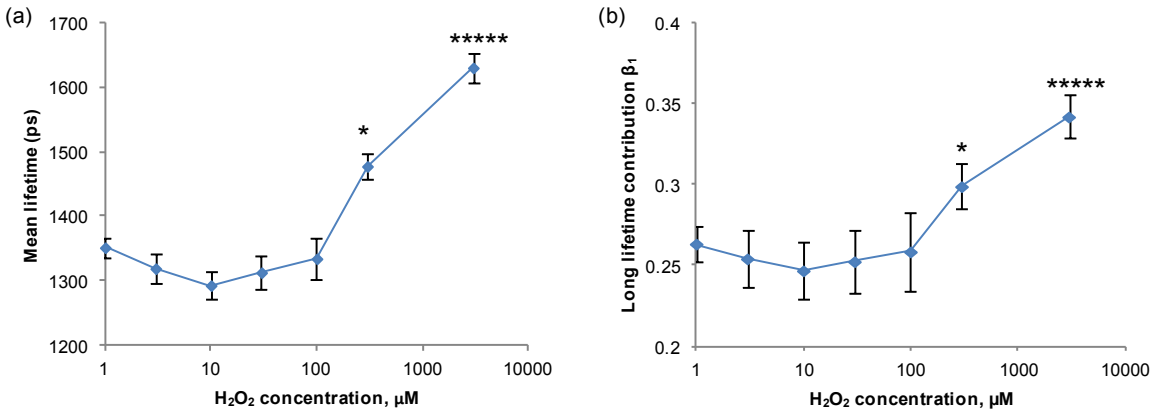

Figure 6-17 Global fit results for a hydrogen peroxide dose response experiment.
(a) Fitted mean lifetime. (b) Fitted long lifetime fraction. (c) Globally fitted lifetimes. Error bars show standard errors across repeat wells. * denotes significant difference from all lower dose values at $p = 0.05$ (Tukey's test); ***** denotes significant difference at $p < 0.005$ (Tukey's test).

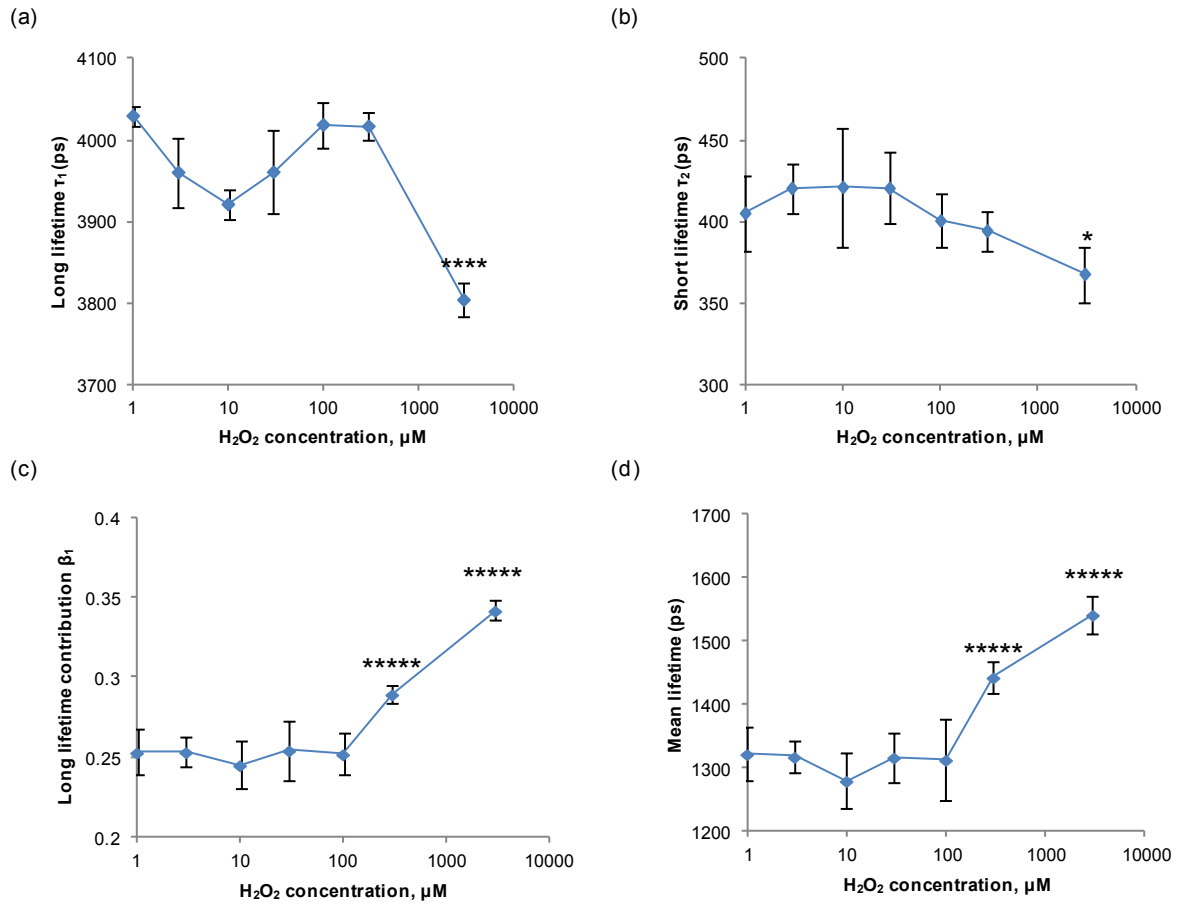

Figure 6-18 Imagewise fit results for a hydrogen peroxide dose response experiment.
(a) Fitted long lifetime τ_1. (b) Fitted short lifetime τ_2. (c) Fitted long lifetime fraction β_1. (d) Fitted mean lifetime. Error bars show standard errors across repeat wells. * denotes significant difference from all lower dose values at p = 0.05 (Tukey's test); ***** denotes significant difference at p < 0.005 (Tukey's test).

Once data had been pre-processed to remove image artefacts, lifetime fits were performed using standard methods. Global fitting showed significant increases in long lifetime fractional contribution at high doses (≥300 µM) of H_2O_2 (Figure 6-17 (b)); high doses showed significant differences from all other doses using Tukey's test for multiple comparisons. As expected, there is a corresponding shift in mean lifetime (Figure 6-17 (a)) for high doses of H_2O_2. Imagewise fitting indicates that there is a significant change in both lifetime components and the fractional contribution of those components at very high dose (Figure 6-18 (a-c)) and suggest that the increase in mean lifetime apparent at 300 µM may be assigned primarily to changes in the relative contributions of short and long lifetimes (Figure 6-18 (c) and (d)).

The increase in mean lifetime with increasing dose of H_2O_2 is in broad agreement with previous studies in colon cancer cells[322], although the doses at which the fitted lifetime contribution increased is greater here than previously reported: no significant change is seen at 100 µM treatment. These observations provide some validation for previously published work in which the authors used phasor analysis in a study of colon cancer cells subjected to H_2O_2[322]: for a linear projection between two phasor positions to be valid,

changes must be attributable only to a change in the fractional contribution of states represented by those phasors, which is borne out at doses < 300 μM in our data.

6.6.4 Breast cancer cell line screening

Following discussions with investigators in the Skala group at Vanderbilt University, the potential for using autofluorescence lifetime to discriminate between breast cancer cell lines exhibiting different drug sensitivities was investigated. The Skala group have published work in which lifetime imaging as well as optical redox ratio is investigated as a method of distinguishing between cell lines. A list of cell lines investigated and notes on their relevant properties is outlined in Table 6-7. Crucially, this small panel of cells provides non-cancerous as well as cancerous lines exhibiting different estrogen receptor status and includes lines with and without overexpression of the epidermal growth factor receptor protein HER2. Also included is a drug-resistant line MCF7-DoxR, which is generated from wild type MCF7 in the Lam lab by applying selection pressure with increasing doxorubicin doses, up to 17 μM.

Cell line	ATCC catalogue number	Classification	ER status	HER2 status	Responsive to anthracycline treatment?	Source
MCF7-WT	HTB-22	Luminal A	+	-	Y	ATCC
MCF7-DoxR	†	Luminal A	+	-	N	Lam lab
MCF10A	CRL-10317	Basal	-	-	Y	Skala lab
SK-BR-3	HTB-30	HER2	-	+	Y	Lam lab
BT474	HTB-20	Luminal B	+	+	Y	Lam lab

Table 6-7 Summary of cell lines investigated.[331–336]

†MCF7-DoxR cells were generated from MCF7-WT by selection under doxorubicin treatment in the Lam lab.

In our experiments, three separate plates were seeded: the first with MCF7-WT and MCF7-DoxR, the second with SK-BR-3 and MCF10A, and the third with BT474. Bird et al.[314] have shown previously that seeding density, linked to confluency, affects measured fluorescence lifetime in MCF10A cells. In order to test for similar effects, each cell type was plated at four densities, from 300 to 10000 cells per well. Six wells were seeded per density per cell line. To avoid potential background effects, MCF7-DoxR were seeded in standard growth media rather than doxorubicin supplemented media: though the investigation undertaken in section 6.5.2 showed low fluorescence signal from doxorubicin with the filter set used throughout, MCF7-DoxR media contains doxorubicin at 17 times the concentration characterised in Figure 6-6, and no adverse effects on the cell population are expected by removing selection pressure for the 24 hours between seeding and imaging. MCF10A were seeded in supplemented MBEM[312] supplied by the Skala lab. Data acquisition was conducted under normal imaging conditions, with standard imaging media replacing growth media approximately one hour before the acquisitions were started.

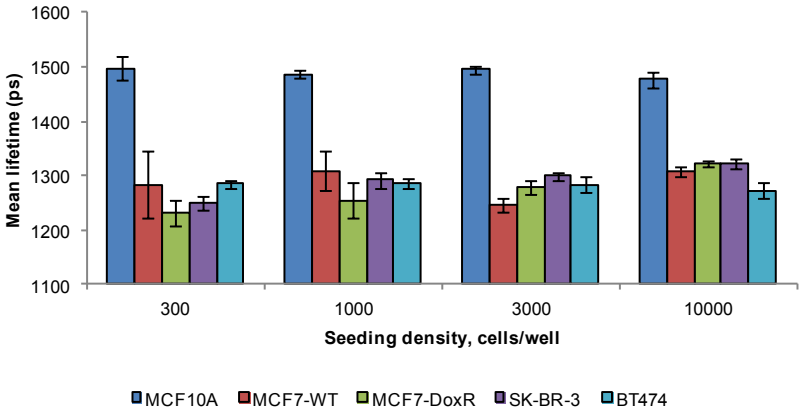

Figure 6-19 Mean lifetimes across cell types and seeding densities.

The results of these plates are summarised by plotting mean lifetimes, showing variations by cell line and cell seeding density, in Figure 6-19. From the data shown in Figure 6-19, there are no significant trends linking lifetime and seeding density (Tukey's honestly significant difference test, $p > 0.05$) for any of the individual cell lines, including the "non-cancerous" model MCF10A. There is a statistically significant (Tukey's honestly significant difference test , $p < 0.05$) difference in mean lifetime for MCF10A and breast cancer cell lines (MCF7-WT, MCF7-DoxR, SK-BR-3 and BT474) across all seeding densities, but no clear difference between differently classified cancer cell lines.

The result that MCF10A lifetime does not vary with seeding density is not consistent with the findings of Bird et al.[314], who proposed that increased cell "crowding" would result in a decrease in oxygen availability and thus an increase in free NADH resulting from inhibition of the ETC. It is notable that the densities used in the experiment described above were necessarily lower than those used by Bird et al., as it was found that seeding at densities corresponding to the highest used in that paper (approximately 3.7×10^5 cells per well in a 96 well plate) resulted in cells being extremely overgrown after 24 hours of incubation. It is possible that this increased rate of growth reflects some change in cellular metabolic state due to stress: of five cell lines sent to South Kensington from Vanderbilt in the same delivery, only MCF10A grew following thawing after the package containing the cyrovials was held in customs.

The results in Figure 6-19 are also in contrast with the findings of Walsh et al., who observe that adenocarcinoma cell lines (including MCF7-WT and SK-BR-3) exhibit longer lifetimes in relation to non-malignant MCF10A, despite having a higher glycolytic index[337]. The authors suggest that the complex downstream signalling of receptors such as ER and HER2, which drive both glycolytic metabolism and the expression of NADH-binding proteins, may be the reason for the complex behaviour of NADH lifetime. It is possible that unidentified differences in media composition between our study and the published work might explain these different results. However, as media for growing MCF10A was provided by the Skala lab, and growth media for cancerous cell lines was made up as outlined in published work, it seems unlikely that the different outcomes are due to different growth factor or estrogen content in media. It is conceivable that differences in cell proliferation may cause differences in lifetimes that may

mask other changes[304,312]. In future, it may be possible by phase contrast microscopy, well-chosen staining methods[338] or ptychography[339] to determine the number of mitotic cells.

For future work, it may be beneficial to screen all cell types used here on a single plate with fewer repeat wells per plate, in order to avoid any potential differences in temperature stability between experiments. For a fuller understanding of the differences between our experiment and published works, it would be instructive to carry out standard measurements of glucose uptake and lactate secretion in order to attempt to correlate lifetime with glycolytic index. In addition, it is noted that the lifetime signal from doxorubicin-resistant MCF7 is not significantly different from that of wild type MCF7, apparently indicating that our autofluorescence lifetime measurements were not able to predict whether cells will respond to anthracycline treatment.

6.6.5 Doxorubicin response

An experiment was planned in order to establish whether dosing cells with doxorubicin induced a shift in autofluorescence lifetime due to cytotoxic effects of the treatment. Following on from section 6.6.5, both wild-type and drug resistant cell lines were tested. In principle, MCF7-DoxR should provide a negative control for treatment.

Cells were seeded at 1×10^4 cells per well in normal growth media and incubated for twenty four hours prior to treatment with different doses of doxorubicin up to 3 μM. Doxorubicin was prepared at the desired final concentration in growth media that was subsequently used to replace media, rather than adding more concentrated doxorubicin to media in wells. After a twenty four hour treatment period, cells were washed and immersed in imaging media.

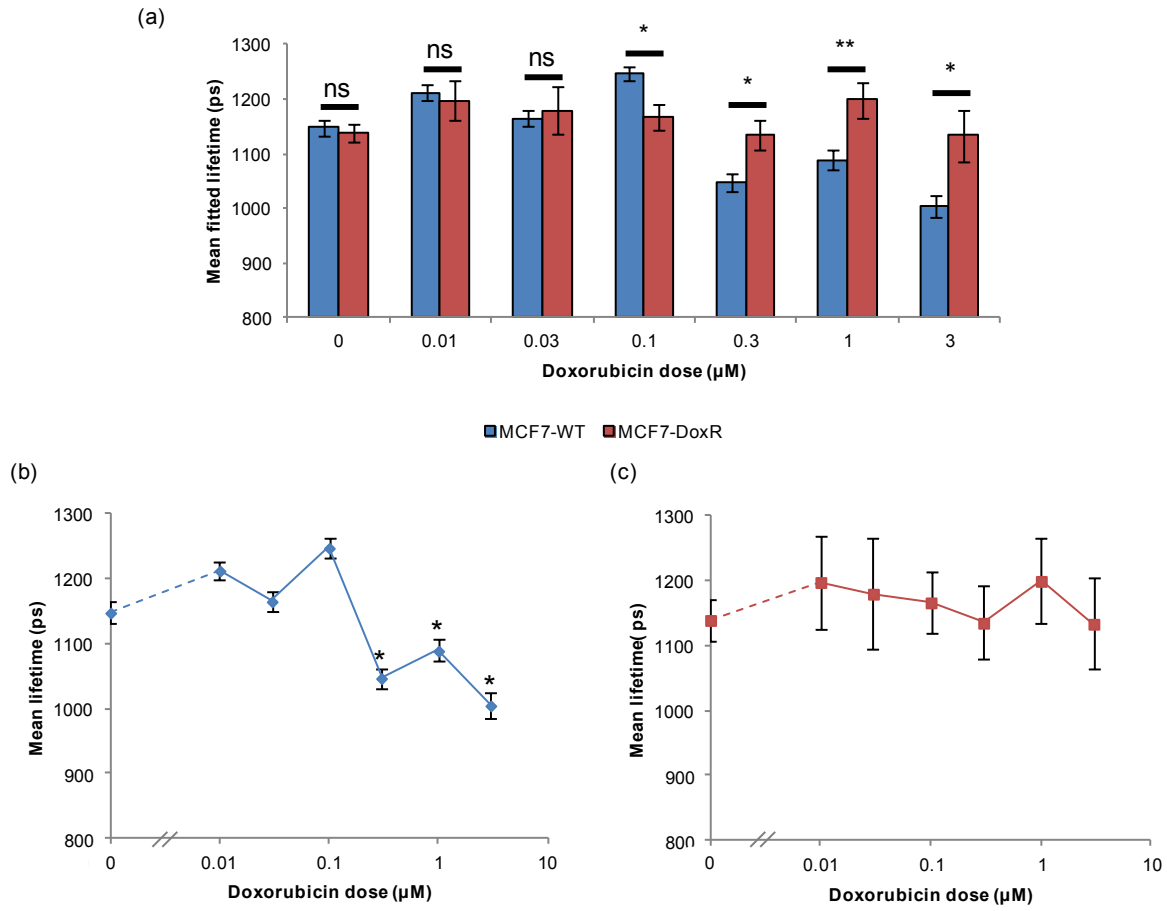

Figure 6-20 Doxorubicin treatment dose response, fitted mean lifetimes.

(a) Fitted mean lifetimes presented as paired comparisons between sensitive and resistant cell lines. (b) Fitted mean lifetimes presented as a dose response plot for wild type cells. (c) Fitted mean lifetimes presented as a dose response plot for resistant cell line MCF7-DoxR. . Error bars represent standard errors over repeat wells, significance assessed by Student's T-test in (a) and Dunnett's test in (b) and (c).

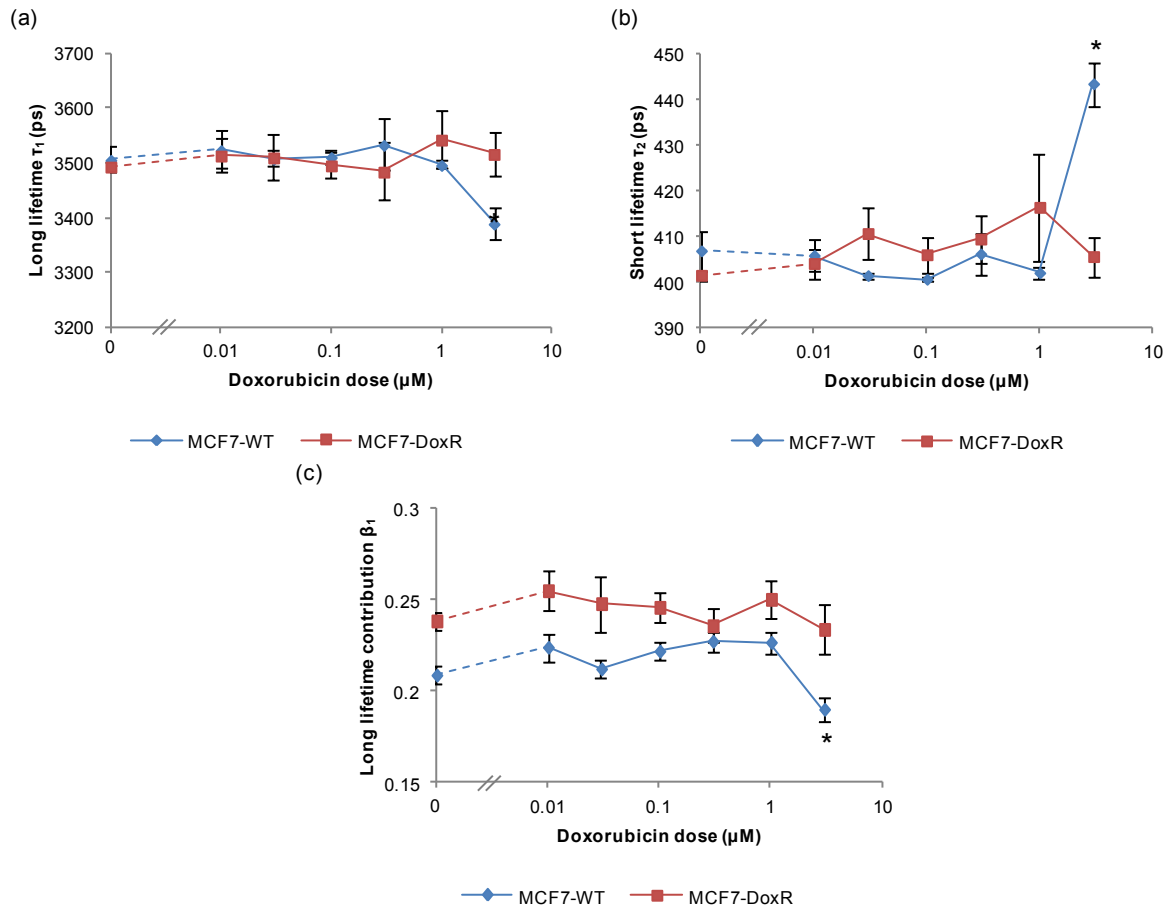

Figure 6-21 Fit parameters for drug resistant and sensitive cells plotted against drug concentration.
(a) Fitted long lifetime. (b) Fitted short lifetime. (c) Fitted long lifetime component. Error bars represent standard errors across repeat wells. Statistically significant differences from untreated cells at p=0.05 are signified by * (Dunnett's test).

Fitted lifetime results are shown in Figure 6-20, both as a direct comparison between resistant and sensitive cell lines, and as dose response plots. Fitted mean lifetimes for sensitive cells deviate from those for resistant cells for treatment concentrations ≥ 0.1 μM, at significance levels indicated in Figure 6-20 (a). If comparisons are instead drawn between the untreated cases and successive points in each dose response, no doses are significantly different (p = 0.05) for MCF7-DoxR cells (Figure 6-20 (c)), whilst lifetimes associated with doses ≥ 0.3 μM are significantly different from untreated lifetime (Figure 6-20 (b)), where Dunnett's test has been applied to test for differences between a single control value and multiple experiment values. Other fit parameters are presented as plots against dose in Figure 6-21 in an attempt to extract more information on the underlying cause of the observed changes in mean lifetime data. Only at the highest dose is any one of the fit parameters significantly different from the untreated case. Changes in both long lifetime (Figure 6-21 (a)) and the fractional contribution of long lifetime (Figure 6-21 (c)) contribute to the shortening of mean lifetime.

This dataset serves to highlight the complexity of interpreting autofluorescence lifetime data at a molecular level: changes cannot simply be attributed to changes in the free:bound ratio of NADH, but is

likely also linked to a change in the proteins to which NADH binds, or cross-talk from NADPH fluorescence[310].

6.6.6 Cisplatin response

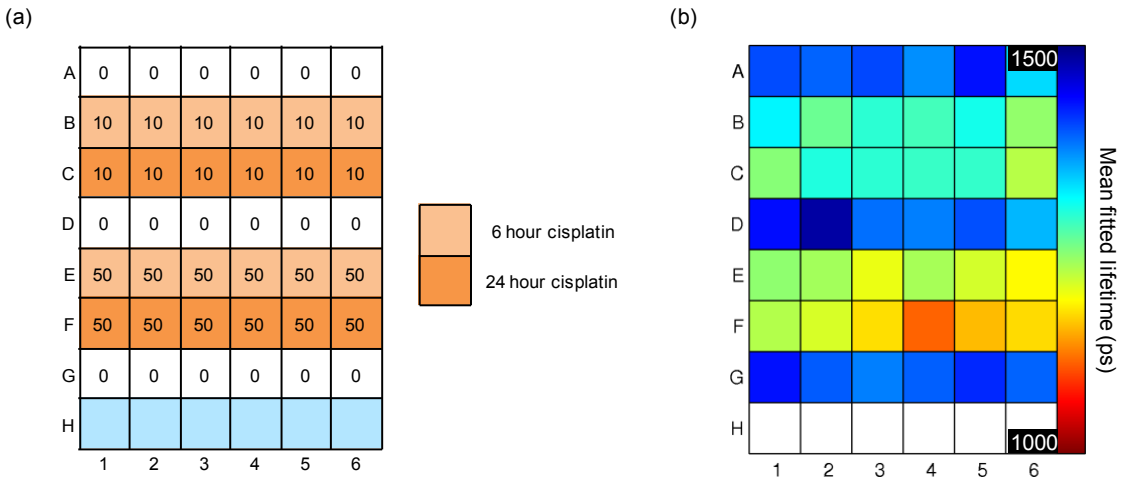

Figure 6-22 Plate maps for cisplatin experiment.
(a) Plate map showing treatment time and dose (in μM) for MCF7-WT cells exposed to cisplatin. (b) Mean fitted lifetimes displayed wellwise in a plate map.

A plate for investigating NADH lifetime readouts of time- and dose-dependent responses to cisplatin treatment was designed as shown in Figure 6-22 (a). Similarly to doxorubicin experiments, cells were seeded, treated and washed at 24 hour intervals; an additional step was added six hours prior to imaging for addition of the 6 hour dose treatments. As before, cells were imaged at 37°C in imaging media. Cells were sufficiently densely seeded such that no pre-find operation was required and the first 10 fields of view spiralling outwards from the centre of each well were imaged. Five time-gated images were collected for each time-delay of the GOI resulting in an average acquisition time of 25 s seconds for each field of view, including sample translation, cell finding and autofocus. For each field of view, a phase contrast image was also captured using the non-FLIM imaging path.

Figure 6-23 presents exemplar fields of view in phase contrast alongside false colour images showing mean lifetime, illustrating changes in mean lifetime. Figure 6-24 summarises fit results for cells untreated or treated with cisplatin 6 hours or 12 hours before being imaged with mean lifetime values obtained from global fitting to a double exponential decay model across the images in each well. Figure 6-24 (d) shows the changes in mean autofluorescence lifetime obtained from global fitting to a double exponential decay model across all the images for each condition (i.e. across repeat wells) and indicates a significant decrease in mean autofluorescence lifetime following cisplatin treatment, reflecting the changes seen in exemplar fields. There is no significant difference between conditions with the same dose but different treatment times, but each of the three doses is significantly different from each other (Tukey's test, $p < 0.01$). Figure 6-24 (a) and (b) show the variation of the short and long lifetimes with cisplatin dose and

exposure time and Figure 6-24 (c) shows the corresponding changes in the fractional contribution from the long ("bound NADH") component to the autofluorescence signal, which decreases with increased cisplatin dose and treatment time. According to Tukey's test, the short lifetime components measured in this experiment and the long lifetime components of the cisplatin treated cells do not vary significantly for different cisplatin treatments, although all the cisplatin treated cells present a significantly shorter long component lifetime than the untreated cells.

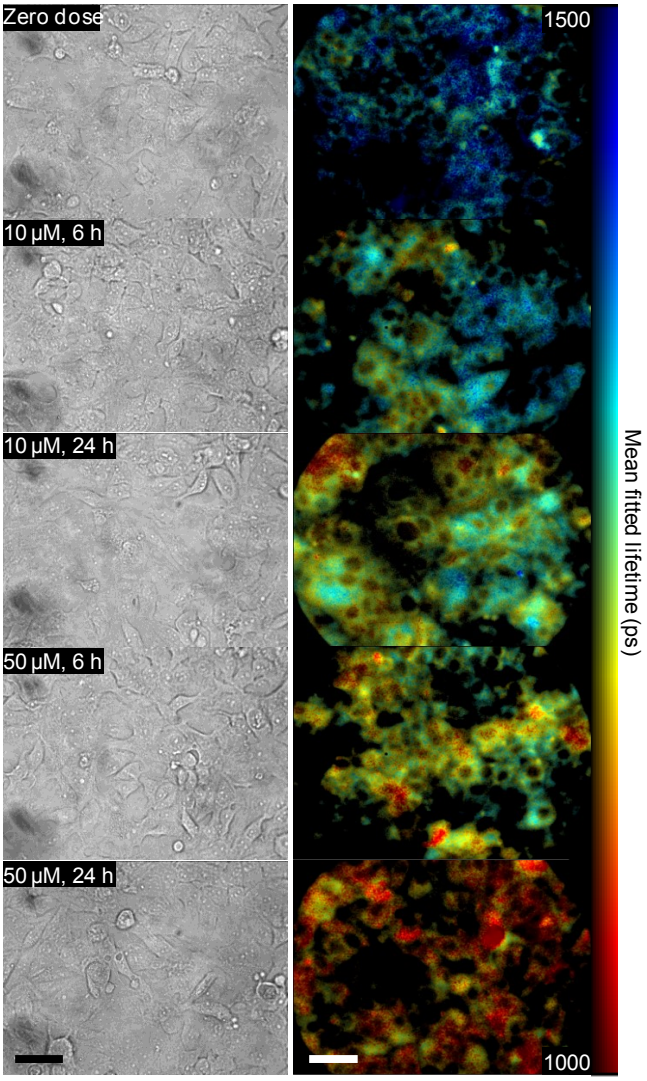

Figure 6-23 Exemplar fields of view across cisplatin dose and treatment time, showing phase contrast and false-coloured mean lifetime images.
Scale bars = 50 µm.

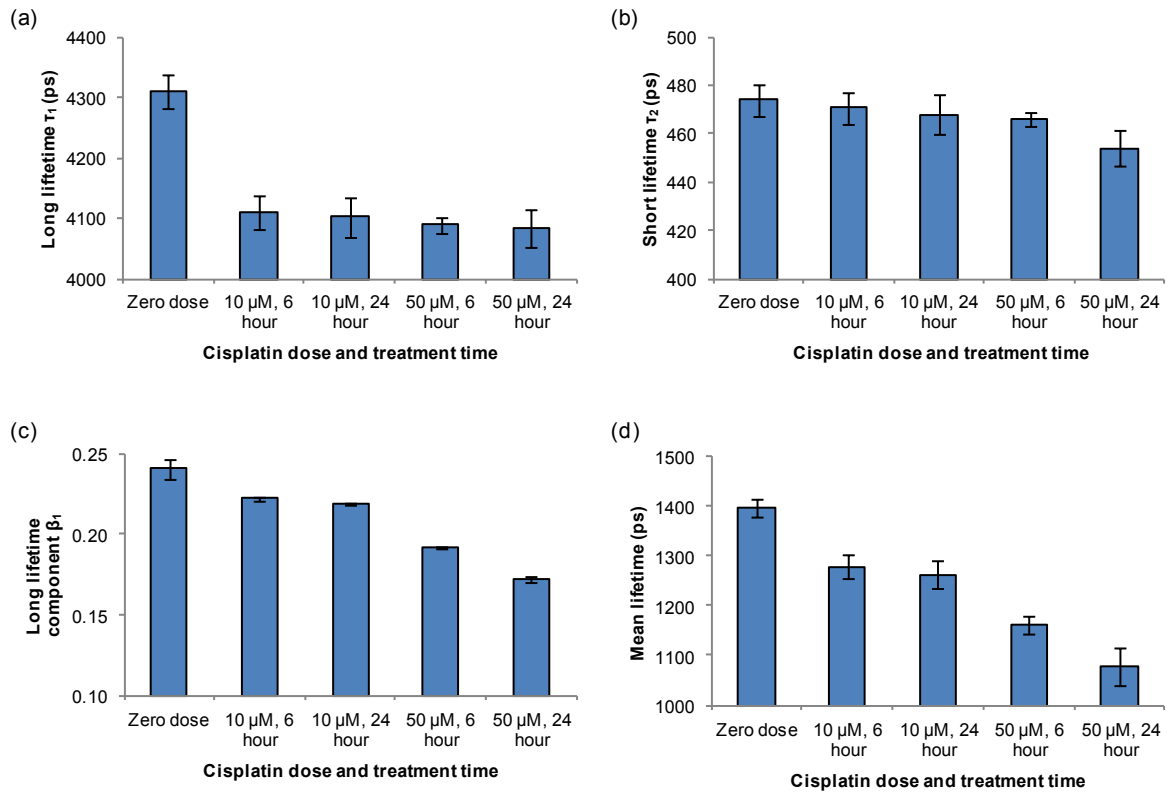

Figure 6-24 Fitted parameters from cisplatin treated cells.
(a) Long lifetime component. (b) Short lifetime component. (c) Long lifetime contribution. (d) Mean lifetime. In all cases, error bars show standard errors calculated across repeat wells.

Previous work has shown that treatment of MCF7 cells with cisplatin results in an increase in glycolysis over the timescales probed in this experiment[340]. Separately, Skala *et al.*[299] has reported that an increase in glycolysis results in a decrease in both lifetime components in a biexponential fit to NADH autofluorescence data, with a concomitant decrease in the contribution of the long lifetime component. The results presented here are consistent with these two published works. However, it is noted that treatment with cisplatin also leads ultimately to apoptosis: as mentioned in section 6.3 above, previous work has reported that apoptosis induced by staurosporine is linked to an increase in mean NADH fluorescence lifetime[318,341]. The cause of such changes has been argued to be that the cell shifts towards oxidative phosphorylation in order to more effectively generate ATP. The difference between this previous work and our results may be due to the specific modes of action of cisplatin and staurosporine and/or the rate at which apoptosis is occurs with these two compounds, but further work is needed to investigate this in more detail.

6.7 Tissue autofluorescence

Distinct from the project undertaken to investigate high content FLIM of cell metabolites, the FLIM plate reader was used to validate measurements of tissue autofluorescence taken with a point-probe arthroscope designed to aid in monitoring the progress of structural protein degradation in osteoarthritis.

This project was undertaken as a collaboration between the Photonics group at Imperial College London, and the Kennedy Institute of Rheumatology at the University of Oxford. The following sections detail the biological context in which the project was undertaken, the experimental considerations and modifications to the FLIM plate reader that were made as part of this project, and results from porcine models for osteoarthritis.

6.7.1 Biological background and motivation

Osteoarthritis (OA) is the most prevalent form of degenerative joint disease: 8.75 million people in the UK have sought treatment for this condition[342]. There is currently an unmet clinical need for a means of detecting OA early in its progression in order to prevent irreversible loss of joint function. The current "gold standard" of OA detection is radiography, but X-ray images of affected joints only exhibit evidence of OA after significant degradation of cartilage has occurred. Improving resolution of imaging instruments employing magnetic resonance imaging (MRI) or ultrasound provides a means of detecting OA earlier in its progression. This is achieved primarily by enabling documentation of joint effusion (excess fluid) and fibrillation, both of which have been suggested as possible early indicators of OA[343]. Other imaging techniques such as optical coherence tomography (OCT) have also been investigated as minimally invasive means of detecting early-stage OA[344]. Alternatively, biochemical changes in the cartilage extracellular matrix (ECM) that precede development of irreversible OA symptoms might be employed: this might include testing synovial fluid, serum or urine for biomarkers related to inflammation or fibrillation[343,345]. Another option is to test synovial fluid for collagen- or proteoglycan-related products of bone and ECM breakdown[343,346], or for the presence of proteolytic enzymes associated with cartilage degradation[347,348].

The composition of articular cartilage is roughly 45% aggrecan proteoglycans and 45% type II collagen, the remainder consisting of minor components. The presence of intermolecular cross links in collagen render cartilage fluorescent under UV excitation[349], and it is proposed that the fluorescence lifetime of cartilage depends on the local environment of the cross links: it follows that degradation of cartilage associated with OA might result in changes in autofluorescence lifetime. Researchers in our lab, in collaboration with the Kennedy Institute of Rheumatology at the University of Oxford, have developed a compact multidimensional fluorimeter coupled to a fibre optic probe to investigate the feasibility of utilising a FLIM-based arthroscope for minimally-invasive needle biopsy, with the aim of developing an instrument capable of reading out molecular-level changes in early OA[350]. We use wide field imaging measurements conducted on the plate reader to validate single point measurements taken with the point probe system. All samples presented in this section were prepared by Dr Mohammad Nickdel.

6.7.2 Development of methods

The wide field UV-excited FLIM microscope that forms the basis of the automated FLIM plate reader is a useful tool in early studies of cartilage degradation. The facility to make use of pulsed, tuneable laser sources in the UV-range made this instrument the prime choice for validating point probe measurements,

and the ability to automate the acquisition process allows relatively large areas of cartilage to be investigated with minimal user intervention. However, several specific issues were raised in the course of investigations that were unique to imaging tissue in this manner.

Firstly, it was decided that imaging should be performed using a 4x objective (Olympus 4x, NA 0.16) in order to survey large joint areas quickly. Such an objective suffers much more than the standard 40x objective from stray room light: it was deemed necessary always to cover the plexiglass window of the microscope incubator to minimise any chance of background giving rise to an anomalous long lifetime in the fit, and all acquisitions were performed with the transmitted light condenser tilted out of the image path to avoid reflections. Furthermore, the lens is not designed for use with UV excitation. However, using the imaging typical imaging parameters (integration time: 0.15 s, power density after objective: 357 $\mu W\ cm^{-2}$) it was found that integrated signal from a background measurement of TBS (Tris-buffered saline) on a sonicated coverslip was around 1% of typical signal from samples. Background contribution from the objective is therefore considered to be negligible.

Samples were mounted differently depending on type. The excised porcine cartilage samples presented here were laid on 170 μm coverslips for imaging. It was found that it was necessary to clean these coverslips before acquiring data to avoid contaminations (dust) being conflated with the sample signal. All coverslips were sonicated for five minutes in acetone before being rinsed in MilliQ water and dried on a hot plate.

Previous studies of cartilage autofluorescence in the group involved fitting a monoexponential decay model along with an offset value. In the absence of a physical reason for the presence of an offset, we instead supposed that a relatively long decay component was being misassigned. This supposition was confirmed by work performed by Joao Lagarto and Clifford Talbot using an excitation source with a lower repetition rate (5 MHz). Lifetime components that are on the same scale as repetition period are accounted for in the model fitted by *FLIMfit*[78].

6.7.3 Results

These experiments were designed to illustrate changes in autofluorescence lifetime upon proteolytic degradation of cartilage by matrix metalloproteinases (MMPs), a group of enzymes implicated in the development of OA. Bacterial collagenase was used as a positive control, since this treatment is known to rapidly degrade cartilage in a way analogous to degradation by multiple proteinases *in vivo*. Articular cartilage samples used in these experiments had been excised from specimens obtained from a slaughterhouse, frozen and thawed three times to kill chondrocytes, and stored at -20°C before being thawed for treatment. Excised sections of cartilage (~ 5 mm x 5 mm x 2.5 mm) were cut in two and one half of each sample was incubated at 37°C in treatment solution: either 50 μg/ml bacterial collagenase for 24 hours, or 50 μg/ml MMP-1 for 48 hours. The second half of each sample was kept in buffer for the

same period. Five repeat samples were prepared and imaged per condition. Following treatment, samples were frozen for transport from the Kennedy Institute to Imperial College London.

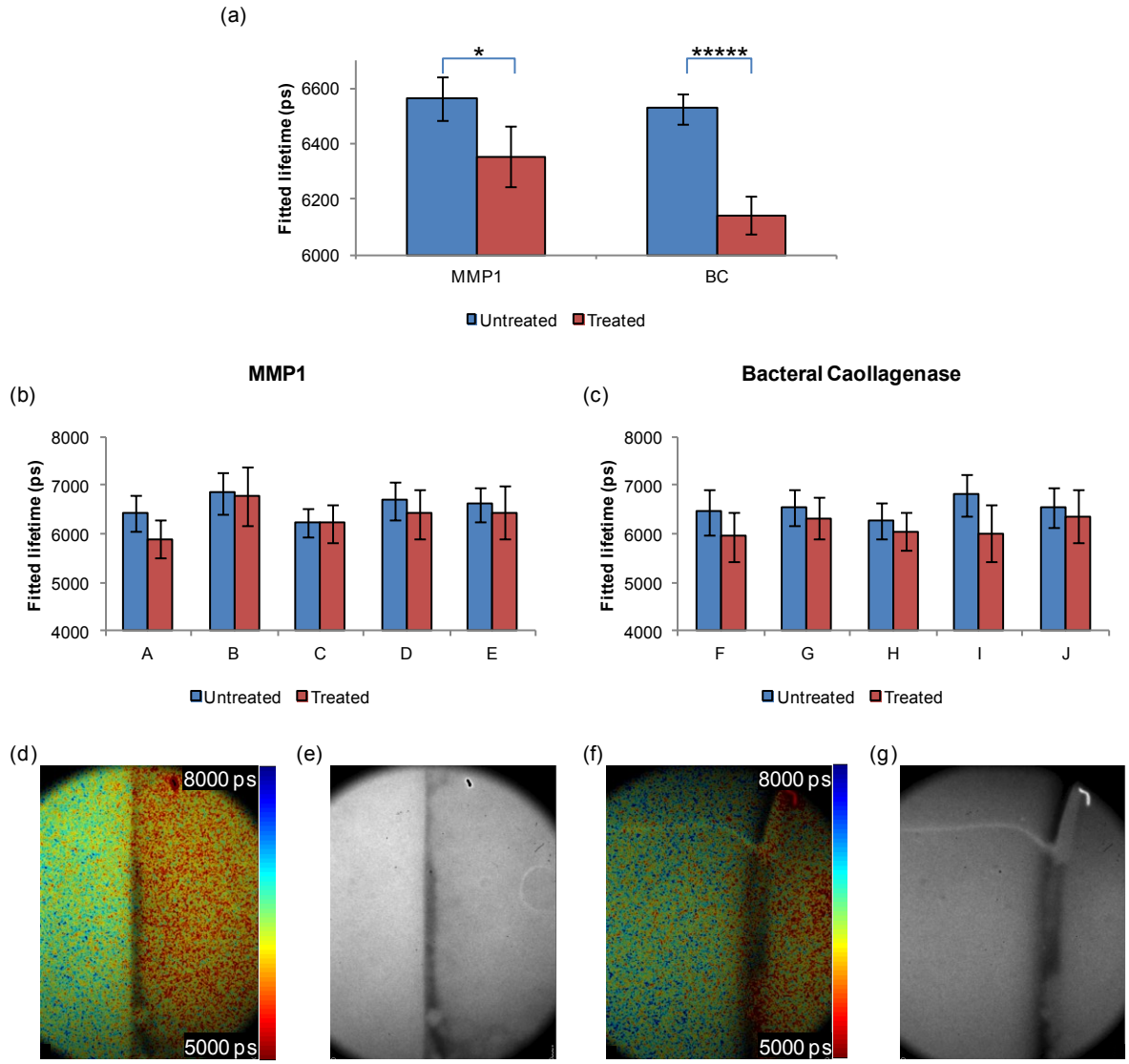

Figure 6-25 Results of wide field time gated FLIM imaging of enzyme-treated porcine cartilage explants.

(a) Average lifetimes in regions of interest averaged across five samples per condition; error bars show standard error across repeat samples. (b) Data presented in treated/untreated pairs by sample for MMP1-treated cases (50 μg/ml, 48 hours), error bars show standard deviation across pixels in regions of interest. (c) Data presented in treated/untreated pairs by sample for bacterial collagenase-treated cases (50 μg/ml, 24 hours), error bars show standard deviation across pixels in regions of interest. (d) FLIM and (e) intensity images for exemplar fields from MMP1-treated sample A. (f) FLIM and (g) intensity images for exemplar fields from bacterial collagenase-treated sample F.

6.7.4 Conclusions

We have illustrated that the plate reader can be a useful tool for probing cartilage autofluorescence lifetimes in the laboratory. We have confirmed, using a crude model based on excised porcine articular cartilage, that degradation of ECM using enzymes associated with OA progression can be read out by changes in autofluorescence lifetime. This work provides validation to measurements taken using a fibre optic probe-based fluorometer which acts as a prototype for a FLIM arthroscope for applications to

osteoarthritis. The imaging capability of the FLIM plate reader highlights potential issues with using such a point probe system in a clinical setting: in particular, heterogeneity displayed across cartilage samples and lifetime anomalies introduced by stray connective tissue may be linked to erroneous results in a non-imaging instrument such as might be used for needle biopsies.

6.8 Summary

The results presented in this chapter have demonstrated the feasibility of undertaking 96 well plate-format experiments investigating NADH lifetime in cells, characterising potential issues inherent in using UV excitation in the FLIM plate reader. It has been shown to be possible to minimise the background fluorescence from cell culture media by omitting selected components without adversely affecting cells over medium- and long duration imaging experiments. Using this modified media was shown not to induce changes in autofluorescence lifetime linked to changes in metabolic state either immediately after switching from cell culture media or over a typical plate reading FLIM experiment. Judicious choice of well plate has also been shown to be important in terms of background fluorescence contribution with more expensive, glass-bottomed plates being a necessity when using pulsed UV excitation for FLIM studies of NADH autofluorescence. In addition, there has been shown to be no time-varying fluorescent background associated with any of the microscope or external optics that present problems with reproducibility of measurements across a 96 well plate, allaying concerns that varying instrument performance might alter lifetime measurements across a plate acquisition.

Metabolic modulators with clearly defined biochemical action have been applied to a breast cancer cell line in order to test the ability of the instrument to measure changes in NADH lifetime parameters in cells when they are changed in a predictable fashion. Rotenone and FCCP both exhibit the predicted response in mean lifetime. Additionally, the experiments with rotenone illustrated the advantage of an automated means of delivering solutions to wells in a time course experiment. It was found that staurosporine, chosen to induce an apoptotic response in cells, exhibited strong fluorescence itself, precluding its use in cellular autofluorescence experiments under UV excitation.

Work was undertaken to explore the ability of the FLIM plate reader to read out cytotoxic effects of cancer therapies, and to investigate the possibility of discriminating between tumours with different classifications. It has been shown that MCF7 cells show an NADH lifetime response to treatment with cisplatin and, to a lesser extent, to doxorubicin. These observations are rendered statistically significant in part due to the number of automated repeats that are inherent in plate reader experiments. In experiments in which different cell lines were screened against each other, measured differences in fitted lifetime parameters did not always agree with previously reported findings. For future experiments, biochemical methods might usefully be employed to explain differences between findings reported here and those reported elsewhere.

Both empirically and from literature, it is evident that interpreting lifetime measurements derived from NADH autofluorescence is not always straightforward. In future work, it will perhaps be necessary to correlate results acquired from FLIM studies carried out on the plate reader with other methods of measuring cell metabolism, including biochemical methods, that have not formed part of the investigations presented here due to constraints on time and limited expertise. However, the advantages conferred by conducting such experiments on the plate reader, in terms of throughput and automation of time course studies, would add value to future studies of metabolism based on NADH lifetime imaging both by making a wider range of assays practical and by increasing the number of cells assayed.

The biological relevance of a plate reader capable of reading out autofluorescence lifetime as a surrogate for metabolic state includes applications in stratified medicine and drug discovery, as well as basic research. In the latter case, extensions of previous studies into diseases associated with metabolic changes such as cancer[312] or to stem cell differentiation for which autofluorescence can provide a label-free readout[322,351,352] might benefit from the additional throughput afforded by the system described here. Furthermore, autofluorescence readouts could be combined with other readouts of cell signalling, for example by FLIM-FRET, to further probe the underlying mechanisms of disease.

For stratified medicine, the application of cellular autofluorescence based readouts has been proposed to improve the clinical outcomes of cancer therapies through the ability to assay the metabolic response of cells derived from an individual patient's tumours to a number of different therapeutic conditions. Here a single multiwell plate-based experiment could allow rapid analysis of the likely response of the patient to specific drugs, doses or adjuvant treatments, thereby minimising drug resistance to therapy and improving efficacy. Such an approach may realise higher physiological relevance when implemented with tumour spheroid and other 3D cell culture techniques[351], which are becoming increasingly widely adopted.

For drug discovery there is potential for using cellular autofluorescence lifetime readouts to inform on the off-target metabolic response of drug candidates, particularly when combined with advances in and increasing commercial availability of stem cell-derived hepatic and cardiac cells[353]. The ability to perform these experiments in a plate reader format would permit systematic studies of metabolic changes in the context of drug toxicology and the dose-dependence of such effects. This could thus form the basis of new screening tools to help address the significant problem of late stage attrition in the pharmaceutical industry. To this end, cellular autofluorescence intensity has previously been explored as a tool to study toxicology in a plate reader format[354]; it is envisaged that the additional information on parameters such as NAD(P)H binding afforded by the FLIM plate reader might add value to such work.

6.9 Future work

The modifications to the FLIM plate reader described in this chapter allow the instrument to be deployed for UV-wavelength excitation FLIM studies. The flexibility of the instrument could be further enhanced by the addition of other imaging modalities: combining UV-excited NADH lifetime imaging with

intensity imaging at longer wavelengths would allow fluorescence intensity associated with FAD to be measured, and hence optical redox ratio to be calculated. Such a combination of methods has been implemented in a two-photon excitation system, and published works have shown the advantages that such a combination might afford in further discriminating between cell lines exhibiting different drug sensitivities and receptor statuses[312]. Implementing an additional spectral channel is in principle quite possible with the plate reader system: by combining excitation beam paths with a dichroic mirror and an excitation filter wheel, a broadband supercontinuum laser source might afford both intensity and time-resolved measurements of FAD fluorescence. Alternatively, automating the means of selecting between pulsed laser and mercury lamp excitation source could also allow intensity measurements of FAD fluorescence. Alternatively, the ability to resolve fluorescence polarisation in FLIM would give further information on NADH binding in response to various treatments, noting that such an approach has been implemented on a multiphoton microscope[355] but without the degree of automation or the speed associated with high content imaging. Implementing time-resolved anisotropy imaging on the plate reader would require a greater number of detected photons to resolve more complex anisotropy decays and would thus increase the image acquisition time.

There is a trade-off in the implementation of the FLIM microscope between field of view and resolution: generally, increasing the number of cells interrogated by increasing the field of view decreases the spatial resolution, which is determined by the density of resolution elements on the HRI. Depending on the particular biology to which the instrument is applied, it may be necessary or informative to acquire FLIM images with greater spatial resolution. Such measurements would potentially inform on the subcellular localisation of different NADH lifetimes or allow segmentation of cells to separate cytoplasmic NADH signal from mitochondrial signal. Modifying the instrument by using a different objective lens or introducing a lens relay system between the intermediate image plane and the photocathode of the HRI on the left hand port of the microscope would allow such imaging to be performed.

Recently, work has been published by the Duchen group in which the authors cast doubt on the canonical approaches to interpretation of metabolism-related autofluorescence lifetime data[310]. In this paper, the authors suggest that the origin of lifetime shifts in mammalian cell lines upon metabolic modulation to be less to do with different NADH binding partners than to do with a shift in the balance between signal originating from NADH and NADPH. This paper further emphasises both the interest in reading out NADH and NADPH autofluorescence lifetimes, as well as the difficulty in interpreting them in terms of specific biochemical changes within the cell, as discussed in section 6.2.

Chapter 7: Conclusions and outlook

7.1 Summary of thesis

This PhD thesis has described the development and application of an automated FLIM multiwell plate reader for high content analysis. During the course of this PhD project, I have undertaken research into three main areas. The first concerned the construction and development of hardware and software tools to create a functional, flexible automated FLIM plate reader to enable quantitative lifetime-based imaging assays for high content analysis. The second addressed its application to FRET-based assays utilising genetically expressed fluorophores and the third concerned its application to label-free autofluorescence lifetime-based readouts applied to assays of cellular metabolism and tissue matrix properties.

Having introduced the basic principles of fluorescence imaging, including the phenomenon of FRET and the foundations of FLIM, Chapter 2 of the thesis provided a brief review of the state-of-the-art in high content analysis imaging instruments, including alternative work towards FLIM-HCA published before and during my PhD project that provides some context for the development of the FLIM plate reader presented here. Chapter 3 concerned the hardware components required to implement the FLIM plate reader and the software development that continued throughout the project to enable the instrument to meet the demands placed upon it for assays developed either as part of the main biological application areas of the PhD thesis or in the course of smaller collaborative projects. Of the areas of instrument development, perhaps the most immediately useful across all biological applications was the enhancement of the basic cell prefind methods to encompass the use of low magnification lenses, multiple spectral channels and phase contrast imaging to increase flexibility and decrease the time spent searching for cells in sparely labelled or seeded cell samples. I further improved the functionality and flexibility of the instrumentation by increasing the degree of control over acquisition parameters in automated acquisition sequences to enable optimal parameters to be used to minimise acquisition times. Some aspects of instrument development, including the integration of automated liquid handling and the capability to acquire phase contrast or bright field images in line with FLIM acquisitions, were not used extensively for all the application experiments presented in this thesis but they will benefit a range of future experiments.

In Chapters 4 and 5, the FLIM plate reader was deployed to investigate biological signalling processes in cells using fluorescence lifetime to read out FRET signals. Chapter 4 concerned experiments utilising intermolecular FRET probes. The first application was an investigation of the SUMO1 post-translational modification of the oncogene product transcription factor FOXM1 in response to anthracycline treatment in breast cancer cells, carried out under the auspices of the Lam laboratory at Imperial College London. This was a challenging series of experiments due in part to problems with establishing transfection protocols yielding sufficiently high expression of the donor FOXM1-eGFP construct to be useful for imaging. In addition, the presence of multiple means of interaction between FOXM1 and SUMO1 meant that interpretation of the results of FRET experiments was not entirely straightforward.

Nevertheless, it was possible to establish that FOXM1 SUMOylation measured by FRET in MCF7 cells occurs in a treatment time-dependent manner, with a peak in the extent of modification at 6-8 hours post-treatment followed by a decrease over 21-24 hours post-treatment. This result was corroborated by parallel biochemical methods conducted by collaborators in the Lam laboratory. The second series of experiments concerning intermolecular FRET, undertaken with Anca Margineanu and Sean Warren in the Photonics group at Imperial College London, utilised fluorescent protein-based FRET constructs generated and tested by Jia Chan at UCL and sought to demonstrate a prototype protein-protein interaction screen by assaying the FRET signal resulting from potential interactions between derivatives of the MST1 protein and RASSF family protein constructs. This proof of principle screen identified the RASSF binding partners of MST1 and illustrated the potential of the FLIM plate reader to be used to screen for protein-protein interactions. Chapter 5 reported on the application of intramolecular FRET biosensors of GTPase activity in two different collaborative projects with the cell-cell adhesion signalling group in the National Heart and Lung Institute at Imperial College London. Working with the Braga laboratory at NHLI, experiments were undertaken with the goal of establishing the spatio-temporal profile of RhoA activation in response to calcium switch stimulation in human keratinocytes. Separately, in a parallel collaboration with the Braga laboratory, Rac1 activation in response to overexpression of the GTPase activating protein CdGAP was investigated. In both cases, FLIM-FRET results following assay optimisation were promising and supported hypotheses based on biochemical results: RhoA activation was found to increase 60 minutes after stimulation with calcium and Rac1 activity was found to be reduced both at lateral membranes and globally within cells by overexpression of CdGAP. An additional outcome of these projects was the development of a manual image segmentation tool developed for use on touch screen tablet and smartphone devices.

Chapter 6 concerned the use of autofluorescence lifetime imaging to investigate cell metabolism and structural protein degradation. While this has previously been established in small-scale imaging experiments, to date, as far as I am aware, the FLIM plate reader described in this thesis is the first reported HCA instrument for automated assays of cellular and tissue autofluorescence using single photon excitation and the experiments presented here are the only such exemplars of label-free HCA-FLIM assays using autofluorescence lifetime as a readout. This instrument development was subject to specific challenges, distinct from those encountered for visible wavelength HCA-FLIM and multiphoton autofluorescence lifetime imaging. In particular, optimisation of experimental parameters to minimise fluorescent background was required, and it was necessary to establish that cell metabolism was not adversely affected by either prolonged time on the microscope or by imaging with ultrafast UV-wavelength excitation sources. Experiments with known metabolic modulators illustrated that the autofluorescence lifetime imaging plate reader measured the expected changes in NADH fluorescence lifetime: stimulation with rotenone was found to increase mean lifetime, whilst treatment with the mitochondrial uncoupler FCCP was found to decrease mean lifetime. Studies of drug response and cell line screening yielded encouraging results, with reductions in lifetime being observed with both cisplatin

treatment time and treatment dose, which suggest FLIM-HCA of autofluorescence might be applicable in the areas of personalised medicine and toxicology studies. It was apparent throughout the project, however, that the measured autofluorescence lifetime of cells depends on many factors, and that future experiments could benefit from a close interaction with biochemists and other experts in metabolomics to aid interpretation of complex autofluorescence lifetime readouts. Chapter 6 also presented first results applying FLIM to autofluorescence of cartilage, for which lifetime changes could be correlated with collagen degradation, indicating the potential to use autofluorescence readouts as an indicator of osteoarthritis.

7.2 Ongoing projects and future work

Inevitably, the finite time available for each aspect of my PhD research has led to many avenues for investigation and development remaining for future work. Here I outline a few such developments that are being addressed in our laboratory. Instrument development is expected to progress according to the needs expressed by collaborators and colleagues. In particular, fully automated filter control for Nipkow disk optical sectioning has been implemented on the plate reader such that multiplexed FLIM and FRET imaging may be conducted in depth-resolved as well as wide-field modalities: it is foreseen that such capabilities might be useful when studying cells cultured in 3-D environments that are expected to give results with greater physiological relevance than, for example, monolayers of cells on coverslips. This could be extended for multiphoton imaging to the implementation of a multifoci tandem-scanning multiphoton FLIM microscope in the plate reader for automated imaging of cellular autofluorescence, including in tumour spheroids, tissue explants and other thick samples – although throughput is likely to be significantly lower than the current FLIM plate reader owing to the lower efficiency of multiphoton excitation. Further characterisation of the enabling technology for HCA-FLIM in the current implementation – the GOI – is currently being carried out within the Photonics group at Imperial College London in conjunction with Kentech Instruments Ltd. with the goal of optimising future design and fabrication of devices for FLIM acquisitions. Finally, development is ongoing to adapt the control acquisition software to an open-source platform (MicroManager), with the eventual goal of providing OpenFLIM-HCA to the wider fluorescence imaging community: a protocol for building and running a cheap, effective and flexible FLIM plate reader that does not require the purchase of software licences or highly specialised instrumentation.

The wide range of biological groups engaging in FRET experiments represents a rich source of mutually beneficial collaborations that could be explored to apply the FLIM plate reader to address diverse biological questions. Such application areas might include investigating receptor phosphorylation in response to drug treatment and more extensive investigation of signalling pathways, e.g. relating to FOXM1 and anthracycline resistance. In the latter case, the deployment of multiplexed FRET experiments – using multiple FRET systems with fluorophores in different spectral windows – is an avenue that may be explored with the automated FLIM plate reader. Further collaborations have already

been established and preliminary experiments are underway. A particular goal has been to establish the utility of the FLIM pate reader with cells expressing fluorescent proteins labelling proteins at endogenous levels, which is desirable to minimise the interference with biological processes that can result from over expression of target proteins. Working with the Ellenberg laboratory at EMBL, I have explored the prospect for FLIM to read out interactions of mitotic machinery without overexpressing fluorescent protein constructs by adopting genome-editing labelling techniques implemented by Robert Mahen. Preliminary data (Figure 7-1) suggests that such systems exhibit sufficient fluorescence in telophase and metaphase cells that FLIM on the plate reader is possible; future experiments will make use of the automated acquisition capabilities of the instrument to investigate the effects of homozygous versus heterozygous genome editing, as well as the nature of protein interactions at different stages of mitosis.

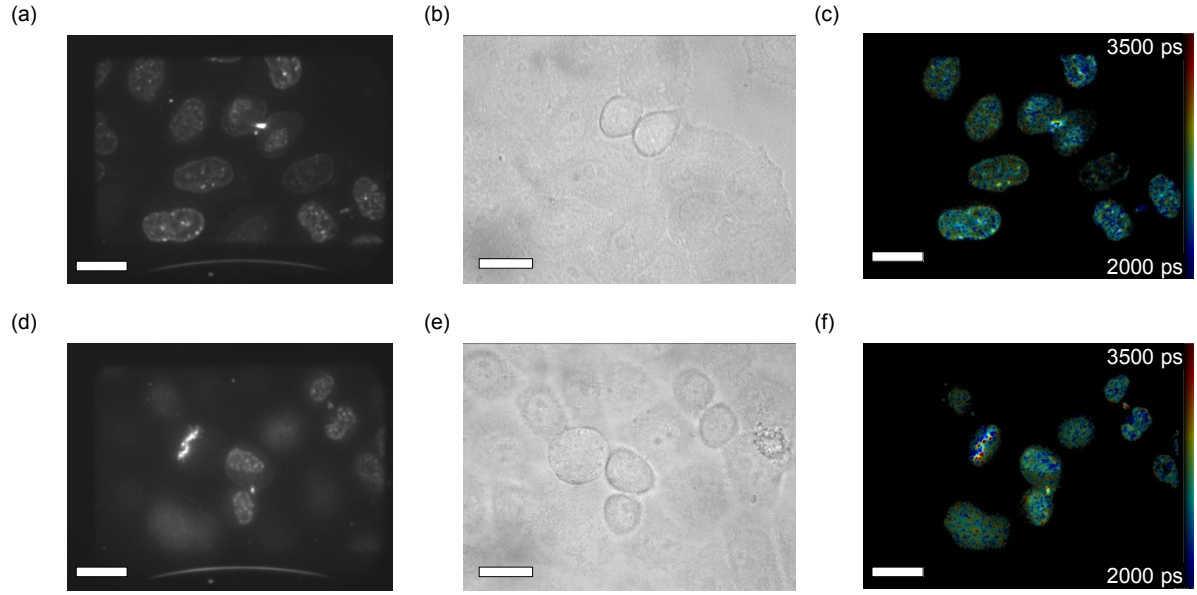

Figure 7-1 Preliminary data acquired with FLIM plate reader during a project to investigate protein-protein interactions during mitosis in genome-edited cell lines expressing fluorescent protein fusions at endogenous levels.

(a) Integrated intensity image of a field of view showing cells in interphase and telophase. (b) Bright field image of the same field of view (with small offset). (c) FLIM image showing results of a monoexponential fit to data from the same field of view. (d) Integrated intensity image of a field of view showing cells in interphase and metaphase. (e) Bright field image of the same field of view (with small offset). (f) FLIM image showing results of a monoexponential fit to data from the same field of view. Scale bars 50 μm.

Work is also continuing on the project concerning RASSF-family interactions with MST1 and its derivatives. As outlined at the end of Chapter 4, it may be possible to establish a model for FRET interactions that would allow the dissociation constant K_d to be established from lifetime and intensity measurements taken using the FLIM plate reader. To date, however, it has only been possible to investigate relative dissociation constants (Figure 7-2), due to the lack of optical sectioning inherent in wide-field illumination; furthermore, without any data to corroborate lifetime measurements, such an approach must be treated with caution. Nevertheless, optically sectioned FLIM data has recently been implemented in the plate reader using a motorised Nipkow disk unit in the plate reader to provide

improved quantitation of intensity measurements with the goal of establishing a series of absolute values for dissociation constants. It is further intended that a protein interaction that is better characterised than the RASSF-MST1 interaction might be investigated in order that K_d results obtained using the FLIM plate reader could be correlated to those measured using an alternative technique.

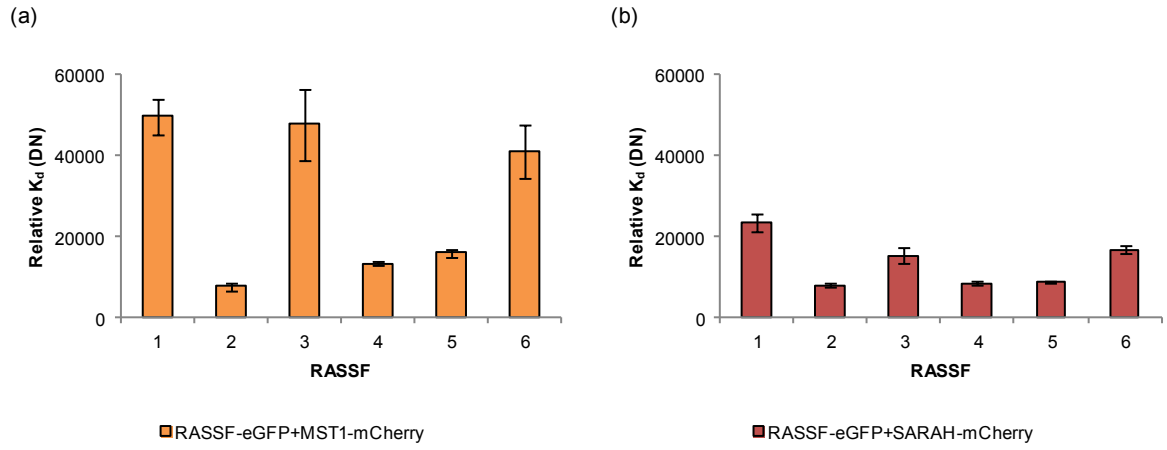

Figure 7-2 Preliminary data showing relative dissociation constants as calculated from FLIM plate reader data as outlined in Chapter 4: section 4.2.7.

(a) Relative K_d calculated for interactions between classical RASSF family members fused to eGFP and full length MST1 protein fused to mCherry. (b) Relative K_d calculated for interactions between classical RASSF family members fused to eGFP and truncated SARAH domain fused to mCherry.

There have been many potential applications for metabolite imaging emerging in the literature including investigations of stem cell differentiation, cancer screening and toxicology. Many of these experiments could benefit from the automation and statistical robustness that can be established using FLIM plate reader instrumentation to excite metabolite autofluorescence. Collaborations with groups involved in metabolomics could be fruitful as biochemical experiments conducted in parallel with autofluorescence-based assays should provide a clearer picture of the molecular changes taking place inside cells and contributing to autofluorescence lifetime changes. In particular, assaying the response to drugs in patient-derived cell cultures, as proposed by the Skala laboratory at Vanderbilt University, could prove useful for stratifying patient cohorts for therapy. In general, there seems to be significant potential for HCA-FLIM of cellular autofluorescence as a diagnostic and toxicological tool for drug discovery and personalised medicine.

Publications and conferences

Publications

L. Chen, S. Kumar, **D. J. Kelly**, N. Andrews, M. J. Dallman, P. M. W. French, J. McGinty. "Remote focal scanning optical projection tomography with an electrically tunable lensf" *Biomedical Optics Express*. In press.

D. J. Kelly, S. C. Warren, S. Kumar, J. L. Lagarto, B. T. Dyer, A. Margineanu, E. W.-F. Lam, C. Dunsby, P. M. W. French. "An automated multiwell plate reading flim microscope for live cell autofluorescence lifetime assays" *J. Innov. Opt. Health Sci.* **7,** 1450025 (2014). doi: 10.1142/S1793545814500254

S. S. Myatt, M. Kongsema, C. W.-Y. Man, **D. J. Kelly**, A. R. Gomes, P. Khongkow, U. Karunarathna, S. Zona, J. K. Langer, C. W. Dunsby, R. C. Coombes, P. M. French, J. J. Brosens, E. W.-F. Lam. "SUMOylation inhibits FOXM1 activity and delays mitotic transition." *Oncogene* 1–14 (2013). doi:10.1038/onc.2013.546

S. C. Warren, A. Margineanu, D. Alibhai, **D. J. Kelly**, C. Talbot, Y. Alexandrov, I. Munro, M. Katan, C. Dunsby, P. M. W. French. "Rapid global fitting of large fluorescence lifetime imaging microscopy datasets" *PLoS One* **8,** e70687 (2013). doi: 10.1371/journal.pone.0070687 1.

D. Alibhai, **D. J. Kelly**, S. Warren, S. Kumar, A. Margineau, R. A. Serwa, E. Thinon, Y. Alexandrov, E. J. Murray, F. Stuhmeier, E. W. Tate, M. A. A. Neil, C. Dunsby, P. M. W. French. "Automated fluorescence lifetime imaging plate reader and its application to Förster resonant energy transfer readout of Gag protein aggregation." *J. Biophotonics* **6,** 398–408 (2013). doi: 0.1002/jbio.201200185

H. B. Manning, M. B. Nickdel, K. Yamamoto, J. L. Lagarto, **D. J. Kelly**, C. B. Talbot, G. Kennedy, J. Dudhia, J. Lever, C. Dunsby, P. French, Y. Itoh. "Detection of cartilage matrix degradation by autofluorescence lifetime." *Matrix Biol.* **32,** 32–8 (2013). doi: 10.1016/j.matbio.2012.11.012

K.-K. Ho, V. A. McGuire, C.-Y. Koo, K. W. Muir, N. de Olano, E. Maifoshie, **D. J. Kelly**, U. B. McGovern, L. J. Monteiro, A. R. Gomes, A. R. Nebreda, D. G. Campbell, J. S. C. Arthur, E. W.-F. Lam. "Phosphorylation of FOXO3a on Ser-7 by p38 promotes its nuclear localization in response to doxorubicin." *J. Biol. Chem.* **287,** 1545–55 (2012). doi: 10.1074/jbc.M111.284224

S. Kumar, D. Alibhai, A. Margineanu, R. Laine, G. Kennedy, J. McGinty, S. Warren, **D. J. Kelly**, Y. Alexandrov, I. Munro, C. Talbot, D. W. Stuckey, C. Kimberly, B. Viellerobe, F. Lacombe, E. W.-F. Lam, H. Taylor, *et al.* "FLIM FRET Technology for Drug Discovery: Automated Multiwell-Plate High-Content Analysis, Multiplexed Readouts and Application in Situ." *Chemphyschem* **12,** 609–26 (2011). doi: 10.1002/cphc.201000874

Conferences

A. Margineanu, J. Chan, **D. J. Kelly**, S. C. Warren, S. Kumar, M. Katan, C. Dunsby, P. M. W. French. "Screening for protein-protein interactions using Förster resonant energy transfer (FRET) and fluorescence lifetime microscopy (FLIM)", International Photochemistry Conference, 2013, Leuven, Belgium. Poster presentation by A. Margineanu.

D. J. Kelly, D. Alibhai, S. C. Warren, S. Kumar, A. Margineanu, F. Stuhmeier, E. J. Murray, M. Katan, E. W. Lam, M. A. Neil, C. Dunsby, P. M. French. "An Automated FLIM Multiwell Plate Reader for High Content Analysis", Optical Molecular Probes, Imaging and Drug Delivery 2013, Hawaii, USA, 2013. Oral presentation by D. J. Kelly.

S. Coda, **D. J. Kelly**, J. Lagarto, H. Manning, R. Patalay, H. Sparks, A. Thompson, S. Warren, J. Dudhia, G. Kennedy, M. Nickdel, C. Talbot, K. Yamamoto, M. A. Neil, Y. Itoh, J. McGinty, G. Stamp, *et al.* "Autofluorescence lifetime imaging and metrology for medical research and clinical diagnosis", Optical Molecular Probes, Imaging and Drug Delivery 2013, Hawaii, USA, 2013. Oral presentation by P. M. W. French.

M. B. Nickdel, H. B. Manning, K. Yamamoto, J. L. Lagarto, **D. J. Kelly**, C. B. Talbot, G. Kennedy, J. Dudhia, J. Lever, C. Dunsby, P. M. W. French, Y. Itoh. "Detection of cartilage matrix degradation by autofluorescence lifetime", British Society for Matrix Biology Meeting 2013, Oxford, UK, 2013. Oral presentation by M. B. Nickdel.

D. J. Kelly. "Towards high-throughput FLIM: instrumentation and applications", 40th Scottish Microscopy Group Symposium, Edinburgh, UK, 2012. Oral presentation by D. J. Kelly.

D. Alibhai, **D. J. Kelly**, S. C. Warren, S. Kumar, A. Margineanu, R. A. Serwa, E. Thinon, Y. Alexandrov, E. J. Murray, F. Stuhmeier, E.W. Tate, M. A. A. Neil, C. Dunsby, P. M. W. French. "HCA of HIV-1 protein-protein interactions using automated, wide-field, time-gated, optically-sectioned FLIM", High Content Analysis 2012, San Francisco, USA, 2012. Oral presentation by D. Alibhai.

D. Alibhai, S. Kumar, **D. J. Kelly**, S. C. Warren, Y. Alexandrov, I. Munro, J. McGinty, C. Talbot, E. J. Murray, F. Stuhmeier, M. A. A. Neil, C. Dunsby, P. M. W. French. "An automated wide-field time-gated optically sectioning fluorescence lifetime imaging multiwell plate reader for high-content analysis of protein-protein interactions", Three-dimensional and Multidimensional Microscopy: Image Acquisition and Processing XVIII, BiOS, San Francisco, USA, 2011. Oral presentation by D. Alibhai.

D. J. Kelly, S. Kumar, A. Margineanu, S. C. Warren, D. Alibhai, P. O'Gara, S. Harding, M. A. A. Neil, C. Dunsby, P. M. W. French. "Automated multiwell plate FLIM of cellular autofluorescence for label-free HCA cytotoxicity assays", Scientific Meeting of Photonics4Life 2011, Karlsruhe, Germany, 2011. Oral presentation by D. J. Kelly.

S. Kumar, D. Alibhai, **D. J. Kelly**, R. Laine, A. Margineanu, S. C. Warren, Y. Alexandrov, I. Munro, T. Murray, F. Stuhmeier, C. Dunsby, M. A. A. Neil, P. M. W. French. "Fluorescence lifetime imaging microscopy in a high content screening context", MipTec, 2011, Basel, Switzerland. Oral presentation by S. Kumar.

References

1. B. Valeur. "Molecular Fluorescence: Principles and Applications" **8,** , Wiley VCH, Weinheim, (2012).

2. R. C. Hilborn. "Einstein coefficients, cross sections, f values, dipole moments, and all that" *Am. J. Phys.* **50,** 982 (1982). doi:10.1119/1.12937 doi: 10.1119/1.12937

3. M. Kasha. "Characterization of electronic transitions in complex molecules" *Discuss. Faraday Soc.* **9,** 14–19 (1950). doi:10.1039/df9500900014 doi: 10.1039/df9500900014

4. M. Sauer, J. Hofkens, J. Enderlein. "Basic Principles of Fluorescence Spectroscopy" 1–30 , Wiley VCH, Weinheim, (2011).

5. J. R. Lakowicz. "Principles of Fluorescence Spectroscopy" , Springer, New York, (2006).

6. Evrogen. "Yellow fluorescent protein TagYFP" (2014). at <http://www.evrogen.com/products/TagYFP/TagYFP_Detailed_description.shtml>

7. L. O. Björn, P. Huovinen. in *Photobiol. Sci. Life Light* (Björn, L. O.) **48,** 479–502 , Springer, New York, (2008). doi:10.1007/978-0-387-72655-7_18 doi: 10.1007/978-0-387-72655-7_18

8. T. Zimmermann. in *Microsc. Tech.* (Rietdorf, J.) 245–265 , Springer, Berlin Heidelberg, (2005). doi:10.1007/b102216doi:10.1007/b102216 doi: 10.1007/b102216

9. M. Baruah, W. Qin, C. Flors, J. Hofkens, R. A. L. Vallée, D. Beljonne, M. Van der Auweraer, W. M. De Borggraeve, N. Boens. "Solvent and pH dependent fluorescent properties of a dimethylaminostyryl borondipyrromethene dye in solution." *J. Phys. Chem. A* **110,** 5998–6009 (2006). doi:10.1021/jp054878u doi: 10.1021/jp054878u

10. E. A. Jares-Erijman, T. M. Jovin. "FRET imaging." *Nat. Biotechnol.* **21,** 1387–95 (2003). doi:10.1038/nbt896 doi: 10.1038/nbt896

11. A. N. Bader, E. G. Hofman, J. Voortman, P. M. P. Van Bergen En Henegouwen, H. C. Gerritsen. "Homo-FRET imaging enables quantification of protein cluster sizes with subcellular resolution" *Biophys. J.* **97,** 2613–22 (2009). doi:10.1016/j.bpj.2009.07.059 doi: 10.1016/j.bpj.2009.07.059

12. J. Siegel, K. Suhling, S. Lévêque-Fort, S. E. D. Webb, D. M. Davis, D. Phillips, Y. Sabharwal, P. M. W. French. "Wide-field time-resolved fluorescence anisotropy imaging (TR-FAIM): Imaging the rotational mobility of a fluorophore" *Rev. Sci. Instrum.* **74,** 182 (2003). doi:10.1063/1.1519934 doi: 10.1063/1.1519934

13. J. Autschbach. "Why the Particle-in-a-Box Model Works Well for Cyanine Dyes but Not for Conjugated Polyenes" *J. Chem. Educ.* **84,** 1840 (2007). doi:10.1021/ed084p1840 doi: 10.1021/ed084p1840

14. M. L. Barcellona, G. Cardiel, E. Gratton. "Time-resolved fluorescence of DAPI in solution and bound to polydeoxynucleotides." *Biochem. Biophys. Res. Commun.* **170,** 270–80 (1990).

15. G. Cosa, K. S. Focsaneanu, J. R. McLean, J. P. McNamee, J. C. Scaiano. "Photophysical properties of fluorescent DNA-dyes bound to single- and double-stranded DNA in aqueous buffered solution." *Photochem. Photobiol.* **73,** 585–99 (2001).

16. A. W. Krause, W. W. Carley, W. W. Webb. "Fluorescent erythrosin B is preferable to trypan blue as a vital exclusion dye for mammalian cells in monolayer culture." *J. Histochem. Cytochem.* **32,** 1084–90 (1984).

17. D. Ribble, N. B. Goldstein, D. A. Norris, Y. G. Shellman. "A simple technique for quantifying apoptosis in 96-well plates." *BMC Biotechnol.* **5,** 12 (2005). doi:10.1186/1472-6750-5-12 doi: 10.1186/1472-6750-5-12

18. S. Kasibhatla, G. P. Amarante-Mendes, D. Finucane, T. Brunner, E. Bossy-Wetzel, D. R. Green. "Acridine Orange/Ethidium Bromide (AO/EB) Staining to Detect Apoptosis." *CSH Protoc.* **2006,** 4493 (2006). doi:10.1101/pdb.prot4493 doi: 10.1101/pdb.prot4493

19. T. Ng, A. Squire, G. Hansra, F. Bornancin, C. Prevostel, A. Hanby, W. Harris, D. Barnes, S. Schmidt, H. Mellor, P. I. Bastiaens, P. J. Parker. "Imaging protein kinase Calpha activation in cells." *Science (80-.).* **283,** 2085–9 (1999).

20. H. M. Eilken, S.-I. Nishikawa, T. Schroeder. "Continuous single-cell imaging of blood generation from haemogenic endothelium." *Nature* **457,** 896–900 (2009). doi:10.1038/nature07760 doi: 10.1038/nature07760

21. D. A. Sipkins, X. Wei, J. W. Wu, J. M. Runnels, D. Côté, T. K. Means, A. D. Luster, D. T. Scadden, C. P. Lin. "In vivo imaging of specialized bone marrow endothelial microdomains for tumour engraftment." *Nature* **435,** 969–73 (2005). doi:10.1038/nature03703 doi: 10.1038/nature03703

22. P. D. Kaiser, J. Maier, B. Traenkle, F. Emele, U. Rothbauer. "Recent progress in generating intracellular functional antibody fragments to target and trace cellular components in living cells." *Biochim. Biophys. Acta* (2014). doi:10.1016/j.bbapap.2014.04.019doi:10.1016/j.bbapap.2014.04.019 doi: 10.1016/j.bbapap.2014.04.019

23. A.-S. Rinaldi, G. Freund, D. Desplancq, A.-P. Sibler, M. Baltzinger, N. Rochel, Y. Mély, P. Didier, E. Weiss. "The use of fluorescent intrabodies to detect endogenous gankyrin in living cancer cells." *Exp. Cell Res.* **319,** 838–49 (2013). doi:10.1016/j.yexcr.2013.01.011 doi: 10.1016/j.yexcr.2013.01.011

24. D. C. Prasher, V. K. Eckenrode, W. W. Ward, F. G. Prendergast, M. J. Cormier. "Primary structure of the Aequorea victoria green-fluorescent protein." *Gene* **111,** 229–33 (1992).

25. M. Chalfie, Y. Tu, G. Euskirchen, W. Ward, D. Prasher. "Green fluorescent protein as a marker for gene expression" *Science (80-.).* **263,** 802–805 (1994). doi:10.1126/science.8303295 doi: 10.1126/science.8303295

26. R. Y. Tsien. "The green fluorescent protein." *Annu. Rev. Biochem.* **67,** 509–44 (1998). doi:10.1146/annurev.biochem.67.1.509 doi: 10.1146/annurev.biochem.67.1.509

27. L. A. Gross, G. S. Baird, R. C. Hoffman, K. K. Baldridge, R. Y. Tsien. "The structure of the chromophore within DsRed, a red fluorescent protein from coral." *Proc. Natl. Acad. Sci. U. S. A.* **97,** 11990–5 (2000). doi:10.1073/pnas.97.22.11990 doi: 10.1073/pnas.97.22.11990

28. N. C. Shaner, G. H. Patterson, M. W. Davidson. "Advances in fluorescent protein technology." *J. Cell Sci.* **120,** 4247–60 (2007). doi:10.1242/jcs.005801 doi: 10.1242/jcs.005801

29. F. Yang, L. G. Moss, G. N. Phillips. "The molecular structure of green fluorescent protein." *Nat. Biotechnol.* **14,** 1246–51 (1996). doi:10.1038/nbt1096-1246 doi: 10.1038/nbt1096-1246

30. E. Snapp. "Design and use of fluorescent fusion proteins in cell biology." *Curr. Protoc. cell Biol.* **Chapter 21,** (2005). doi:10.1002/0471143030.cb2104s27 doi: 10.1002/0471143030.cb2104s27

31. G.-J. Kremers, S. G. Gilbert, P. J. Cranfill, M. W. Davidson, D. W. Piston. "Fluorescent proteins at a glance" *J. Cell Sci.* **124,** 2676–2676 (2011). doi:10.1242/jcs.095059 doi: 10.1242/jcs.095059

32. O. V Stepanenko, O. V Stepanenko, D. M. Shcherbakova, I. M. Kuznetsova, K. K. Turoverov, V. V Verkhusha. "Modern fluorescent proteins: from chromophore formation to novel intracellular applications." *Biotechniques* **51,** 313–4, 316, 318 passim (2011). doi:10.2144/000113765 doi: 10.2144/000113765

33. J. Goedhart, D. von Stetten, M. Noirclerc-Savoye, M. Lelimousin, L. Joosen, M. a Hink, L. van Weeren, T. W. J. Gadella, A. Royant. "Structure-guided evolution of cyan fluorescent proteins towards a quantum yield of 93%." *Nat. Commun.* **3,** 751 (2012). doi:10.1038/ncomms1738 doi: 10.1038/ncomms1738

34. G. S. Filonov, K. D. Piatkevich, L.-M. Ting, J. Zhang, K. Kim, V. V Verkhusha. "Bright and stable near-infrared fluorescent protein for in vivo imaging." *Nat. Biotechnol.* **29,** 757–61 (2011). doi:10.1038/nbt.1918 doi: 10.1038/nbt.1918

35. G. T. Hanson, R. Aggeler, D. Oglesbee, M. Cannon, R. a Capaldi, R. Y. Tsien, S. J. Remington. "Investigating mitochondrial redox potential with redox-sensitive green fluorescent protein indicators." *J. Biol. Chem.* **279,** 13044–53 (2004). doi:10.1074/jbc.M312846200 doi: 10.1074/jbc.M312846200

36. R. Heim, A. B. Cubitt, R. Y. Tsien. "Improved green fluorescence." *Nature* **373,** 663–4 (1995). doi:10.1038/373663b0 doi: 10.1038/373663b0

37. N. C. Shaner, R. E. Campbell, P. A. Steinbach, B. N. G. Giepmans, A. E. Palmer, R. Y. Tsien. "Improved monomeric red, orange and yellow fluorescent proteins derived from Discosoma sp. red fluorescent protein." *Nat. Biotechnol.* **22,** 1567–72 (2004). doi:10.1038/nbt1037 doi: 10.1038/nbt1037

38. E. M. Merzlyak, J. Goedhart, D. Shcherbo, M. E. Bulina, A. S. Shcheglov, A. F. Fradkov, A. Gaintzeva, K. A. Lukyanov, S. Lukyanov, T. W. J. Gadella, D. M. Chudakov. "Bright monomeric red fluorescent protein with an extended fluorescence lifetime." *Nat. Methods* **4,** 555–7 (2007). doi:10.1038/nmeth1062 doi: 10.1038/nmeth1062

39. N. C. Shaner, M. Z. Lin, M. R. McKeown, P. A. Steinbach, K. L. Hazelwood, M. W. Davidson, R. Y. Tsien. "Improving the photostability of bright monomeric orange and red fluorescent proteins." *Nat. Methods* **5,** 545–51 (2008). doi:10.1038/nmeth.1209 doi: 10.1038/nmeth.1209

40. R. E. Campbell, O. Tour, A. E. Palmer, P. a Steinbach, G. S. Baird, D. a Zacharias, R. Y. Tsien. "A monomeric red fluorescent protein." *Proc. Natl. Acad. Sci. U. S. A.* **99,** 7877–82 (2002). doi:10.1073/pnas.082243699 doi: 10.1073/pnas.082243699

41. M. A. Rizzo, G. H. Springer, B. Granada, D. W. Piston. "An improved cyan fluorescent protein variant useful for FRET." *Nat. Biotechnol.* **22,** 445–9 (2004). doi:10.1038/nbt945 doi: 10.1038/nbt945

42. M. A. Rizzo, D. W. Piston. "High-contrast imaging of fluorescent protein FRET by fluorescence polarization microscopy." *Biophys. J.* **88,** L14–6 (2005). doi:10.1529/biophysj.104.055442 doi: 10.1529/biophysj.104.055442

43. T. Nagai, K. Ibata, E. S. Park, M. Kubota, K. Mikoshiba, A. Miyawaki. "A variant of yellow fluorescent protein with fast and efficient maturation for cell-biological applications." *Nat. Biotechnol.* **20,** 87–90 (2002). doi:10.1038/nbt0102-87 doi: 10.1038/nbt0102-87

44. R. D. Anderson, J. Zhou, S. M. Hecht. "Fluorescence resonance energy transfer between unnatural amino acids in a structurally modified dihydrofolate reductase." *J. Am. Chem. Soc.* **124,** 9674–5 (2002).

45. A. R. Katritzky, T. Narindoshvili. "Fluorescent amino acids: advances in protein-extrinsic fluorophores." *Org. Biomol. Chem.* **7,** 627–34 (2009). doi:10.1039/b818908k doi: 10.1039/b818908k

46. K. Lang, L. Davis, J. Torres-Kolbus, C. Chou, A. Deiters, J. W. Chin. "Genetically encoded norbornene directs site-specific cellular protein labelling via a rapid bioorthogonal reaction." *Nat. Chem.* **4,** 298–304 (2012). doi:10.1038/nchem.1250 doi: 10.1038/nchem.1250

47. B. A. Griffin, S. R. Adams, R. Y. Tsien. "Specific Covalent Labeling of Recombinant Protein Molecules Inside Live Cells" *Science (80-.).* **281,** 269–272 (1998). doi:10.1126/science.281.5374.269 doi: 10.1126/science.281.5374.269

48. C. C. Spagnuolo, R. J. Vermeij, E. A. Jares-Erijman. "Improved photostable FRET-competent biarsenical-tetracysteine probes based on fluorinated fluoresceins." *J. Am. Chem. Soc.* **128,** 12040–1 (2006). doi:10.1021/ja063212q doi: 10.1021/ja063212q

49. C. Szent-Gyorgyi, B. F. Schmidt, B. a Schmidt, Y. Creeger, G. W. Fisher, K. L. Zakel, S. Adler, J. a J. Fitzpatrick, C. a Woolford, Q. Yan, K. V Vasilev, P. B. Berget, M. P. Bruchez, J. W. Jarvik, A. Waggoner. "Fluorogen-activating single-chain antibodies for imaging cell surface proteins." *Nat. Biotechnol.* **26,** 235–40 (2008). doi:10.1038/nbt1368 doi: 10.1038/nbt1368

50. J. Ziauddin, D. M. Sabatini. "Microarrays of cells expressing defined cDNAs." *Nature* **411,** 107–10 (2001). doi:10.1038/35075114 doi: 10.1038/35075114

51. H. Erfle, B. Neumann, U. Liebel, P. Rogers, M. Held, T. Walter, J. Ellenberg, R. Pepperkok. "Reverse transfection on cell arrays for high content screening microscopy." *Nat. Protoc.* **2,** 392–9 (2007). doi:10.1038/nprot.2006.483 doi: 10.1038/nprot.2006.483

52. A. Meng, H. Tang, B. A. Ong, M. J. Farrell, S. Lin. "Promoter analysis in living zebrafish embryos identifies a cis-acting motif required for neuronal expression of GATA-2." *Proc. Natl. Acad. Sci. U. S. A.* **94,** 6267–72 (1997).

53. A. L. Parker, C. Newman, S. Briggs, L. Seymour, P. J. Sheridan. "Nonviral gene delivery: techniques and implications for molecular medicine" *Expert Rev. Mol. Med.* **5,** 1–15 (2004). doi:10.1017/S1462399403006562 doi: 10.1017/S1462399403006562

54. R. Grisshamer, S. K. Buchanan. in *Struct. Biol. Membr. Proteins* (Grisshammer, R. & Buchanan, S. K.) 15–28 , Royal Society of Chemistry, Cambridge, (2006). doi:10.1039/9781847552563doi:10.1039/9781847552563 doi: 10.1039/9781847552563

55. M. H. Porteus, D. Baltimore. "Chimeric nucleases stimulate gene targeting in human cells." *Science (80-.).* **300,** 763 (2003). doi:10.1126/science.1078395 doi: 10.1126/science.1078395

56. H. Ochiai, N. Sakamoto, K. Fujita, M. Nishikawa, K. Suzuki, S. Matsuura, T. Miyamoto, T. Sakuma, T. Shibata, T. Yamamoto. "Zinc-finger nuclease-mediated targeted insertion of reporter genes for quantitative imaging of gene expression in sea urchin embryos." *Proc. Natl. Acad. Sci. U. S. A.* **109,** 10915–20 (2012). doi:10.1073/pnas.1202768109 doi: 10.1073/pnas.1202768109

57. H. Yang, H. Wang, C. S. Shivalila, A. W. Cheng, L. Shi, R. Jaenisch. "One-step generation of mice carrying reporter and conditional alleles by CRISPR/Cas-mediated genome engineering." *Cell* **154,** 1370–9 (2013). doi:10.1016/j.cell.2013.08.022 doi: 10.1016/j.cell.2013.08.022

58. T. Förster. "Energy migration and fluorescence" *J. Biomed. Opt.* **17,** 011002 (2012). doi:10.1117/1.JBO.17.1.011002 doi: 10.1117/1.JBO.17.1.011002

59. T. Förster. "Zwischenmolekulare Energiewanderung und Fluoreszenz" *Ann. Phys.* **437,** 55–75 (1948). doi:10.1002/andp.19484370105 doi: 10.1002/andp.19484370105

60. N. Akrap, T. Seidel, B. G. Barisas. "Förster distances for fluorescence resonant energy transfer between mCherry and other visible fluorescent proteins." *Anal. Biochem.* **402,** 105–6 (2010). doi:10.1016/j.ab.2010.03.026 doi: 10.1016/j.ab.2010.03.026

61. P. A. Steinbach. "Spectra" *Documents* (2010). at <http://www.tsienlab.ucsd.edu/Documents/>

62. G. Weber. "Dependence of the polarization of the fluorescence on the concentration" *Trans. Faraday Soc.* **50,** 552 (1954). doi:10.1039/tf9545000552 doi: 10.1039/tf9545000552

63. D. Alibhai, D. J. Kelly, S. Warren, S. Kumar, A. Margineau, R. A. Serwa, E. Thinon, Y. Alexandrov, E. J. Murray, F. Stuhmeier, E. W. Tate, M. A. A. Neil, C. Dunsby, P. M. W. French. "Automated fluorescence lifetime imaging plate reader and its application to Förster resonant energy transfer readout of Gag protein aggregation." *J. Biophotonics* **6,** 398–408 (2013). doi:10.1002/jbio.201200185 doi: 10.1002/jbio.201200185

64. D. M. Grant, W. Zhang, E. J. McGhee, T. D. Bunney, C. B. Talbot, S. Kumar, I. Munro, C. Dunsby, M. A. A. Neil, M. Katan, P. M. W. French. "Multiplexed FRET to image multiple signaling events in live cells." *Biophys. J.* **95,** L69–71 (2008). doi:10.1529/biophysj.108.139204 doi: 10.1529/biophysj.108.139204

65. H. E. Grecco, P. Roda-Navarro, A. Girod, J. Hou, T. Frahm, D. C. Truxius, R. Pepperkok, A. Squire, P. I. H. Bastiaens. "In situ analysis of tyrosine phosphorylation networks by FLIM on cell arrays." *Nat. Methods* **7,** 467–72 (2010). doi:10.1038/nmeth.1458 doi: 10.1038/nmeth.1458

66. H. Imamura, K. P. Huynh Nhat, H. Togawa, K. Saito, R. Iino, Y. Kato-Yamada, T. Nagai, H. Noji. "Visualization of ATP levels inside single living cells with fluorescence resonance energy transfer-based genetically encoded indicators" *PNAS* **106,** 15651–15656 (2009).

67. R. Laine, D. W. Stuckey, H. Manning, S. C. Warren, G. Kennedy, D. Carling, C. Dunsby, A. Sardini, P. M. W. French. "Fluorescence lifetime readouts of Troponin-C-based calcium FRET sensors: a quantitative comparison of CFP and mTFP1 as donor fluorophores." *PLoS One* **7,** e49200 (2012). doi:10.1371/journal.pone.0049200 doi: 10.1371/journal.pone.0049200

68. N. Mochizuki, S. Yamashita, K. Kurokawa, Y. Ohba, T. Nagai, a Miyawaki, M. Matsuda. "Spatio-temporal images of growth-factor-induced activation of Ras and Rap1." *Nature* **411,** 1065–8 (2001). doi:10.1038/35082594 doi: 10.1038/35082594

69. N. Komatsu, K. Aoki, M. Yamada, H. Yukinaga, Y. Fujita, Y. Kamioka, M. Matsuda. "Development of an optimized backbone of FRET biosensors for kinases and GTPases." *Mol. Biol. Cell* **22,** 4647–56 (2011). doi:10.1091/mbc.E11-01-0072 doi: 10.1091/mbc.E11-01-0072

70. M. Rehm, H. Dussmann, R. U. Janicke, J. M. Tavare, D. Kogel, J. H. M. Prehn. "Single-cell fluorescence resonance energy transfer analysis demonstrates that caspase activation during

apoptosis is a rapid process. Role of caspase-3." *J. Biol. Chem.* **277,** 24506–14 (2002). doi:10.1074/jbc.M110789200 doi: 10.1074/jbc.M110789200

71. G. W. Gordon, G. Berry, X. H. Liang, B. Levine, B. Herman. "Quantitative fluorescence resonance energy transfer measurements using fluorescence microscopy." *Biophys. J.* **74,** 2702–13 (1998). doi:10.1016/S0006-3495(98)77976-7 doi: 10.1016/S0006-3495(98)77976-7

72. A. Hoppe, K. Christensen, J. A. Swanson. "Fluorescence resonance energy transfer-based stoichiometry in living cells." *Biophys. J.* **83,** 3652–64 (2002). doi:10.1016/S0006-3495(02)75365-4 doi: 10.1016/S0006-3495(02)75365-4

73. S. Pelet, M. J. R. Previte, P. T. C. So. "Comparing the quantification of Forster resonance energy transfer measurement accuracies based on intensity, spectral, and lifetime imaging." *J. Biomed. Opt.* **11,** 34017 (2006). doi:10.1117/1.2203664 doi: 10.1117/1.2203664

74. S. Ganesan, S. M. Ameer-Beg, T. T. C. Ng, B. Vojnovic, F. S. Wouters. "A dark yellow fluorescent protein (YFP)-based Resonance Energy-Accepting Chromoprotein (REACh) for Förster resonance energy transfer with GFP." *Proc. Natl. Acad. Sci. U. S. A.* **103,** 4089–94 (2006). doi:10.1073/pnas.0509922103 doi: 10.1073/pnas.0509922103

75. S. V Koushik, S. S. Vogel. "Energy migration alters the fluorescence lifetime of Cerulean: implications for fluorescence lifetime imaging Forster resonance energy transfer measurements." *J. Biomed. Opt.* **13,** 031204 (2008). doi:10.1117/1.2940367 doi: 10.1117/1.2940367

76. D. R. Matthews, G. O. Fruhwirth, G. Weitsman, L. M. Carlin, E. Ofo, M. Keppler, P. R. Barber, I. D. C. Tullis, B. Vojnovic, T. Ng, S. M. Ameer-Beg. "A multi-functional imaging approach to high-content protein interaction screening." *PLoS One* **7,** e33231 (2012). doi:10.1371/journal.pone.0033231 doi: 10.1371/journal.pone.0033231

77. S. S. Vogel, C. Thaler, P. S. Blank, S. V Koushik. in *FLIM Microsc. Biol. Med.* (Periasamy, A. & Clegg, R. M.) **1076,** 245–305 , CRC Press, Boca Raton, (2009). doi:10.1007/978-1-62703-649-8_22 doi: 10.1007/978-1-62703-649-8_22

78. S. C. Warren, A. Margineanu, D. Alibhai, D. J. Kelly, C. Talbot, Y. Alexandrov, I. Munro, M. Katan, C. Dunsby, P. M. W. French. "Rapid global fitting of large fluorescence lifetime imaging microscopy datasets" *PLoS One* **8,** e70687 (2013). doi:10.1371/journal.pone.0070687 doi: 10.1371/journal.pone.0070687

79. S. Padilla-Parra, N. Audugé, H. Lalucque, J.-C. Mevel, M. Coppey-Moisan, M. Tramier. "Quantitative comparison of different fluorescent protein couples for fast FRET-FLIM acquisition." *Biophys. J.* **97,** 2368–76 (2009). doi:10.1016/j.bpj.2009.07.044 doi: 10.1016/j.bpj.2009.07.044

80. E. Hebisch, J. Knebel, J. Landsberg, E. Frey, M. Leisner. "High variation of fluorescence protein maturation times in closely related Escherichia coli strains." *PLoS One* **8,** e75991 (2013). doi:10.1371/journal.pone.0075991 doi: 10.1371/journal.pone.0075991

81. S. S. Vogel, B. W. van der Meer, P. S. Blank. "Estimating the distance separating fluorescent protein FRET pairs." *Methods* **66,** 131–8 (2014). doi:10.1016/j.ymeth.2013.06.021 doi: 10.1016/j.ymeth.2013.06.021

82. S. S. Vogel, T. A. Nguyen, B. W. van der Meer, P. S. Blank. "The impact of heterogeneity and dark acceptor states on FRET: implications for using fluorescent protein donors and acceptors." *PLoS One* **7,** e49593 (2012). doi:10.1371/journal.pone.0049593 doi: 10.1371/journal.pone.0049593

83. R. E. Dale. "Fluorescence depolarization and orientation factors for excitation-energy transfer between isolated donor and acceptor fluorophore pairs at fixed inter-molecular separations" *Acta Phys. Pol. A* **54,** 743–756 (1978).

84. R. Roy, S. Hohng, T. Ha. "A practical guide to single-molecule FRET." *Nat. Methods* **5,** 507–16 (2008). doi:10.1038/nmeth.1208 doi: 10.1038/nmeth.1208

85. S. Inoué. in *Handb. Biol. confocal Microsc.* (Pawley, J.) 1–20 , Springer, New York, (2006).

86. M. Minsky. "Microscopy Apparatus" (1961).

87. M. D. Egger, M. Petran. "New Reflected-Light Microscope for Viewing Unstained Brain and Ganglion Cells" *Science (80-.).* **157,** 305–307 (1967). doi:10.1126/science.157.3786.305 doi: 10.1126/science.157.3786.305

88. D. Toomre, J. B. Pawley. in *Handb. Biol. confocal Microsc.* (Pawley, J. B.) 221–238 , Springer, New York, (2006).

89. Thermo Scientific. "Thermo Scientific ArrayScan Confocal Module," 1–2 , (2014).

90. M. Beurg, R. Fettiplace, J.-H. Nam, A. J. Ricci. "Localization of inner hair cell mechanotransducer channels using high-speed calcium imaging." *Nat. Neurosci.* **12,** 553–8 (2009). doi:10.1038/nn.2295 doi: 10.1038/nn.2295

91. B. Vogt, L. Yan, M. Szulczewski, K. W. Eliceiri. "Swept field confocal overcomes point-scanning microscopy limitations" *Laser Focus World* 55–59 (2010). at <http://www.laserfocusworld.com/index.html>

92. W. Denk, J. Strickler, W. Webb. "Two-photon laser scanning fluorescence microscopy" *Science (80-.).* **248,** 73–76 (1990). doi:10.1126/science.2321027 doi: 10.1126/science.2321027

93. W. Denk, D. W. Piston, W. W. Webb. in *Handb. Biol. confocal Microsc.* (Pawley, J. B.) 535–549 , Springer, New York, (2006).

94. P. T. C. So. "Two-photon Fluorescence Light Microscopy" *Encycl. life Sci.* 1–5 (2002). at <www.els.net>

95. P. A. A. De Beule, S. Kumar, M. A. A. Neil, C. Dunsby, A. Naylor, D. M. Owen, U. Anand, P. M. P. Lanigan, R. K. P. Benninger, D. M. Davis, P. Anand, C. Benham, P. M. W. French. "Multifocal multiphoton excitation and time correlated single photon counting detection for 3-D fluorescence lifetime imaging." *Opt. Express* **15,** 12548–61 (2007).

96. A. Esposito, T. Oggier, H. C. Gerritsen, F. Lustenberger, F. S. Wouters. "All-solid-state lock-in imaging for wide-field" **13,** 9812–9821 (2005).

97. Y. Sun, R. N. Day, A. Periasamy. "Investigating protein-protein interactions in living cells using fluorescence lifetime imaging microscopy." *Nat. Protoc.* **6,** 1324–40 (2011). doi:10.1038/nprot.2011.364 doi: 10.1038/nprot.2011.364

98. G. I. Redford, R. M. Clegg. "Polar plot representation for frequency-domain analysis of fluorescence lifetimes." *J. Fluoresc.* **15,** 805–15 (2005). doi:10.1007/s10895-005-2990-8 doi: 10.1007/s10895-005-2990-8

99. G.-J. Kremers, E. B. van Munster, J. Goedhart, T. W. J. Gadella. "Quantitative lifetime unmixing of multiexponentially decaying fluorophores using single-frequency fluorescence lifetime imaging microscopy." *Biophys. J.* **95,** 378–89 (2008). doi:10.1529/biophysj.107.125229 doi: 10.1529/biophysj.107.125229

100. R. A. Colyer, C. Lee, E. Gratton. "A novel fluorescence lifetime imaging system that optimizes photon efficiency." *Microsc. Res. Tech.* **71,** 201–13 (2008). doi:10.1002/jemt.20540 doi: 10.1002/jemt.20540

101. S. Kwok, C. Lee, S. a Sánchez, T. L. Hazlett, E. Gratton, Y. Hayashi. "Genetically encoded probe for fluorescence lifetime imaging of CaMKII activity." *Biochem. Biophys. Res. Commun.* **369,** 519–25 (2008). doi:10.1016/j.bbrc.2008.02.070 doi: 10.1016/j.bbrc.2008.02.070

102. W. Becker. "The bh TCSPC Handbook" , Berlin, (2012). at <http://www.becker-hickl.de/pdf/SPC-handbook-5ed-36a.pdf>

103. M. Wahl, T. Röhlicke, H.-J. Rahn, R. Erdmann, G. Kell, A. Ahlrichs, M. Kernbach, A. W. Schell, O. Benson. "Integrated multichannel photon timing instrument with very short dead time and high throughput." *Rev. Sci. Instrum.* **84,** 043102 (2013). doi:10.1063/1.4795828 doi: 10.1063/1.4795828

104. J. McGinty, J. Requejo-Isidro, I. Munro, C. B. Talbot, P. a Kellett, J. D. Hares, C. Dunsby, M. a a Neil, P. M. W. French. "Signal-to-noise characterization of time-gated intensifiers used for wide-field time-domain FLIM" *J. Phys. D. Appl. Phys.* **42,** 135103 (2009). doi:10.1088/0022-3727/42/13/135103 doi: 10.1088/0022-3727/42/13/135103

105. C. J. de Grauw, H. C. Gerritsen. "Multiple Time-Gate Module for Fluorescence Lifetime Imaging" *Appl. Spectrosc.* **55,** (2001).

106. E. G. Hofman, M. O. Ruonala, A. N. Bader, D. van den Heuvel, J. Voortman, R. C. Roovers, A. J. Verkleij, H. C. Gerritsen, P. M. P. van Bergen En Henegouwen. "EGF induces coalescence of different lipid rafts." *J. Cell Sci.* **121,** 2519–28 (2008). doi:10.1242/jcs.028753 doi: 10.1242/jcs.028753

107. M. Zuker, A. G. Szabo, L. Bramall, D. T. Krajcarski, B. Selinger. "Delta function convolution method (DFCM) for fluorescence decay experiments" *Rev. Sci. Instrum.* **56,** 14 (1985). doi:10.1063/1.1138457 doi: 10.1063/1.1138457

108. Y. Prokazov, E. Turbin, M. Vitali, A. Herzog, B. Michaelis, W. Zuschratter, K. Kemnitz. "Reborn quadrant anode image sensor" *Nucl. Instruments Methods Phys. Res. Sect. A Accel. Spectrometers, Detect. Assoc. Equip.* **604,** 221–223 (2009). doi:10.1016/j.nima.2009.01.074 doi: 10.1016/j.nima.2009.01.074

109. M. Vitali, F. Picazo, Y. Prokazov, A. Duci, E. Turbin, C. Götze, J. Llopis, R. Hartig, A. J. W. G. Visser, W. Zuschratter. "Wide-Field Multi-Parameter FLIM: long-term minimal invasive observation of proteins in living cells." *PLoS One* **6,** e15820 (2011). doi:10.1371/journal.pone.0015820 doi: 10.1371/journal.pone.0015820

110. J. L. Wiza, J. Ladislas Wiza. "Microchannel plate detectors" *Nucl. Instruments Methods* **162,** 587–601 (1979). doi:10.1016/0029-554X(79)90734-1 doi: 10.1016/0029-554X(79)90734-1

111. H. Sparks, S. Warren, J. Guedes, N. Yoshida, T. C. Charn, N. Guerra, T. Tatla, C. Dunsby, P. French. "A flexible wide-field FLIM endoscope utilising blue excitation light for label-free

contrast of tissue." *J. Biophotonics* **11,** 1–11 (2014). doi:10.1002/jbio.201300203 doi: 10.1002/jbio.201300203

112. J. Philip, K. Carlsson. "Theoretical investigation of the signal-to-noise ratio in fluorescence lifetime imaging." *J. Opt. Soc. Am. A. Opt. Image Sci. Vis.* **20,** 368–79 (2003). doi:10.1364/JOSAA.20.000368 doi: 10.1364/JOSAA.20.000368

113. A. D. Elder, C. F. Kaminski, J. H. Frank. "φ2 FLIM: a technique for alias-free frequency domain fluorescence lifetime imaging" *Opt. Express* **17,** 3722–3731 (2009). doi:10.1364/OE.17.023181. doi: 10.1364/OE.17.023181.

114. Eli Lilly, National Institutes of Health Chemical Genomics Center. "Guidance for Assay Development & HTS" , (2007).

115. J.-H. Zhang. "A Simple Statistical Parameter for Use in Evaluation and Validation of High Throughput Screening Assays" *J. Biomol. Screen.* **4,** 67–73 (1999). doi:10.1177/108705719900400206 doi: 10.1177/108705719900400206

116. X. D. Zhang. "A pair of new statistical parameters for quality control in RNA interference high-throughput screening assays." *Genomics* **89,** 552–61 (2007). doi:10.1016/j.ygeno.2006.12.014 doi: 10.1016/j.ygeno.2006.12.014

117. Z. Surviladze, A. Waller, Y. Wu, E. Romero, B. S. Edwards, A. Wandinger-Ness, L. A. Sklar. "Identification of a small GTPase inhibitor using a high-throughput flow cytometry bead-based multiplex assay." *J. Biomol. Screen.* **15,** 10–20 (2010). doi:10.1177/1087057109352240 doi: 10.1177/1087057109352240

118. C. B. Black, T. D. Duensing, L. S. Trinkle, R. T. Dunlay. "Cell-based screening using high-throughput flow cytometry." *Assay Drug Dev. Technol.* **9,** 13–20 (2011). doi:10.1089/adt.2010.0308 doi: 10.1089/adt.2010.0308

119. B. Larson, P. Banks, N. Pierre, G. Cameron. "Automation of HTRF elF4E Kinase Assay Using a 3D Tumoroid-Based Cell Model," , Vermont, (2013).

120. I. Remy, S. W. Michnick. "Regulation of Apoptosis by the Ft1 Protein, a New Modulator of Protein Kinase B/Akt" *Mol. Cell. Biol.* **24,** 1493–1504 (2004). doi:10.1128/MCB.24.4.1493-1504.2004 doi: 10.1128/MCB.24.4.1493-1504.2004

121. D. D. Dudgeon, S. Shinde, Y. Hua, T. Y. Shun, J. S. Lazo, C. J. Strock, K. A. Giuliano, D. L. Taylor, P. A. Johnston, P. A. Johnston. "Implementation of a 220,000-compound HCS campaign to identify disruptors of the interaction between p53 and hDM2 and characterization of the confirmed hits." *J. Biomol. Screen.* **15,** 766–82 (2010). doi:10.1177/1087057110375304 doi: 10.1177/1087057110375304

122. M. Nadler-Holly, M. Breker, R. Gruber, A. Azia, M. Gymrek, M. Eisenstein, K. R. Willison, M. Schuldiner, A. Horovitz. "Interactions of subunit CCT3 in the yeast chaperonin CCT/TRiC with Q/N-rich proteins revealed by high-throughput microscopy analysis." *Proc. Natl. Acad. Sci. U. S. A.* **109,** 18833–8 (2012). doi:10.1073/pnas.1209277109 doi: 10.1073/pnas.1209277109

123. W. Link, J. Oyarzabal, B. G. Serelde, M. I. Albarran, O. Rabal, A. Cebriá, P. Alfonso, J. Fominaya, O. Renner, S. Peregrina, D. Soilán, P. a Ceballos, A.-I. Hernández, M. Lorenzo, P. Pevarello, T. G. Granda, G. Kurz, *et al.* "Chemical interrogation of FOXO3a nuclear translocation identifies potent and selective inhibitors of phosphoinositide 3-kinases." *J. Biol. Chem.* **284,** 28392–400 (2009). doi:10.1074/jbc.M109.038984 doi: 10.1074/jbc.M109.038984

124. F. Zanella, A. Rosado, B. García, A. Carnero, W. Link. "Chemical genetic analysis of FOXO nuclear-cytoplasmic shuttling by using image-based cell screening." *Chembiochem* **9,** 2229–37 (2008). doi:10.1002/cbic.200800255 doi: 10.1002/cbic.200800255

125. A. Rosado, F. Zanella, B. Garcia, A. Carnero, W. Link. "A dual-color fluorescence-based platform to identify selective inhibitors of Akt signaling." *PLoS One* **3,** e1823 (2008). doi:10.1371/journal.pone.0001823 doi: 10.1371/journal.pone.0001823

126. A. Fiebitz, L. Nyarsik, B. Haendler, Y.-H. Hu, F. Wagner, S. Thamm, H. Lehrach, M. Janitz, D. Vanhecke. "High-throughput mammalian two-hybrid screening for protein-protein interactions using transfected cell arrays." *BMC Genomics* **9,** 68 (2008). doi:10.1186/1471-2164-9-68 doi: 10.1186/1471-2164-9-68

127. H. Takanaga, B. Chaudhuri, W. B. Frommer. "GLUT1 and GLUT9 as major contributors to glucose influx in HepG2 cells identified by a high sensitivity intramolecular FRET glucose sensor." *Biochim. Biophys. Acta* **1778,** 1091–9 (2008). doi:10.1016/j.bbamem.2007.11.015 doi: 10.1016/j.bbamem.2007.11.015

128. H. Tian, L. Ip, H. Luo, D. C. Chang, K. Q. Luo. "A high throughput drug screen based on fluorescence resonance energy transfer (FRET) for anticancer activity of compounds from herbal medicine." *Br. J. Pharmacol.* **150,** 321–34 (2007). doi:10.1038/sj.bjp.0706988 doi: 10.1038/sj.bjp.0706988

129. A. Esposito, C. P. Dohm, M. Bähr, F. S. Wouters. "Unsupervised fluorescence lifetime imaging microscopy for high content and high throughput screening." *Mol. Cell. Proteomics* **6,** 1446–54 (2007). doi:10.1074/mcp.T700006-MCP200 doi: 10.1074/mcp.T700006-MCP200

130. A. Esposito, H. C. Gerritsen, F. S. Wouters. "Fluorescence lifetime heterogeneity resolution in the frequency domain by lifetime moments analysis." *Biophys. J.* **89,** 4286–99 (2005). doi:10.1529/biophysj.104.053397 doi: 10.1529/biophysj.104.053397

131. P. R. Barber, I. D. C. Tullis, G. P. Pierce, R. G. Newman, J. Prentice, M. I. Rowley, D. R. Matthews, S. M. Ameer-Beg, B. Vojnovic. "The Gray Institute 'open' high-content, fluorescence lifetime microscopes." *J. Microsc.* **251,** 154–67 (2013). doi:10.1111/jmi.12057 doi: 10.1111/jmi.12057

132. D. M. Grant, D. S. Elson, D. Schimpf, C. Dunsby, E. Auksorius, I. Munro, M. A. A. Neil, P. M. W. French, E. Nye, G. Stamp, P. Courtney. "Optically sectioned fluorescence lifetime imaging using a Nipkow disk microscope and a tunable ultrafast continuum excitation source" *Opt. Lett.* **30,** 3353–3355 (2005).

133. C. B. Talbot, J. McGinty, D. M. Grant, E. J. McGhee, D. M. Owen, W. Zhang, T. D. Bunney, I. Munro, B. Isherwood, R. Eagle, A. Hargreaves, M. Katan, C. Dunsby, M. A. A. Neil, P. M. W. French. "High speed unsupervised fluorescence lifetime imaging confocal multiwell plate reader for high content analysis" *J. Biophoton.* **1,** 514–521 (2008). doi:10.1002/jbio.200810054 doi: 10.1002/jbio.200810054

134. S. Kumar, D. Alibhai, A. Margineanu, R. Laine, G. Kennedy, J. McGinty, S. Warren, D. J. Kelly, Y. Alexandrov, I. Munro, C. Talbot, D. W. Stuckey, C. Kimberly, B. Viellerobe, F. Lacombe, E. W.-F. Lam, H. Taylor, *et al.* "FLIM FRET Technology for Drug Discovery: Automated Multiwell-Plate High-Content Analysis, Multiplexed Readouts and Application in Situ." *Chemphyschem* **12,** 609–26 (2011). doi:10.1002/cphc.201000874 doi: 10.1002/cphc.201000874

135. Newport. “Fiber Optics : How to Choose an Optic for Free Space Fiber Coupling” 1–3 (2004). at <http://assets.newport.com/webDocuments-EN/images/Tech_Note_14_Fiber_Coupling.pdf>

136. C. Yeo. “Optical Fiber Dispersion” *fiberoptics4sale.com* (2010). at <http://www.fiberoptics4sale.com/wordpress/optical-fiber-dispersion/>

137. C.-W. Chang, M.-A. Mycek. “Enhancing precision in time-domain fluorescence lifetime imaging.” *J. Biomed. Opt.* **15,** 056013 (2011). doi:10.1117/1.3494566 doi: 10.1117/1.3494566

138. University of Dundee, Open Microscopy Environment. “The Open Microscopy Environment” (2014).

139. C. Allan, J.-M. Burel, J. Moore, C. Blackburn, M. Linkert, S. Loynton, D. Macdonald, W. J. Moore, C. Neves, A. Patterson, M. Porter, A. Tarkowska, B. Loranger, J. Avondo, I. Lagerstedt, L. Lianas, S. Leo, *et al.* “OMERO: flexible, model-driven data management for experimental biology.” *Nat. Methods* **9,** 245–53 (2012). doi:10.1038/nmeth.1896 doi: 10.1038/nmeth.1896

140. F. Ambriz-Colin, M. Torres-Cisneros, J. G. Avina-Cervantes, J. E. Saavedra-Martinez, O. Debeir, J. J. Sanchez-Mondragon. “Detection of biological cells in phase-contrast video microscopy” in *2006 Multiconference Electron. Photonics* 239–243 , IEEE, (2006). doi:10.1109/MEP.2006.335672doi:10.1109/MEP.2006.335672 doi: 10.1109/MEP.2006.335672

141. A. E. Carpenter, T. R. Jones, M. R. Lamprecht, C. Clarke, I. H. Kang, O. Friman, D. A. Guertin, J. H. Chang, R. A. Lindquist, J. Moffat, P. Golland, D. M. Sabatini. “CellProfiler: image analysis software for identifying and quantifying cell phenotypes.” *Genome Biol.* **7,** R100 (2006). doi:10.1186/gb-2006-7-10-r100 doi: 10.1186/gb-2006-7-10-r100

142. PHOTONIS. “Intensifier Tube SN 0404906 Test Sheet,” 1–2 , (2004).

143. PHOTONIS. “Intensifier Tube SN 0920264 Test Sheet,” 1–2 , (2009).

144. Kentech Instruments Ltd. “Operations Manual for High Rate Imager Serial No. J0404261,” 1–34 , (2004).

145. ProxiVision GmbH. “Proxitronic - Phosphor Screens,” 1–5 , (2000).

146. M. Köllner, J. Wolfrum. “How many photons are necessary for fluorescence-lifetime measurements?” *Chem. Phys. Lett.* **200,** 199–204 (1992). doi:10.1016/0009-2614(92)87068-Z doi: 10.1016/0009-2614(92)87068-Z

147. J. McGinty. “Development of wide-field fluorescence lifetime imaging for biomedical applications” (2006).

148. A. D. Payne, A. A. Dorrington, M. J. Cree, D. A. Carnegie. “Image Intensifier Characterisation” in *Image Vis. Comput. New Zeal.* , (2006).

149. J. M. Levitt, A. Baldwin, A. Papadakis, S. Puri, J. Xylas, K. Münger, I. Georgakoudi. “Intrinsic fluorescence and redox changes associated with apoptosis of primary human epithelial cells.” *J. Biomed. Opt.* **11,** 064012 (2006). doi:10.1117/1.2401149 doi: 10.1117/1.2401149

150. Kentech Instruments Ltd. “‘Interesting ideas’” (2011). at <http://www.kentech.co.uk/index.html?/&2>

151. A. F. Santos, A. B. Zaltsman, R. C. Martin, A. Kuzmin, Y. Alexandrov, E. P. Roquemore, R. A. Jessop, M. G. M. van Erck, J. H. Verheijen. "Angiogenesis: an improved in vitro biological system and automated image-based workflow to aid identification and characterization of angiogenesis and angiogenic modulators." *Assay Drug Dev. Technol.* **6,** 693–710 (2008). doi:10.1089/adt.2008.146 doi: 10.1089/adt.2008.146

152. S. V Koushik, H. Chen, C. Thaler, H. L. Puhl, S. S. Vogel. "Cerulean, Venus, and VenusY67C FRET reference standards." *Biophys. J.* **91,** L99–L101 (2006). doi:10.1529/biophysj.106.096206 doi: 10.1529/biophysj.106.096206

153. P. Sarkar, S. V Koushik, S. S. Vogel, I. Gryczynski, Z. Gryczynski. "Photophysical properties of Cerulean and Venus fluorescent proteins." *J. Biomed. Opt.* **14,** 034047 (2009). doi:10.1117/1.3156842 doi: 10.1117/1.3156842

154. M. L. Markwardt, G.-J. Kremers, C. A. Kraft, K. Ray, P. J. C. Cranfill, K. A. Wilson, R. N. Day, R. M. Wachter, M. W. Davidson, M. A. Rizzo. "An improved cerulean fluorescent protein with enhanced brightness and reduced reversible photoswitching." *PLoS One* **6,** e17896 (2011). doi:10.1371/journal.pone.0017896 doi: 10.1371/journal.pone.0017896

155. A. Villoing, M. Ridhoir, B. Cinquin, M. Erard, L. Alvarez, G. Vallverdu, P. Pernot, R. Grailhe, F. Mérola, H. Pasquier. "Complex fluorescence of the cyan fluorescent protein: comparisons with the H148D variant and consequences for quantitative cell imaging." *Biochemistry* **47,** 12483–92 (2008). doi:10.1021/bi801400d doi: 10.1021/bi801400d

156. Olympus. "IX81-ZDC: Focus Drift Compensating Microscope Instructions," , (2010).

157. A. Edelstein, N. Amodaj, K. Hoover, R. Vale, N. Stuurman. "Computer control of microscopes using μManager." *Curr. Protoc. Mol. Biol.* **Chapter 14,** Unit14.20 (2010). doi:10.1002/0471142727.mb1420s92 doi: 10.1002/0471142727.mb1420s92

158. R. Geiss-Friedlander, F. Melchior. "Concepts in sumoylation: a decade on." *Nat. Rev. Mol. Cell Biol.* **8,** 947–56 (2007). doi:10.1038/nrm2293 doi: 10.1038/nrm2293

159. Y. Wang, M. Dasso. "SUMOylation and deSUMOylation at a glance." *J. Cell Sci.* **122,** 4249–52 (2009). doi:10.1242/jcs.050542 doi: 10.1242/jcs.050542

160. ONS. "Statistical Bulletin: Cancer Registration Statistics, England, 2011," 1–20 , (2013). at <http://www.ons.gov.uk/ons/dcp171778_315795.pdf>

161. ONS. "Statistical Bulletin: Cancer Incidence and Mortality in the United Kingdom , 2010," **10,** 1–24 , (2012).

162. S. H. Giordano, Y.-L. Lin, Y. F. Kuo, G. N. Hortobagyi, J. S. Goodwin. "Decline in the use of anthracyclines for breast cancer." *J. Clin. Oncol.* **30,** 2232–9 (2012). doi:10.1200/JCO.2011.40.1273 doi: 10.1200/JCO.2011.40.1273

163. K. K. Jain, E. S. Casper, N. L. Geller, T. B. Hakes, R. J. Kaufman, V. Currie, W. Schwartz, C. Cassidy, G. R. Petroni, C. W. Young. "A prospective randomized comparison of epirubicin and doxorubicin in patients with advanced breast cancer." *J. Clin. Oncol.* **3,** 818–26 (1985).

164. V. G. Kaklamani, W. J. Gradishar. "Epirubicin Versus Doxorubicin: Which Is the Anthracycline of Choice for the Treatment of Breast Cancer?" *Clin. Breast Cancer* **4,** S26–S33 (2003). doi:10.3816/CBC.2003.s.012 doi: 10.3816/CBC.2003.s.012

165. D. Gewirtz. "A critical evaluation of the mechanisms of action proposed for the antitumor effects of the anthracycline antibiotics adriamycin and daunorubicin" *Biochem. Pharmacol.* **57,** 727–741 (1999). doi:10.1016/S0006-2952(98)00307-4 doi: 10.1016/S0006-2952(98)00307-4

166. C. A. Frederick, L. D. Williams, G. Ughetto, G. A. van der Marel, J. H. van Boom, A. Rich, A. H. Wang. "Structural comparison of anticancer drug-DNA complexes: adriamycin and daunomycin." *Biochemistry* **29,** 2538–49 (1990).

167. S. Charak, D. K. Jangir, G. Tyagi, R. Mehrotra. "Interaction studies of Epirubicin with DNA using spectroscopic techniques" *J. Mol. Struct.* **1000,** 150–154 (2011). doi:10.1016/j.molstruc.2011.06.013 doi: 10.1016/j.molstruc.2011.06.013

168. L. J. Monteiro, P. Khongkow, M. Kongsema, J. R. Morris, C. Man, D. Weekes, C.-Y. Koo, A. R. Gomes, P. H. Pinto, V. Varghese, L. M. Kenny, R. Charles Coombes, R. Freire, R. H. Medema, E. W.-F. Lam. "The Forkhead Box M1 protein regulates BRIP1 expression and DNA damage repair in epirubicin treatment." *Oncogene* (2012). doi:10.1038/onc.2012.491doi:10.1038/onc.2012.491 doi: 10.1038/onc.2012.491

169. O. Bar-On, M. Shapira, D. D. Hershko. "Differential effects of doxorubicin treatment on cell cycle arrest and Skp2 expression in breast cancer cells." *Anticancer. Drugs* **18,** 1113–21 (2007). doi:10.1097/CAD.0b013e3282ef4571 doi: 10.1097/CAD.0b013e3282ef4571

170. G. Minotti, P. Menna, E. Salvatorelli, G. Cairo, L. Gianni. "Anthracyclines: molecular advances and pharmacologic developments in antitumor activity and cardiotoxicity." *Pharmacol. Rev.* **56,** 185–229 (2004). doi:10.1124/pr.56.2.6 doi: 10.1124/pr.56.2.6

171. D. S. Riddick, C. Lee, S. Ramji, E. C. Chinje, R. L. Cowen, K. J. Williams, A. V Patterson, I. J. Stratford, C. S. Morrow, A. J. Townsend, Y. Jounaidi, C. Chen, T. Su, H. Lu, P. S. Schwartz, D. J. Waxman. "Cancer chemotherapy and drug metabolism." *Drug Metab. Dispos.* **33,** 1083–96 (2005). doi:10.1124/dmd.105.004374 doi: 10.1124/dmd.105.004374

172. K. J. A. Davies, J. H. Doroshow. "Redox Cycling of Anthracyclines by Cardiac Mitochondria" *J. Biol. Chem.* **261,** 3060–3067 (1986).

173. J. Laoukili, M. R. H. Kooistra, A. Brás, J. Kauw, R. M. Kerkhoven, A. Morrison, H. Clevers, R. H. Medema. "FoxM1 is required for execution of the mitotic programme and chromosome stability." *Nat. Cell Biol.* **7,** 126–36 (2005). doi:10.1038/ncb1217 doi: 10.1038/ncb1217

174. P. Raychaudhuri, H. J. Park. "FoxM1: a master regulator of tumor metastasis." *Cancer Res.* **71,** 4329–33 (2011). doi:10.1158/0008-5472.CAN-11-0640 doi: 10.1158/0008-5472.CAN-11-0640

175. C.-Y. Koo, K. W. Muir, E. W.-F. Lam. "FOXM1: From cancer initiation to progression and treatment." *Biochim. Biophys. Acta* **1819,** 28–37 (2012). doi:10.1016/j.bbagrm.2011.09.004 doi: 10.1016/j.bbagrm.2011.09.004

176. U. B. McGovern, R. E. Francis, B. Peck, S. K. Guest, J. Wang, S. S. Myatt, J. Krol, J. M.-M. Kwok, A. Polychronis, R. C. Coombes, E. W.-F. Lam. "Gefitinib (Iressa) represses FOXM1 expression via FOXO3a in breast cancer." *Mol. Cancer Ther.* **8,** 582–91 (2009). doi:10.1158/1535-7163.MCT-08-0805 doi: 10.1158/1535-7163.MCT-08-0805

177. F. Zhao, E. W.-F. Lam. "Role of the forkhead transcription factor FOXO-FOXM1 axis in cancer and drug resistance." *Front. Med.* **6,** 376–80 (2012). doi:10.1007/s11684-012-0228-0 doi: 10.1007/s11684-012-0228-0

178. J. Millour, D. Constantinidou, A. V Stavropoulou, M. S. C. Wilson, S. S. Myatt, J. M.-M. Kwok, K. Sivanandan, R. C. Coombes, R. H. Medema, J. Hartman, a E. Lykkesfeldt, E. W.-F. Lam. "FOXM1 is a transcriptional target of ERalpha and has a critical role in breast cancer endocrine sensitivity and resistance." *Oncogene* **29,** 2983–95 (2010). doi:10.1038/onc.2010.47 doi: 10.1038/onc.2010.47

179. J. Millour, N. de Olano, Y. Horimoto, L. J. Monteiro, J. K. Langer, R. Aligue, N. Hajji, E. W. F. Lam. "ATM and p53 regulate FOXM1 expression via E2F in breast cancer epirubicin treatment and resistance." *Mol. Cancer Ther.* **10,** 1046–58 (2011). doi:10.1158/1535-7163.MCT-11-0024 doi: 10.1158/1535-7163.MCT-11-0024

180. J. R. Carr, H. J. Park, Z. Wang, M. M. Kiefer, P. Raychaudhuri. "FoxM1 mediates resistance to herceptin and paclitaxel." *Cancer Res.* **70,** 5054–63 (2010). doi:10.1158/0008-5472.CAN-10-0545 doi: 10.1158/0008-5472.CAN-10-0545

181. P. A. Madureira, R. Varshochi, D. Constantinidou, R. E. Francis, R. C. Coombes, K.-M. Yao, E. W.-F. Lam. "The Forkhead box M1 protein regulates the transcription of the estrogen receptor alpha in breast cancer cells." *J. Biol. Chem.* **281,** 25167–76 (2006). doi:10.1074/jbc.M603906200 doi: 10.1074/jbc.M603906200

182. I. Wierstra. "The transcription factor FOXM1c binds to and transactivates the promoter of the tumor suppressor gene E-cadherin" *Cell Cycle* **10,** 760–766 (2011). doi:10.4161/cc.10.5.14827 doi: 10.4161/cc.10.5.14827

183. E. Gemenetzidis, D. Elena-Costea, E. K. Parkinson, A. Waseem, H. Wan, M.-T. Teh. "Induction of human epithelial stem/progenitor expansion by FOXM1." *Cancer Res.* **70,** 9515–26 (2010). doi:10.1158/0008-5472.CAN-10-2173 doi: 10.1158/0008-5472.CAN-10-2173

184. Z. Xie, G. Tan, M. Ding, D. Dong, T. Chen, X. Meng, X. Huang, Y. Tan. "Foxm1 transcription factor is required for maintenance of pluripotency of P19 embryonal carcinoma cells." *Nucleic Acids Res.* **38,** 8027–38 (2010). doi:10.1093/nar/gkq715 doi: 10.1093/nar/gkq715

185. D. A. Sanders, C. S. Ross-Innes, D. Beraldi, J. S. Carroll, S. Balasubramanian. "Genome-wide mapping of FOXM1 binding reveals co-binding with estrogen receptor alpha in breast cancer cells." *Genome Biol.* **14,** R6 (2013). doi:10.1186/gb-2013-14-1-r6 doi: 10.1186/gb-2013-14-1-r6

186. Y. Tan, P. Raychaudhuri, R. H. Costa. "Chk2 mediates stabilization of the FoxM1 transcription factor to stimulate expression of DNA repair genes." *Mol. Cell. Biol.* **27,** 1007–16 (2007). doi:10.1128/MCB.01068-06 doi: 10.1128/MCB.01068-06

187. S. S. Myatt, E. W.-F. Lam. "The emerging roles of forkhead box (Fox) proteins in cancer." *Nat. Rev. Cancer* **7,** 847–59 (2007). doi:10.1038/nrc2223 doi: 10.1038/nrc2223

188. S. S. Myatt, M. Kongsema, C. W.-Y. Man, D. J. Kelly, A. R. Gomes, P. Khongkow, U. Karunarathna, S. Zona, J. K. Langer, C. W. Dunsby, R. C. Coombes, P. M. French, J. J. Brosens, E. W.-F. Lam. "SUMOylation inhibits FOXM1 activity and delays mitotic transition." *Oncogene* 1–14 (2013). doi:10.1038/onc.2013.546doi:10.1038/onc.2013.546 doi: 10.1038/onc.2013.546

189. M. A. Glozak, N. Sengupta, X. Zhang, E. Seto. "Acetylation and deacetylation of non-histone proteins." *Gene* **363,** 15–23 (2005). doi:10.1016/j.gene.2005.09.010 doi: 10.1016/j.gene.2005.09.010

190. A. Kimura, K. Matsubara, M. Horikoshi. "A decade of histone acetylation: marking eukaryotic chromosomes with specific codes." *J. Biochem.* **138,** 647–62 (2005). doi:10.1093/jb/mvi184 doi: 10.1093/jb/mvi184

191. F. Baumgart, M. Corral-Escariz, J. Pérez-Gil, I. Rodríguez-Crespo. "Palmitoylation of R-Ras by human DHHC19, a palmitoyl transferase with a CaaX box." *Biochim. Biophys. Acta* **1798,** 592–604 (2010). doi:10.1016/j.bbamem.2010.01.002 doi: 10.1016/j.bbamem.2010.01.002

192. D. Komander, M. Rape. "The ubiquitin code." *Annu. Rev. Biochem.* **81,** 203–29 (2012). doi:10.1146/annurev-biochem-060310-170328 doi: 10.1146/annurev-biochem-060310-170328

193. S. P. Jackson, D. Durocher. "Regulation of DNA damage responses by ubiquitin and SUMO." *Mol. Cell* **49,** 795–807 (2013). doi:10.1016/j.molcel.2013.01.017 doi: 10.1016/j.molcel.2013.01.017

194. J. Schimmel, K. Eifler, J. O. Sigurðsson, S. a G. Cuijpers, I. a Hendriks, M. Verlaan-de Vries, C. D. Kelstrup, C. Francavilla, R. H. Medema, J. V Olsen, A. C. O. Vertegaal. "Uncovering SUMOylation Dynamics during Cell-Cycle Progression Reveals FoxM1 as a Key Mitotic SUMO Target Protein." *Mol. Cell* 1–14 (2014). doi:10.1016/j.molcel.2014.02.001doi:10.1016/j.molcel.2014.02.001 doi: 10.1016/j.molcel.2014.02.001

195. M. S. Rodriguez, C. Dargemont, R. T. Hay. "SUMO-1 conjugation in vivo requires both a consensus modification motif and nuclear targeting." *J. Biol. Chem.* **276,** 12654–9 (2001). doi:10.1074/jbc.M009476200 doi: 10.1074/jbc.M009476200

196. J. Song, L. K. Durrin, T. a Wilkinson, T. G. Krontiris, Y. Chen. "Identification of a SUMO-binding motif that recognizes SUMO-modified proteins." *Proc. Natl. Acad. Sci. U. S. A.* **101,** 14373–8 (2004). doi:10.1073/pnas.0403498101 doi: 10.1073/pnas.0403498101

197. E. Meulmeester, M. Kunze, H. H. Hsiao, H. Urlaub, F. Melchior. "Mechanism and consequences for paralog-specific sumoylation of ubiquitin-specific protease 25." *Mol. Cell* **30,** 610–9 (2008). doi:10.1016/j.molcel.2008.03.021 doi: 10.1016/j.molcel.2008.03.021

198. H. Dinkel, K. Van Roey, S. Michael, N. E. Davey, R. J. Weatheritt, D. Born, T. Speck, D. Krüger, G. Grebnev, M. Kuban, M. Strumillo, B. Uyar, A. Budd, B. Altenberg, M. Seiler, L. B. Chemes, J. Glavina, *et al.* "The eukaryotic linear motif resource ELM: 10 years and counting." *Nucleic Acids Res.* **42,** D259–66 (2014). doi:10.1093/nar/gkt1047 doi: 10.1093/nar/gkt1047

199. V. G. Wilson, P. R. Heaton. "Ubiquitin proteolytic system: focus on SUMO." *Expert Rev. Proteomics* **5,** 121–35 (2008). doi:10.1586/14789450.5.1.121 doi: 10.1586/14789450.5.1.121

200. A. Werner, A. Flotho, F. Melchior. "The RanBP2/RanGAP1*SUMO1/Ubc9 complex is a multisubunit SUMO E3 ligase." *Mol. Cell* **46,** 287–98 (2012). doi:10.1016/j.molcel.2012.02.017 doi: 10.1016/j.molcel.2012.02.017

201. R. Steinacher, P. Schär. "Functionality of human thymine DNA glycosylase requires SUMO-regulated changes in protein conformation." *Curr. Biol.* **15,** 616–23 (2005). doi:10.1016/j.cub.2005.02.054 doi: 10.1016/j.cub.2005.02.054

202. J. R. Morris, C. Boutell, M. Keppler, R. Densham, D. Weekes, A. Alamshah, L. Butler, Y. Galanty, L. Pangon, T. Kiuchi, T. Ng, E. Solomon. "The SUMO modification pathway is involved in the BRCA1 response to genotoxic stress." *Nature* **462,** 886–90 (2009). doi:10.1038/nature08593 doi: 10.1038/nature08593

203. J. R. Danielsen, L. K. Povlsen, B. H. Villumsen, W. Streicher, J. Nilsson, M. Wikström, S. Bekker-Jensen, N. Mailand. "DNA damage-inducible SUMOylation of HERC2 promotes RNF8 binding via a novel SUMO-binding Zinc finger." *J. Cell Biol.* **197,** 179–87 (2012). doi:10.1083/jcb.201106152 doi: 10.1083/jcb.201106152

204. L. Anders, N. Ke, P. Hydbring, Y. J. Choi, H. R. Widlund, J. M. Chick, H. Zhai, M. Vidal, S. P. Gygi, P. Braun, P. Sicinski. "A systematic screen for CDK4/6 substrates links FOXM1 phosphorylation to senescence suppression in cancer cells." *Cancer Cell* **20,** 620–34 (2011). doi:10.1016/j.ccr.2011.10.001 doi: 10.1016/j.ccr.2011.10.001

205. E. W.-F. Lam, J. J. Brosens, A. R. Gomes, C.-Y. Koo. "Forkhead box proteins: tuning forks for transcriptional harmony." *Nat. Rev. Cancer* **13,** 482–95 (2013). doi:10.1038/nrc3539 doi: 10.1038/nrc3539

206. X. Dai, Z. Yue, M. E. Eccleston, J. Swartling, N. K. H. Slater, C. F. Kaminski. "Fluorescence intensity and lifetime imaging of free and micellar-encapsulated doxorubicin in living cells." *Nanomedicine* **4,** 49–56 (2008). doi:10.1016/j.nano.2007.12.002 doi: 10.1016/j.nano.2007.12.002

207. D. Kelly. "Towards high throughput FLIM: a plate reading FLIM microscope and applications in drug discovery and basic research" (2011).

208. "Semrock" at <http://www.semrock.com/>

209. "Chroma" at <http://www.chroma.com/>

210. T. Nakabayashi, H.-P. Wang, M. Kinjo, N. Ohta. "Application of fluorescence lifetime imaging of enhanced green fluorescent protein to intracellular pH measurements." *Photochem. Photobiol. Sci.* **7,** 668–70 (2008). doi:10.1039/b800391b doi: 10.1039/b800391b

211. K. Suhling, D. M. Davis. "Probing the local environment of green fluorescent protein (GFP) with fluorescence lifetime imaging (FLIM) and time- resolved fluorescence anisotropy imaging (tr-FAIM)" in *Biomed. Top. Meet. (Optical Soc. Am.* 8–10 , Miami, (2002).

212. A. V. Gohar, R. Cao, P. Jenkins, W. Li, J. P. Houston, K. D. Houston. "Subcellular localization-dependent changes in EGFP fluorescence lifetime measured by time-resolved flow cytometry." *Biomed. Opt. Express* **4,** 1390–400 (2013). doi:10.1364/BOE.4.001390 doi: 10.1364/BOE.4.001390

213. M. Deng. "Proteolytic cleavage of FOXM1 by caspases" (2006).

214. A. M. Richter, G. P. Pfeifer, R. H. Dammann. "The RASSF proteins in cancer; from epigenetic silencing to functional characterization." *Biochim. Biophys. Acta* **1796,** 114–28 (2009). doi:10.1016/j.bbcan.2009.03.004 doi: 10.1016/j.bbcan.2009.03.004

215. V. Sherwood, A. Recino, A. Jeffries, A. Ward, A. D. Chalmers. "The N-terminal RASSF family: a new group of Ras-association-domain-containing proteins, with emerging links to cancer formation." *Biochem. J.* **425,** 303–11 (2010). doi:10.1042/BJ20091318 doi: 10.1042/BJ20091318

216. S. F. Scrace, E. O'Neill, E. O. Neill. "RASSF Signalling and DNA Damage : Monitoring the Integrity of the Genome?" *Mol. Biol. Int.* **2012,** 141732 (2012). doi:10.1155/2012/141732 doi: 10.1155/2012/141732

217. E. Hwang, K.-S. Ryu, K. Pääkkönen, P. Güntert, H.-K. Cheong, D.-S. Lim, J.-O. Lee, Y. H. Jeon, C. Cheong. "Structural insight into dimeric interaction of the SARAH domains from Mst1 and

RASSF family proteins in the apoptosis pathway." *Proc. Natl. Acad. Sci. U. S. A.* **104,** 9236–41 (2007). doi:10.1073/pnas.0610716104 doi: 10.1073/pnas.0610716104

218. F. Yuan, Q. Xie, J. Wu, Y. Bai, B. Mao, Y. Dong, W. Bi, G. Ji, W. Tao, Y. Wang, Z. Yuan. "MST1 promotes apoptosis through regulating Sirt1-dependent p53 deacetylation." *J. Biol. Chem.* **286,** 6940–5 (2011). doi:10.1074/jbc.M110.182543 doi: 10.1074/jbc.M110.182543

219. A. Koturenkiene. "Molecular basis for apoptotic Ras signalling through Nore1-MST1 multi-protein complex formation" (2008).

220. C. M. Deane. "Protein Interactions: Two Methods for Assessment of the Reliability of High Throughput Observations" *Mol. Cell. Proteomics* **1,** 349–356 (2002). doi:10.1074/mcp.M100037-MCP200 doi: 10.1074/mcp.M100037-MCP200

221. J. J. Chan, D. Flatters, F. Rodrigues-Lima, J. Yan, K. Thalassinos, M. Katan. "Comparative analysis of interactions of RASSF1-10." *Adv. Biol. Regul.* **53,** 190–201 (2013). doi:10.1016/j.jbior.2012.12.001 doi: 10.1016/j.jbior.2012.12.001

222. M. D. Vos, A. Martinez, C. Elam, A. Dallol, B. J. Taylor, F. Latif, G. J. Clark. "A role for the RASSF1A tumor suppressor in the regulation of tubulin polymerization and genomic stability." *Cancer Res.* **64,** 4244–50 (2004). doi:10.1158/0008-5472.CAN-04-0339 doi: 10.1158/0008-5472.CAN-04-0339

223. R. E. Itoh, K. Kurokawa, Y. Ohba, H. Yoshizaki, N. Mochizuki, M. Matsuda. "Activation of Rac and Cdc42 Video Imaged by Fluorescent Resonance Energy Transfer-Based Single-Mole" *Mol. Cell. Biol.* **22,** 6582–6591 (2002). doi:10.1128/MCB.22.18.6582–6591.2002 doi: 10.1128/MCB.22.18.6582–6591.2002

224. H. Yoshizaki, Y. Ohba, K. Kurokawa, R. E. Itoh, T. Nakamura, N. Mochizuki, K. Nagashima, M. Matsuda. "Activity of Rho-family GTPases during cell division as visualized with FRET-based probes." *J. Cell Biol.* **162,** 223–32 (2003). doi:10.1083/jcb.200212049 doi: 10.1083/jcb.200212049

225. E. Sahai, C. J. Marshall. "RHO-GTPases and cancer." *Nat. Rev. Cancer* **2,** 133–42 (2002). doi:10.1038/nrc725 doi: 10.1038/nrc725

226. A. Hall. "Rho family GTPases." *Biochem. Soc. Trans.* **40,** 1378–82 (2012). doi:10.1042/BST20120103 doi: 10.1042/BST20120103

227. D. R. Cook, K. L. Rossman, C. J. Der. "Rho guanine nucleotide exchange factors: regulators of Rho GTPase activity in development and disease." *Oncogene* 1–15 (2013). doi:10.1038/onc.2013.362doi:10.1038/onc.2013.362 doi: 10.1038/onc.2013.362

228. J. McCormack, N. J. Welsh, V. M. M. Braga. "Cycling around cell-cell adhesion with Rho GTPase regulators." *J. Cell Sci.* **126,** 379–91 (2013). doi:10.1242/jcs.097923 doi: 10.1242/jcs.097923

229. N. J. Welsh. "Guanine nucleotide exchange factor regulation of adherens junction biogenesis and maturation" (2013).

230. V. Vasioukhin. in *Adherens Junctions from Mol. Mech. to Tissue Dev. Dis.* (Harris, T.) **60,** 379–414 , Springer Netherlands, Dordrecht, (2012). doi:10.1007/978-94-007-4186-7 doi: 10.1007/978-94-007-4186-7

231. J. M. Brandner, M. Haftek, C. M. Niessen. "Adherens Junctions , Desmosomes and Tight Junctions in Epidermal Barrier Function" *Open Dermatol. J.* **4,** 14–20 (2010).

232. E. Sprecher, R. Bergman, G. Richard, R. Lurie, S. Shalev, D. Petronius, a Shalata, Y. Anbinder, R. Leibu, I. Perlman, N. Cohen, R. Szargel. "Hypotrichosis with juvenile macular dystrophy is caused by a mutation in CDH3, encoding P-cadherin." *Nat. Genet.* **29,** 134–6 (2001). doi:10.1038/ng716 doi: 10.1038/ng716

233. J. E. Lai-Cheong, K. Arita, J. A. McGrath. "Genetic diseases of junctions." *J. Invest. Dermatol.* **127,** 2713–25 (2007). doi:10.1038/sj.jid.5700727 doi: 10.1038/sj.jid.5700727

234. S. A. Kim, C.-Y. Tai, L.-P. Mok, E. A. Mosser, E. M. Schuman. "Calcium-dependent dynamics of cadherin interactions at cell-cell junctions." *Proc. Natl. Acad. Sci. U. S. A.* **108,** 9857–62 (2011). doi:10.1073/pnas.1019003108 doi: 10.1073/pnas.1019003108

235. R. Kalaji, A. P. Wheeler, J. C. Erasmus, S. Y. Lee, R. G. Endres, L. P. Cramer, V. M. M. Braga. "ROCK1 and ROCK2 regulate epithelial polarisation and geometric cell shape." *Biol. Cell* **104,** 435–51 (2012). doi:10.1111/boc.201100093 doi: 10.1111/boc.201100093

236. C. M. Niessen, D. Leckband, A. S. Yap. "Tissue organization by cadherin adhesion molecules: dynamic molecular and cellular mechanisms of morphogenetic regulation." *Physiol. Rev.* **91,** 691–731 (2011). doi:10.1152/physrev.00004.2010 doi: 10.1152/physrev.00004.2010

237. H. Clevers, R. Nusse. "Wnt/β-catenin signaling and disease." *Cell* **149,** 1192–205 (2012). doi:10.1016/j.cell.2012.05.012 doi: 10.1016/j.cell.2012.05.012

238. A. S. Yap, E. M. Kovacs. "Direct cadherin-activated cell signaling: a view from the plasma membrane." *J. Cell Biol.* **160,** 11–6 (2003). doi:10.1083/jcb.200208156 doi: 10.1083/jcb.200208156

239. S. J. Heasman, L. M. Carlin, S. Cox, T. Ng, A. J. Ridley. "Coordinated RhoA signaling at the leading edge and uropod is required for T cell transendothelial migration." *J. Cell Biol.* **190,** 553–63 (2010). doi:10.1083/jcb.201002067 doi: 10.1083/jcb.201002067

240. J. G. Rheinwald, H. Green. "Serial cultivation of strains of human epidermal keratinocytes: the formation of keratinizing colonies from single cells" *Cell* **6,** 331–344 (1975).

241. F. M. Watt, D. L. Mattey, D. R. Garrod. "Calcium-induced reorganization of desmosomal components in cultured human keratinocytes." *J. Cell Biol.* **99,** 2211–5 (1984).

242. K. J. Hodivala, F. M. Watt. "Evidence that cadherins play a role in the downregulation of integrin expression that occurs during keratinocyte terminal differentiation." *J. Cell Biol.* **124,** 589–600 (1994).

243. T. Aasen, J. C. Izpisúa Belmonte. "Isolation and cultivation of human keratinocytes from skin or plucked hair for the generation of induced pluripotent stem cells." *Nat. Protoc.* **5,** 371–82 (2010). doi:10.1038/nprot.2009.241 doi: 10.1038/nprot.2009.241

244. E. Calautti, M. Grossi, C. Mammucari, Y. Aoyama, M. Pirro, Y. Ono, J. Li, G. P. Dotto. "Fyn tyrosine kinase is a downstream mediator of Rho/PRK2 function in keratinocyte cell-cell adhesion." *J. Cell Biol.* **156,** 137–48 (2002). doi:10.1083/jcb.200105140 doi: 10.1083/jcb.200105140

245. L. Luo. "Rho GTPases in neuronal morphogenesis." *Nat. Rev. Neurosci.* **1,** 173–80 (2000). doi:10.1038/35044547 doi: 10.1038/35044547

246. N. A. Mack, H. J. Whalley, S. Castillo-Lluva, A. Malliri. "The diverse roles of Rac signaling in tumorigenesis" *Cell Cycle* **10,** 1571–1581 (2011). doi:10.4161/cc.10.10.15612 doi: 10.4161/cc.10.10.15612

247. S. S. McAllister. "Got a light? Illuminating lung cancer." *Sci. Transl. Med.* **4,** 142fs22 (2012). doi:10.1126/scitranslmed.3004446 doi: 10.1126/scitranslmed.3004446

248. V. M. M. Braga, A. S. Yap. "The challenges of abundance: epithelial junctions and small GTPase signalling." *Curr. Opin. Cell Biol.* **17,** 466–74 (2005). doi:10.1016/j.ceb.2005.08.012 doi: 10.1016/j.ceb.2005.08.012

249. G. Izumi, T. Sakisaka, T. Baba, S. Tanaka, K. Morimoto, Y. Takai. "Endocytosis of E-cadherin regulated by Rac and Cdc42 small G proteins through IQGAP1 and actin filaments." *J. Cell Biol.* **166,** 237–48 (2004). doi:10.1083/jcb.200401078 doi: 10.1083/jcb.200401078

250. B. Baum, M. Georgiou. "Dynamics of adherens junctions in epithelial establishment, maintenance, and remodeling." *J. Cell Biol.* **192,** 907–17 (2011). doi:10.1083/jcb.201009141 doi: 10.1083/jcb.201009141

251. X. R. Bustelo, V. Sauzeau, I. M. Berenjeno. "GTP-binding proteins of the Rho/Rac family: regulation, effectors and functions in vivo." *Bioessays* **29,** 356–70 (2007). doi:10.1002/bies.20558 doi: 10.1002/bies.20558

252. F. Liu, L. Jia, A.-M. Thompson-Baine, J. M. Puglise, M. B. A. Ter Beest, M. M. P. Zegers. "Cadherins and Pak1 control contact inhibition of proliferation by Pak1-betaPIX-GIT complex-dependent regulation of cell-matrix signaling." *Mol. Cell. Biol.* **30,** 1971–83 (2010). doi:10.1128/MCB.01247-09 doi: 10.1128/MCB.01247-09

253. O. DeLeon, J. M. Puglise, F. Liu, J. Smits, M. B. ter Beest, M. M. Zegers. "Pak1 regulates the orientation of apical polarization and lumen formation by distinct pathways." *PLoS One* **7,** e41039 (2012). doi:10.1371/journal.pone.0041039 doi: 10.1371/journal.pone.0041039

254. A. Togawa, J. Sfakianos, S. Ishibe, S. Suzuki, Y. Fujigaki, M. Kitagawa, I. Mellman, L. G. Cantley. "Hepatocyte Growth Factor stimulated cell scattering requires ERK and Cdc42-dependent tight junction disassembly." *Biochem. Biophys. Res. Commun.* **400,** 271–7 (2010). doi:10.1016/j.bbrc.2010.08.060 doi: 10.1016/j.bbrc.2010.08.060

255. J. J. McCormack. "The regulation of cell-cell adhesion by GTPase activating proteins" (2013).

256. K. Makrogianneli, L. M. Carlin, M. D. Keppler, D. R. Matthews, E. Ofo, A. Coolen, S. M. Ameer-Beg, P. R. Barber, B. Vojnovic, T. Ng. "Integrating receptor signal inputs that influence small Rho GTPase activation dynamics at the immunological synapse." *Mol. Cell. Biol.* **29,** 2997–3006 (2009). doi:10.1128/MCB.01008-08 doi: 10.1128/MCB.01008-08

257. A. Chatterjee, L. Wang, D. L. Armstrong, S. Rossie. "Activated Rac1 GTPase translocates protein phosphatase 5 to the cell membrane and stimulates phosphatase activity in vitro." *J. Biol. Chem.* **285,** 3872–82 (2010). doi:10.1074/jbc.M109.088427 doi: 10.1074/jbc.M109.088427

258. A. Bürkle. "Poly(ADP-ribose). The most elaborate metabolite of NAD+." *FEBS J.* **272,** 4576–89 (2005). doi:10.1111/j.1742-4658.2005.04864.x doi: 10.1111/j.1742-4658.2005.04864.x

259. N. Pollak, C. Dölle, M. Ziegler. "The power to reduce: pyridine nucleotides--small molecules with a multitude of functions." *Biochem. J.* **402,** 205–18 (2007). doi:10.1042/BJ20061638 doi: 10.1042/BJ20061638

260. B. Alberts, A. Johnson, J. Lewis, M. Raff, K. Roberts, P. Walter. "Molecular Biology of the Cell" **chapter231,** 471 , Garland Science, (2002).

261. D. H. Williamson, P. Lund, H. A. Krebs. "The redox state of free nicotinamide-adenine dinucleotide in the cytoplasm and mitochondria of rat liver." *Biochem. J.* **103,** 514–27 (1967).

262. F. Sun, C. Dai, J. Xie, X. Hu. "Biochemical issues in estimation of cytosolic free NAD/NADH ratio." *PLoS One* **7,** e34525 (2012). doi:10.1371/journal.pone.0034525 doi: 10.1371/journal.pone.0034525

263. T. G. Scott, R. D. Spencer, N. J. Leonard, G. Weber. "Synthetic spectroscopic models related to coenzymes and base pairs. V. Emission properties of NADH. Studies of fluorescence lifetimes and quantum efficiencies of NADH, AcPyADH, [reduced acetylpyridineadenine dinucleotide] and simplified synthetic models" *J. Am. Chem. Soc.* **92,** 687–695 (1970).

264. Q. Yu, A. A. Heikal. "Two-photon autofluorescence dynamics imaging reveals sensitivity of intracellular NADH concentration and conformation to cell physiology at the single-cell level." *J. Photochem. Photobiol. B.* **95,** 46–57 (2009). doi:10.1016/j.jphotobiol.2008.12.010 doi: 10.1016/j.jphotobiol.2008.12.010

265. W. Zheng, D. Li, J. Y. Qu. "Monitoring changes of cellular metabolism and microviscosity in vitro based on time-resolved endogenous fluorescence and its anisotropy decay dynamics." *J. Biomed. Opt.* **15,** 037013 (2010). doi:10.1117/1.3449577 doi: 10.1117/1.3449577

266. J. C. Schell, J. Rutter. "The long and winding road to the mitochondrial pyruvate carrier" *Cancer Metab.* **1,** 1–9 (2013). doi:10.1186/2049-3002-1-6 doi: 10.1186/2049-3002-1-6

267. J. R. Lakowicz, H. Szmacinski, K. Nowaczyk, M. L. Johnson. "Fluorescence lifetime imaging of free and protein-bound NADH." *Proc. Natl. Acad. Sci. U. S. A.* **89,** 1271–5 (1992).

268. K. F. LaNoue, a C. Schoolwerth. "Metabolite transport in mitochondria." *Annu. Rev. Biochem.* **48,** 871–922 (1979). doi:10.1146/annurev.bi.48.070179.004255 doi: 10.1146/annurev.bi.48.070179.004255

269. K. Blinova, S. Carroll, S. Bose, A. V Smirnov, J. J. Harvey, J. R. Knutson, R. S. Balaban. "Distribution of mitochondrial NADH fluorescence lifetimes: steady-state kinetics of matrix NADH interactions." *Biochemistry* **44,** 2585–94 (2005). doi:10.1021/bi0485124 doi: 10.1021/bi0485124

270. K. Blinova, R. L. Levine, E. S. Boja, G. L. Griffiths, Z.-D. Shi, B. Ruddy, R. S. Balaban. "Mitochondrial NADH Fluorescence is Enhanced by Complex I Binding" *Biochemistry* **47,** 9636–9645 (2008). doi:10.1021/bi800307y.Mitochondrial doi: 10.1021/bi800307y.Mitochondrial

271. J. M. Berg, J. L. Tymoczko, L. Stryer. "Biochemistry" , W H Freeman, New York, (2002). at <http://www.ncbi.nlm.nih.gov/books/NBK21154/>

272. W. S. Kunz, W. Kunz. "Contribution of different enzymes to flavoprotein fluorescence of isolated rat liver mitochondria." *Biochim. Biophys. Acta* **841,** 237–46 (1985).

273. W. Ying. "NAD+/NADH and NADP+/NADPH in cellular functions and cell death: regulation and biological consequences." *Antioxid. Redox Signal.* **10,** 179–206 (2008). doi:10.1089/ars.2007.1672 doi: 10.1089/ars.2007.1672

274. O. Warburg, F. Wind, E. Negelein. "Über den Stoffwechsel der Tumore" , Springer, Berlin, (1926).

275. M. G. Vander Heiden, L. C. Cantley, C. B. Thompson. "Understanding the Warburg effect: the metabolic requirements of cell proliferation." *Science* **324,** 1029–33 (2009). doi:10.1126/science.1160809 doi: 10.1126/science.1160809

276. R. A. Cairns, I. S. Harris, T. W. Mak. "Regulation of cancer cell metabolism." *Nat. Rev. Cancer* **11,** 85–95 (2011). doi:10.1038/nrc2981 doi: 10.1038/nrc2981

277. L. A. Demetrius, D. K. Simon. "An inverse-Warburg effect and the origin of Alzheimer's disease." *Biogerontology* **13,** 583–94 (2012). doi:10.1007/s10522-012-9403-6 doi: 10.1007/s10522-012-9403-6

278. F. Q. Schafer, G. R. Buettner. "Redox environment of the cell as viewed through the redox state of the glutathione disulfide/glutathione couple" *Free Radic. Biol. Med.* **30,** 1191–1212 (2001). doi:10.1016/S0891-5849(01)00480-4 doi: 10.1016/S0891-5849(01)00480-4

279. L. Kussmaul, J. Hirst. "The mechanism of superoxide production by NADH:ubiquinone oxidoreductase (complex I) from bovine heart mitochondria." *Proc. Natl. Acad. Sci. U. S. A.* **103,** 7607–12 (2006). doi:10.1073/pnas.0510977103 doi: 10.1073/pnas.0510977103

280. J. Cartwright. "Natural biomarker can signal cancer" *Chem. World* (2009). at <http://www.rsc.org/chemistryworld/News/2009/April/08040903.asp>

281. M. L. Circu, T. Y. Aw. "Reactive oxygen species, cellular redox systems, and apoptosis." *Free Radic. Biol. Med.* **48,** 749–62 (2010). doi:10.1016/j.freeradbiomed.2009.12.022 doi: 10.1016/j.freeradbiomed.2009.12.022

282. J. D. Watson. "Type 2 diabetes as a redox disease." *Lancet* **383,** 841–3 (2014). doi:10.1016/S0140-6736(13)62365-X doi: 10.1016/S0140-6736(13)62365-X

283. E. H. Sarsour, M. G. Kumar, L. Chaudhuri, A. L. Kalen, P. C. Goswami. "Redox control of the cell cycle in health and disease." *Antioxid. Redox Signal.* **11,** 2985–3011 (2009). doi:10.1089/ARS.2009.2513 doi: 10.1089/ARS.2009.2513

284. G. Waris, H. Ahsan. "Reactive oxygen species: role in the development of cancer and various chronic conditions." *J. Carcinog.* **5,** 14 (2006). doi:10.1186/1477-3163-5-14 doi: 10.1186/1477-3163-5-14

285. H. Ueno, H. Miyoshi, K. Ebisui, H. Iwamura. "Comparison of the inhibitory action of natural rotenone and its stereoisomers with various NADH-ubiquinone reductases." *Eur. J. Biochem.* **225,** 411–7 (1994).

286. R. Benz, S. McLaughlin. "The molecular mechanism of action of the proton ionophore FCCP (carbonylcyanide p-trifluoromethoxyphenylhydrazone)" *Biophys. J.* **41,** 381–398 (1983).

287. G. L. Robinson, D. Dinsdale, M. Macfarlane, K. Cain. "Switching from aerobic glycolysis to oxidative phosphorylation modulates the sensitivity of mantle cell lymphoma cells to TRAIL." *Oncogene* **31,** 4996–5006 (2012). doi:10.1038/onc.2012.13 doi: 10.1038/onc.2012.13

288. Q. Zhang, S.-Y. Wang, C. Fleuriel, D. Leprince, J. V Rocheleau, D. W. Piston, R. H. Goodman. "Metabolic regulation of SIRT1 transcription via a HIC1:CtBP corepressor complex." *Proc. Natl.*

Acad. Sci. U. S. A. **104,** 829–33 (2007). doi:10.1073/pnas.0610590104 doi: 10.1073/pnas.0610590104

289. H. Pelicano, D. S. Martin, R.-H. Xu, P. Huang. "Glycolysis inhibition for anticancer treatment." *Oncogene* **25,** 4633–46 (2006). doi:10.1038/sj.onc.1209597 doi: 10.1038/sj.onc.1209597

290. L. Xue, S. Chiu, N. L. Oleinick. "Staurosporine-induced death of MCF-7 human breast cancer cells: a distinction between caspase-3-dependent steps of apoptosis and the critical lethal lesions" *Exp. Cell Res.* **283,** 135–145 (2003). doi:10.1016/S0014-4827(02)00032-0 doi: 10.1016/S0014-4827(02)00032-0

291. S. Teramoto, T. Tomita, H. Matsui, E. Ohga, T. Matsuse, Y. Ouchi. "Hydrogen peroxide-induced apoptosis and necrosis in human lung fibroblasts: protective roles of glutathione" *Jpn. J. Pharmacol.* **79,** 33–40 (1999).

292. G. Kroemer, B. Dallaporta, M. Resche-Rigon. "The mitochondrial death/life regulator in apoptosis and necrosis." *Annu. Rev. Physiol.* **60,** 619–42 (1998). doi:10.1146/annurev.physiol.60.1.619 doi: 10.1146/annurev.physiol.60.1.619

293. T. C. Jorgenson, W. Zhong, T. D. Oberley. "Redox imbalance and biochemical changes in cancer." *Cancer Res.* **73,** 6118–23 (2013). doi:10.1158/0008-5472.CAN-13-1117 doi: 10.1158/0008-5472.CAN-13-1117

294. Y. P. Hung, J. G. Albeck, M. Tantama, G. Yellen. "Imaging cytosolic NADH-NAD(+) redox state with a genetically encoded fluorescent biosensor." *Cell Metab.* **14,** 545–54 (2011). doi:10.1016/j.cmet.2011.08.012 doi: 10.1016/j.cmet.2011.08.012

295. E. J. Dell, B. M. G. Labtech. "Detection of NADH and NADPH with the Omega ' s High Speed , Full UV / Vis Absorbance Spectrometer" 3–4 (2008).

296. J. L. Sporty, M. M. Kabir, K. W. Turteltaub, T. Ognibene, S. J. Lin, G. Bench. "Single sample extraction protocol for the quantification of NAD and NADH redox states in Saccharomyces cerevisiae" *J. Sep. Sci.* **31,** 3202–3211 (2008). doi:10.1002/jssc.200800238.Single doi: 10.1002/jssc.200800238.Single

297. Y. Avi-Dor, J. M. Olson, M. D. Doherty, N. O. Kaplan. "Fluorescence of pyridine nucleotides in mitochondria" *J. Biol. Chem.* **237,** 2377–2383 (1962).

298. B. Chance, B. Schoener, R. Oshino, F. Itshak. "Oxidation-reduction ratio studies of mitochondria in freeze-trapped samples. NADH and flavoprotein fluorescence signals" *J. Biol. Chem.* **254,** 4764–4771 (1979).

299. M. C. Skala, K. M. Riching, D. K. Bird, A. Gendron-Fitzpatrick, J. Eickhoff, K. W. Eliceiri, P. J. Keely, N. Ramanujam. "In vivo multiphoton fluorescence lifetime imaging of protein-bound and free nicotinamide adenine dinucleotide in normal and precancerous epithelia." *J. Biomed. Opt.* **12,** 024014 (2007). doi:10.1117/1.2717503 doi: 10.1117/1.2717503

300. S. Huang, A. A. Heikal, W. W. Webb. "Two-photon fluorescence spectroscopy and microscopy of NAD(P)H and flavoprotein." *Biophys. J.* **82,** 2811–25 (2002). doi:10.1016/S0006-3495(02)75621-X doi: 10.1016/S0006-3495(02)75621-X

301. J. H. Ostrander, C. M. McMahon, S. Lem, S. R. Millon, J. Q. Brown, V. L. Seewaldt, N. Ramanujam. "Optical redox ratio differentiates breast cancer cell lines based on estrogen receptor

status." *Cancer Res.* **70,** 4759–66 (2010). doi:10.1158/0008-5472.CAN-09-2572 doi: 10.1158/0008-5472.CAN-09-2572

302. S. Maleki, R. Sepehr, K. Staniszewski, N. Sheibani, C. M. Sorenson, M. Ranji. "Optical cryo-imaging of kidney mitochondrial redox state in diabetic mouse models" in *SPIE BiOS* (Farkas, D. L., Nicolau, D. V. & Leif, R. C.) 82252A–82252A–6 , International Society for Optics and Photonics, (2012). doi:10.1117/12.909394doi:10.1117/12.909394 doi: 10.1117/12.909394

303. W. L. Rice, D. L. Kaplan, I. Georgakoudi. "Two-photon microscopy for non-invasive, quantitative monitoring of stem cell differentiation." *PLoS One* **5,** e10075 (2010). doi:10.1371/journal.pone.0010075 doi: 10.1371/journal.pone.0010075

304. I. Georgakoudi, K. P. Quinn. "Optical imaging using endogenous contrast to assess metabolic state." *Annu. Rev. Biomed. Eng.* **14,** 351–67 (2012). doi:10.1146/annurev-bioeng-071811-150108 doi: 10.1146/annurev-bioeng-071811-150108

305. V. V Ghukasyan, F. Kao. "Monitoring Cellular Metabolism with Fluorescence Lifetime of Reduced Nicotinamide Adenine Dinucleotide" *J. Phys. Chem.* **113,** 11532–11540 (2009).

306. R. Niesner, B. Peker, P. Schlüsche, K.-H. Gericke. "Noniterative biexponential fluorescence lifetime imaging in the investigation of cellular metabolism by means of NAD(P)H autofluorescence." *Chemphyschem* **5,** 1141–9 (2004). doi:10.1002/cphc.200400066 doi: 10.1002/cphc.200400066

307. B. Chance, P. Cohen, F. Jobsis, B. Schoener. "Intracellular oxidation-reduction states in vivo." *Science* **137,** 499–508 (1962).

308. J. R. Lakowicz. "Principles of Fluorescence" 1 , Springer, New York, (2006). at <http://books.google.co.uk/books?id=-PSybuLNxcAC>

309. L. K. Klaidman, A. C. Leung, J. D. Adams Jr. "High-performance liquid chromatography analysis of oxidised and reduced pyridine dinucleotides in specific brain regions" 312–317 (1995).

310. T. S. Blacker, Z. F. Mann, J. E. Gale, M. Ziegler, A. J. Bain, G. Szabadkai, M. R. Duchen. "Separating NADH and NADPH fluorescence in live cells and tissues using FLIM." *Nat. Commun.* **5,** 3936 (2014). doi:10.1038/ncomms4936 doi: 10.1038/ncomms4936

311. M. C. Skala, K. M. Riching, A. Gendron-Fitzpatrick, J. Eickhoff, K. W. Eliceiri, J. G. White, N. Ramanujam. "In vivo multiphoton microscopy of NADH and FAD redox states, fluorescence lifetimes, and cellular morphology in precancerous epithelia." *Proc. Natl. Acad. Sci. U. S. A.* **104,** 19494–9 (2007). doi:10.1073/pnas.0708425104 doi: 10.1073/pnas.0708425104

312. A. J. Walsh, R. S. Cook, H. C. Manning, D. J. Hicks, A. Lafontant, C. L. Arteaga, M. C. Skala. "Optical metabolic imaging identifies glycolytic levels, sub-types and early treatment response in breast cancer" *Cancer Res.* **73,** 6164–6174 (2013).

313. N. D. Evans, L. Gnudi, O. J. Rolinski, D. J. S. Birch, J. C. Pickup. "Glucose-dependent changes in NAD(P)H-related fluorescence lifetime of adipocytes and fibroblasts in vitro: potential for non-invasive glucose sensing in diabetes mellitus." *J. Photochem. Photobiol. B.* **80,** 122–9 (2005). doi:10.1016/j.jphotobiol.2005.04.001 doi: 10.1016/j.jphotobiol.2005.04.001

314. D. K. Bird, L. Yan, K. M. Vrotsos, K. W. Eliceiri, E. M. Vaughan, P. J. Keely, J. G. White, N. Ramanujam. "Metabolic mapping of MCF10A human breast cells via multiphoton fluorescence

lifetime imaging of the coenzyme NADH." *Cancer Res.* **65,** 8766–73 (2005). doi:10.1158/0008-5472.CAN-04-3922 doi: 10.1158/0008-5472.CAN-04-3922

315. H. Schneckenburger, M. Wagner, P. Weber, W. S. L. Strauss, R. Sailer. "Autofluorescence lifetime imaging of cultivated cells using a UV picosecond laser diode." *J. Fluoresc.* **14,** 649–54 (2004).

316. D. Li, W. Zheng, J. Y. Qu. "Time-resolved spectroscopic imaging reveals the fundamentals of cellular NADH fluorescence." *Opt. Lett.* **33,** 2365–7 (2008).

317. H.-W. Wang, Y.-H. Wei, H.-W. Guo. "Reduced nicotinamide adenine dinucleotide (NADH) fluorescence for the detection of cell death." *Anticancer. Agents Med. Chem.* **9,** 1012–7 (2009).

318. H.-W. Wang, V. Gukassyan, C.-T. Chen, Y.-H. Wei, H.-W. Guo, J.-S. Yu, F.-J. Kao. "Differentiation of apoptosis from necrosis by dynamic changes of reduced nicotinamide adenine dinucleotide fluorescence lifetime in live cells." *J. Biomed. Opt.* **13,** 054011 (2008). doi:10.1117/1.2975831 doi: 10.1117/1.2975831

319. R. Nahta, D. Yu, M.-C. Hung, G. N. Hortobagyi, F. J. Esteva. "Mechanisms of disease: understanding resistance to HER2-targeted therapy in human breast cancer." *Nat. Clin. Pract. Oncol.* **3,** 269–80 (2006). doi:10.1038/ncponc0509 doi: 10.1038/ncponc0509

320. K. König, A. Uchugonova, E. Gorjup. "Multiphoton fluorescence lifetime imaging of 3D-stem cell spheroids during differentiation." *Microsc. Res. Tech.* **74,** 9–17 (2011). doi:10.1002/jemt.20866 doi: 10.1002/jemt.20866

321. B. K. Wright, L. M. Andrews, J. Markham, M. R. Jones, C. Stringari, M. A. Digman, E. Gratton. "NADH distribution in live progenitor stem cells by phasor-fluorescence lifetime image microscopy." *Biophys. J.* **103,** L7–9 (2012). doi:10.1016/j.bpj.2012.05.038 doi: 10.1016/j.bpj.2012.05.038

322. C. Stringari, J. L. Nourse, L. a Flanagan, E. Gratton. "Phasor fluorescence lifetime microscopy of free and protein-bound NADH reveals neural stem cell differentiation potential." *PLoS One* **7,** e48014 (2012). doi:10.1371/journal.pone.0048014 doi: 10.1371/journal.pone.0048014

323. D. J. Kelly, S. C. Warren, S. Kumar, J. L. Lagarto, B. T. Dyer, A. Margineanu, E. W.-F. Lam, C. Dunsby, P. M. W. French. "An automated multiwell plate reading FLIM microscope for live cell autofluorescence lifetime assays" *J. Innov. Opt. Health Sci.* **7,** 1450025 (2013). doi:10.1142/S1793545814500254 doi: 10.1142/S1793545814500254

324. "Mass Spectrometry of Proteins and Peptides" 554 , Springer, (2000). at <http://books.google.com/books?id=tjeBdjwCIe8C&pgis=1>

325. P. M. Dixon, J. H. K. Pechmann. "A statistical test to show negligible trend" *Ecology* **86,** 1751–1756 (2008).

326. A. R. Feinstein. "Principles of Medical Statistics" 713 , CRC Press, Boca Raton, (2001).

327. T. J. Cleophas, A. H. Zwinderman. "Statistics Applied to Clinical Studies" 69–75 , Springer Netherlands, Dordrecht, (2012). doi:10.1007/978-94-007-2863-9doi:10.1007/978-94-007-2863-9 doi: 10.1007/978-94-007-2863-9

328. A. Trujillo-Ortiz, R. Hernandez-Walls. "BFTest: Brown-Forsythe's test for homogeneity of variances. A MATLAB file." (2003). at <http://www.mathworks.co.uk/matlabcentral/fileexchange/3412-bftest>

329. N. Pokala. "dunnett.m" *MATLAB Cent. File Exch.* (2012). at <http://www.mathworks.co.uk/matlabcentral/fileexchange/38157-dunnett-m>

330. P. A. Duffy. in *Methods Mol. Biol. Vitr. Toxic. Test. Protoc.* (O'Hare, S. & Atterwill, C. K.) **43,** 219–26 , Humana Press, New York, (1995). doi:10.1385/0-89603-282-5:219 doi: 10.1385/0-89603-282-5:219

331. G. Batist, A. Tulpule, B. K. Sinha, A. G. Katki, C. E. Myers, K. H. Cowan. "Overexpression of a novel anionic glutathione transferase in multidrug-resistant human breast cancer cells." *J. Biol. Chem.* **261,** 15544–9 (1986).

332. L. N. Harris, L. Yang, V. Liotcheva, S. Pauli, J. D. Iglehart, O. M. Colvin, T. S. Hsieh. "Induction of Topoisomerase II Activity after ErbB2 Activation Is Associated with a Differential Response to Breast Cancer Chemotherapy Advances in Brief Induction of Topoisomerase II Activity after ErbB2 Activation Is Associated with a Differential Respon" *Clin. Cancer Res.* **7,** 1497–1504 (2001).

333. E. Gajewski, S. Gaur, S. A. Akman, L. Matsumoto, J. N. A. van Balgooy, J. H. Doroshow. "Oxidative DNA base damage in MCF-10A breast epithelial cells at clinically achievable concentrations of doxorubicin." *Biochem. Pharmacol.* **73,** 1947–56 (2007). doi:10.1016/j.bcp.2007.03.022 doi: 10.1016/j.bcp.2007.03.022

334. K. Subik, J.-F. Lee, L. Baxter, T. Strzepek, D. Costello, P. Crowley, L. Xing, M.-C. Hung, T. Bonfiglio, D. G. Hicks, P. Tang. "The Expression Patterns of ER, PR, HER2, CK5/6, EGFR, Ki-67 and AR by Immunohistochemical Analysis in Breast Cancer Cell Lines" *Breast Cancer Basic Clin. Res.* **4,** 35–41 (2010).

335. S. K. Manna, C. Gangadharan, D. Edupalli, N. Raviprakash, T. Navneetha, S. Mahali, M. Thoh. "Ras puts the brake on doxorubicin-mediated cell death in p53-expressing cells." *J. Biol. Chem.* **286,** 7339–47 (2011). doi:10.1074/jbc.M110.191916 doi: 10.1074/jbc.M110.191916

336. D. L. Holliday, V. Speirs. "Choosing the right cell line for breast cancer research." *Breast Cancer Res.* **13,** 215 (2011). doi:10.1186/bcr2889 doi: 10.1186/bcr2889

337. C. B. Walsh, E. I. Franses. "Ultrathin PMMA films spin-coated from toluene solutions" *Thin Solid Films* **429,** 71–76 (2003). doi:10.1016/S0040-6090(03)00031-2 doi: 10.1016/S0040-6090(03)00031-2

338. A. El-Labban, A. Zisserman, Y. Toyoda, A. Bird, A. Hyman. "Dynamic Time Warping for Automated Cell Cycle Labelling" in *Microsc. Image Anal. with Appl. Biol.* 1–6 , (2011).

339. J. Marrison, L. Räty, P. Marriott, P. O'Toole. "Ptychography--a label free, high-contrast imaging technique for live cells using quantitative phase information." *Sci. Rep.* **3,** 2369 (2013). doi:10.1038/srep02369 doi: 10.1038/srep02369

340. H. Alborzinia, S. Can, P. Holenya, C. Scholl, E. Lederer, I. Kitanovic, S. Wölfl. "Real-time monitoring of cisplatin-induced cell death." *PLoS One* **6,** e19714 (2011). doi:10.1371/journal.pone.0019714 doi: 10.1371/journal.pone.0019714

341. J.-S. Yu, H.-W. Guo, C.-H. Wang, Y.-H. Wei, H.-W. Wang. "Increase of reduced nicotinamide adenine dinucleotide fluorescence lifetime precedes mitochondrial dysfunction in staurosporine-induced apoptosis of HeLa cells." *J. Biomed. Opt.* **16,** 036008 (2011). doi:10.1117/1.3560513 doi: 10.1117/1.3560513

342. Arthritis Research UK. "OSTEOARTHRITIS IN GENERAL PRACTICE," 1–36 , (2013).

343. D. Heinegård, T. Saxne. "The role of the cartilage matrix in osteoarthritis." *Nat. Rev. Rheumatol.* **7,** 50–6 (2011). doi:10.1038/nrrheum.2010.198 doi: 10.1038/nrrheum.2010.198

344. M. J. O'Malley, C. R. Chu. "Arthroscopic optical coherence tomography in diagnosis of early arthritis." *Minim. Invasive Surg.* **2011,** 671308 (2011). doi:10.1155/2011/671308 doi: 10.1155/2011/671308

345. A. Mobasheri. "Osteoarthritis year 2012 in review: biomarkers." *Osteoarthritis Cartilage* **20,** 1451–64 (2012). doi:10.1016/j.joca.2012.07.009 doi: 10.1016/j.joca.2012.07.009

346. C. R. Chu, A. A. Williams, C. H. Coyle, M. E. Bowers. "Early diagnosis to enable early treatment of pre-osteoarthritis." *Arthritis Res. Ther.* **14,** 212 (2012). doi:10.1186/ar3845 doi: 10.1186/ar3845

347. P. Zrimšek, V. K. Kos, J. Mrkun, M. Kosec. "Diagnostic Value of MMP-2 and MMP-9 in Synovial Fluid for Identifying Osteoarthritis in the Distal Interphalangeal Joint in Horses" *Acta Vet. Brno* **76,** 87–95 (2007). doi:10.2754/avb200776010087 doi: 10.2754/avb200776010087

348. J. H. Ryu, A. Lee, J. H. Na, S. Lee, H. J. Ahn, J. W. Park, C.-H. Ahn, B.-S. Kim, I. C. Kwon, K. Choi, I. Youn, K. Kim. "Optimization of matrix metalloproteinase fluorogenic probes for osteoarthritis imaging." *Amino Acids* **41,** 1113–22 (2011). doi:10.1007/s00726-010-0769-y doi: 10.1007/s00726-010-0769-y

349. G. A. Wagnieres, W. M. Star, B. C. Wilson. "Invited Review ln Vivo Fluorescence Spectroscopy and Imaging for Oncological Applications" *Photochem. Photobiol.* **68,** 603–632 (1998).

350. H. B. Manning, M. B. Nickdel, K. Yamamoto, J. L. Lagarto, D. J. Kelly, C. B. Talbot, G. Kennedy, J. Dudhia, J. Lever, C. Dunsby, P. French, Y. Itoh. "Detection of cartilage matrix degradation by autofluorescence lifetime." *Matrix Biol.* **32,** 32–8 (2013). doi:10.1016/j.matbio.2012.11.012 doi: 10.1016/j.matbio.2012.11.012

351. A. Uchugonova, K. König. "Two-photon autofluorescence and second-harmonic imaging of adult stem cells." *J. Biomed. Opt.* **13,** 054068 (2011). doi:10.1117/1.3002370 doi: 10.1117/1.3002370

352. J. M. Squirrell, J. J. Fong, C. A. Ariza, A. Mael, K. Meyer, N. K. Shevde, A. Roopra, G. E. Lyons, T. J. Kamp, K. W. Eliceiri, B. M. Ogle. "Endogenous fluorescence signatures in living pluripotent stem cells change with loss of potency." *PLoS One* **7,** e43708 (2012). doi:10.1371/journal.pone.0043708 doi: 10.1371/journal.pone.0043708

353. Cellular Dynamics International. "iCell products" at <http://www.cellulardynamics.com/>

354. A. Bednarkiewicz, R. M. Rodrigues, M. P. Whelan. "Non-invasive monitoring of cytotoxicity based on kinetic changes of cellular autofluorescence." *Toxicol. In Vitro* **25,** 2088–94 (2011). doi:10.1016/j.tiv.2011.09.008 doi: 10.1016/j.tiv.2011.09.008

355. H. D. Vishwasrao, A. A. Heikal, K. A. Kasischke, W. W. Webb. "Conformational dependence of intracellular NADH on metabolic state revealed by associated fluorescence anisotropy." *J. Biol. Chem.* **280,** 25119–26 (2005). doi:10.1074/jbc.M502475200 doi: 10.1074/jbc.M502475200

356. C. Thaler, S. V Koushik, P. S. Blank, S. S. Voge, S. S. Vogel. "Quantitative multiphoton spectral imaging and its use for measuring resonance energy transfer." *Biophys. J.* **89,** 2736–49 (2005). doi:10.1529/biophysj.105.061853 doi: 10.1529/biophysj.105.061853

357. S. V Koushik, H. Chen, C. Thaler, H. L. Puhl, S. S. Vogel. "Cerulean, Venus, and VenusY67C FRET reference standards." *Biophys. J.* **91,** L99–L101 (2006). doi:10.1529/biophysj.106.096206 doi: 10.1529/biophysj.106.096206

358. Addgene. "C5V plasmid map" at <http://www.addgene.org/26394/sequences>

359. Addgene. "C17V plasmid map" at <http://www.addgene.org/26395/sequences>

360. Addgene. "C32V plasmid map" at <http://www.addgene.org/26396/sequences/>

361. J. J. Chan. "Comparative Analysis of Interactions of the RASSF Family Mediated by the Ras-association (RA) and SARAH domains" (2013).

362. PHOGEMON project. "Raichu1237x sequence" at <http://www.fret.lif.kyoto-u.ac.jp/e-phogemon/data/pRaichu1237X.nuc>

Appendix 1: Derivation of expression for appropriate thresholding of HRI photon counting images

To establish the magnitude of CCD noise, 100 images acquired with the CCD capped were analysed. The average standard deviation calculated across repeat images is denoted σ_{CCD}. The distribution of background intensities was found to be well modelled by a Gaussian with mean zero and variance σ_{CCD}^2.

When images are convolved with a circular kernel of radius r, effective CCD noise becomes:

$$\tilde{\sigma}_{CCD} = -\frac{\pi r^2 \cdot \sigma_{CCD}}{\sqrt{\pi r^2}} = \sqrt{\pi r^2} \cdot \sigma_{CCD}$$

If the extent of the "cloud" of signal from a single photon event is smaller than the kernel, the total number of counts in the cluster is given by the maximum value of the smoothed cluster.

Since CCD noise follows a Gaussian distribution with mean zero and variance , the probability of a false positive in a pixel is given by

$$p_1 = \frac{1}{2}\left[1 + \mathrm{erf}\left(\frac{-t}{\sqrt{2} \cdot \tilde{\sigma}_{CCD}}\right)\right]$$

where t is the threshold value above which a photon event is counted in the smoothed image. Since p_1 is small and the number of pixels per image n_{pix} is large, a Poisson approximation may be adopted to describe the distribution of false positives in the image with mean $\lambda = n_{pix} \cdot p_1$. The probability of more than zero false positives in the image is given by

$$\begin{aligned} p &= 1 - P(\mathrm{FP} = 0) \\ &= 1 - \frac{\lambda^0 \exp(-\lambda)}{0!} \\ &\approx n_{px} \cdot p_1 \\ &\approx \frac{n_{px}}{2}\left[1 + \mathrm{erf}\left(-\frac{t}{\sqrt{2} \cdot \tilde{\sigma}_{\mathrm{CCD}}}\right)\right] \end{aligned}$$

since p and therefore λ is small. Therefore, for a desired false positive rate p per image, the appropriate thresholding is given by

$$t = \sqrt{2} \cdot \sqrt{\pi r^2} \cdot \sigma_{\mathrm{CCD}} \cdot \mathrm{erf}^{-1}\left(1 - \frac{2p}{n_{px}}\right)$$

Appendix 2: FRET constructs: further details

Maps showing plasmids used in the work presented in this thesis are shown here, where available. In cases where collaborators were unable to provide plasmid maps or sequences, as complete a summary as possible of the process used to generate the plasmids is presented with references.

Cerulean-Venus FRET constructs

Descriptions of the process for generating C5V, C17V and C32V FRET constructs are found in literature[356,357]. Plasmid maps for constructs exist on Addgene, where the plasmids were sourced from. Based on the plasmid map and sequence for C5V, the linker between the two fluorescent proteins is identified as consisting of S-G-L-R-S amino acids. Work published previously by the group that originally generated the constructs identifies the five amino acid linker as flexible[82]. Plasmid maps downloaded from Addgene are presented in Figure A2 - 1 for reference.

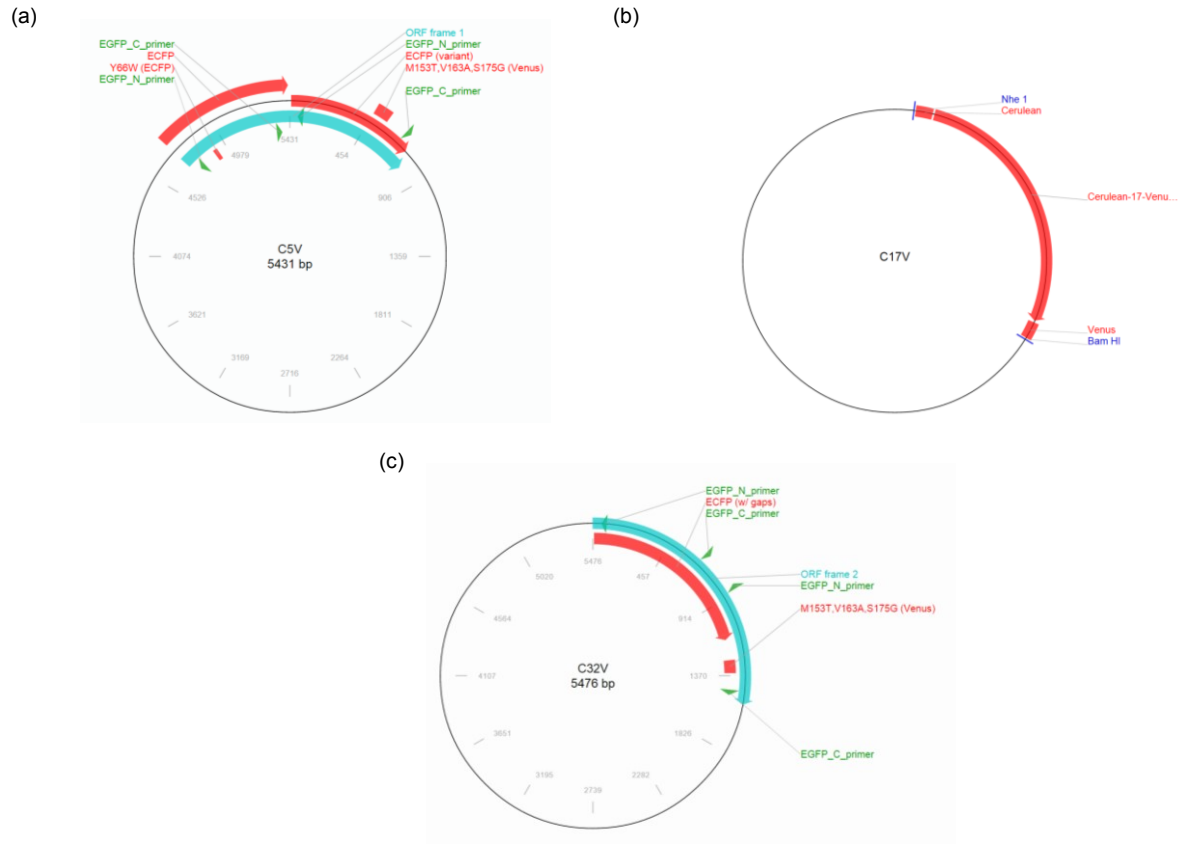

Figure A2 - 1 Plasmid maps for Cerulean-Venus FRET constructs downloaded from Addgene, for reference.
(a) C5V[358]; (b) C17V[359]; (c) C32V[360]. Restriction site labels and resistance genes omitted for clarity.

FOXM1-SUMOylation constructs

FOXM1-EGFP constructs were generated by Steve Myatt, a former post-doc in the Lam group. No plasmid map, sequence or cloning strategy could be sourced for the FOXM1 constructs; it is known,

however, that full length FOXM1/FOXM1mut were subcloned into peGFP-C1 vector (Clontech) to generate donor constructs[188], whilst the SUMO1-TRT was generated by replacing the mRFP1 sequence present on the construct gifted from the Ng lab[202].

RASSF-family interaction screen constructs

A complete description of the constructs and cloning methods is presented in Jia Chan's Ph. D. thesis[361]. In summary, donor constructs were cloned using the Gateway® cloning method (Invitrogen), inserting the RASSF family gene of interest into pDONR207 entry vectors and then combining with compatible destination vectors generated by inserting an RfC.1 Gateway® reading frame cassette into commercially pEGFP-C1 vector (Clontech). The RASSF1-EGFP plasmid (Figure 4-18 (c)) is presented in Figure A2 - 2 (a). Acceptor constructs are generated by restriction digest and ligation, using KOD polymerase to generate inserts with BglII and HindIII restriction sites which are then ligated into the multiple cloning site of a pmCherry-C1 vector. An exemplar plasmid map for the full length MST1-mCherry construct (Figure 4-18 (c)) is presented in Figure A2 - 2 (b).

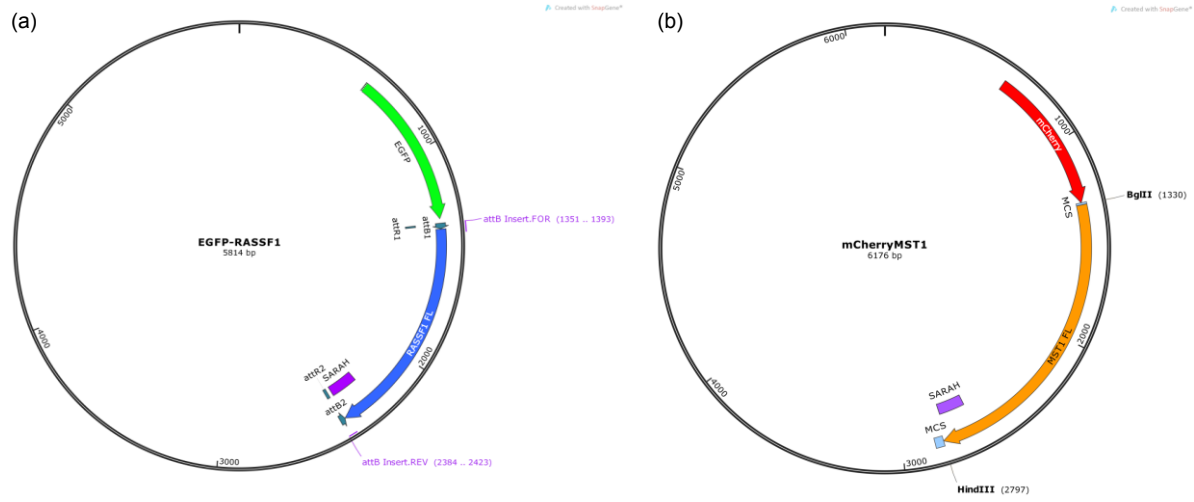

Figure A2 - 2 Exemplar plasmid maps from RASSF family interaction screen for reference.
(a) EGFP-RASSF1; (b) mCherry-MST1. Rendered in SnapGene.

Small GTPase activation constructs

The methods used for generating GFP-mRFP variants of small GTPase biosensors have been described previously[256]; in summary, the sensor region was excised from between the original CFP and YFP fluorescent proteins and inserted between mRFP1 and EGFP in a modified pEGFP-N1 vector (Clontech). This was done in such a way as to preserve the linkers in the original Raichu construct, determined in the original publication to be L-D between the acceptor and the protein binding domain, T-G-G-G-G-T between the binding domain and the small GTPase, and G-G-R between the GTPase and the donor[224] (schematic representations of constructs are found in Figure 5-2 and Figure 5-10). For reference, a map of the *original* Raichu probe rendered in SnapGene to highlight relevant regions is presented in Figure A2 - 3.

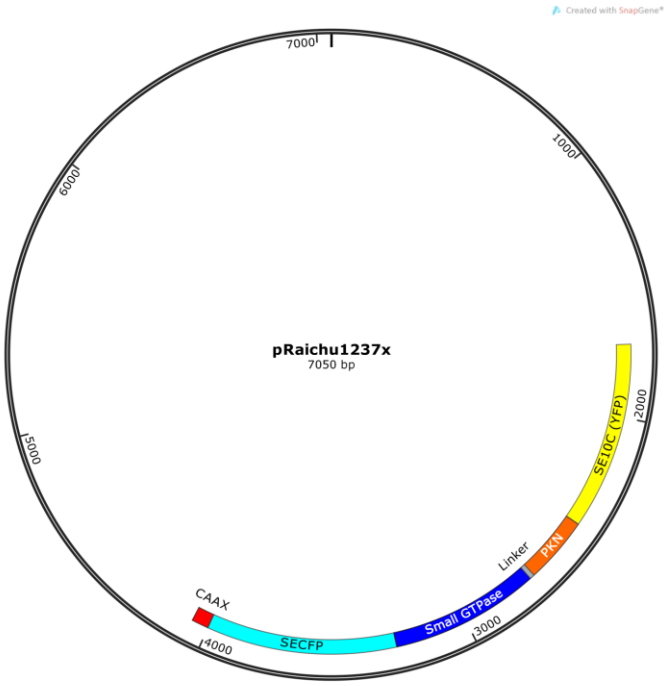

Figure A2 - 3 Plasmid maps for original Raichu probe for reference.
Sequence downloaded from Phogemon website[362]; rendered in SnapGene.